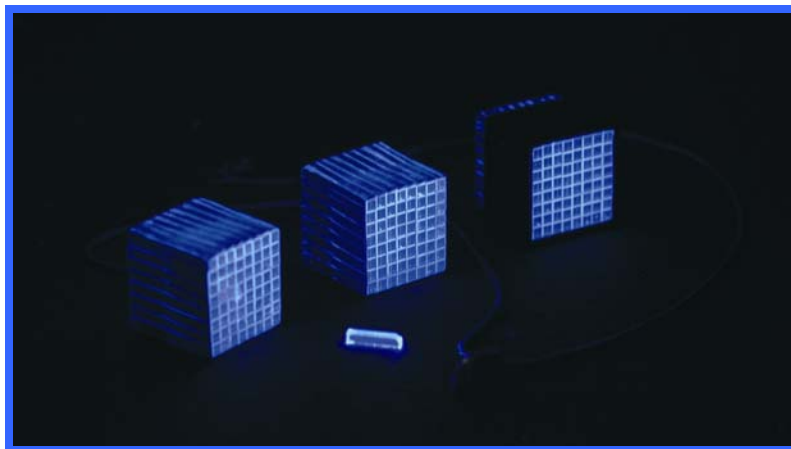




DISSERTATION

Evaluation of New Inorganic Scintillators for Application in a Prototype Small Animal PET Scanner



Claudia Kuntner

May 2003

DISSERTATION

**Evaluation of New Inorganic Scintillators for
Application in a Prototype Small Animal PET
Scanner**

ausgeführt zum Zwecke der Erlangung des akademischen Grades eines Doktors der
technischen Wissenschaften unter der Leitung von

Univ. Prof. Dr. Hannes Aiginger
Atominstitut der Österreichischen Universitäten (E141)

und

Dr. Paul Lecoq
CERN, Schweiz

eingereicht an der Technischen Universität Wien
Technisch-Naturwissenschaftliche Fakultät

von

Dipl.-Ing. Claudia Kuntner

Matr.Nr. 9426532
Weinbergstrasse 33
A - 3512 Mautern

Genf, am 21. Mai 2003

Kurzfassung

Positronen-Emissions-Tomographie (PET) ist eine wichtige Methode bei der Studie von neuen Pharmazeutika ebenso wie in der Gehirn und genetischen Forschung. Kleine Tiere wie Mäuse werden oft verwendet um ausgeklügelte Modelle menschlicher Krankheiten zu testen. Um die reduzierten Dimensionen der Organe abzubilden, benötigt man eine Messtechnik mit hoher räumlicher Auflösung. In den meisten medizinischen Diagnosegeräten werden anorganische Szintillatoren verwendet. Die erreichbare Leistung eines PET Scanners ist eng verbunden mit den Szintillationseigenschaften der Kristalle. In den letzten Jahren wurde versucht neue Szintillatoren mit hoher Lichtausbeute, großer Detektionseffizienz und schneller Abklingzeit zu entwickeln. Die meisten untersuchten Verbindungen sind Cer dotierte Szintillatoren, wie z.B. LSO:Ce, YAP:Ce, LuAP:Ce, und seit kurzem auch gemischte $\text{Lu}_x(\text{RE}^{3+})_{1-x}\text{AlO}_3\text{:Ce}$ Kristalle. Diese Kristalle sind von hohem Interesse für die medizinische Anwendung, da sie eine hohe Dichte (außer YAP:Ce), eine kurze Abklingzeit und eine hohe Lichtausbeute aufweisen.

Diese Arbeit behandelt die Entwicklung von Cer dotierten LuYAP Kristallen (mit verschiedener Yttrium Konzentration), für eine Anwendung in mehreren Kleintier PET Scannern. Die Szintillationseigenschaften und Mechanismen von auf Lutetium basierenden Oxyorthosilikaten wurden studiert.

Die Ergebnisse der Lichtausbeute, Energieauflösung und Abklingzeit für alle untersuchten Verbindungen werden präsentiert. Die Nicht-Proportionalität der Lichtausbeute von der Energie der Photonen, und die intrinsische Energieauflösung werden ebenso diskutiert. Die optischen Charakteristiken wie z.B. die Anregungs-, Emissions-, und Absorptionsspektren wurden gemessen, und wichtige Zusammenhänge mit den Szintillationseigenschaften werden dargelegt.

Eine Reihe von Forschern untersuchen zurzeit Phoswich Detektoren für die Anwendung von depth-of-interaction (DOI) Messungen in PET. Die Crystal Clear Collaboration plant mehrer Kleintier PETs unter der Verwendung von LuYAP und LSO Kristallen zu konstruieren. Der Kristall der Interaktion wird an Hand der aufgenommenen Pulsform identifiziert. Die ersten Resultate von der Kombination der LuYAP:Ce und der LSO:Ce Kristalle in der Phoswich Anordnung werden präsentiert. Der neue DOI Detektor ist einsetzbar für hoch auflösende PET.

Abstract

In the study of new pharmaceuticals as well as brain and genetic research, Positron Emission Tomography (PET) is a useful method. It has also recently entered the clinical domain in cardiology and particularly in oncology. Small animals such as mice, are often used to validate sophisticated models of human disease. High spatial resolution PET instrumentation is therefore necessary due to the reduced dimensions of the organs. Inorganic scintillators are employed in most of the diagnostic imaging devices. The ultimate performance of the PET scanner is tightly bound to the scintillation properties of the crystals. In the last years there has been an effort to develop new scintillating materials characterized by high light output, high detection efficiency and fast decay time. The most studied systems are mainly Ce^{3+} -doped crystals such as LSO:Ce, YAP:Ce, LuAP:Ce, and recently also mixed $\text{Lu}_x(\text{RE}^{3+})_{1-x}\text{AlO}_3\text{:Ce}$ crystals. These crystals are very attractive for medical application because of their high density (with the exception of YAP:Ce), short decay time, and high light output.

This work deals with the development of cerium doped LuYAP crystals, with varying amount of yttrium, for application in several small animal PET scanners. In addition the scintillation properties and mechanism of lutetium based oxyorthosilicates are investigated.

The results in light yield, energy resolution and decay time are presented for all the studied compounds. The light yield non-proportionality on photon energy was studied as well as the intrinsic energy resolution. Optical characteristics such as excitation, emission and absorption spectra were measured and important correlations with the scintillation properties are pointed out.

Phoswich detectors are currently being considered by a number of investigators for depth of interaction (DOI) measurements in PET. The Crystal Clear Collaboration plans to construct several small animal PET scanners using LuYAP and LSO crystals. The identification of the layer of interaction is done using the pulse shape of the corresponding scintillator material. First results on the combination of LuYAP:Ce crystals with LSO:Ce crystals in phoswich geometry for the final PET scanner are presented. The experimental results show that the new DOI technique is applicable for high-resolution PET systems.

To my parents

"Beta decay was... like a dear old friend. There would always be a special place in my heart reserved especially for it."

Chien-Shiung Wu
1912 - 1997

Contents

1	General Introduction	1
1.1	Inorganic Scintillators in Medical Imaging	1
1.1.1	Small Animal Studies	2
1.2	Crystal Clear Collaboration	2
1.3	Scope of this Thesis	4
2	PET Imaging	5
2.1	PET Overview	5
2.1.1	Radiopharmaceuticals	5
2.1.2	Conventional PET	7
2.2	Coincidence Detection and Dead Time	9
2.3	Scintillator Requirements for PET	10
2.3.1	Detection Efficiency	11
2.3.2	Photoelectric Fraction	11
2.3.3	Decay Time	13
2.3.4	Light Output	14
2.3.5	Energy Resolution	14
2.4	Scintillation Detector Module Trends for PET	15
2.5	Future Directions	18
2.5.1	Fully 3-D PET	18
2.5.2	Time of Flight PET	18
2.5.3	Solid State Photodetectors	19
2.5.4	Depth of Interaction	19
2.6	Small Animal PET Scanner	21
2.7	References	23

3	Scintillation Materials	25
3.1	Crystal Growth	26
3.1.1	Czochralski Growth – Crystal Pulling	26
3.1.2	Bridgman / Stockbarger Technique	27
3.1.3	Growth of Oxide Crystals	28
3.1.4	Production of $\text{Lu}_{1-x}\text{Y}_x\text{AlO}_3\text{:Ce}$	29
3.1.5	Crystallography and Phase Diagram for LuAP	30
3.2	Luminescence of Inorganic Crystals	33
3.2.1	The Energy Band Model	33
3.2.2	Conditions for Luminescence of a Center	35
3.3	Physical Mechanism of Scintillation	37
3.3.1	Energy Bands and Transitions in Inorganic Crystals	38
3.3.2	Scintillation Efficiency	39
3.4	General Characteristics of Inorganic Scintillators	41
3.4.1	Decay Time	41
3.4.2	Afterglow	42
3.4.3	Theory on Energy Resolution	43
3.4.4	Non-Proportional Response	44
3.4.5	Temperature Response	45
3.4.6	Optical Properties	46
3.5	References	47
4	Experimental Techniques	51
4.1	Introduction	51
4.2	Optical Characterization	51
4.3	Light Output and Energy Resolution	53
4.3.1	Experimental Procedure	54
4.4	Scintillation Decay Time	56
4.5	Low Temperature Thermoluminescence	58
4.5.1	Theory of the Glow Curve	59
4.5.2	Experimental Set-up	60
4.6	Tagging Measurements in the Phoswich Assembly	61
4.7	References	62

5	Luminescence and Scintillation Properties of $\text{Lu}_{1-x}\text{Y}_x\text{AP}:\text{Ce}$ Crystals	63
5.1	Luminescence Properties of Cerium-Activated Compounds	63
5.1.1	Excitation Spectra	64
5.1.2	Absorption Spectra.....	65
5.1.3	UV excited Emission Spectra	67
5.1.4	X-ray excited Emission Spectra.....	69
5.2	Light Output and Energy Resolution.....	70
5.2.1	Experimental Procedure.....	70
5.2.2	Results for the LuAP and $\text{Lu}_{0.8}\text{Y}_{0.2}\text{AP}$ Samples	70
5.2.3	Results for the $\text{Lu}_{0.7}\text{Y}_{0.3}\text{AP}$ Samples from BTCP	74
5.2.4	Reproducibility of the Measurements	77
5.3	Intrinsic Energy Resolution.....	77
5.4	Non-Proportional Response	78
5.4.1	Degree of Non-Proportionality σ_{np}	81
5.5	Scintillation Decay Time.....	82
5.5.1	Results for the LuAP and $\text{Lu}_{0.8}\text{Y}_{0.2}\text{AP}$ Samples	82
5.5.2	Results for the $\text{Lu}_{0.7}\text{Y}_{0.3}\text{AP}$ Samples.....	83
5.6	Low Temperature TL	86
5.6.1	Thermoluminescence Study on LuAP	86
5.6.2	Thermoluminescence Study on $\text{Lu}_{0.8}\text{Y}_{0.2}\text{AP}$	87
5.6.3	Thermoluminescence Study on $\text{Lu}_{0.7}\text{Y}_{0.3}\text{AP}$	92
5.7	Discussion and Conclusion	95
5.7.1	Bridgman Samples – LuAP and $\text{Lu}_{0.8}\text{Y}_{0.2}\text{AP}$	95
5.7.2	Czochralski Samples – $\text{Lu}_{0.7}\text{Y}_{0.3}\text{AP}$	96
5.8	References	99
6	Properties of the $\text{Lu}_{0.7}\text{Y}_{0.3}\text{AP}$ Crystals from the Production Phase	101
6.1	Optical Properties	101
6.1.1	Excitation Spectra	101
6.1.2	Absorption Spectra.....	102
6.1.3	Emission Spectra.....	105
6.2	Light Yield, Energy Resolution and Decay Time	107
6.3	Discussion and Conclusion	110

6.4	References	112
7	Luminescence and Scintillation Properties of LSO Crystals and Derivates	113
7.1	Optical Properties	113
7.1.1	The Role of Cerium Sites in LSO	113
7.1.2	UV-Excitation Spectra	114
7.1.3	UV induced Emission Spectra	116
7.1.4	Absorption Spectra.....	118
7.2	Light Output and Energy Resolution	119
7.2.1	Experimental Procedure.....	119
7.2.2	Results for the LSO Crystals from CTI	121
7.2.3	Results for the LSO PM Samples	123
7.2.4	Results for the LYSO and MLS Samples	124
7.3	Scintillation Pulse Shape.....	126
7.4	Low Temperature TL	128
7.4.1	Thermoluminescence Spectra LSO.....	128
7.5	Discussion and Conclusion	128
7.6	References	131
8	Detector Design and Electronics	133
8.1	Simulation	133
8.1.1	Assumption for the Monte Carlo Simulation.....	133
8.1.2	Multi-Ring versus Multi-Head Design	134
8.2	General Design ClearPET	136
8.2.1	Construction of a Detector Module.....	136
8.2.2	Design Study for the Scanner	138
8.2.3	Design of the PrimatePET in Jülich.....	140
8.3	Electronic Read-Out.....	141
8.3.1	Front End Unit	142
8.3.2	Evaluation	143
8.3.3	Distinction of Pulses (LSO – LuYAP)	144
8.4	Phoswich Combination Study with the XP2020Q.....	145
8.5	Discussion and Conclusion	147

8.6	References	148
9	Test Measurements with the 2-Head Prototype	149
9.1	Set-Up of the 2-Head System.....	149
9.2	Line Source.....	151
9.3	Point-Like Source.....	152
9.4	Conclusion.....	153
9.5	References	153
10	Summary and Outlook	155
A	Detection of Scintillation	159
A.1	Light Collection.....	159
A.2	Spectral Response.....	162
A.3	Photomultipliers	163
B	Material and Methods	167
B.1	Dimensions and Density of the Crystals	167
	Acknowledgements	171
	Curriculum Vitae	173

Chapter 1

General Introduction

1.1 Inorganic Scintillators in Medical Imaging

Inorganic scintillators are employed in most of the current medical diagnostic imaging modalities using x-rays or γ -rays such as SPECT (single photon emission computer tomography) or PET (positron emission tomography) scanners. This is explained by the comparatively good detection efficiency of inorganic scintillators for hard radiation. Yet, the various diagnostic methods differ considerably and consequently the radiation detector requirements differ. These requirements are not always met by the scintillator properties. This is one reason for continuous scintillator R&D. The other reasons are the need for (1.) new, digital diagnostic systems with an excellent image quality and a short image acquisition time and (2.) excellent quality real-time imaging systems for interventional radiology at a low radiation dose.

The ultimate performance of the PET camera is strongly tied to both the physical and scintillation properties of the crystals. For this reason, researchers have investigated virtually all known scintillator crystals for possible use in PET. Despite this massive effort, only a few different scintillators were found so far that have a suitable combination of characteristics, and only two (thallium-doped sodium iodide and bismuth germanate) have found widespread use. However, systematic and in depth studies of the physics underlying the fundamental scintillation mechanism in different materials have led several groups, including the Crystal Clear Collaboration at CERN, to recently develop new scintillators doped with cerium, which appear to surpass all previously used materials in most respects and promise to be the basis for the next generation of PET cameras.

1.1.1 Small Animal Studies

In the last years, the need for specialized positron emission tomography scanners designed to experimental small animal studies was recognized. At the front line of organic research, molecular and cellular biologists engineer new molecular arrangements, including genes and proteins. Having produced these new strains, the next task is to investigate what happens when they are implanted in living tissue. The researchers want to know how the new genes “express” themselves. In a different area – pharmaceutical research – the effects of potential new drugs have to be established as quickly as possible. In the past, results have been obtained “in vitro”, by either killing the samples or by taking biopsies. Until recently there has been no other way of studying the effects of genetic manipulation or drug administration. Now researchers have found how imaging techniques used in medical diagnostic can be adapted for genetic or drug research, providing an immediate picture of how the modified tissue behaves “in vivo”.

For small animal studies a device with high spatial resolution is needed. The required spatial resolution for small animal PET would be in the range of 1 mm FWHM. This requirement is not fulfilled for clinical PET scanners. For this reason many groups have developed and are further developing dedicated high-resolution small animal PET scanners, as they can be considered as good benchmarks of technical developments for their possible implementation in human machines.

1.2 Crystal Clear Collaboration

The Crystal Clear Collaboration (CCC) is an academic network of laboratories interested in the development and use of scintillation materials. In 1990 the collaboration was set-up and registered as RD-18 project at CERN. The aim of the collaboration is to use the expertise available at CERN on the use of scintillating materials in High Energy Physics detectors to develop applications of such materials in basic research and other fields.

At present, the development of a high-resolution small animal PET scanner is one of the main projects of the collaboration. The idea is to validate at the prototype level new technologies developed in the field of high-energy physics in order to convince industrial partners to use them in commercial animal PET and eventually human scanners.

The collaboration consists of 22 laboratories from all over Europe and America with more than 80 experts working in different fields of material science and radiation detection and instrumentation.

In the Crystal Clear Collaboration 4 centres have agreed to produce, in close collaboration with the other laboratories, a small animal PET scanner the so-called “ClearPET”, for their respective hospitals or medical centres. The projects and research programs in the four centres are:

- **France:** CERMEP (Centre d’Exploitation et de Recherches Medicales par Emission de Positons) University Claude Bernard Lyon
 - 1-ring system for mice and rats
 - Research on new PET tracer, cognitive physiology, neurology and oncology
- **Belgium:** IIHE (Inter-University Institute for High Energies) VUB (Vrije Universiteit Brussel) Brussels
 - 1-ring system for mice and rats
 - Drug development
- **Germany:** ZEL (Zentrallabor für Elektronik) and IME (Institut für Medizin), Forschungszentrum Jülich
 - 4-ring system for primates - PrimatePET
 - Research on brain diseases like Alzheimer and Parkinson
- **Switzerland:** University Lausanne
 - 2-head system for mice and rats
 - Research in the field of neurology

The ClearPET scanner will consist of phoswich detectors made of LSO:Ce and LuYAP:Ce pixels, which are read out by multianode photomultipliers. Phoswich detectors are used to obtain a depth of interaction (DOI) information for improving the spatial resolution in all the field of view. LuYAP:Ce is a new scintillation material, and is due to the similar density as LSO the ideal scintillator for a combination with LSO in phoswich detectors. The two crystals have a different decay time, and the observation of the decay time allows determining in which crystal the interaction occurred. The aim of the project is to construct a scanner with high resolution (< 2 mm), high sensitivity and low dead time since dynamic studies should be carried out.

Another important issue is multimodality, which means that the PET scanner is combined with a computer tomography (CT) and/or a magnetic resonance (MRI) system

in one unit. The present plan is to combine the small animal PET scanner with a micro x-ray CT system.

1.3 Scope of this Thesis

The design of a scintillation detector based on LSO/LuYAP phosphor detectors and position-sensitive photodetectors (multianode photomultiplier) was evaluated.

The scope of this thesis was the optimization of the scintillation materials with an emphasis on the $\text{Lu}_{1-x}\text{Y}_x\text{AlO}_3\text{:Ce}$ (x varying from 0 to 0.3), $\text{Lu}_2\text{SiO}_5\text{:Ce}$ and other oxyorthosilicate crystals. This includes the characterization of the scintillation properties and the study on the fundamental scintillation mechanism. The close collaboration and feed-back with the producer of the LuYAP crystals made it possible to exert an influence on the crystal growth conditions and therefore to improve the crystal quality. Since the first grown ingots significant progress has been made in the crystal growth process resulting in large crystal ingots and important improvements of the scintillation properties. The evaluation of the LuYAP crystals is of special importance since the growth of these crystals is very delicate, at a time where reliable and reproducible mass production is being developed.

This thesis is organized as following. Chapter 2 reviews the techniques used nowadays for PET imaging and the scintillator requirements for medical application. Attention is paid to the different scintillators used for both human and small animal PET scanners and an outlook is given for future developments. Chapter 3 is dedicated to the scintillation materials and includes the production of the crystals as well as the mechanism of scintillation in inorganic compounds. The experimental methods that were used for investigations are discussed in chapter 4. Chapter 5, 6 and 7 are devoted to the studied compounds. In chapter 5 the luminescence and scintillation properties of LuAlO_3 , $\text{Lu}_{0.8}\text{Y}_{0.2}\text{AlO}_3$, and $\text{Lu}_{0.7}\text{Y}_{0.3}\text{AlO}_3$ doped with cerium are presented. In chapter 6 preliminary results on the first delivery of $\text{Lu}_{0.7}\text{Y}_{0.3}\text{AlO}_3$ crystals produced in large quantities for the final scanners are given. Chapter 7 deals with the scintillation and luminescence in $\text{Lu}_2\text{SiO}_5\text{:Ce}$ and other oxyorthosilicates. In chapter 8 the detector design of the general 4-Ring ClearPET scanner is described. The design results from information obtained by simulating the geometry with GEANT3 and other simulation tools. The electronic set-up, which is capable to distinguish the LSO from the LuYAP layer by pulse shape discrimination, is also explained in this chapter. In chapter 9 first results obtained with the test 2-head prototype are presented. Finally, the results of the evaluation of the different scintillators are summarized in chapter 10 and a short outlook on the further CCC activity is given.

Chapter 2

PET Imaging

2.1 PET Overview

Positron emission tomography (PET) is a nuclear medical imaging technique whereby a biologically active compound (i.e. a drug) labelled with a positron emitter is introduced into the body (tracer) either by injection or inhalation. This compound then accumulates in the patient and the pattern of its following radioactive emission is used to assess the distribution of the isotope and hence the tracer compounds [1]. Since the image that is produced is of the distribution of the drug within the body, PET is able of determining where certain metabolic processes occur and measuring the rate at which these processes take place. Therefore, it is able to determine if the biological function of an organ is deteriorated, while many other forms of medical imaging - such as computer tomography (CT), magnetic resonance imaging (MRI), and ultrasound - are normally used to determine the physical structure of the organ. Thus, PET is most frequently used to receive information about the biological function of organs and diseases. Examples are neurological diseases (like Alzheimer's disease) where physical effects are only observable on a microscopic level, heart disease, or oncology (cancer), where the metabolic rates gives information on whether the tissue is cancerous and how it responds to treatments.

2.1.1 Radiopharmaceuticals

In 1932, the inventor of the cyclotron Ernest Lawrence recognized the possibilities of the cyclotron for medicine. Together with his brother John, they started using isotopes produced in a cyclotron as biological tracers. Treating a patient with leukaemia, he administered a radioactive isotope of phosphate. It was the first time that a radioactive isotope had been used in the treatment of a human disease. John Lawrence became known as the father of nuclear medicine.

Nowadays, a broad spectrum of positron emitters is used in PET imaging. In most cases, these PET tracer molecules retain the biological properties of unlabeled molecules. Carbon (^{11}C), nitrogen (^{13}N), and oxygen (^{15}O) are present in organic molecules, while other atoms can be substituted or used as analogs. For example, fluorine (^{18}F) can be substituted for hydrogen.

Typically, radionuclides used in positron imaging have very short half-lives ranging from two minutes to two hours (Table 2.1). Because of their short half-lives, ^{11}C , ^{13}N and ^{15}O , can only be used when a cyclotron is installed near the imaging device. In general, ^{18}F is most often used because it has a two-hour half-life and can be distributed from a central radiopharmacy or institution having a cyclotron. Although, many types of positron emitters have been used to label hundreds of molecules to study basic physiology and disease processes, one molecule has been used far more than any other. This molecule is ^{18}F -FluoroDeoxyGlucose (FDG) and is used in the majority of clinical PET producers. FDG has a broad clinical application because every cell – particularly tumor cells - uses glucose as fuel.

Table 2.1 Properties of frequently used PET isotopes (the range is given for water).

Radionuclide	Half-life [min]	E_{max} of the e^+ [keV]	Max range [mm]	Mean range [mm]	Use	For
Carbon - 11	20.4	960	5	0.28	Amino-acids	Clinical research
Nitrogen - 13	9.9	1198	5.4	1.4	Ammonia (NH_3)	Cardiology
Oxygen - 15	2.05	1732	8.2	1.5	H_2O , CO , CO_2	Clinical research
Fluorine - 18	109.7	633	2.4	0.22	FDG and F- dopamine	Oncology, Cardiology and Neurology

Radiotracers like FDG are designed so that they spread throughout the body but only accumulate in tissues when they encounter a specific enzyme, protein or gene. The radiotracer builds up by binding to proteins on the cell surface, known as receptors, or by becoming trapped in the cells, as metabolic or enzymatic processes alter its chemical structure. The distribution of the radiotracer therefore provides information on the distribution and concentration of specific molecular targets in the body, such as receptors, enzymes and transporters. In addition, how quickly the tracer accumulates in or clears from tissues often relates to the rates of biological processes in the body (for example rates of transport, synthesis, metabolism and excretion).

However, the radiotracer can also be a drug that is labelled with a positron-emitting radionuclide, in which case its distribution as a function of time mimics that of the drug.

Exactly what is measured in a particular study depends on the radiotracer used. The goal is to design radiotracers that are specific to particular molecular targets or genetic processes, and there are many examples of PET radiotracers that meet this challenge.

2.1.2 Conventional PET

When a nucleus decays by positron emission, a proton in the nucleus converts into a neutron, and a positron and a neutrino are ejected. The neutrino leaves the scene without any trace. Depending on the energy of the positron, it travels only a short path before it encounters an electron. The mean free path-length of commonly used radionuclides is given in the fifth column in Table 2.1. This mean range limits the spatial resolution achievable with PET. The positron-electron pair annihilates creating two γ -rays of energy 511 keV. To conserve the momentum, the two photons must propagate away from each other at an angle of $180 \pm 0.6^\circ$. The distance between the emission and annihilation of the positron plus the photon non-collinearity cause an uncertainty in positioning the event.

A typical PET scanner consists of a planar ring of small photon detectors (Figure 2.1), with each photon detector placed in time coincidence with each of the individual detectors on the other side of the ring. The majority of PET scanners use scintillation detectors to record the pairs of annihilation photons. The scintillator is segmented into an array of crystals and is read out by a matrix of photomultiplier tubes. Photon interaction in the scintillator produces light that is converted into electrons and amplified by the photomultipliers. When a pair of detectors simultaneously detect the 511 keV photons, a positron must have annihilated somewhere on the line (also known as chord) connecting the two detectors. The summary of all lines of response gives the necessary set of projections to perform computed tomography for a single plane.

Multiple detector rings allow obtaining images from multiple slices, and therefore a three-dimensional image of the patient. In a “2-D PET” system, septa of tungsten or lead collimator plates are placed between the detector rings to shield the detectors from out of plane coincidences as well as from Compton scattered photons coming from another part of the body. The coincidences between nearly adjacent “cross-plane” rings are usually added to the closed “direct-plane” to increase the detection efficiency. Modern systems can be operated with removed (retracted) septa, where coincidences between many planes are accepted resulting in three-dimensional imaging (“3-D PET”). With septa retracted, the increased solid angle and consequently a higher 511 – 511 keV coincidence rate compensates to a certain extent for the increased Compton-scattering background.

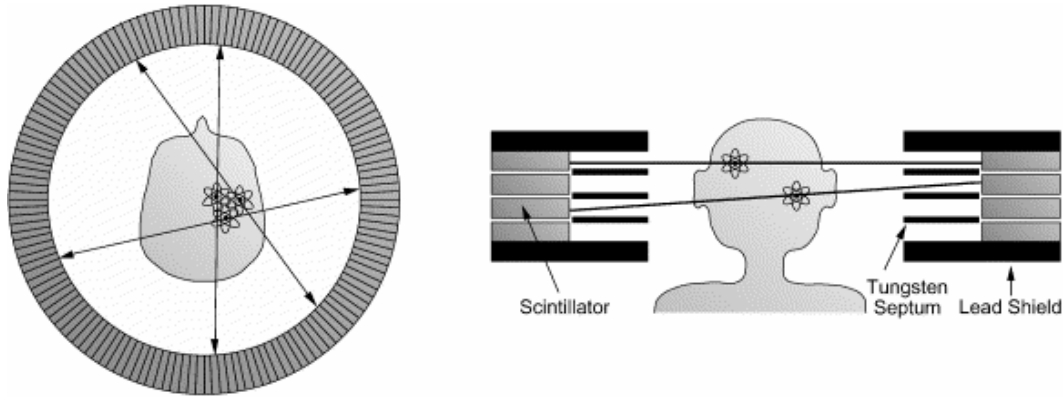
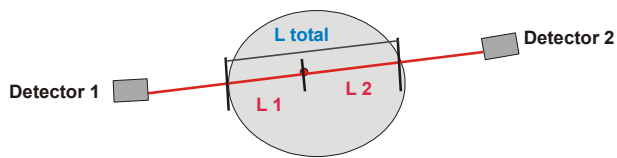


Figure 2.1 PET camera. When the crystals in opposing hemispheres simultaneously detect 511 keV gammas, a positron is assumed to have annihilated on the line connecting them. Multiple planes are stacked up, as shown in the picture, to form a volumetric image. Tungsten septa reduce out-of plane contributions (2-D PET).

Before the reconstruction of the data, the attenuation of the photons through the patient has to be measured. To determine the density of the body, a transmission scan similar to a CT scan with a positron point or line source is done (usually ^{68}Ge). The source is rotating between the patient and the inner detector ring. When comparing the data to a blank measurement (without patient) the absorption for all possible chords can be calculated. Due to the emission of the two γ -rays with an angle of 180° the attenuation factors can be exactly determined. With a given thickness L_{total} of the absorbing material and a constant attenuation coefficient μ , the probability P_{12} that no interaction of the photons with tissue take place before reaching the coincidence detectors is



$$P_{12} = e^{-\mu L_1} \cdot e^{-\mu L_2} = e^{-\mu L_{total}}, \quad (2.1)$$

thus the attenuation is independent on the point where the annihilation took place and only depends on the attenuation length between the detectors. L_1 and L_2 are the length from the annihilation point to the detectors.

When performing transmission scans, one distinguishes between a so-called “hot” and “cold” transmission. The “cold” scan is done before the radioactive tracer is applied to the patient and the “hot” indicates the transmission measurement after the PET scan, when there is still some rest activity of the tracer in the patient.

2.2 Coincidence Detection and Dead Time

Due to the principle of PET, the image depends highly on the validity of the events measured under coincidence. All events or Prompts (P) that are found in coincidence are Trues (T), Randoms (R) or Scatter (S). These events are related by the formula:

$$P = T + R + S \quad (2.2)$$

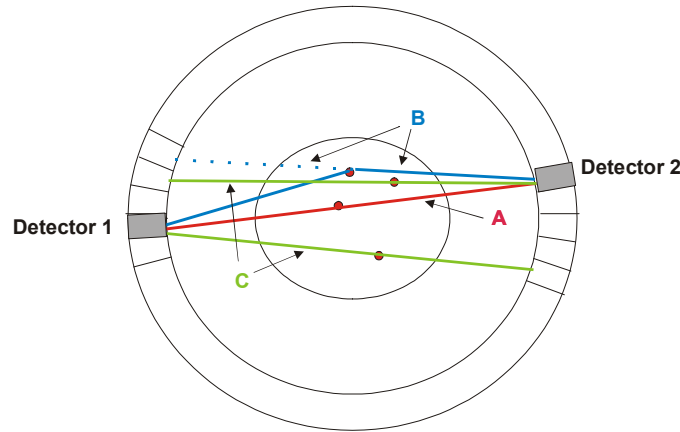


Figure 2.2 Types of coincidence events between detector 1 and detector 2: A – true coincidence, B – scattered coincidence, and C – random coincidence.

False events contaminate the true coincidence counting rate and thus the quality of the final image to a great extent. The different types of detected events in coincidence set-up are shown in Figure 2.2.

Random errors can occur at any time simply because two completely unrelated photons happen to arrive within the electronic coincidence time window $2\Delta t$ (typically 10 – 20 ns). Random coincidences show up as a continuous background in an image. Using the standard BGO crystal (the properties of this scintillator are described later), $2\Delta t$ is in the order of 10 ns. A much smaller $2\Delta t$ will reduce the background significantly. Furthermore, if $2\Delta t$ is very small, time-of-flight information can be used to select a region of interest; for example at $2\Delta t = 1$ ns, the diameter of such a region will be 15 cm.

The true-to-random coincidence ratio is also affected by energy selection. The random coincidence intensity is approximately proportional to the square of the singles-spectrum intensity. For given singles rates S_1 and S_2 for a pair of detectors and a coincidence window of width $2\Delta t$, events will be found in coincidence due to random occurrence with a rate: $R = 2 \Delta t S_1 S_2$.

A system without septa has considerably more Compton-scattered events in the singles spectrum, than in the true coincidence spectrum. Consequently, in the scattered coincidence spectrum there are relatively more events in the region of the Compton continuum than in the photopeak in comparison with the corresponding parts of the true coincidence spectrum. Therefore, selection of photopeak events will improve the true-to-scatter coincidence ratio. A good energy resolution and high full-energy peak intensity are important properties of a scintillator.

Scattered coincidences arise when one or both photons are scattered on the way to the detector and thus destroy the correct chord. The main mechanism is Compton scattering, involving a change in photon energy, but normally the energy resolution of the scintillators is insufficient to discriminate against small angle Compton scattering.

Another important aspect of a PET scanner is dead time, i.e. the time in which a coincidence cannot be registered because the system is too busy handling a previous coincidence event. Several parts of the system contribute to the dead time and the detector is one of them. Taking the BGO response time of 300 ns (scintillation decay time) as the dead time, we would lose about 3% of the events at a rate of 10^5 per second per readout channel, which is approximately the maximum rate of a 64 scintillator-column block in a modern PET system. However, it should be noted that the actual dead time of a block is at the microsecond level due to the signal processing (shaping times). If the scintillator columns were read out individually, the rate would be only ~ 1000 per second and the dead time of the scintillator/detector including electronics would be negligible.

2.3 Scintillator Requirements for PET

The scintillator requirements for PET are best determined by evaluating their influence on the PET detector requirements. The ideal properties and their objective are:

- | | | |
|-----------------------------|---|---|
| • High density | ↔ | high detection efficiency |
| • High atomic number | ↔ | high photoelectric fraction |
| • Short decay time | ↔ | good coincidence timing |
| • High light output | ↔ | good spatial resolution |
| • Good energy resolution | ↔ | good scatter rejection |
| • Emission > 300 nm | ↔ | good spectral match to photodetector |
| • Transparent to emission | ↔ | low light self-absorption |
| • Refractive index near 1.5 | ↔ | good transmission from crystal to photodetector |

- | | | | |
|---|-----------------|---|-------------------------------------|
| • | Non-hygroscopic | ⇔ | easier packaging |
| • | Radiation hard | ⇔ | stable and long crystal performance |
| • | Rugged | ⇔ | easy to machine |
| • | Economic growth | ⇔ | reasonable cost |

Some of the objectives and properties are now discussed in more detail.

2.3.1 Detection Efficiency

With any PET detector design, a high detection efficiency (> 85%) is necessary, which implies that the detector depth (i.e. the thickness in radial direction) be at least two attenuation lengths thick. While this criterion can be fulfilled with a scintillator of any density (or attenuation length), a high density is desired to minimize the thickness of the crystals and thus the resolution degradation artefact caused by penetration of the 511 keV photons into the crystal ring. This is also known as radial elongation and described later.

When using a high density scintillator one can reduce the size of the individual pixels and thus improve the spatial resolution of the detector.

2.3.2 Photoelectric Fraction

When a photon beam enters material, the attenuation is caused by four major types of interactions. The four processes are **coherent scattering**, the **photoelectric effect**, the **Compton effect** and the **pair production**. Each of these processes can be represented by its own attenuation coefficient, which varies in its particular way with the photon energy and with the atomic number of the absorbing material. The total mass attenuation coefficient is the sum of the individual coefficients for these processes:

$$\frac{\mu}{\rho} = \frac{\sigma_{coh}}{\rho} + \frac{\tau}{\rho} + \frac{\sigma_c}{\rho} + \frac{\kappa}{\rho} \quad (2.3)$$

where σ_{coh} , τ , σ_c and κ are attenuation coefficients for coherent scattering, photoelectric effect, Compton effect and pair production, respectively.

The probability that a photoelectric effect happens is given by the photoelectric attenuation coefficient τ . It increases with the density ρ and the atomic number Z of the absorber. The photoelectric interaction with an electron from, for example the K shell is proportional to the third to fourth power of the atomic number.

$$\tau \propto \rho \cdot \frac{Z^{n+1}}{A} \approx \rho \cdot Z^n, \quad (n = 3 - 3.6) \quad (2.4)$$

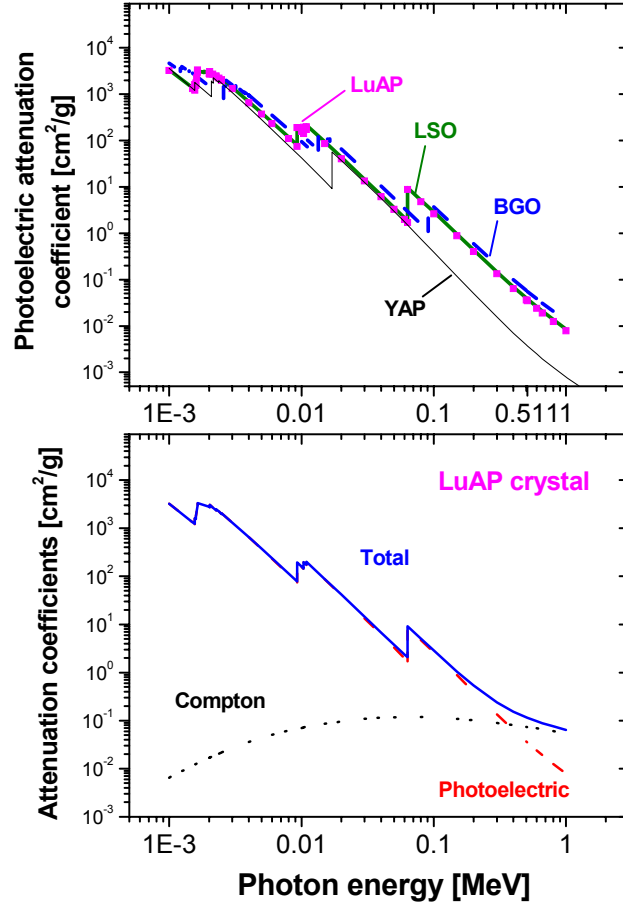


Figure 2.3 Energy dependence of the photoelectric attenuation coefficient (upper picture) for different scintillators. In the lower picture the mass attenuation coefficients depending on the energy are shown for the LuAP crystal.

For light elements the exponent has a value of $n \approx 3.6$ and for elements with high atomic number $n \approx 3$. The photoelectric attenuation coefficient is also depending on the energy of the photon beam. τ decreases steadily with $1/E^3 - 4$ for photon energies over the K-shell energy of the absorbing atom. For energies high above 511 keV the probability decreases more slowly with about $1/E_\gamma$.

$$\tau \propto \rho \cdot \frac{Z^{n+1}}{A \cdot E_\gamma^3} \approx \rho \cdot \frac{Z^n}{E_\gamma^3}, \quad (E_\gamma \ll 511 \text{ keV}) \quad (2.5)$$

$$\tau \propto \rho \cdot \frac{Z^{n+1}}{A \cdot E_\gamma} \approx \rho \cdot \frac{Z^n}{E_\gamma}, \quad (E_\gamma \gg 511 \text{ keV}) \quad (2.6)$$

The photoelectric attenuation coefficient for different scintillation crystals and the attenuation coefficients (photoelectric, Compton, total) for the LuAP (lutetium aluminium perovskite) crystal depending on the energy are shown in Figure 2.3.

2.3.3 Decay Time

The scintillation decay time has an influence on the timing resolution as well as on the dead time. When multiple decay lifetime components are present, the dead time is affected most by the slowest decay component. While the relationship between the dead time and the decay time is difficult to quantify (specially in the case with more decay components), most PET cameras trigger at the single photoelectron level, so the dead time can be defined as the time that it takes for the scintillation intensity to drop to the level of 1 photon/MeV/ns.

Timing resolution is ascertained by the scintillation photon intensity I_0 (photons/MeV/ns) immediately after excitation. If the scintillator has multiple decay time components, the fastest one has the largest influence on I_0 . To reduce random coincidences a good timing resolution (< 5 ns FWHM) is necessary. As already mentioned before [section 2.2], the random coincidence rate is given by $2S^2\Delta t$, where S is the single rate and Δt is the coincidence time window (typically 10 – 20 ns). When imaging higher activities (like imaging with short half-life isotopes) or with fully 3-D PET, the random coincidence become more and more important, as the coincidence rate scales linearly with the activity being imaged (i.e. like S) whereas the random rate scales like S^2 . Better timing resolution will enable to use shorter coincidence windows to reduce the random fraction. Anyhow, there is a minimum coincidence width of 3 ns for human PET, due to the time of flight differences across the tomograph ring.

If the timing is good enough, this decay time difference can be used to localize the position of the annihilation along the chord. PET scanners were built using BaF₂ scintillators and this principle, but they are not common. The system-wide coincidence timing resolution is typically 500 ps FWHM, which localizes the annihilation point to a line segment of about 8 cm. This is quite large compared to the size of the crystals, but anyhow, the additional information can be used to reduce noise in the image.

2.3.4 Light Output

The light output has an influence on many parameters, like the timing, spatial and energy resolution. For a given decay time, a higher light output yields a higher intensity I_0 and so a better timing resolution. The spatial resolution is affected by the ability of the block detector module to identify the crystal of interaction, which is limited by the counting rate. If the light output of a scintillator is high, more crystals can be read out with the same number of PMTs (light sharing), allowing the crystal size to become smaller. The spatial resolution is mainly depending on the crystal size, thus a small crystal leads to a higher spatial resolution.

An important point is that a crystal with a high light yield can help to reduce the background due to Compton-scatter in the patient by improving the energy resolution. As the annihilation photons lose energy when they scatter, good energy resolution (for which high light output is necessary) will allow identifying and rejecting scattered events. For example for the typical BGO block detectors, the energy resolution for 511 keV is 12% - 20% FWHM and the lower energy threshold is normally set to 350 keV. Using these parameters, in a conventional 2-D PET, 10 - 20% of the coincidences are scattered photons, compared to 40 - 60% in a fully 3-D PET.

2.3.5 Energy Resolution

The energy resolution plays an important role when operating a PET system in 3-D mode. Due to the retracted septa the Compton-scattering contribution increases which leads to a blurring of the image. This background is reduced only by accepting events in the full-energy peak of the pulse-height spectrum (the better the resolution, the better the reduction will be). For a typical PET scanner energy resolutions are: for BGO 20% FWHM (full width half maximum) and for NaI:Tl ~10% FWHM. However, many events with 511 keV quanta interacting in a scintillator due to Compton effect will be eliminated as well. Consequently, depending on the PET system and specific application, one has to decide whether a full-energy peak window is used or a more relaxed window.

In a small-animal PET system the Compton scattering in a small animal plays a minor role. Consequently, Compton events in the pulse height spectrum are primarily due to scattering in the scintillator and can be accepted. Therefore, the threshold can be decreased.

2.4 Scintillation Detector Module Trends for PET

In 1948, NaI(Tl) (sodium iodide) was discovered by Hofstaedter [2]. It quickly became the scintillator of choice for radiation detection because of its high light output, i.e. efficient conversion of absorbed γ -ray energy to scintillation photons. The large light pulses are easily processed by conventional pulse-shaping electronics.

From 1952 to 1958, Hal Anger developed the scintillation camera, also known as the Anger Camera, using the NaI(Tl) crystal. Developed fifty years ago, this technique remains the most commonly used tool in nuclear medicine today.

The major disadvantage of NaI(Tl) is the low detection efficiency for photons above 200 keV due to the low density and moderately low atomic number. At the energies typically used in SPECT (140 keV) the detection efficiency of NaI(Tl) is satisfactory, and it is used almost exclusively in that application. However, for an application in PET, NaI(Tl) has been replaced by materials with higher density and higher atomic number. An additional disadvantage of NaI(Tl) is that it is highly hygroscopic. As a result, there has been a great effort into the development of hermetic packaging to protect the material from moisture in the atmosphere.

BGO ($\text{Bi}_4\text{Ge}_3\text{O}_{12}$, bismuth germanate) came up in the early 1970s with initial studies reported by Weber and Monchamp [3]. Although the light output of BGO is only 15% of that of NaI(Tl), its higher detection efficiency due to the higher density and higher atomic number, has made it a very popular choice for the detection of radiation above a few hundred keV. Today, PET is the major ongoing application of BGO crystals despite the fact that their relatively slow decay time of 300 ns limits coincidence timing resolution.

The most commonly used PET detector module is known as a block detector, as shown in Figure 2.4. A block of BGO scintillator crystal is partially sawn through to create a group of quasi-independent crystals that are optically coupled to four photomultiplier tubes. When a γ -ray interacts in the crystal, the resulting scintillation light is emitted isotropically, but limited by the saw cuts in their lateral dispersion when travelling to the PMT. The position (i.e. the crystal element) of the γ -ray interaction is then determined by the analog ratio of the photomultiplier tube output signal. The energy of the γ -ray is determined and a timing pulse is generated by the sum of these four signals. A typical PET detector module has 80% detection efficiency, 20% FWHM energy resolution, 2 ns FWHM timing resolution, 4 μs dead time, and 5 mm FWHM position resolution for 511 keV gammas [4].

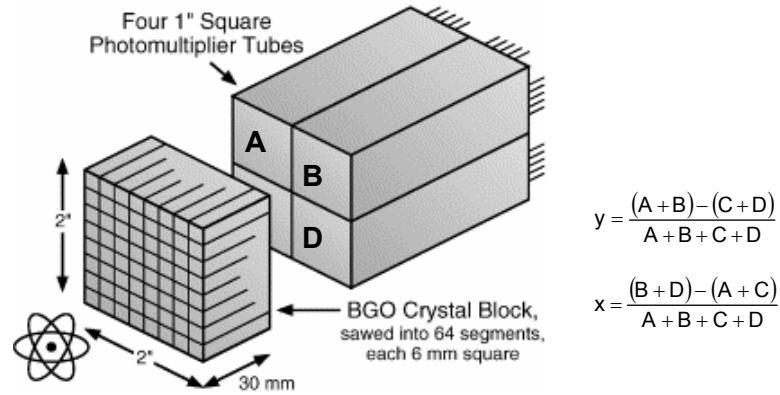


Figure 2.4 Conventional PET detector module. Multiple photomultiplier tubes detect the scintillation light emitted after a γ -ray interaction. The position is determined by the ratio of the analog signal from the 4 PMTs (A, B, C, D), and the energy by the sum of the signals.

Scintillators with extremely short decay time constants offer the possibility of time-of-flight PET, in which opposing detectors measure the difference in the arrival time of two γ -rays. In this way, the position of the annihilation event can be localized along the line connecting the two detectors. Two scintillator crystals that would be useful are CsF (cesium fluoride) and BaF₂ (barium fluoride). CsF has very low light output and is very hygroscopic and consequently, has not been often used despite its short decay time of 4 ns. BaF₂ has an even faster decay time of < 1 ns, greater light output, and is non-hygroscopic. Therefore, in the early 1980s it was used in several PET scanners [5]. However, because of its low density and atomic number, it never reached the performance of BGO. Another disadvantage of BaF₂ is that the decay time spectrum consists of two components, where the fast one emits in the extreme UV (220 nm).

A PET scanner based only on GSO (Gd₂SiO₅:Ce, gadolinium oxyorthosilicate) crystals has also been reported [6]. The fabrication of GSO crystals requires great care, because the crystals cleave easily. Thus, special techniques and mechanics are needed to avoid cracking the crystal during the cutting procedure.

LSO (Lu₂SiO₅:Ce, lutetium oxyorthosilicate) has first been reported by Melcher [7] in 1992 and offers the best combination of properties for PET. It has high density and high atomic number for good γ -ray detection efficiency, a short decay constant for good coincidence timing and high light output that allows the use of many small elements per PMT. In addition, it is mechanically rugged and non-hygroscopic. LSO has a low level of natural radioactivity as a result of the presence of ¹⁷⁶Lu, but the counting rate from this isotope is small compared to the typical counting rates from the injected traces. LSO has been used in a high-resolution brain tomograph [8] and high-resolution animal

tomographs [9]. Large-scale commercial production of LSO has been realized during 1999, and widespread use of this scintillator is expected in the future.

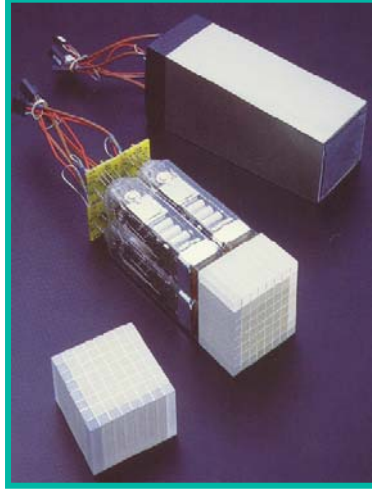


Figure 2.5 Picture of a LSO matrix coupled to four photomultiplier tubes (reproduced from CTI).

Table 2.2 Inorganic scintillators for medical imaging. The scintillators are sorted by their density.

Scintillator	Chemical formula	Density [g/cm ³]	Light Yield [ph/MeV]	Peak emission λ [nm]	Decay time τ [ns]
NaI:Tl		3.67	38 000	415	230
CsI:Tl		4.51	54 000	550	1000
CsF		4.64	1 900	390	2 - 4
BaF ₂		4.89	10 000	220, 325	0.6, 630
YAP	YAlO ₃ :Ce	5.5	21 000	350	28
GSO	Gd ₂ SiO ₅ :Ce	6.71	8 000 - 10 000	440	30 - 60
BGO	Bi ₄ Ge ₃ O ₁₂	7.13	9 000	480	300
LSO	Lu ₂ SiO ₅ :Ce	7.34	27 000	420	40
PWO	PbWO ₄	8.28	100	420	5 + 15
LuAP	LuAlO ₃ :Ce	8.34	11 400	365	18

At about the same time (in 1994), first studies on the LuAP (LuAlO₃:Ce) scintillator were published [10-13]. The lutetium aluminium perovskite crystal is the lutetium analog of YAP, a scintillator known for its high light output and short decay time, albeit relatively low density (5.5 g/cm³) and atomic number [14]. The material properties of LuAP make it very attractive as a gamma detection scintillator. Its density is 8.34 g/cm³, which is even higher than that of LSO (7.34 g/cm³). This gives it an attenuation length and photoelectric interaction for 511 keV γ -rays of 1.1 cm and 32%, respectively. The light output was found to be around 11400 ph/MeV and the decay time is only 18 ns. It

is non-hygroscopic, is relatively hard and free of cleavage planes, so it is relatively easy to cut and polish. Its melting point of 1960 °C is significantly lower than that of LSO (2320 °C).

Table 2.2 summarizes the properties of common scintillators.

2.5 Future Directions

At the present time, the development of a high-resolution positron emission tomograph (PET) with a spatial resolution of 2 - 3 mm or even smaller is one of the major fields of research. To reach this challenge several applications of new detector technology, which means new photodetectors (multianode photomultipliers, avalanche photodiodes, PIN diodes, etc.) and scintillation crystals (LSO, LuAP, GSO, etc.) are under investigation.

2.5.1 Fully 3-D PET

One of the major ongoing research for which the scintillation material is crucial, is fully 3-D PET. As mentioned before, the requirements on the dead time and energy resolution are much higher compared to conventional 2-D PET. At the moment, BGO is mostly used for this 3-D PET machines, largely because most 3-D PET scanners are combinations with 2-D PET scanners (i.e. have removable septa) and because no reasonable alternative exists.

2.5.2 Time of Flight PET

Time-of-flight PET has long been a desired goal, but unfortunately has not yet realized its potential due to the lack of appropriate scintillators. As mentioned before [section 2.4], a number of positron emission scanners were built with BaF₂. The disadvantage of this crystal is the emission in the extreme UV range of the fast component, where it is difficult to find a suitable photomultiplier. Other disadvantages are the poor density and effective atomic number, which lead to poor spatial resolution and efficiency. Should a scintillator be discovered that combines the fast decay time of BaF₂ with a short attenuation length and high light output, the performance of PET would improve significantly.

2.5.3 Solid State Photodetectors

One of the current developments at the moment is the combination of PET with other imaging systems such as CT, MRI and SPECT. Especially the combination of PET/MRI would provide useful information about the anatomy as well as the physiology of the patient. Combined PET/MRI detectors [15], and combined PET/SPECT scanners [16] have already been built. The replacement of the photomultipliers, which was absolutely necessary in combination of PET with MRI due to the high magnetic field, by a solid state photodetector such as an avalanche photodiode (APD) array, is one of the most potential fields of research. The successful development of economical, reliable APD arrays would change the requirements for PET scintillators. Due to the lower signal to noise ratio compared to a PMT, a higher light output and initial intensity would be required in order to obtain the essential timing and energy resolution. The dead time could be highly reduced just because of the fact that each crystal could be individually coupled to the APD. The quantum efficiency of APDs is significantly higher than PMTs, so the counting statistic has a lower influence on the energy resolution and a better energy resolution may be achievable. At CERN APD's are successfully used in the ECAL/CMS experiment for the readout of PWO crystals and show promising results.

2.5.4 Depth of Interaction

In order to reduce the number of detector modules (and hence the cost) and to increase the efficiency, a reduction of the ring diameter would be necessary. Unfortunately, there is also a certain drawback like a resolution degradation artefact caused by the penetration of the 511 keV photons into the crystal ring. The origin of this artefact that is also known as radial elongation, parallax error or radial astigmatism, is shown in Figure 2.6.

If photons hit the detector ring at an oblique angle they can penetrate into neighbouring crystals before the interaction takes place. This may cause a misinterpretation of the lines of interaction i.e. events are related to chords that do not pass the source. The spatial resolution impairment increases for objects placed further away from the centre of the ring. This artefact can be reduced significantly if the detection system is not only able to identify the crystal of interaction but also the depth of interaction within that crystal. With such information, the events can be assigned to the chord that connect the interaction points in the crystal (rather than the crystals themselves), and so no mispositioning errors are generated.

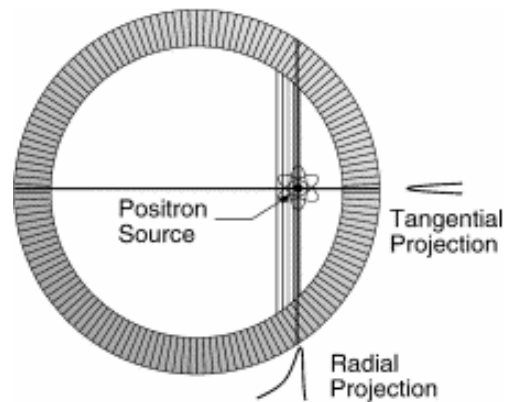


Figure 2.6 Origin of radial elongation: 511 keV γ -rays that are incident at an oblique angle can penetrate into the detector ring before interacting and being detected. This leads to a blurring of the image that worsens as the source is moved away from the centre of the ring.

The development of detector modules that are able to determine the depth of interaction is an active field of research. There are three general approaches that have been developed to measure the interaction depth shown in Figure 2.7. The first (a) is a phoswich system, in which the scintillator block of a conventional PET consists of two or more layers of scintillation crystals. They either differ in decay time, in light output, in wavelength or the layers are shifted with respect to each other. The readout electronic should be able to distinguish the scintillation pulses (in either the decay time or light output) and therefore to identify the right crystal of interaction. A high-resolution PET scanner that uses a 15 mm deep phoswich detector made of GSO and LSO has recently been built [17].

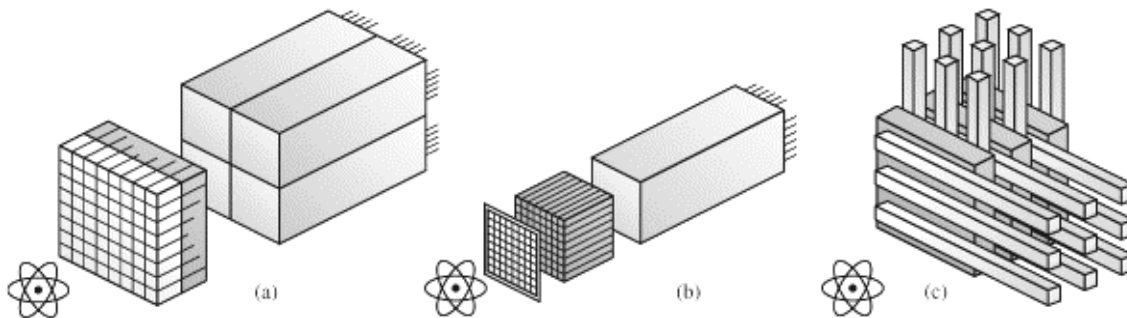


Figure 2.7 Depth of interaction measurement concepts. In the left picture, a conventional PET detector module is stratified in depth with two different materials - the depth is distinguished by decay time. In the middle picture, the scintillation light is shared between two photodetectors - the ratio determines the depth. The detector on the right is constructed of a stack of imaging planes - the layer at which the interaction is observed identifies the depth.

The second technique for determining the depth of interaction is to utilize light sharing Figure 2.7 (b). For this design each scintillator element is coupled to two photodetectors, usually on opposing ends of the crystal. The amount of light observed by each detector depends on the point of the γ -ray interaction in the crystal. From the ratio of the observed scintillation light the interaction depth can be estimated. Recent advances in pixel photodetectors like PIN photodiode arrays, avalanche photodiode arrays (APD) and multianode photomultiplier tubes have greatly contributed to this design system. At present, no PET scanner using this design has been built but several are under construction.

The third approach to measure the depth of interaction is a detector design where the detector consists of a stack of multiple layers of two-dimensional imaging planes. One plane, where the interaction of the γ -ray is observed, identifies the depth while a 2-D detector gives the other two coordinates.

2.6 Small Animal PET Scanner

Much of the detector research for PET imaging over the past years has focused on developing scanners for imaging animals. Biologists are creating sophisticated models of human disease in laboratory animals, particularly in the mouse, which shares roughly 95% of its genes with humans. An increasing number of important mouse models are being used to develop new therapeutic approaches for a range of deadly diseases including cancer and Alzheimer's. Imaging allows individual animals to be tracked non-invasively over time, which can speed up experiments and reduce the number of animals used in research.

Twenty years ago, Positron Emission Tomography was still in its infancy. The limitation to use the available PET scanners to image small animals was the spatial resolution. Although even at that time, external coincidence detection was used to determine kinetic rate constants in vivo in rats [18, 19]. The development of bismuth germanate (BGO) PET detector block with an intrinsic resolution better than 5 mm offered the chance of tomographic imaging. The first PET image of a rat brain was produced in 1991 from Ingvar *et al.* [20] using a Scanditronix PC-2048-15B clinical PET scanner. In the same year Rajeswaran *et al.* [21] published rat brain images, obtained using a pair of BGO detectors. The latter device proved to be the prototype for the first small animal PET scanner RATPET [22]. In addition to the RATPET prototype, a number of other designs [23] were proposed that were all using the at that time "conventional" hardware components.

By the mid-1990's, a number of research groups had realized that the field of small animal PET could provide a fruitful area for technological innovation. It was possible to justify the building and testing of new hardware material, in the name of small animal scanning, at considerable lower cost than would have been incurred by a full-sized tomograph. This process included the development of avalanche photodiodes at Sherbrooke [24], the implementation of barium fluoride crystals, a photosensitive wire chamber in Brussels [25] and the use of yttrium aluminium perovskite (YAP) crystals in Jülich [26] see also Figure 2.8.

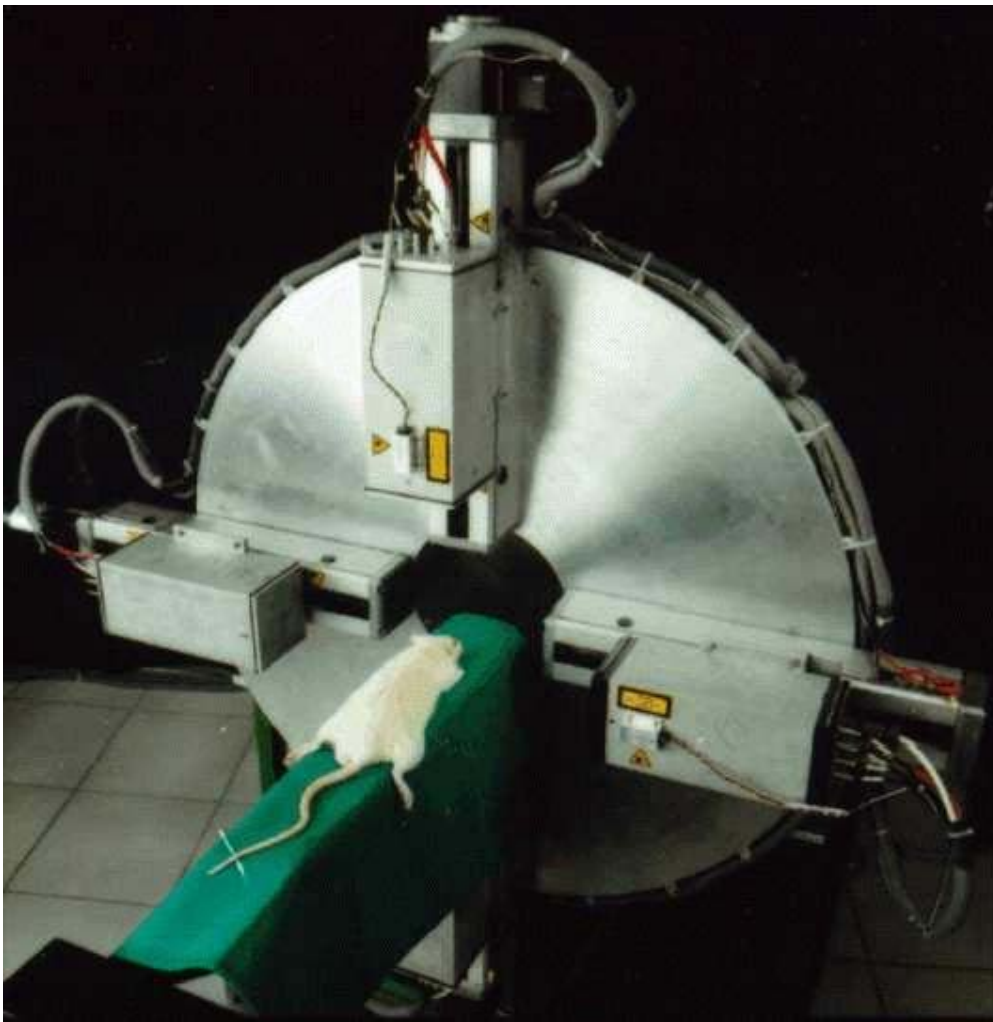


Figure 2.8 Picture of the TierPET at the Forschungszentrum Jülich.

The most important developments are those, which have led to an implementation in commercially available PET scanners, that is, the use of lutetium oxyorthosilicate (LSO)

and the use of multiproportional wirechamber technology for positron emission tomography, in microPET [26] and HIDAC [28], respectively.

2.7 References

- [1] H. N. Wagner, *Clinical PET: Its Time Has Come*, J. Nucl. Med. 32 (1991) 561-564.
- [2] R. Hofstaedter, *Alkali Halide Scintillation Counters*, Phys. Rev. 74 (1948) 100-101.
- [3] M. J. Weber, R. R. Monchamp, *Luminescence of $\text{Bi}_4\text{Ge}_3\text{O}_{12}$: Spectral and decay properties*, J. Appl. Phys. 44 (1973) 5495.
- [4] W. W. Moses, S. E. Derenzo, T. F. Budinger, *PET detector modules based on novel detector technologies*, Nucl. Instr. and Meth. A 353 (1994) 189-194.
- [5] M. Yamamoto, D. C. Ficke, M. M. Ter-Pogossian, IEEE Trans. Med. Imaging MI-1 (1982) 187.
- [6] S. Holte, H. Ostertag, M. Kesselber, J. Comput. Assist. Tomogr. 11 (1987) 691.
- [7] C. L. Melcher, J. S. Schweitzer, *Cerium-doped Lutetium Oxyorthosilicate: A Fast, Efficient New Scintillator*, IEEE Trans. Nucl. Sci. 39 (1992) 502-505.
- [8] M. Schmand, L. Eriksson, M. E. Casey, *et al.*, *Performance results of a new DOI detector block for a High Resolution PET – LSO Research Tomograph HRRT*, IEEE Trans. Nucl. Sci. NS145 (1998) 3000-3006.
- [9] A. F. Chatziioannou, S. R. Cherry, Y. Shao, *et al.*, *Performance evaluation of microPET: a high-resolution lutetium oxyorthosilicate PET scanner for animal imaging*, J. Nucl. Med. 40 (1999) 1164-1175.
- [10] B. I. Minkov, *Promising new lutetium based single crystals for fast scintillators*, Functional Materials 1 (1994) 103-105.
- [11] W. W. Moses, S. E. Derenzo, A. Fyodorov, M. Korzhik, A. Gektin, B. Minkov, V. Aslanov, *$\text{LuAlO}_3\text{:Ce}$ - A high density, high speed scintillator for gamma detection*, IEEE Trans. Nucl. Sci. 42 (1995) 275-279.
- [12] A. Lempicki, M. H. Randles, D. Wisniewski, M. Balcerzyk, C. Brecher, A. J. Wojtowicz, *$\text{LuAlO}_3\text{:Ce}$ and other Aluminate Scintillators*, IEEE Trans. Nucl. Sci. 42 (1995) 280-284.
- [13] M. Moszynski, D. Wolski, T. Ludziejewski, *LuAP , A new fast scintillator*, Proc. Int. Conf on Inorganic Scintillators, SCINT95, 1996, Delft University Press.
- [14] M. V. Korzhik, O. V. Misevich, A. A. Fyodorov, *$\text{YAlO}_3\text{:Ce}$ scintillators: application for x- and soft γ -ray detection*, Nucl. Instr. and Meth. B 72 (1992) 499-501.

- [15] Y. Shao, S. R. Cherry, K. Farahani, *et al.*, *Development of a PET Detector System Compatible with MRI/NMR Systems*, IEEE Trans. Nucl. Sci. NS44 (1997) 1167-1171.
- [16] M. Schmand, M. Dahlbom, L. Eriksson, *et al.*, J. Nucl. Med. 39 (1998).
- [17] M. Schmand, L. Eriksson, M. Casey, *et al.*, IEEE Trans. Nucl. Sci. 45 (1998) 3000.
- [18] A. H. Lockwood, P. J. Kenny, *Serial measurements of positron-emitting isotope activity in rat brain*, Stroke 12 (1981) 173-176.
- [19] H. Nakai, H. Matsuda, E. Takara, M. Diksic, E. Meyer, Y. L. Yamamoto, *Simultaneous in vivo measurement of lumped constant and rate constants in experimental cerebral ischemia using F-18 FDG*, Stroke 18 (1987) 158-167.
- [20] M. Ingvar, L. Eriksson, G. A. Rogers, S. Stone-Elander, L. Widen, J. Cereb. Blood Flow Metab. 11 (1991) 926-931.
- [21] S. Rajeswaran, S. P. Hume, J. E. Cremer, *et al.*, J. Neurosci. Methods 40 (1991) 223-232.
- [22] P. M. Bloomfield, S. Rajeswaran, T. J. Spinks, *et al.*, *The design and physical characteristics of a small animal positron emission tomograph*, Phys. Med. Biol. 40 (1995) 1105-1126.
- [23] C. A. Burnham, J. Bradshaw, D. Kaufman, D. Chesler, G. L. Brownell, IEEE Trans. Nucl. Sci. NS-31 (1984) 632-646.
- [24] R. Lecomte, J. Cadorette, P. Richard, S. Rodrigue, D. Rouleau, *Design and Engineering Aspects of a High Resolution Positron Tomograph for Small Animal Imaging*, IEEE Trans. Nucl. Sci. 41 (1994) 1446-1452.
- [25] P. Bruyndonckx, X. Liu, S. Tavernier, S. Zhang, *Performance study of a 3D small animal PET scanner based on BaF₂ crystals and a photo sensitive wire chamber*, Nucl. Instr. and Meth. A 392 (1997) 407-413.
- [26] S. Weber, H. Herzog, M. Cremer, *et al.*, *Evaluation of the TierPET system*, IEEE Trans. Nucl. Sci. 46 (1999) 1177-1183.
- [27] S. R. Cherry, Y. Shao, R. W. Silverman, *et al.*, *MicroPET: A High Resolution PET Scanner for Imaging Small Animals*, IEEE Trans. Nucl. Sci. 44 (1997) 1161-1166.
- [28] A. P. Jeavons, R. A. Chandler, C. A. R. Dettmar, *A 3D HIDAC-PET Camera with Sub-millimetre Resolution for Imaging Small Animals*, IEEE Trans. Nucl. Sci. 46 (1999) 468-473.

Chapter 3

Scintillation Materials

In many fields of scientific research one is interested in detecting the passage of radiation through matter. The fact that some materials emit light when struck by radiation is known since many years, and this principle is the basis for scintillation detectors.

A scintillating crystal can be described as a material that exhibits a property known as luminescence. When these material are exposed to certain forms of energy (radiation, heat, etc.) they absorb and reemit the energy in form of visible light. The amount of light produced is proportional to the amount of energy deposited in the scintillator. If the reemission occurs immediately (10^{-8} s – time for atomic transitions) after absorption, the process is called *fluorescence*. If the emission is delayed because the excited state is metastable, the process is called *phosphorescence* or *afterglow*. In such cases, the delay time between absorption and emission may last from few microseconds up to hours depending on the material.

According to the type of excitations, one distinguishes between *photoluminescence* and *radioluminescence* depending on whether the material was excited by light (visible or UV) or ionizing radiation, respectively.

One of the first physicists who observed the phenomenon of scintillation was Ernest Rutherford in 1911, who reported about the light produced when α -particles hit a zinc sulphide screen. Since then, a large number of different scintillating materials have been developed for specific application in the fields of physics, biology and medicine.

This chapter treats of the principle of scintillation materials, which means the production of a scintillator (crystal growth), and the fundamental scintillation mechanism.

3.1 Crystal Growth

Crystal growing is a quite delicate and complex process. Especially when certain properties or particular phases of a solid are desired, care has to be taken on the exact stoichiometry and temperature during the growing procedure. In the following subsections, phase diagrams and standard crystal growing procedures are discussed with a special emphasis on the LuAlO_3 (LuAP) and $\text{Lu}_{1-x}\text{Y}_x\text{AlO}_3$ (LuYAP) crystals doped with cerium.

3.1.1 Czochralski Growth – Crystal Pulling

The technique originates, and takes its name, from pioneering work by Czochralski in 1917 [1], who pulled single crystal wires of low melting point metals from the melt. Crystal pulling is in fact the dominant technique for the commercial production of silicon and a very wide range of compound semiconductors, metals, oxides and halides.

In its simplest form shown in Figure 3.1 (A) the technique consists of a crucible, which contains the raw material to be crystallized surrounded by a heater capable of melting the charge. The pull rod with a chuck attached to its lower end is mounted co-axially above the crucible. A seed crystal is attached to the chuck and the pull rod is lowered until the end of the seed crystal is dipped into the melt. The melt temperature is carefully adjusted until a meniscus is supported by the end of the seed. Once a thermal steady state has been achieved, the pull rod is slowly lifted and rotated and crystallization onto the end of the seed occurs. Lifting rates vary with the material, the size of the crystal and the amount of dopant in the melt but are in the range of a few tenths of a millimetre per hour up to tenths of centimetres per hour. Crystal rotation rates usually range from a few up to a maximum of a few hundred revolutions per minute.

To increase the diameter of the crystal from the seed, small and careful heater power reduction is imposed either manually or under automatic control. The whole crystal growth assembly is located within an envelope containing an inert ambient gas or, alternatively, is evacuated. This is done to protect the crystal and melt from attack by atmospheric gases and from ambient temperature fluctuations.

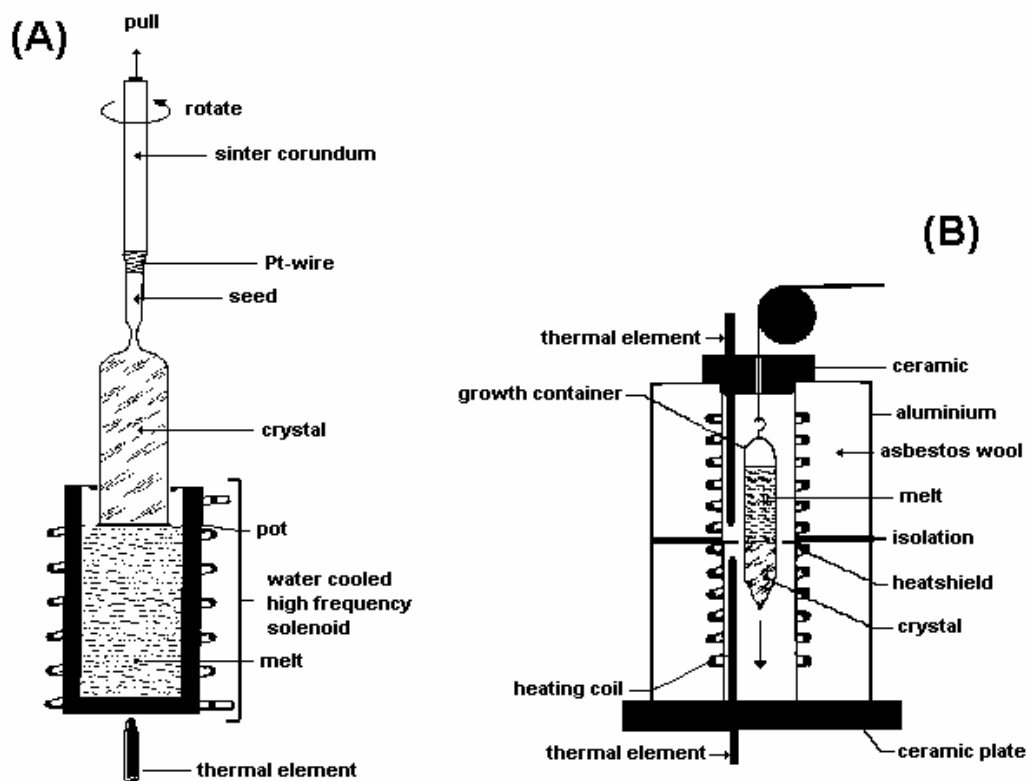


Figure 3.1 Schematic drawing of the (A) Czochralski and (B) Bridgman growing technique.

3.1.2 Bridgman / Stockbarger Technique

In this crystal growing method, the melt is moved through a temperature gradient. The pioneering work was done by Bridgman in 1925 [2] and a similar work was also presented by Stockbarger in 1963 [3].

A picture of the growing technique is shown in Figure 3.1 (B). There is a high temperature zone, an adiabatic loss zone and a low temperature zone. The upper and lower temperature zones are generally independently controlled and the lossy zone is either unheated or poorly insulated [4]. The shape of the axial temperature profile is more readily controlled and/or modified by using two independent heating zones. The crystal can be grown with and without using a seed. Without seeding the crystallization happens spontaneous in nearly all directions.

The conditions pertaining at the three-phase boundary between melt, crystal and crucible are critical to obtain single crystals. One issue is the avoidance of keying of the crystal to the crucible. This requires chemical inertness and a thermal contraction

coefficient of the crystal greater than that of the crucible so that as both cool to room temperature the crystal contracts away from the crucible wall.

The advantage of this growing method is that the whole charge is transformed into a crystal and nearly nothing of the starting material remains in the crucible. This fact is of importance when looking at the cost of the raw material (rare earths are rather expensive).

3.1.3 Growth of Oxide Crystals

The stimulus for the single crystal growth of oxides was supplied by the discovery of pulsed laser action in ruby (1960). Oxide single crystals have been grown from the melt, vapour and solution but, for the size and quality demanded by most specifications, only melt growth processes are generally applicable and of these the Czochralski technique has proved to be the most adaptable. The melting temperature range of oxide crystals is very wide starting from lead germanate (738 °C) to that of lutetium oxyorthosilicate (2320 °C). A short list illustrating the growth conditions for the materials of optical and scintillation interest is provided in Table 3.1.

Table 3.1 Typical conditions for the growth of oxide crystals [4-6].

Compound	Melting point (°C)	Crucible material	Atmosphere	Pulling rate (mm/h)	Rotation rate (rpm)
Pb₅Ge₃O₁₁	738	Au	O ₂	1-10	10-20
CaWO₄	1600	Ir	Ar + O ₂ or N ₂ + O ₂	1-10	5-40
YAlO₃	1870	Ir	Ar + O ₂ or N ₂ + O ₂	1-10	10-20
LuAlO₃	1960	Ir	Ar	2-4	
Gd₂(SiO₄)O	2170	Ir	N ₂ or N ₂ + O ₂	0.5-2	6-60
Y₂(SiO₄)O	2220	Ir	N ₂ or N ₂ + O ₂	0.5-2	6-30
Lu₂(SiO₄)O	2320	Ir	N ₂ or N ₂ + O ₂	0.5-5	20-65

The basic problem associated with oxide crystal growth can be divided into two types namely, those which are technological in character and those which derive from the fundamental nature of oxides in relation to defect control. The technological problems arise from the form in which the source material is available and from the high temperatures involved. The fundamental problems are encountered because of the hard, brittle nature of many oxides, their complex crystal structure and from growth-induced defects, which can limit the quality.

3.1.4 Production of $\text{Lu}_{1-x}\text{Y}_x\text{AlO}_3\text{:Ce}$

The main part of the studied LuYAP crystals was grown with the Czochralski method in the Bogoroditsk Techno Chemical Plant (BTCP) in Russia.

At the beginning of this project the boules were rather small with a size of around 50 mm in length and 20 mm in diameter. The growth of the lutetium Perovskites is a delicate process as discussed in section 3.1.5. By improving the crystal growth conditions and adapting new technology it was possible to enlarge the boules.

In Figure 3.2 two pictures can be seen from a LuYAP ingot grown with the Czochralski method.



Figure 3.2 Pictures of the oven (left side) and of LuYAP ingots (right side) grown in the Bogoroditsk Techno Chemical Plant (Russia) in September 2001.

Currently, the boules have a size of around 30 mm in diameter and 150 mm in length. From these ingots little pixels ($2 \times 2 \times 8 \text{ mm}^3$ or $2 \times 2 \times 10 \text{ mm}^3$) are cut. The amount of crystals depends on the precision and thickness of the saw used. After cutting, the crystals are polished – normally on all faces. A picture of these little pixels is shown in Figure 3.3.

The characterization of these pixel crystals is a main part of this thesis.

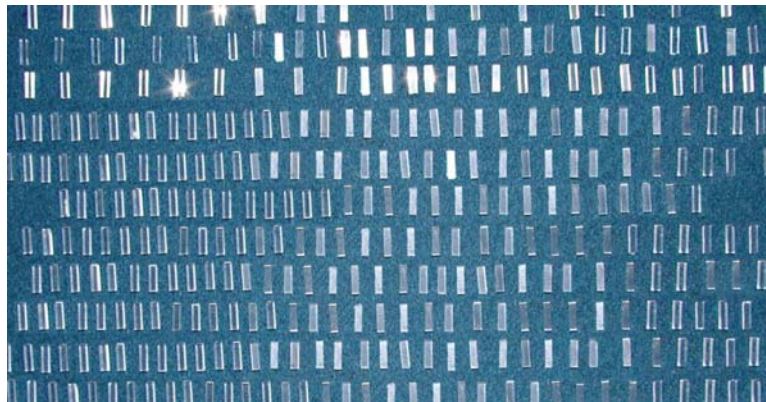


Figure 3.3 Picture of a number of LuYAP pixels with a size of 2 x 2 x 8 mm³.

3.1.5 Crystallography and Phase Diagram for LuAP

When growing a crystal it can appear in different phases, which normally have different properties. For the $\text{Lu}_2\text{O}_3 - \text{Al}_2\text{O}_3$ system, three different crystallographic phases can appear. These are the *Perovskite*, the *Garnet* and the *Monoclinic* phase. A phase diagram of the $\text{Lu}_2\text{O}_3 - \text{Al}_2\text{O}_3$ system is shown in Figure 3.4.

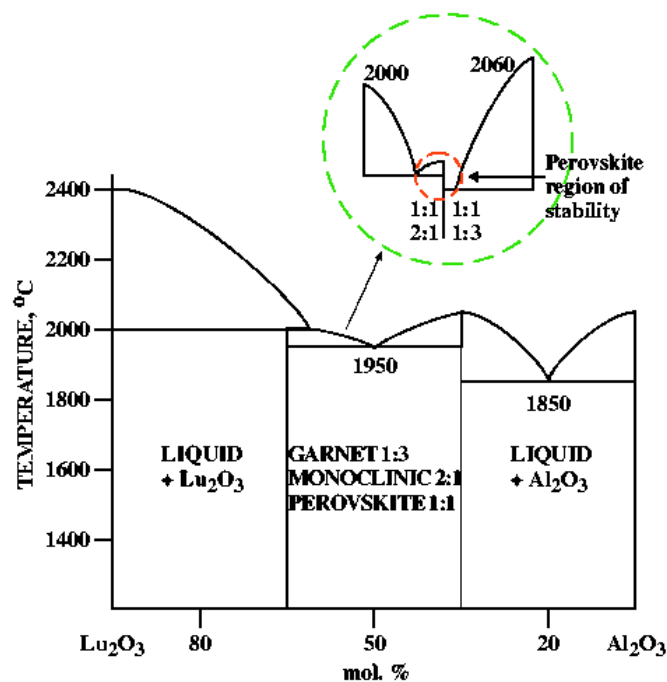


Figure 3.4 Phase diagram of the $\text{Lu}_2\text{O}_3 - \text{Al}_2\text{O}_3$ System.

As shown by [7-9] and in the phase diagram the preferred crystallization phase is the Garnet phase, which also has scintillation properties that are listed in Table 3.2. Unfortunately the desired properties for most of the applications only appear in the Perovskite phase. Thus, to obtain a crystal in the Perovskite phase not only a very high precision in the stoichiometry of the starting raw material (50 mol% Lu_2O_3 and 50 mol.% Al_2O_3) is needed, but strong requirements on the precision of the heating system must result in a control of the temperature in any part of the melt in a range smaller than $\pm 3^\circ\text{C}$. Seeding the crystal is a particularly delicate part of the process as it locally introduces temperature variations, which easily exceed the $\pm 3^\circ\text{C}$ of the Perovskite phase stability.

A way to overcome this temperature and stoichiometry stabilization problem is to grow mixed Perovskite crystals using yttrium or other rare earth ions ($\text{Lu}_x(\text{RE}^{3+})_{1-x}\text{AlO}_3:\text{Ce}$) [10-15].

Table 3.2 summarizes the crystallographic and physical properties of some crystals discussed in this work.

Table 3.2 Crystallographic and physical properties of selected Oxide single crystals [7, 16, 17].

	$\text{Y}_3\text{Al}_5\text{O}_{12}$	$\text{Lu}_3\text{Al}_5\text{O}_{12}$	YAlO_3	LuAlO_3	$\text{Lu}_2(\text{SiO}_4)\text{O}$
Structure	Cubic	Cubic	Orthorhombic	Orthorhombic	Monoclinic
Phase	Garnet	Garnet	Perovskite	Perovskite	
Space group	O_h^{10}	O_h^{10}	D_{2h}^{16}	D_{2h}^{16}	C2/c
Unit cell parameters (Å)			a = 5.176 b = 5.332 c = 7.356	a = 5.100 b = 5.330 c = 7.294	a = 14.254 b = 10.241 c = 6.641 $\gamma = 122.20^\circ$
Density (g/cm³)	4.55	6.71	5.35	8.34	7.41
Effective Z	32.0	62.91	33.5	64.94	66
Attenuation length (cm)	2.58	1.34	2.63	1.05	1.23
Emission wavelength (nm)	520	510	365	365	420
Decay time (ns)	65	58 + slow (2 μs)	28	18	40
Refractive Index	1.82		1.95	1.94	1.808
Bandgap (eV)			8	8.5	6.4

Generally, in these crystals, Ce^{3+} dopant ions act as activator. They can mainly replace those lattice ions having the same charge and similar ionic radius. When looking at the different ionic radii from yttrium³⁺ $r_i = 0.89 \text{ Å}$ und lutetium³⁺ $r_i = 0.85 \text{ Å}$, it becomes clear that a replacement of Y with Ce ($r_i = 1.04 \text{ Å}$) is easier than for Lu. For this reason, the distribution coefficient of cerium in lutetium orthoaluminate, which means the fraction of the concentration in the melt that actually is taken into the crystal lattice, is not as high as desired (around 15% [17]). This circumstance negatively affects the light

output. Aluminium³⁺ ions with an ionic radius of 0.51 Å are rarely replaced by Ce³⁺ ions. Figure 3.5 shows a drawing of the orthorhombic structure of the LuAP:Ce crystal.

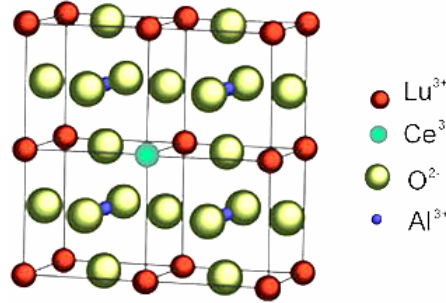


Figure 3.5 Schematic drawing of the orthorhombic crystal structure of the LuAlO₃:Ce crystal. It can be clearly seen that the cerium ion replaces the lutetium ions in the lattice.

Generally, various point defects or complexes arise in crystals such as oxygen vacancies V_O , colour centres associated with them, oxygen interstitials, etc. These defects influence the scintillation properties of the crystal, usually in an unwanted way.

X-ray Diffractometry

To study the unit cell parameter of our crystals, selected LSO, LuAP and LuYAP samples were sent to J. M. Moreau (ESIA, Annecy, France) for x-ray diffraction measurements (Laue method). Using a monochromatic x-ray beam and a goniometer one can determine the crystal structure, the unit cell parameters and the principal axes of the samples. J. M. Moreau measured the unit cell parameters and the principal axes of the samples and set the results to our disposal (see Table 3.3).

Table 3.3 Unit cell parameters and principal axes measured with x-ray diffractometry by J. M. Moreau for selected crystals.

	LuAP	Lu _{0.8} Y _{0.2} AP	LSO
Unit cell	a = 5.02	a = 5.14	a = 14.26
parameters (Å)	b = 5.32	b = 7.25	b = 6.57
	c = 7.31	c = 4.95	c = 10.23
			β = 120.7°
Principal axes	[1 0 0]	[0 1 -4]	[3 0 4]
	[0 1 0]	[4 0 1]	[0 1 0]
	[0 0 1]	[0 1 0]	[5 0 -3]

The unit cell values found for the LuAP and LSO crystals are comparable to results found by other authors [7, 16] given in Table 3.2.

3.2 Luminescence of Inorganic Crystals

The luminescence of an organic compound like anthracene is an inherent molecular property, characteristic also of the material in the vapour or solution phases. By contrast the luminescence of inorganic crystals is a crystalline property, and it is not normally exhibited in other phases.

The majority of efficient inorganic luminescent materials are impurity-activated, which means that their luminescence is due to the presence of small concentrations of specific impurities. Typical systems are the alkali halides activated by heavy metals such as thallium (e.g. NaI:Tl, CsI:Tl) or oxides doped with rare earth ions (LSO:Ce, YAP:Ce). Apart from crystals, oxide or fluoride inorganic glasses may also be activated by similar impurities and luminescent. In some crystals the activator is not an added impurity, but a stoichiometric excess of one of the constituents of the solid (e.g. BGO, BaF₂). The excess ions occupy interstitial positions in the crystal lattice and function as luminescent centres. Such crystals are called self-activated. A few pure crystals, notably diamond, are also luminescent. In this case it appears that the luminescence centres are associated with defects in the crystal lattice, and that atoms or ions situated near these defects act as activators. Thus the general pattern for luminescence in an inorganic solid is a crystal or glass containing emission centres, which may be either interstitial or substitutional impurities, excess atoms or ions, or atoms or ions associated with defects.

3.2.1 The Energy Band Model

Perfect Crystals

A suitable model for the discussion of inorganic crystals is provided by the collective electron or band theory from Bloch (1928).

The electronic energy states of an isolated atom or molecule consist of a series of discrete levels defined by Schrödinger's equation. In an inorganic crystal lattice the outer electronic energy levels are perturbed by mutual interactions between the atoms or ions, and they are broadened into a series of continuous allowed energy bands, separated by forbidden energy regions. The inner energy levels are practically undisturbed and retain their normal character. A schematic figure of the energy bands is shown in Figure 3.6 (a).

For an insulator or a low temperature semi-conductor the lower energy bands are completely filled while the higher bands are empty. The highest filled band, the valence band, is separated from the lowest empty band known as the conduction band, by an

energy gap E_g of a few electron volts. Electrons from the valence band may be raised into the conduction band by the absorption of a photon leaving positive holes in the valence band. Photoconduction can then take place by the independent motion of the electrons in the conduction and the holes in the valence band.

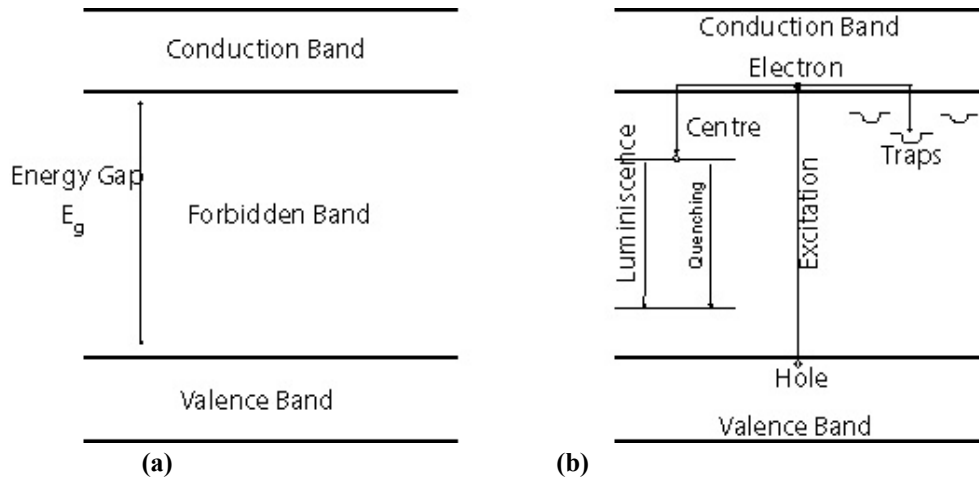


Figure 3.6 (a) Energy bands in ideal insulating crystal and (b) energy bands in impurity-activated crystal phosphor showing excitation, luminescence, quenching and trapping processes.

Alternatively the excited electron may remain bound to the positive hole. This system, which constitutes an *exciton*, carries no charge and is free to migrate through the crystal lattice. The exciton band corresponds to a band of energies below the conduction band. In principle the two bands can be distinguished by the absence of any photoconduction associated with exciton migration. By analogy to single molecules, promotion of an electron into the exciton band constitutes excitation, while similar promotion into the conduction band constitutes ionization. Electrons in the conduction band and holes in the valence band may subsequently recombine to form excitons.

In semi-conductors the energy gap E_g between the valence and the conduction band is sufficiently small for some electrons to be able to acquire the excitation energy thermally. In insulating crystals the energy gap is large enough that the concentration of free carriers is negligible at normal temperatures, in the absence of high electric fields of excitation by ultraviolet or ionizing radiation.

Imperfect Crystals

The simple model is only true for insulators having a perfect crystal lattice. In practice, variations in the energy bands due to defects and impurities in the crystal lattice occur,

producing local electronic energy levels in the normally forbidden region between conduction and valence bands. If these levels are unoccupied, electrons (or excitons) moving in the conduction band may enter these centres. There are mainly three types of centres:

- a) *Luminescence centres*, in which the transition to the ground state is accompanied by photon emission.
- b) *Quenching centres*, in which radiationless dissipation of excitation energy can take place.
- c) *Traps*, which have metastable levels from which the electrons may subsequently return to the conduction band by acquiring thermal energy, or fall to the valence band by radiationless transition.

The same centres may contain luminescence, quenching and/or trapping levels since their relative population is determined by the Boltzmann statistical distribution.

The luminescence centres and traps arise from impurities like interstitial ions and/or defects. They introduce local discrete energy levels corresponding to the ground and excited state of a centre. The excitation of a centre requires the capture of an electron from the conduction band and a hole from the valence band either by capturing an exciton or by electron-hole recombination at a centre.

The traps arise from other lattice variations and provide additional levels for the electrons below the conduction band (or holes above the valence band). The energy level system for an impurity-activated crystal phosphor is shown in Figure 3.6 (b).

3.2.2 Conditions for Luminescence of a Centre

The theoretical model of configuration co-ordinate from Hippel (1936) and Seitz (1938, 1939) is often used to discuss the conditions for luminescence emission or thermal quenching of a centre. It is a rather general model and it is usable for all luminescent materials (including organic scintillators). In Figure 3.7 the potential energies of the ground and excited electronic state of the luminescent centre are plotted against the x configuration coordinate of the centre. The curves aAa' and bBb' represent the vibrational amplitude of the centre in the ground and excited state, respectively. The minima of the curves (point A and B) indicate the stable energy positions of the two states.

At room temperature, the thermal vibrations lead to displacements from the minimum potential energy position according to energies of kT .

If a centre absorbs a photon with the energy $h\nu$ (or is excited by the capture of an exciton) a transition from the ground to the excited electronic state takes place. The transition occurs along a vertical line AC on the diagram, since by the Franck-Condon principle, electronic transitions involved in absorption or emission occur in a short time compared with that of atomic or ionic movements. Directly after this transition the system moves to the point of minimum potential energy (from C to B) and gives the excessive vibrational energy thermally to its neighbours. The time spent in B depends on the probability of the optical transition which gives rise to the luminescence emission $h\nu'$. After this transition the centre in the ground state returns from D to A by thermally dissipating the rest vibrational energy.

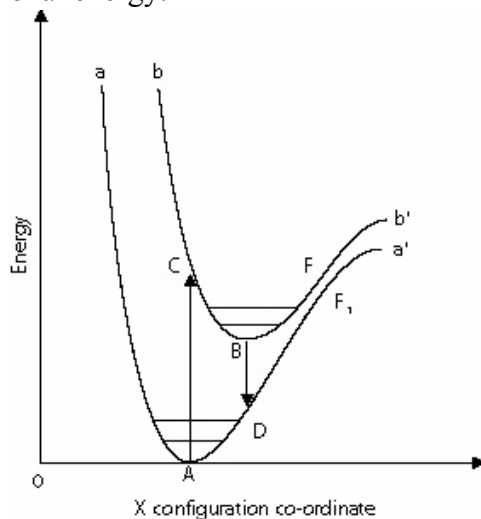


Figure 3.7 Potential energy diagram of luminescent centre. aAa' represents the ground state and bBb' the excited state. AC is the absorption transition, BD the luminescence emission and FF_1 the region of internal quenching.

Figure 3.8 shows the origin of the absorption and emission spectra corresponding to the AC and BD transition, respectively.

- The emission spectrum is at lower energies (longer wavelengths) than the absorption spectrum (Stoke's law).
- The overlap of the absorption and emission spectrum depends on the relative positions of the potential energy curves of the ground and excited states.
- Vibrational structure in the absorption and emission spectrum arise from transitions to the vibrational sub-levels of the excited and ground states.
- In inorganic scintillators, the emission spectrum tends to be broader than the absorption spectrum of the luminescence centres.

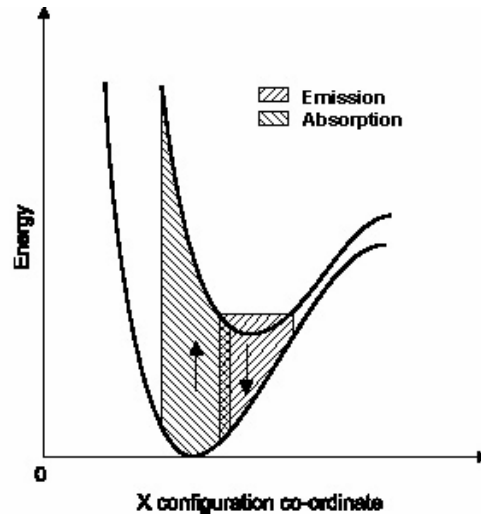


Figure 3.8 Absorption and luminescence emission transition showing the origin of the overlap of absorption and emission spectra.

3.3 Physical Mechanism of Scintillation

The scintillation process can be divided in three stages: a) the primary interaction of radiation with matter, relaxation and thermalization of the resulting electrons and holes to electron-hole pair energies roughly equal to the bandgap energy E_g , b) further relaxation, formation of excitonic states, and energy transport to the luminescence centres, and c) luminescence. It is well-known that crystals having a high light output under photoexcitation can give a rather low light emission under excitation by charged particles, x-rays or γ -rays [19]. This is primarily a consequence of energy losses in stages a) and b).

The primary interaction of an x-ray or γ -ray will result in the production of one or more energetic electrons, depending on the energy and the interaction mechanism (photoelectric effect, Compton effect, electron-positron pair formation). X-rays produced by recombination of electrons with holes in core levels (from the photoelectric effect) will also produce electrons by the mechanism mentioned above. Heavy charged particles and low-energy electrons transfer their energy primarily by ionization, thus producing electrons and holes. High-energy electrons transfer their energy by production of bremsstrahlung, which in turn gives pair formation.

Various models have been used for the description of these complicated processes of energy dissipation: simple phenomenological [20], “crazy carpentry” [21], plasmon

[22], and polaron [23]. These models consider only a single mechanism and do not take into account the whole variety of processes taking place. A detailed description of these models would go beyond the scope of this thesis and can be found in literature.

3.3.1 Energy Bands and Transitions in Inorganic Crystals

Let us consider a crystal irradiated by x-rays or γ -ray quanta with such energy that the photoelectric effect predominates [19]. Figure 3.9 shows a typical energy band scheme of a wide gap crystal with a narrow valence band width ΔE_v .

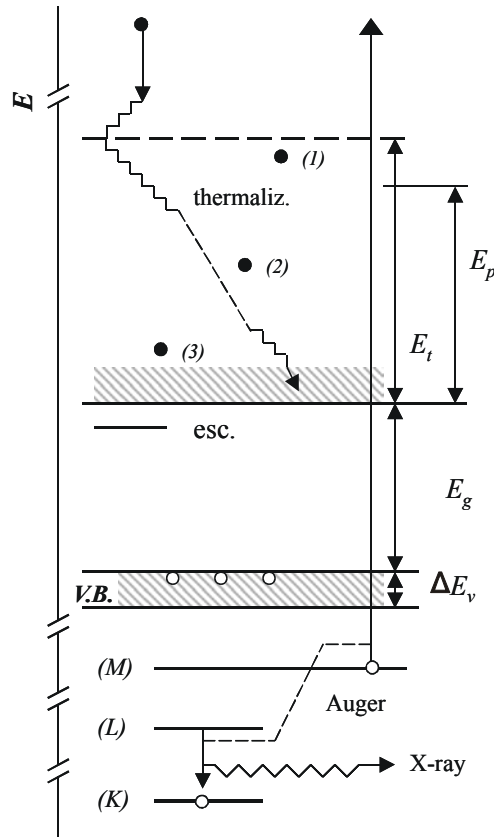


Figure 3.9 Energy bands and possible transitions in an ionic crystal.

The scintillation response of the crystal can be attributed to the primary photoelectron and the hole in an inner shell of the atom. The relaxation of the atom with the hole in an inner shell occurs by a cascade of radiative (x-ray emission) and non-radiative Auger transitions in roughly 10^{-15} to 10^{-13} s. The secondary x-rays are re-absorbed, also primarily by the photoelectric effect. The fast photoelectrons and the Auger electrons interact with the shells of atoms giving rise to an avalanche of secondary carriers. The

avalanche process continues till the generated electrons (and photons) are unable to create further ionization. As soon as the electron energy falls below the ionization threshold E_i the electrons simply emit phonons until the bottom of the conduction band is reached. This is the process of electron thermalization.

At $E > E_i$ electron-electron relaxation predominates, whether by direct ionization or via plasmon creation [22]. Real energy loss occurs at $E < E_i$ due to electron-phonon scattering. The energy loss of an electron with an energy $E \leq E_i$ (position 1 in Figure 3.9) is more than that for an electron with $E \approx E_i/2$ (position 2) and an electron with $E \geq 0$ (position 3). The possibility of an electron to appear at a certain position between the bottom of the conduction band and the threshold at E_i involves the discreteness of the electronic levels of the atoms and the creation of plasmons in the crystal.

From a comparison of the time scales of electron-electron relaxation (10^{-15} to 10^{-13} s), electron-phonon relaxation (10^{-12} to 10^{-11} s) and the lifetimes of excited luminescence centres ($\tau > 10^{-9}$ s) we may conclude that these three processes can be considered as events following each other.

3.3.2 Scintillation Efficiency

The essential feature required of any scintillator is to be an effective converter of ionizing radiation to visible light. The mechanism of scintillation is described by the well-known phenomenological formula for the efficiency [24]

$$\eta = \beta \times S \times Q, \quad 0 \leq \eta, \beta, S, Q \leq 1 \quad (3.1)$$

This relationship expresses the overall quantum efficiency of the process as the product of three parameters β , S and Q , the efficiencies of the three consecutive steps (conversion, transfer and luminescence) into which the overall process can be conveniently divided.

The first of those parameters, β , describes the efficiency of the conversion process, in which the energy E_γ of a γ -particle is used to produce a large number of electron-hole pairs. For a material of bandgap E_g it takes at least an energy $E_{min} = bE_g$, to produce a single electron-hole pair, where b is around 1.5 to 2.0 for ionic crystals and 3 to 4 for materials with a covalent type of binding (semi-conductors). The value E_{min} is also called ionization threshold [19]. Thus, the maximum possible number of electron-hole pairs is E_γ / bE_g and the conversion efficiency, β , will be given by:

$$\beta = \frac{n_{e-h}}{E_\gamma / bE_g}, \quad (3.2)$$

where n_{e-h} is the number of electron-hole pairs actually produced by one stopped photon. Since the energy E_t needed to produce one electron-hole pair can be expressed by:

$$E_t = E_\gamma / n_{e-h}, \quad (3.3)$$

it follows that:

$$\beta = b E_g / E_t. \quad (3.4)$$

The second parameter in equation (3.1) S , describes the efficiency of the transfer process, while the third, Q , describes the quantum efficiency of the centre itself. The number of photons produced by a single γ -particle will be:

$$n_{ph} = n_{e-h} S Q = \frac{E_\gamma}{b E_g} \beta S Q \quad (3.5)$$

Hence the light output LO, the number of photons per MeV, can be expressed as

$$LO = n_{ph} / E_\gamma = \frac{10^6}{b E_g} \beta S Q, \quad (3.6)$$

and can be calculated assuming that E_g (in eV), b , β , S and Q are known. Measurements of E_g and Q are standard in optical spectroscopy of solids while β can be found using the proper material constants. For many activators Q is close to unity.

Formula (3.6) shows that crystals with a narrow bandgap can have high scintillation efficiency. This is confirmed for alkali-halide crystals at low temperature. The efficiency of the scintillators based on pure (non-activated) crystals increases in the order fluorides, chlorides, bromides and iodides, i.e. inversely proportional to the bandgap. At room temperature this regularity is not so obvious due to quenching of the luminescence.

Recent works have shown that efficient conversion ($\beta \approx 1$) is expected for wide-bandgap insulators. We are thus left with the transfer efficiency, S , as the principal unknown. The second stage of the scintillation process involves transport and simultaneous or subsequent capture of a hole and an electron by an activator. The holes and electrons migrating through the crystal can also be captured by traps and/or take part in non-radiative recombination. This is a main source of energy loss resulting in a low light output. The quantity $1-S$ is called the migration loss.

In the following table a few entries from Lempicki *et al.* [25] are reproduced for the number of calculated e-h pairs for some scintillators.

Table 3.4 Calculated creation of e-h pairs and observed light output (reproduced from [25]).

Scintillator	Calculated e-h pairs per MeV	Observed light output per MeV	Efficiency η
CSI : Tl	69 444	65 000	0.936
NaI : Tl	75 330	38 000	0.504
BGO	88 889	8 500	0.096
LSO : Ce	69 444	27 300	0.393
LuAP : Ce	55 556	11 300	0.20

If S and Q were equal to unity, then the number of photons (LO) generated per MeV would be equal to the number of electron-hole pairs. This is evidently not the case, except for CsI:Tl, for which the LO is close to the theoretical one. For LuAP and LSO it has been shown that Q is essentially unity, thus identifying an inadequacy in the transfer efficiency ($S < 1$) as the factor primarily responsible for the lower than possible light output.

3.4 General Characteristics of Inorganic Scintillators

As already mentioned in section 2.3, there is considerable interest in finding inorganic materials with optimal scintillation properties. Some of them are light yield, decay time, optical properties, etc. The following paragraphs cover general scintillator properties and also some details of the scintillation mechanism.

3.4.1 Decay Time

The luminescence decay time can be defined as the time interval between the crystal excitation and the detection of the emitted light. It is strongly related to the life-time of the excited states. As explained before, the deexcitation from the excited to the for instance ground state can happen in two ways: through a radiative or a non-radiative transition (thermal quenching). In consequence, the total probability for the transition is given by the sum of the two relative probabilities P_r (radiative transition) and P_{nr} (non-radiative transition). The luminescence decay time τ can be expressed as

$$\tau \propto \frac{1}{P_r + P_{nr}} \quad (3.7)$$

where we take into account that the life time of the excited state is inverse proportional to the deexcitation probability.

Looking at these two equations for the decay time (3.7) and scintillator efficiency (3.18) we can see that they compete with each other. As the non-radiative probability (P_{nr}) increases, the luminescence decay time (τ) decreases, whereas at the same time the luminescence efficiency (η) worsens leading to a weaker emission.

In most scintillators, the intensity of the emission rises instantaneously and reaches a maximum at $t = 0$. The intensity of the emission $J(t)$ (in photons/s) of a scintillator with one type of luminescent centre can decay exponentially with decay time constant τ :

$$J(t) = J(0) \exp\left(-\frac{t}{\tau}\right) \quad (3.8)$$

Where $J(0)$ is the initial intensity, i.e., photons/s at $t = 0$. This case conforms to a linear type of recombination (first-order kinetics) when the concentration of luminescent centres is greater than the concentration of unequilibrium carriers (electrons and holes). The τ is given by [26]

$$\tau = \frac{cm_e}{8\pi \cdot e^2} \cdot \frac{\lambda^2}{fn} \left(\frac{3}{n^2 + 2} \right)^2 \quad (3.9)$$

where f is the oscillator strength of the transition, λ is the wavelength of the transition, and n is the refractive index of the material. Formula (3.9) shows that the decay time increases with wavelength. Consequently the ultraviolet-emitting scintillators tend to be fast, which was confirmed by several experiments.

Calculations using equation (3.9) show that the shortest radiative decay time, which can be obtained for electric dipole transitions is a few nanoseconds. The impurity or thermal quenching may decrease decay time, but this is accompanied with a decrease in the light yield.

In many scintillators, two or more decay time constants are detected. In this case

$$J(t) = \sum_i \frac{(N_{ph})_i}{\tau_i} \exp\left(-\frac{t}{\tau_i}\right) \quad (3.10)$$

where $(N_{ph})_i$ photons are emitted in the decay time component τ_i .

3.4.2 Afterglow

A scintillator can display a long-time luminescence (several microseconds and up) which is called afterglow. The afterglow origin is phosphorescence rising in a crystal due to the thermal release of the carriers from the traps. The traps are formed due to defects and impurities existing in the crystal as well as those created by irradiation. The residual impurities and point defects can form additional centres of luminescence (phosphorescence) in the crystal. The intensity, spectral composition, and decay time of

the afterglow depend on the purity of raw material, crystal pulling conditions, heat treatment, and dose of irradiation.

3.4.3 Theory on Energy Resolution

One of the main tasks of γ -spectrometry is discrimination of the γ -rays with slightly different energies. It is important to achieve a minimum photopeak or γ -line width in the pulse-height spectrum resulting from monoenergetic γ -quanta.

Following Birks [18] the mean output pulse of \bar{Q}_0 electrons arriving at the anode of the photomultiplier tube in a practical scintillation counter equals

$$\bar{Q}_0 = \bar{N}\bar{p}\bar{M} \quad (3.11)$$

where \bar{N} is the mean number of photons created in the scintillator after gamma absorption. \bar{p} is the photon transfer efficiency and represents the probability that a scintillation photon produces an electron at the first dynode. \bar{M} is the mean overall gain of the PMT. The energy resolution $(\Delta E/E)_{FWHM}$ is related to the fractional variance $\nu(Q_0)$ of Q_0 as

$$R = \left(\frac{\Delta E}{E} \right)_{FWHM} = 2.36 \sqrt{\nu(Q_0)} \quad (3.12)$$

The variance is given as

$$\nu(Q_0) \approx \left[\nu(N) - \frac{1}{\bar{N}} \right] + \nu(p) + \frac{1 + \nu(M)}{\bar{N}\bar{p}} \quad (3.13)$$

where $\nu(N)$ is the variance in the number of photons created in the crystal which in case of Poisson statistics equals \bar{N}^{-1} . Therefore the bracketed term represents the deviation in the number of photons from the Poisson statistics. $\nu(p)$ is the transfer variance and $\nu(M)$ is the variance of the photomultiplier gain, typically equal to 0.1 for the XP2020Q [27].

When discussing the energy resolution it is common to introduce the terms intrinsic resolution R_i , transfer resolution R_p and photomultiplier resolution R_M [27]. The intrinsic resolution is equal to the bracketed term and is also known as the intrinsic linewidth or broadening. The transfer resolution and the PMT resolution correspond with the second and last term in (3.13), respectively

$$R^2 = R_i^2 + R_p^2 + R_M^2 \quad (3.14)$$

There are two main contributions to the intrinsic resolution, the non-proportional response (R_{np}) of the scintillator to γ -rays as a function of photon energy and the factor R_{inh} which is connected with inhomogeneity of the crystal leading to local variations in

the light output. Possible origins can be non-uniform distribution of activator ions, crystal defects or flaws in the crystal.

$$R_i^2 = R_{np}^2 + R_{inh}^2 \quad (3.15)$$

The transfer resolution is determined by many factors like the wavelength of the photon and the quantum efficiency of the PMT at this wavelength, the transmission of the scintillation light through the crystal, the reflectivity of the covering material, the angle of incidence of the photons on the photocathode, the non-uniformity of the photocathode, etc.

The combined effect of intrinsic and transfer efficiency is named scintillator resolution R_s and so the energy resolution is given as

$$R^2 = R_s^2 + R_M^2 \quad R_M = 2.36 \sqrt{\frac{1 + \nu(M)}{\bar{N}\bar{p}}} \quad (3.16)$$

where $\bar{N}\bar{p}$ is the number of photoelectrons. For modern scintillation detectors it is often assumed that the transfer resolution is negligible compared to the other components of the energy resolution. Thus the intrinsic resolution can be calculated using

$$R_i^2 = R^2 - R_M^2. \quad (3.17)$$

3.4.4 Non-Proportional Response

The basic principle of scintillation counting is that the light output of the scintillator is proportional to the energy deposited within a crystal. It means that the relative light output LO_R (see equation 3.6) should be constant at various energies of incident γ -rays. However, some scintillators display deviations from stability of excitation spectrum, i.e., relative light output versus energy of incident photon energy E_γ .

This phenomenon of non-proportional response negatively affects the spectrometer characteristics of the detector.

As mentioned before, the non-proportional response also affects the energy resolution of the scintillator. This was studied extensively for the classical scintillators (NaI:Tl and CsI:Tl) in the 1960s and became an important issue nowadays due to the rather poor energy resolution of LSO:Ce [28-32].

The physical reason for the non-proportionality is a statistical process of the creation of secondary electrons and photons for various scintillations [26]. In the energy region up to 1 MeV, the photoelectric absorption and Compton scattering of photons are the only types of interaction. Photoelectric absorption leads to the full energy deposit in the crystal, whereas in Compton interactions only a fraction of the energy is absorbed and the scattered photon can be involved in subsequent interactions (Compton scattering, photoelectric effect or escape the crystal). The complete absorption of the energy is also

possible through a number of Compton encounters (multiple Compton absorption). Therefore, the distribution in number and energy of secondary electrons is determined by the way in which the incident γ -ray transfers its energy to the crystal.

The phenomenon of non-proportional response is also typical for electron excitation of crystals. The Compton Coincidence Technique (CCT) has recently been implemented for the purpose of characterizing light yield non-proportionality of several crystals [33, 34]. The measured electron responses were then used to calculate the photon responses for each of these scintillation crystals. Good agreement was observed between the photon responses calculated in this study and measured photon responses for CsI:Tl. This study also indicated that there are two general electron response shapes. First, the alkali halide scintillators have a single maximum in the range of 10 to 20 keV. Second, other crystals (LSO:Ce, YAP:Ce, BGO) appear to have a monotonically increasing electron response with increasing energy.

The study on the non-proportional response of the light output on photon energies for LSO:Ce and LuYAP:Ce is presented in chapter 5.

3.4.5 Temperature Response

In most applications the scintillators are used at room temperature. During operation the temperature of the detector can vary slightly due to irradiation or change of ambient conditions. It is particularly difficult to keep a stable regime for detector operation for detectors used in certain applications. The change of scintillator light yield with temperature leads to a change of the output signal of the detector. The thermal stability of the scintillation yield is needed for proper operation of the detector.

For direct excitation of a luminescence centre (photoluminescence), the temperature dependence of quantum efficiency q (number of emitted photons/number of incident photons) is determined by the thermal change of probability of non-radiative transitions P_{nr} .

As shown in Figure 3.7, the potential energy curves of the ground and excited state usually approach each other closely at a certain point F . A luminescence centre that reaches F in its excited state can make a non-radiative transition to the corresponding point F_l of the ground state and then dissipate the excess energy thermally. This corresponds to the internal quenching process, which competes with the emission of a photon. The relative probability of emission P_r and of internal quenching P_{nr} depends on the relative position of B and F and on the absolute temperature T . The luminescence quantum efficiency is given by [18]:

$$q = \frac{P_r}{P_r + P_{nr}} \quad (3.18)$$

The probability P_{nr} that the excited centre may be thermally activated is proportional to $\exp(-E_q / kT)$, where k is the Boltzmann's constant and E_q is the quenching energy, so that $P_{nr} = a \cdot \exp(-E_q / kT)$, while the radiative transition probability P_r is not affected by temperature. The quantum efficiency of the luminescence can be written as

$$q(T) = \frac{1}{1 + b \exp(-E_q / kT)} \quad (3.19)$$

where a and $b (= a / P_r)$ are constants. This equation, which was first derived from Mott and Gurney (1939) accounts qualitatively for the variation of luminescence quantum efficiency with temperature.

At low temperatures ($kT \ll E_q$), the radiative decay dominates and quantum efficiency is slowly varying with temperature. For increasing temperature, the non-radiative decay becomes increasingly important and the luminescence is thermally quenched. The thermal quenching causes a reduction in intensity and also in decay time of luminescence because $\tau(T) = \tau_0 q(T)$, where τ_0 is decay time at $T \rightarrow 0$.

3.4.6 Optical Properties

The main optical characteristics of a scintillator are absorption and emission. In most applications, the scintillator should transmit its own emitted light. The emitted light can be absorbed by impurities and defects (background absorption) as well as by the host crystal (reabsorption).

The level of reabsorption depends on physical characteristics of the compound like bandgap width and properties of the activator. This type of absorption can hardly be decreased.

The level of impurity absorption depends on the concentration of residual impurities and point defects. Therefore, the transmission of a crystal is dictated by purity of the raw materials and conditions of the crystal growth. The transmission can vary along the length of the crystal due to a non-uniform concentration of impurities in a particular region of the ingot. In this case, the large crystal may have a higher concentration of residual impurities at one end than the other. This can affect the energy resolution of the detector.

The activator emission can be reabsorbed by the activator centres themselves. The reabsorption is pronounced in the Ce-based and Eu-based crystals because of overlapping of the absorption (f→d) and emission (d→f) bands. As it is clear from the configuration coordinate shown in Figure 3.8, the Stokes shift (the shift between

absorption and emission bands) increases with separation of the equilibrium positions of excited and ground states.

3.5 References

- [1] J. Czochralski, Z. Physik Chem. 92 (1917) 219.
- [2] P. W. Bridgman, Proc. Am. Acad. Arts Sci. 60 (1925) 303.
- [3] D. C. Stockbarger, Rev. Sci. Instrum. 7 (1963) 133.
- [4] D. T. J. Hurle, *Handbook of Crystal Growth Vol.2*, Amsterdam, North-Holland (1993-1994).
- [5] C. L. Melcher, J. S. Schweitzer, C. A. Peterson, R. A. Manente, H. Suzuki, *Crystal Growth and Scintillation Properties of the Rare Earth Oxyorthosilicates*, Proc. Int. Conf on Inorganic Scintillators, SCINT95, 1996, Delft University Press.
- [6] A. G. Petrosyan, K. L. Ovanesyan, G. O. Shirinyan, T. I. Butaeva, C. Pedrini, C. Dujardin, A. Belsky, *Growth and light yield performance of dense Ce^{3+} -doped $(Lu,Y)AlO_3$ solid solution crystals*, Journal of Crystal Growth 211 (2000) 252-256.
- [7] A. G. Petrosyan, G. O. Shirinyan, K. L. Ovanesyan, C. Pedrini, C. Dujardin, *Bridgman single crystal growth of Ce-doped $(Lu_{1-x}Y_x)AlO_3$* , Journal of Crystal Growth 198/199 (1999) 492-496.
- [8] W. W. Moses, S. E. Derenzo, A. Fyodorov, M. Korzhik, A. Gektin, B. Minkov, V. Aslanov, *$LuAlO_3:Ce$ - A high density, high speed scintillator for gamma detection*, IEEE Trans. Nucl. Sci. 42 (1995) 275-279.
- [9] A. Lempicki, M. H. Randles, D. Wisniewski, M. Balcerzyk, C. Brecher, A. J. Wojtowicz, *$LuAlO_3:Ce$ and other Aluminate Scintillators*, IEEE Trans. Nucl. Sci. 42 (1995) 280-284.
- [10] J. A. Mares, *Spectroscopy and characterization of Ce^{3+} -doped pure or mixed $Lu_x(RE^{3+})_{1-x}AlO_3$ scintillators*, J. Alloys and Comp. 300-301 (2000): 95-100.
- [11] J. A. Mares, *et al.*, *Development of new mixed $Lu_x(RE^{3+})_{1-x}AP:Ce$ scintillators ($RE^{3+}=Y^{3+}$ or Gd^{3+}): comparison with other Ce-doped or intrinsic scintillating crystals*, Nucl. Instr. and Meth. A 443 (2000) 331-341.
- [12] J. A. Mares, M. Nikl, J. Chval, J. Kvapil, J. Giba, K. Blacek, *Luminescence and Scintillation Mechanisms in Ce^{3+} doped $(RE^{3+})AlO_3$ Perovskite Crystals*, Proc. Int. Conf on Inorganic Scintillators, SCINT95, 1996, Delft University Press.
- [13] J. A. Mares, *et al.*, *Properties of New Mixed $Lu_x(RE^{3+})_{1-x}AlO_3:Ce$ Scintillators ($RE^{3+} = Y^{3+}$ or Gd^{3+}) Compared with Other Ce-Doped or Intrinsic Scintillator Crystals*, Proc. IEEE Nuclear Science Symposium and Medical Imaging conference (1999), Seattle, Washington, 538-542.

- [14] J. A. Mares, M. Nikl, *Energy transfer, fluorescence and scintillation processes in Cerium-doped $RE^{3+}AlO_3$ fast scintillators*, Acta Phys. Polon. A 90 (1996) 45-54.
- [15] A. Belsky, E. Auffray, P. Lecoq, C. Dujardin, *Progress in the development of $LuAlO_3$ based scintillators*, Proc. IEEE Nuclear Science Symposium and Medical Imaging conference (2000), Lyon, France.
- [16] C. L. Melcher, J. S. Schweitzer, *Cerium-doped Lutetium Oxyorthosilicate: A Fast, Efficient New Scintillator*, IEEE Trans. Nucl. Sci. 39 (1992) 502-505.
- [17] A. Lempicki, C. Brecher, D. Wisniewski, E. Zych, A. J. Wojtowicz, *Lutetium Aluminate: Spectroscopic and Scintillation Properties*, IEEE Trans. Nucl. Sci. 43 (1996) 1316-1320.
- [18] J. B. Birks, *The Theory and Practice of Scintillation Counting*, Oxford, Pergamon Press (1964).
- [19] P. A. Rodnyi, P. Dorenbos, C. W. E. van Eijk, *Energy Loss in Inorganic Scintillators*, Phys. Stat. Sol. B 187 (1995) 15-29.
- [20] W. Shockley, Solid State Electronics 2 (1961) 35.
- [21] W. van Roosbroeck, Phys. Rev. 139 (1965) A1702.
- [22] A. Rothwarf, J. Appl. Phys. 44 (1973) 752.
- [23] D. J. Robbins, J. Electrochem. Soc. 127 (1980) 2694.
- [24] A. Lempicki, A. J. Wojtowicz, E. Berman, *Fundamental limits of scintillator performance*, Nucl. Instr. and Meth. A 333 (1993) 304-311.
- [25] A. Lempicki A., J. Glodo, *Ce-doped scintillators: LSO and LuAP*, Nucl. Instr. and Meth. A 416 (1998) 333-344.
- [26] P. A. Rodnyi, *Physical Processes in Inorganic Scintillators*, New York, CRC Press (1997).
- [27] P. Dorenbos, J. T. M. de Haas, C. W. E. van Eijk, *Non-Proportionality in the Scintillation Response and the Energy Resolution Obtainable with Scintillation Crystal*, IEEE Trans. Nucl. Sci. 42 (1995) 2190-2202.
- [28] P. Dorenbos, J. T. M. de Haas, C. W. E. van Eijk, C. L. Melcher, J. S. Schweitzer, *Non-linear response in the scintillation yield of $Lu_2SiO_5:Ce^{3+}$* , IEEE Trans. Nucl. Sci. 41 (1994) 735-737.
- [29] P. Dorenbos, J. T. M. de Haas, C. W. E. van Eijk, *Non-proportional response of scintillation crystals to x-rays and gamma-rays*, Radiation Measurements 24 (1995) 355-358.
- [30] P. Dorenbos, M. Marsman, C. W. E. van Eijk, *Energy resolution, non-proportionality and absolute light yield of scintillation crystals*, Proc. Int. Conf on Inorganic Scintillators, SCINT95, 1996, Delft University Press.
- [31] P. Dorenbos, *Light Output and energy resolution of Ce^{3+} doped scintillators*; Nucl. Instr. and Meth. A 486 (2002) 208-213.

- [32] M. Balcerzyk, M. Moszynski, M. Kapusta, D. Wolski, J. Pawelke, C. L. Melcher, *YSO, LSO, GSO and LGSO: A Study of Energy Resolution and Nonproportionality*, IEEE Trans. Nucl. Sci. 47 (2000) 1319-1323.
- [33] J. D. Valentine, B. D. Rooney, *Design of a Compton spectrometer experiment for studying scintillator non-linearity and intrinsic energy resolution*, Nucl. Instr. and Meth. A 353 (1994) 37-40.
- [34] W. Mengesha, T. D. Taulbee, B. D. Rooney, J. D. Valentine, *Light Yield Nonproportionality of CsI(Tl), CsI(Na), and YAP*, IEEE Trans. Nucl. Sci. 45 (1998) 456-461.

Chapter 4

Experimental Techniques

4.1 Introduction

In this chapter the experimental techniques that were used for studying scintillating materials are discussed. In order to study the properties of the optically active centres, standard luminescence spectroscopic methods were used. These are optical absorption, luminescence excitation and emission spectroscopy. They are focused first. Then the techniques used to study the luminescence under excitation by ionizing radiation are considered. These concern light output measurements and decay time spectra.

Thereafter, low temperature thermoluminescence measurements are introduced, which are useful to study the effects on kinetic and efficiency of light generation

Finally the experimental technique to scan the constructed pixel, which consists of one LuYAP and one LSO crystal, for the final scanner is presented.

4.2 Optical Characterization

Figure 4.1 displays the set-up that was used for excitation and UV induced emission measurements. The light emitted by a xenon lamp passes through a H10D Jobin Yvon monochromator and excites the sample under study that is mounted on the sample holder. The entrance and exit slits were set to 0.25 nm. The emitted light by the sample is monochromatised using the Triax 320 (300 lines/mm, blaze 250 nm) and detected with a 9789 Emi PMT operating at a voltage of 1100 V.

When measuring excitation spectra, the emission wavelength is fixed and the excitation wavelength is scanned.

On the other hand, when measuring emission spectra, the excitation wavelength is fixed and the emission is recorded.

Optical emission spectra were recorded by measuring the fluorescence spectrum at a fixed excitation wavelength with a CCD camera, which was cooled to 270 K using a Peltier element.

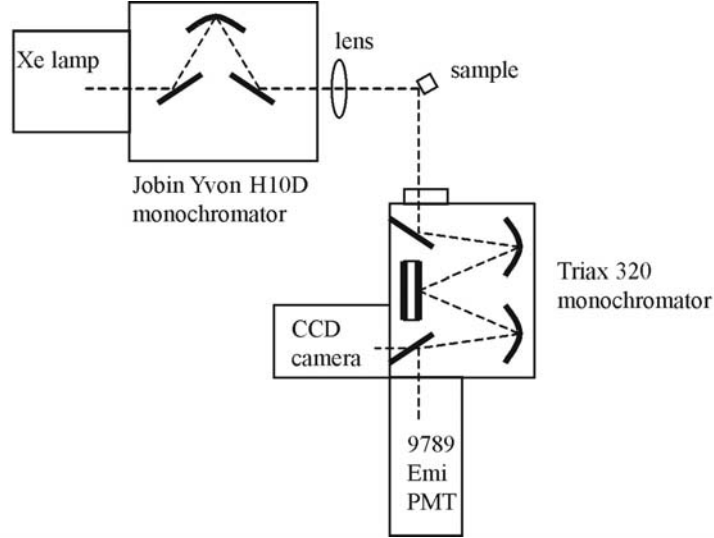


Figure 4.1 Schematic of the experimental set-up for excitation and UV induced emission measurements.

Absorption spectra from the near infrared up to the ultraviolet (UV) domain were measured using a Lambda 900 Perkin Elmer UV/VIS/NIR spectrometer.

When measuring the optical density d , the absorption coefficient $\alpha(\lambda)$ can be calculated using:

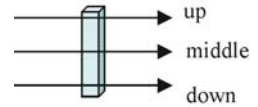
$$d = \log_{10} \frac{I_0}{I}, \quad I = I_0 \cdot e^{-\alpha x} \quad (4.1)$$

thus

$$\alpha = \frac{d \cdot \ln 10}{x} \quad (4.2)$$

where x is the thickness of the samples in cm, I_0 is the initial and I the measured intensity.

Absorption spectra were measured at three points along the crystal axis to study the cerium concentration in the samples and thus also in the ingot.



The cerium concentration was estimated using the empirical formula:

$$Ce \text{ concentration } [\%] = \frac{\alpha(320 \text{ nm})}{108} \quad (4.3)$$

where the absorption coefficient at 320 nm is compared to the absorption coefficient of a sample with well-known cerium concentration.

4.3 Light Output and Energy Resolution

The accurate measurement of the absolute light output of a scintillator is relatively complex and difficult. Photons created by ionizing radiation in the scintillator are affected by many processes that reduce their number before a signal is detected with a photodetector. Parameters like the size of the crystal and its self-absorption, the surface state of the scintillator and the quality of the reflector material, the type of photodetector, the quantum efficiency of the photosensor and the reflectivity/transmission of its entrance window, and finally the photoelectron collection efficiency have to be considered. More information on light collection can be found in Appendix A.

There are different methods for calculating the light output [1] e.g. the pulse method, the single electron method or the comparison method. That is also the reason for the large spread in the published light yield of the most popular crystals, e.g. NaI:Tl, BGO and CsI:Tl.

It is common to express the light output of a scintillator as the number of photoelectrons for a specified type and sensitivity of photodetector [2]. Such measurements of light yield are generally accurate since the used method is simple and reproducible.

While the number of photoelectrons N_{phe} is very important and also sufficient for the user of scintillation counters, it is not enough for scintillator development and research. To get an impression about the properties of a given scintillator (independently from the photomultiplier) and to compare the results with values from other authors the number of photons per MeV (N_{ph}/MeV) is of importance.

The number of photoelectrons can be calculated by comparing the position of the photoelectric peak with the position of the single photoelectron peak assuming a good linearity of the readout chain. It is common to express the number of photoelectrons per MeV of the incident γ -ray.

$$N_{phe} / MeV = \frac{\text{photopeak position}_{ADC}}{\text{single photoe}^{-}_{ADC}} * \text{gain} / E_i \quad (4.4)$$

E_i is the energy of the incident photon, 0.662 MeV or 0.511 MeV, for the reference ^{137}Cs or ^{22}Na source, respectively. The gain represents the amplification of the PMT. If the pedestal is not at zero position of the multichannel analyzer one has to subtract it.

When calculating the light output of the scintillators (N_{ph}/MeV), the integral quantum efficiency is required (see Appendix A.2, equation A.3).

Table 4.1 lists the calculated integral quantum efficiencies of the XP2020Q PMT used for the tested crystals. The values were determined using the measured emission spectra of the crystal combined with the quantum efficiency curves of the PMT given by the manufacturer. The values from the third column were taken from [2] for comparison.

Table 4.1 Integral quantum efficiency for the XP2020Q photomultiplier tube.

Crystal	Integral Quantum Efficiency	QE reference [2]
LSO	0.22	0.21
LYSO	0.22	-
LuAP	0.25	0.25
LuYAP	0.25	-

Thus the light output in number of photons per MeV was calculated using

$$N_{ph} / MeV = \frac{N_{phe} / MeV}{QE}. \quad (4.5)$$

4.3.1 Experimental Procedure

The light output in horizontal geometry was performed with the crystal optically coupled to a XP2020Q photomultiplier by means of silicon oil or grease (Rhodorsil Silicones pâte 4) and covered with several layers of Teflon tape (see Figure 4.2). In vertical geometry the crystals were wrapped with Teflon tape tucked into a Teflon cylinder with an appropriate hole, and coupled with one of the end faces to the PMT. The light output measurement in vertical geometry was performed on both small end faces and the mean value was calculated.

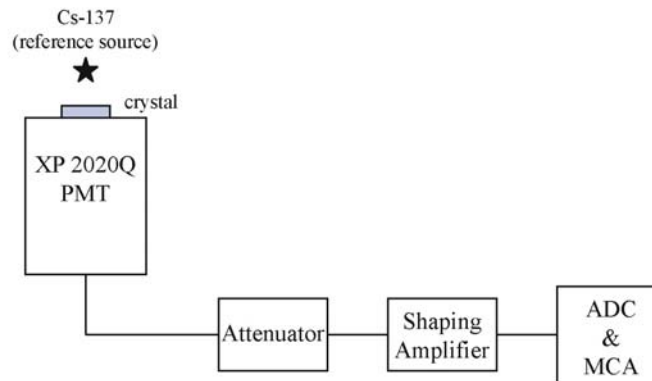


Figure 4.2 Schematic drawing of the set-up used for the light yield measurements in horizontal position of the sample. The reference source used is Cs-137 (662 keV).

A computer program using a simple Gaussian fit applying the Levenberg-Marquardt algorithm for NLSF (non-linear least-squares fitting) determined the FWHM and position of the full-energy peak. High statistics of the measured spectra provided a good accuracy for the fit. All measurements were performed at least three times to increase the accuracy of the measured quantities and the mean value was taken for discussion.

The quoted uncertainty of $\pm 3\%$ in the measurement of the number of photoelectrons includes the statistical uncertainty in determining the centre of the full-energy peak from each scintillator and the reproducibility error. Variations in the PMTs linearity and the amplifier gain calibration are negligible. The uncertainty of about $\pm 5\%$ estimated for the light yield (N_{ph}/MeV) measurements comes from adding the quadratic uncertainty in the photoelectron number and the quantum efficiency uncertainty [2].

Energy spectra were taken for a series of γ -rays emitted by different radioactive sources in the energy range between 31 keV and 1.333 MeV (see Table 4.2). For each γ -peak the number of photoelectrons and the energy resolution were measured.

Table 4.2 The used radioactive sources and γ -rays energies.

Source	Energy of γ -rays [keV]
Ba-133	31
Am-241	60
Ba-133	81
Cd-109	88
Co-57	122
Ba-133	302
Ba-133	356
Na-22	511
Cs-137	662
Mn-54	835
Zn-65	1115
Co-60	1173
Na-22	1275
Co-60	1333

Depending on the type of excitation source used, the photopeak of interest was accompanied by satellite peaks. These peaks are either due to escape of characteristic lutetium K_{α} photons from the crystal or because the source emits more than one type of γ -rays. The processes contributing to the shape of the pulse height spectrum are listed in Table 4.3 ($\alpha = E / m_0 c^2$, $m_0 c^2 = 0.511$ MeV).

Table 4.3 Photon escape and origin of peaks in scintillation pulse amplitude spectrum.

Energy of escaping radiation	Origin	Energy of peak in spectrum	Usual name	E for ^{137}Cs source [keV]
None	Photoelectric (plus x-rays) and multiple absorption processes	E	Photopeak	662
$m_0 c^2$	Pair production and escape of one annihilation photon	$E - m_0 c^2$	1 st pair escape peak	
$2 m_0 c^2$	Pair production and escape of both annihilation photons	$E - 2 m_0 c^2$	2 nd pair escape peak	
$E'' = \frac{E}{1 + 2\alpha}$	Compton 180° scattering	$T_{em} = \frac{E}{1 + (1/2\alpha)}$	Compton edge	477.6
E'' to E	Single Compton scattering	T_{em} to 0	Single Compton distribution	
0 to E	Multiple Compton scattering, etc.	E to 0	Multiple Compton distribution	
$E_K = 63 \text{ keV}$	Escape of lutetium K_α x-rays	$E - E_K$	Lutetium escape peak	599
E escapes, but E'' enters externally	External Compton 180° scattering	$E'' = \frac{E}{1 + 2\alpha}$	Backscatter peak	181.3

4.4 Scintillation Decay Time

The pulse shape studies were performed at CERN as well as at the Soltan Institute for Nuclear Studies in Swierk (Poland). The set-ups in the two laboratories differ from each other.

In Swierk the sample under study was optically coupled to the XP2020Q photomultiplier (Start) and excited by γ -rays of a Cs-137 source. The experimental set-up is shown in Figure 4.3. Once a γ -ray is absorbed in the sample, the generated scintillation pulse is detected by the start PMT and, if the scintillation intensity is sufficiently high, a ‘start’ NIM pulse is generated by a ORTEC 935 constant fraction discriminator (CFD). A few scintillation photons per scintillation event may pass through the slit and be detected by the stop tube. The PMT signal due to these detected photons is transformed into NIM pulses using a ORTEC 935 CFD. The time difference between the start pulse and the stop pulse are recorded using a Time to Amplitude Converter (TAC) and fed into the analyzer.

At CERN the arrangement is slightly different. A fast plastic scintillator is mounted on the start PMT. The sample under study is mounted between the start telescope tube and

the stop PMT. Between these scintillators a ^{22}Na source is placed. This source generates a positron, which annihilates with an electron emitting two collinear 511 keV photons.

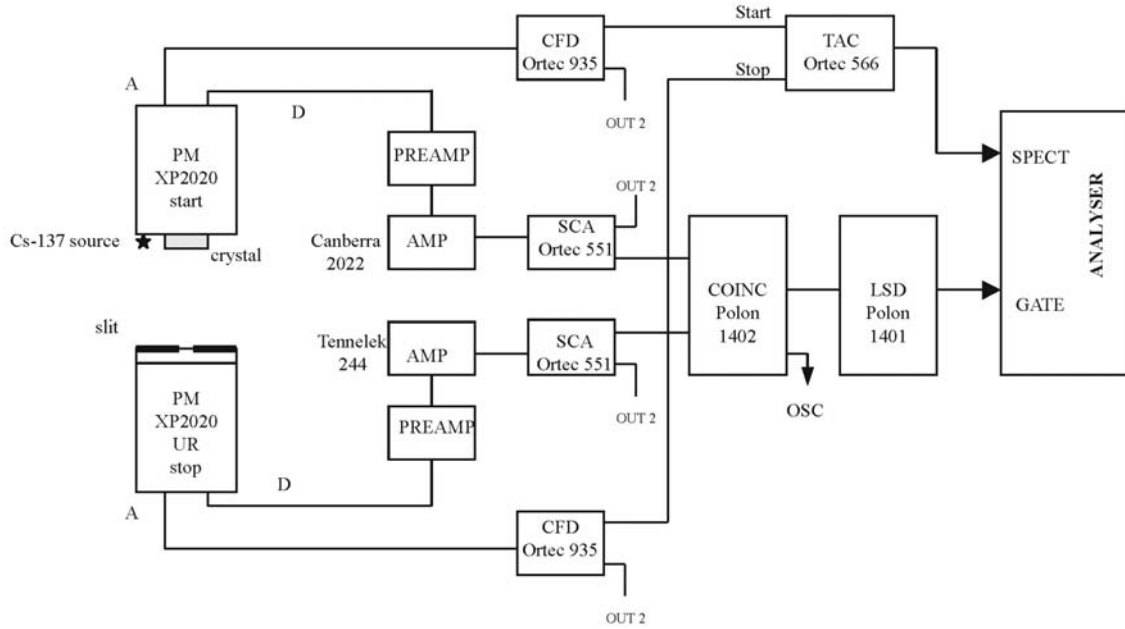


Figure 4.3 Schematic of the set-up used to record scintillation decay time spectra used at Swierk.

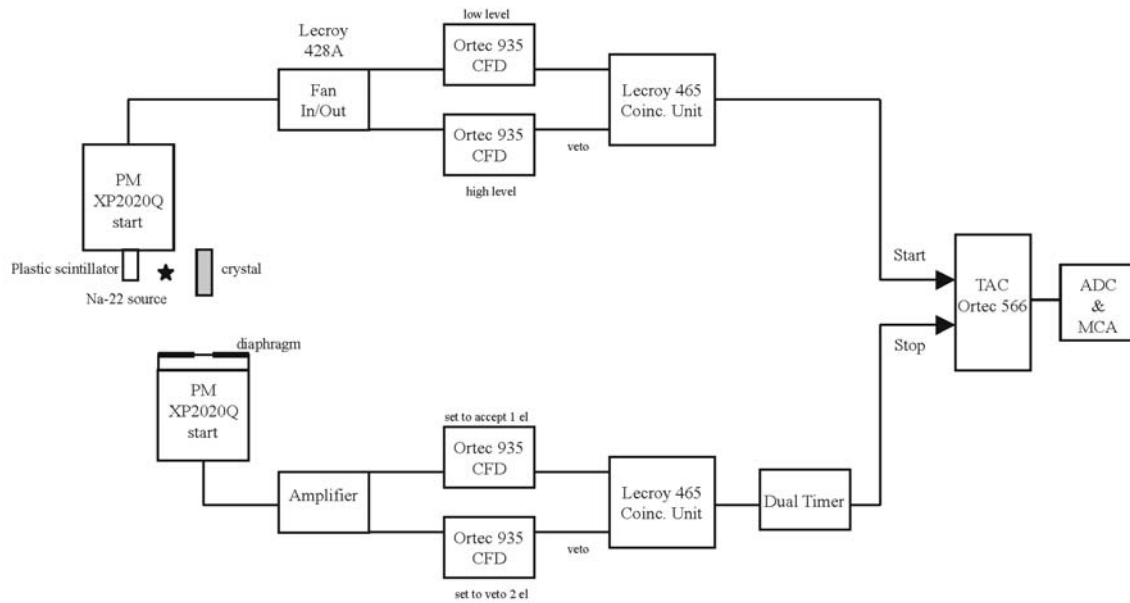


Figure 4.4 Schematic of the set-up used to record scintillation decay time spectra used at CERN.

One of the 511 keV photons is detected by the plastic scintillator. The other 511 keV photon excites the crystal and some scintillation photons may pass through the

diaphragm and are detected in the stop PMT. The electronic arrangement is illustrated in Figure 4.4.

The two methods are based on the single photon counting method introduced by Bollinger *et al.* [3].

4.5 Low Temperature Thermoluminescence

Thermoluminescence (TL) measurements at elevated temperature [4] (above room temperature) have proved to be a useful tool to study the kinetics and efficiency of light generation in wide bandgap scintillator materials. One particularly important issue has been the role of lattice defects and carrier traps in the mechanism by which energy reaches the emitting center. Early thermoluminescence studies of LuAP at 300-700 K [5, 6] provided evidence that recombination of charge carriers via Ce^{3+} is the dominant mechanism by which scintillation light is produced in this material and established parameters of a number of deep traps responsible for TL glow peaks between 300 and 700 K.

Bartram *et al.* [7] measured the scintillation light loss due to those deep traps by directly comparing the thermoluminescence released during the heating of the sample between 34 and 290 °C and integrated radioluminescence output during the preceding steady state γ -irradiation in the same cycle. Unfortunately the measured ratio is severely underestimated since relatively fast components due to shallow traps and responsible for decrease in the time-gated scintillation light yield cannot be properly included in such an experiment.

It has first been shown by Wojtowicz *et al.* [8] that thermoluminescence measurements at low temperatures reveal traps that truly correlate with the light output at room temperature. The existence of these shallow charge traps can negatively affect light output and time properties of scintillation emission [9]. Low temperature thermoluminescence (ltTL) curves were associated with shallow traps in the course of research on scintillation properties of Ce^{3+} - activated materials.

If an inorganic crystal is exposed to ionizing radiation while cold and is then warmed, light is emitted while warming. Such emission of light is called thermoluminescence. The thermoluminescence measurement consists in measuring the light emission when a scintillator is heated at a uniform rate. The curve obtained of light emission against temperature is referred to as the glow curve. It has been generally assumed that TL is due to release of electrons from traps increasing with temperature and the shallower

traps being emptied at lower temperatures. It has been found that a study of the TL curve provides a means of showing how the traps are distributed in depth. Thermoluminescence measurements are a powerful tool to study the distribution of traps with radiative transitions. Not all scintillators reveal TL properties.

4.5.1 Theory of the Glow Curve

The following method to describe the form of the glow curves was developed by Randall and Wilkins [10].

If the energy level of a trapped electron is E eV below the conduction band, the electron has to absorb at least this energy before it can be released from the trap through the conduction band which is the most frequent way. The electrons in the traps are distributed in thermal energies following a Maxwell-Boltzmann distribution. The probability p of an electron escaping from a trap of depth E at temperature T is of the form

$$p = s e^{-E/kT} \quad (4.6)$$

where k is the Boltzmann constant and s is a constant which may vary slowly with temperature.

If the trap is regarded as a potential box, s will express the frequency with which the electron strikes the sides of the box. Therefore we suppose s to be in the order of the vibration frequency of the crystal $\sim 10^{12} \text{ s}^{-1}$.

In order to find the relation between the thermoluminescence temperature and the trap depth, the form of the glow curve when E is single valued and when the temperature rises at a constant rate will be calculated.

If n is the number of electrons in the trap at time t , one can derive from equation (4.6),

$$dn/dt = -n s e^{-E/kT} \quad (4.7)$$

This assumes that there is no retrapping which means that, if an electron is liberated from a trap it always goes straight to a luminescence centre and is not captured on the way. It has been shown that this assumption is largely justified, if the trap density is not too high. The intensity of thermoluminescence I is proportional to the rate of supply of electrons to the luminescence centres,

$$I = C dn/dt = -C n s e^{-E/kT} \quad (4.8)$$

From equation (4.7) follows

$$dn/n = -s e^{-E/kT} dt \quad (4.9)$$

When assuming that $dT = \beta dt$, where β is the heating rate, and integrating, one gets

$$\log n/n_0 = - \int_0^T 1/\beta * s e^{-E/kT'} dT' \quad (4.10)$$

and

$$n = n_0 \exp\left(-\int_0^T 1/\beta * s e^{-E/kT'} dT'\right) \quad (4.11)$$

finally

$$I = Cdn/dt = n_0 C \exp\left(-\int_0^T 1/\beta * s e^{-E/kT'} dT'\right) s \exp(-E/kT) . \quad (4.12)$$

This expression represents the thermoluminescence curve for a scintillator containing traps of one depth.

Since under first-order kinetics (note the asymmetric shapes of glow peaks for LuAP) different traps responsible for different overlapping glow peaks do not interfere, a complex glow curve can be represented as a sum of single-peak terms given by equation (4.12):

$$I(T) = \sum_{i=1}^N n_{0i} s_i \exp\left(-\frac{E_i}{kT}\right) \exp\left[\left(-\frac{s_i}{\beta}\right) \int_{T_0}^T \exp\left(-\frac{E_i}{kT'}\right) dT'\right]. \quad (4.13)$$

Where N is the number of independent traps, T is the true sample temperature (corrected for thermal lag, which is the difference between the true sample temperature and that of the heating element), β is the heating rate, n_{0i} , s_i and E_i are initial concentrations of occupied traps, frequency factors and activation energies (trap depths), respectively.

The rate of carrier's escape from the trap (γ), equal to the reciprocal of carrier's lifetime in the trap (τ_t), can be described by the following equation

$$\gamma = \tau_t^{-1} = s * \exp\left(-\frac{E}{kT}\right). \quad (4.14)$$

Usually the lifetime of the carriers in the traps are calculated for room temperature (297 K) to get a feeling about how the traps modify the scintillation properties, e.g. decay time and light output, of the crystal.

4.5.2 Experimental Set-up

The low temperature thermoluminescence (ltTL) glow curves were measured using a closed-cycle He cooler with a programmable temperature controller. An x-ray tube (DRON), operated at 38 kV and 18 mA, was employed as the primary radiation source. For the scintillation light output of the crystals, the tube was turned on 5 min before starting the irradiation to assure voltage stabilization, with a 1.8 cm thick Cu-Ni-Zn block acting as a shield. The single crystal sample rested with one of its large faces in

thermal contact to a copper plate, in vertical position on a copper pedestal. The light passed through an ARC monochromator (Spectra Pro-500i) and the data was acquired by means of ARC software (spectra card SC-1). The emitted light was measured with a Hamamatsu R928 PMT operating at 700 – 900 V.

Irradiating the samples at 9 K temperature preceded the measurements of ltTL. The set-up is shown in Figure 4.5. For the ltTL experiment, the total emission of a sample was recorded with the detection monochromator set to the UV grating with zeroth order and 1 mm slit. The ltTL were performed in the range of 10 to 300 K at a linear heating rate of 0.151 K/s.

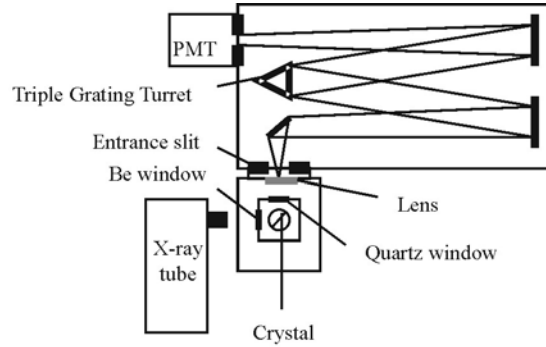


Figure 4.5 Experimental set-up for the low temperature thermoluminescence measurement (top view).

4.6 Tagging Measurements in the Phoswich Assembly

To investigate the influence on energy resolution of the LSO crystal, when the light passes through the LuYAP crystal, a test phoswich assembly was constructed.

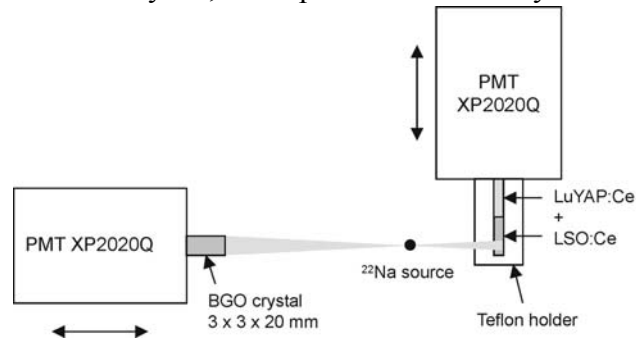


Figure 4.6 Experimental set-up to scan the phoswich crystal assembly. The Na-22 source, the 3x3x20 mm BGO crystal, and the detected signal from the BGO PMT provide an electronically collimated beam (< 2 mm) whose position is adjusted by moving the entire phoswich assembly.

One LSO:Ce crystal and one LuYAP:Ce crystal, each $2 \times 2 \times 10 \text{ mm}^3$, were combined without optical contact in a Teflon holder and the assembly was coupled on the LuYAP

side to the XP2020Q PMT by means of optical grease. This test module was scanned along the crystal axis in millimeter steps using a micrometer. The γ -rays from a small ^{22}Na (511 keV) source ($1 \times 1 \times 10 \text{ mm}^3$) detected in the crystal assembly were set in coincidence with the 2nd γ -rays at 180° detected in a $3 \times 3 \times 20 \text{ mm}^3$ BGO crystal. The set-up is shown in Figure 4.6. By increasing the distance from the reference PMT (BGO) to the source, a small solid angle and thus a small γ -beam with diameter $< 2 \text{ mm}$ was achieved. Whenever a coincidence between the phoswich assembly and the tagging BGO crystal occurred, the signal in the test module was read into the computer.

4.7 References

- [1] E. Sysoeva, V. Tarasov, O. Zelenskaya, *Comparison of the methods for determination of scintillation light yield*, Nucl. Instr. and Meth. A 486 (2002) 67-73.
- [2] M. Moszynski, M. Kapusta, M. Mayhugh, D. Wolski, S. O. Flyckt, *Absolute Light Output of Scintillators*, IEEE Trans. Nucl. Sci. 44 (1997) 1052-1061.
- [3] L. M. Bollinger, G. E. Thomas, *Measurement of the Time Dependence of Scintillation Intensity by a Delayed-Coincidence Method*, The Review of Scientific Instruments 32 (9) (1961) 1044-1050.
- [4] S. W. S. McKeever, *Thermoluminescence of Solids*, Cambridge University Press (1985).
- [5] W. Drozdowski, D. Wisniewski, A. J. Wojtowicz, A. Lempicki, P. Dorenbos, J. T. M. de Haas, C. W. E. van Eijk, A. J. J. Bos, *Thermoluminescence of $\text{LuAlO}_3\text{:Ce}$* , J. Lumin. 72-74 (1997) 756-758.
- [6] W. Drozdowski, D. Wisniewski, A. J. Wojtowicz, A. Lempicki, P. Dorenbos, J. T. M. de Haas, C. W. E. van Eijk, A. J. J. Bos, *Acta Phys. Pol. A* 90 (1996) 377.
- [7] R. H. Bartram, D. S. Hamilton, L. A. Kappers, A. Lempicki, *Electron traps and transfer efficiency of cerium-doped aluminate scintillators*, J. Lumin. 75 (1997) 183-192.
- [8] A. J. Wojtowicz, W. Drozdowski, D. Wisniewski, K. Wisniewski, K. R. Przegietka, H. L. Oczkowski, T. M. Pisters, *Thermoluminescence and scintillation of $\text{LuAlO}_3\text{:Ce}$* , Rad. Meas. 29 (1998) 323-326.
- [9] A. J. Wojtowicz, J. Glodo, W. Drozdowski, K. R. Przegietka, *Electron traps and scintillation mechanism in $\text{YAlO}_3\text{:Ce}$ and $\text{LuAlO}_3\text{:Ce}$ scintillators*, J. Lumin. 79 (1998) 275-291.
- [10] J. T. Randall, M. H. F. Wilkins, *Phosphorescence and electron traps I. The study of trap distribution*, Proc. Roy. Soc. London A 184 (1945) 366-389.

Chapter 5

Luminescence and Scintillation Properties of $\text{Lu}_{1-x}\text{Y}_x\text{AP}:\text{Ce}$ Crystals

5.1 Luminescence Properties of Cerium-Activated Compounds

In this chapter the optical and scintillation properties of the crystals are investigated. The photo luminescence properties of Ce^{3+} are well understood for most compounds. In contrast, the scintillation processes in Ce-activated materials are less known and identified. The problem of variation of the scintillation yield of the Ce^{3+} emission in different materials has been the subject of various physical studies. For the orthoaluminates it has been argued that the scintillation characteristics are based on the recombination mechanism of the Ce^{3+} center's excitation.

The free Ce^{3+} ion has a single electron in ground $4f(^2F_J)$ state, and the excited states are $5d(^2D_J)$ and $6s(^2S_{1/2})$. The spin-orbit interaction splits the 2F_J ground and 2D_J excited states into two pairs of levels, $^2F_{7/2}$ and $^2F_{5/2}$ and $^2D_{5/2}$ and $^2D_{3/2}$ separated by 2250 cm^{-1} and 2500 cm^{-1} , respectively [1]. Electric-dipole $4f$ - $5d$ transitions are parity allowed and have a large oscillator strength. In a crystal with a low local symmetry of Ce^{3+} site, such as $\text{LuAlO}_3:\text{Ce}$, the excited $5d$ level splits into five Stark components, and five $4f$ - $5d$ absorption bands are detected.

The emission of Ce^{3+} ions usually occurs from the lowest $5d$ level to the $^2F_{7/2}$ and $^2F_{5/2}$ levels of the $4f$ ground state. Depending upon the host crystal and the temperature, transitions to the $^2F_{7/2}$ and $^2F_{5/2}$ levels may be resolved. The splitting of the 2F_J states of the Ce^{3+} ion in various crystals is typically about a few hundred cm^{-1} , because the $4f$ electron shell is shielded by the outer closed $5s$ and $5d$ electron shells. The reduction of

the energy of the excited states from the free ion values depends on ligands and the degree of covalency of the cerium-anion bond.

5.1.1 Excitation Spectra

The excitation spectrum measured for the $\text{Lu}_{0.7}\text{Y}_{0.3}\text{AP}$ sample at the emission wavelength of 370 nm exhibits three main bands in the region between 200 to 350 nm peaking at 234, 289, and 312 nm, respectively. Moreover, two minor bands at 217 and 269 nm can be observed, when fitting the spectra with a sum of five Gauss functions. The measured and fitted curve can be seen in Figure 5.1.

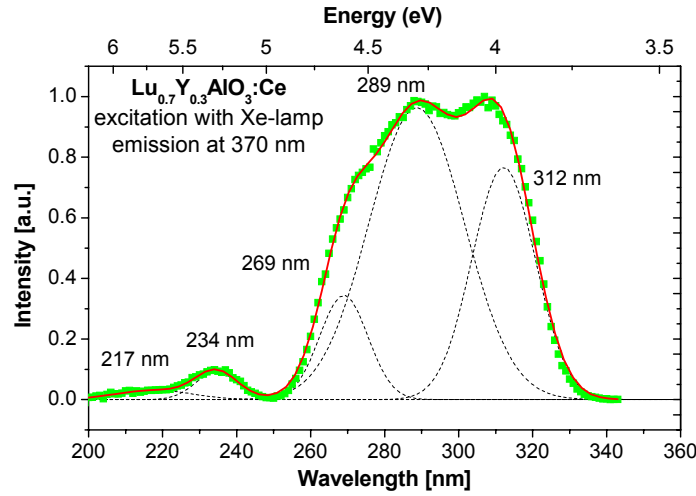


Figure 5.1 UV induced excitation spectrum of $\text{Lu}_{0.7}\text{Y}_{0.3}\text{AP}$ at room temperature. The emitted light was recorded at a wavelength of 370 nm.

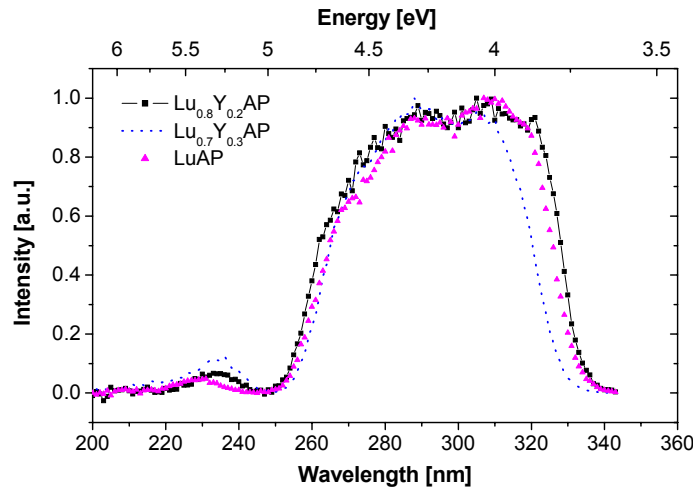


Figure 5.2 UV induced excitation spectra of $\text{Lu}_{0.8}\text{Y}_{0.2}\text{AP}$, $\text{Lu}_{0.7}\text{Y}_{0.3}\text{AP}$, and LuAP taken at room temperature. The emitted light was recorded at a wavelength of 370 nm.

The position of the bands is comparable to results from Lempicki *et al.* [2], who found excitation bands at around 215 nm, 230 nm, 275 nm, 290 nm, and 310 nm for a LuAP:Ce crystal.

Samples from the same batch exhibited about the same shape in the excitation spectra. The spectra obtained for the $\text{Lu}_{0.7}\text{Y}_{0.3}\text{AP}$ crystals show smaller excitation bands compared to the spectra measured for the $\text{Lu}_{0.8}\text{Y}_{0.2}\text{AP}$ and the LuAP crystal. This effect was also observed in the absorption spectra for the respective crystals.

A comparison in excitation spectra for the studied crystal is shown in Figure 5.2.

5.1.2 Absorption Spectra

As mentioned before, absorption spectra were measured at three points along the crystal axis to study the homogeneity of the samples and thus also of the ingot. The results of this study showed that the crystals grown with the Bridgman and Czochralski method behave differently. In Figure 5.3 a comparison of the absorption spectra measured for the LuAP, $\text{Lu}_{0.8}\text{Y}_{0.2}\text{AP}$, and $\text{Lu}_{0.7}\text{Y}_{0.3}\text{AP}$ (batch 1 and batch 2) is shown.

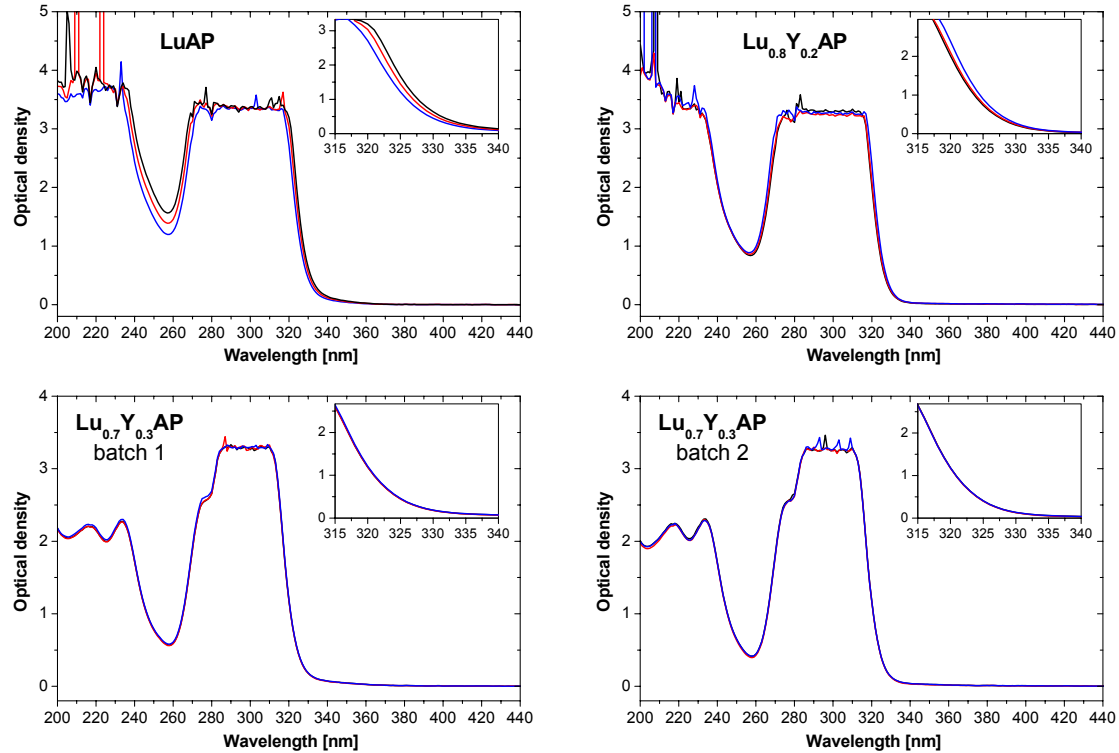


Figure 5.3 Absorption spectra measured at three different points (up, middle, down) within the crystals. The curves are shown for the LuAP, the $\text{Lu}_{0.8}\text{Y}_{0.2}\text{AP}$, and two $\text{Lu}_{0.7}\text{Y}_{0.3}\text{AP}$ samples from batch 1 and batch 2. The inset shows the enlarged region from 315 to 340 nm.

The spectra contain a sequence of five absorption bands in the ultraviolet region, which are not resolved at room temperature. These bands are assigned to Ce^{3+} 4f - 5d bands. At room temperature mainly two to four peaks appear in the absorption spectrum depending on the sample. On the low-energy side an absorption tail can be seen in the spectra, which does not originate from Ce^{3+} 4f - 5d transitions. This has already been observed for YAlO_3 and LuAlO_3 crystals and is in agreement with the results from Dujardin *et al.* [3]. The origin of this additional broad band was assigned to Ce^{4+} ions by Gumanskaya *et al.* [4] but Lempicki [2] and Dujardin [3] assumed that this absorption tail originates from other centers than Ce^{4+} ions, which remain unclear.

The crystals grown with the Bridgman method exhibit diverse shapes of the absorption spectrum measured at three different points within the sample. For the LuAP crystal this difference was more pronounced than for the $\text{Lu}_{0.8}\text{Y}_{0.2}\text{AP}$ samples. The absorption spectra measured for crystals from the same batch varied to a great extent. This indicates that there are inhomogeneities in the crystals and thus in the boule.

For the Czochralski grown samples (batch 1 to batch 3 from the BTCP) no difference in the shape of the absorption spectrum measured at different points within one crystal was found. The variation in the absorption spectra between crystals of the same batch was exiguous, indicating that the gradient of the cerium concentration in the ingot is very small.

An explicit correlation between the absorption coefficient at 335 nm and the vertical light yield was found for the $\text{Lu}_{0.7}\text{Y}_{0.3}\text{AP}:\text{Ce}$ samples from the three studied batches as shown in Figure 5.4. This clearly points out how the self-absorption influences the light output in the fingerlike crystals.

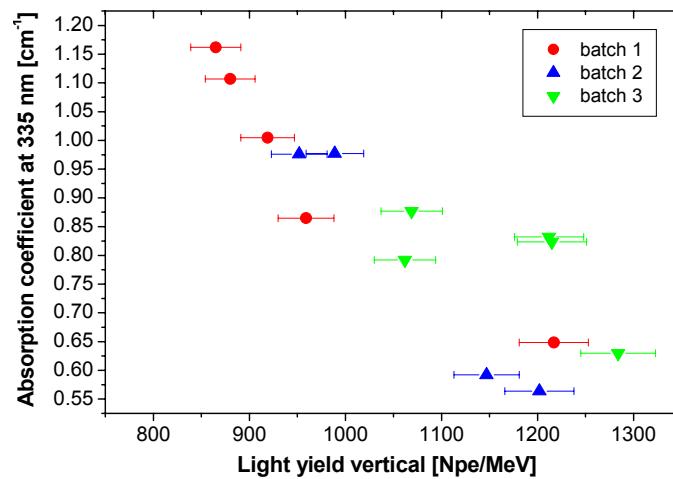


Figure 5.4 Correlation between the absorption coefficient at 335 nm and the light output measured in vertical position.

A slight decrease in the absorption tail from the first to the third batch was detected, which led to the higher light yield measured in vertical position. This decrease reflects the improved crystal growth conditions.

The cerium concentration was derived by comparing the absorption coefficient at 320 nm to the respective coefficient of a sample with well-known cerium content. In the range of the light yield dispersion, no definite correlation between the absorption coefficient at 320 nm and thus the cerium concentration, and the light output was found, as shown in Figure 5.5. Especially for the $\text{Lu}_{0.7}\text{Y}_{0.3}\text{AP}$ samples, the spread in light yield is quite broad compared to the cerium dispersion. This is in agreement with observations of Dujardin *et al.* [3] who reported that the cerium concentration has no dramatic effect on the light yield of the studied samples to a certain extent.

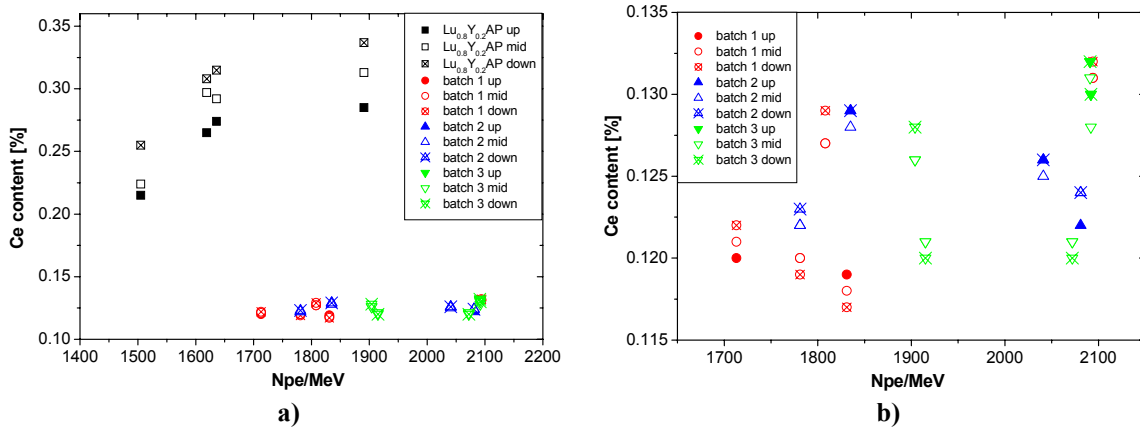
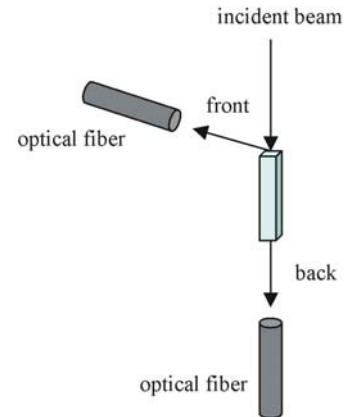


Figure 5.5 Light yield (Npe/MeV) versus derived cerium concentration a) for all the tested samples ($\text{Lu}_{0.8}\text{Y}_{0.2}\text{AP}$ and $\text{Lu}_{0.7}\text{Y}_{0.3}\text{AP}$) and b) enlarged only for the three batches of $\text{Lu}_{0.7}\text{Y}_{0.3}\text{AP}$ crystals.

5.1.3 UV excited Emission Spectra

The UV induced emission spectra of $\text{Lu}_{1-x}\text{Y}_x\text{AP}:\text{Ce}$ crystals were observed to be dependent on the point of measurement as already shown by [5]. The crystals were excited on one small side ($2 \times 2 \text{ mm}^2$) and the emitted photons were recorded on the opposite side (10 mm crystal length) as shown in the scheme on the right side.

Two figures of the recorded emission curves on either side of the crystal (front and back) together with the absorption spectrum from a LuAP crystal and a $\text{Lu}_{0.7}\text{Y}_{0.3}\text{AP}$ sample are presented in Figure 5.6 a) and b).



This measurement reflects the absorption study. It can be seen as a kind of indirect absorption measurement.

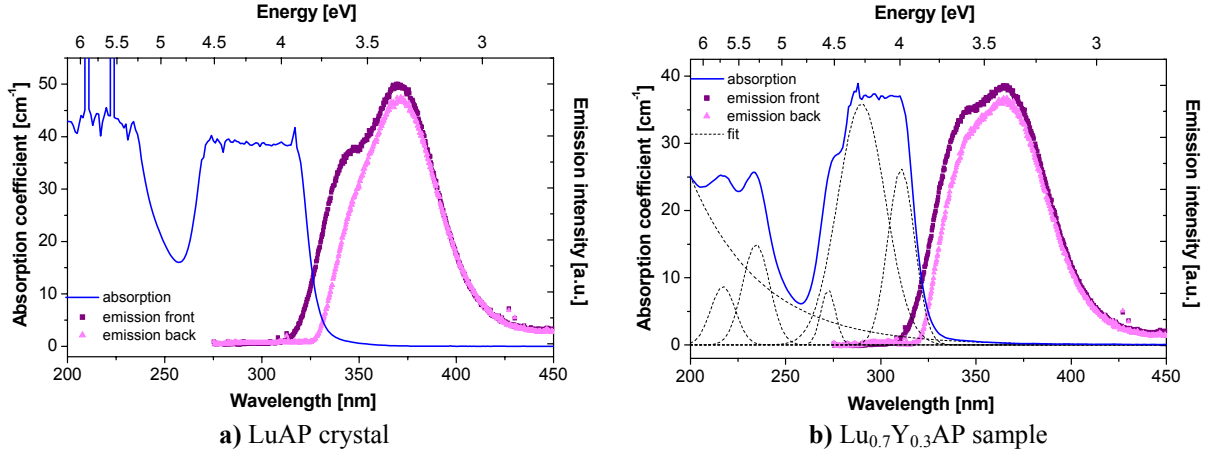


Figure 5.6 Absorption and UV excited emission spectra. The absorption spectrum from LuYAP was fitted with a sum of an exponential function and 5 Gauss functions (dotted curves). The emission spectrum was measured at the side of excitation (dark curves) and on the opposite side (light curves).

It can be seen in the figures that the overlap between the emission spectrum measured on the front side (violet curves) and the absorption spectrum is larger for the LuAP crystal than the LuYAP. This stronger overlap affects the emission bands measured at the rear side of the crystal (pink curves), which are close to the absorption edge

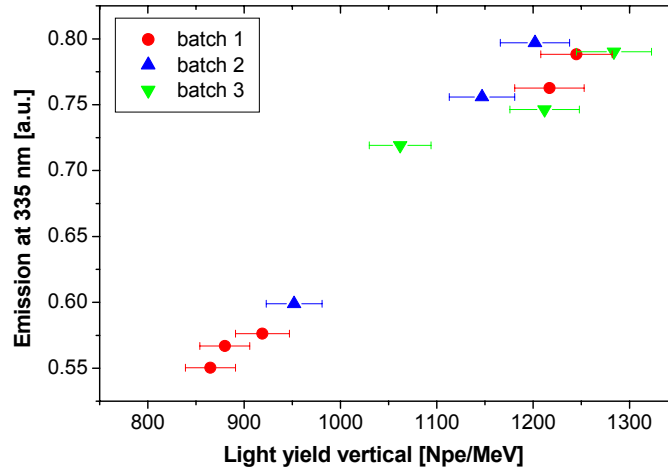


Figure 5.7 Correlation between the emission measured at the rear side of the crystal and the light output measured in vertical position.

A clear correlation between the light yield measured in vertical position and the emission intensity at 335 nm, measured at the back side of the crystal, was found as plotted in Figure 5.7. The spectral overlap between the Ce^{3+} emission and the absorption tail extending up to 350 nm was shown to be responsible for this dependence. A slight trend towards the improvement of this self-absorption can be observed from the first to the third batch of $\text{Lu}_{0.7}\text{Y}_{0.3}\text{AP}$ crystals. As mentioned before, this is related to the improved crystal growth procedure and thus to the reduced absorption tail.

5.1.4 X-ray excited Emission Spectra

The x-ray excited emission spectra for the LuAlO_3 , the $\text{Lu}_{0.8}\text{Y}_{0.2}\text{AP}$ crystal and the LSO crystal are shown in Figure 5.8.

The radioluminescence spectra from $\text{Lu}_{0.8}\text{Y}_{0.2}\text{AP}$ and LuAP are equal due to the same dopant and the similar crystal structure. The broad emission bands peaking at 360 nm at room temperature are related to Ce^{3+} ions. The ground state splitting of Ce^{3+} ions in LuAlO_3 can be seen from the Ce^{3+} emission spectrum at $T = 20$ K (Figure 5.8 right side). The splitting corresponds to transitions from the lowest 5d excited level to the two 4f ground levels, $^2\text{F}_{5/2}$ and $^2\text{F}_{7/2}$.

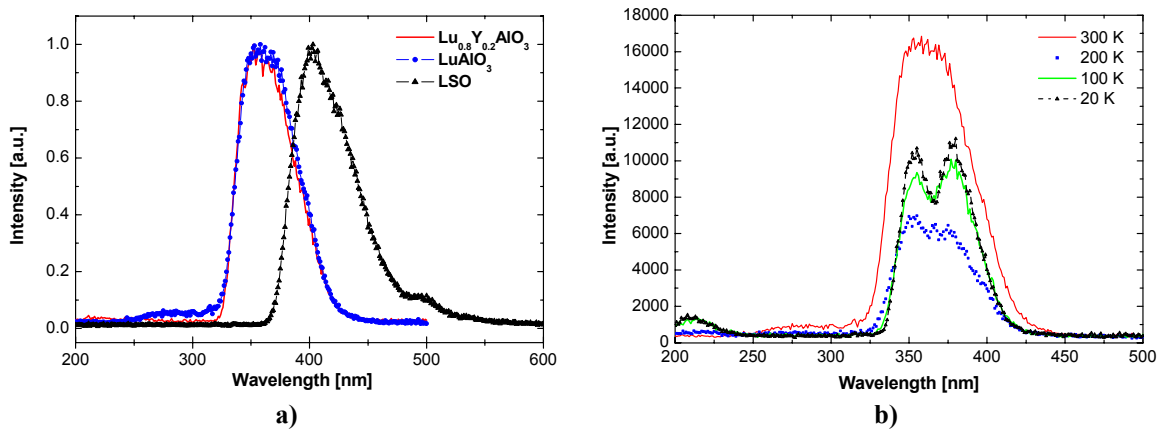


Figure 5.8 a) X-ray excited emission spectra of LuYAP , LSO , and LuAP at room temperature. In b) the x-ray excited emission spectra from the LuYAP crystal at selected lower temperatures are shown. The ground state splitting of Ce^{3+} ions can be seen.

5.2 Light Output and Energy Resolution

5.2.1 Experimental Procedure

The studies reported here were carried out on several batches of $\text{Lu}_{1-x}\text{Y}_x\text{AP}:\text{Ce}$ crystals with different composition. They were grown with different growing methods from various producers. Table 5.1 summarizes the growing method, producer, surface finish and delivery time of all studied crystals. All crystals had a size of $2 \times 2 \times 10 \text{ mm}^3$.

Table 5.1 Summary of the crystals studied for this work

Crystal	Quantity	CCC Number	Growing method	Producer	Ce conc	surface	Delivery time
LuAP	1	1013	Bridgman	Petrosyan	0.5%	Polished	July 2000
$\text{Lu}_{0.8}\text{Y}_{0.2}\text{AP}$	16	1029 – 1044	Bridgman	Petrosyan	0.4%	Polished	Aug 2000
$\text{Lu}_{0.8}\text{Y}_{0.2}\text{AP}$	4	1068 – 1071	Bridgman	Petrosyan	0.55%	1 polished 3 unpolished	Aug 2000
$\text{Lu}_{0.8}\text{Y}_{0.2}\text{AP}$	10	1073 – 1082	Bridgman	Petrosyan	0.25%	Polished	Nov 2001
$\text{Lu}_{0.7}\text{Y}_{0.3}\text{AP}$	14	1085 – 1098	Czochralski	BTCP	0.25%	Polished	Jan 2002
$\text{Lu}_{0.7}\text{Y}_{0.3}\text{AP}$	15	1100 – 1114	Czochralski	BTCP	0.25%	Polished	March 2002
$\text{Lu}_{0.7}\text{Y}_{0.3}\text{AP}$	16	1134 – 1149	Czochralski	BTCP	0.25%	Polished	May 2002

5.2.2 Results for the LuAP and $\text{Lu}_{0.8}\text{Y}_{0.2}\text{AP}$ Samples

The light yield and energy resolution of the **first batch** of $\text{Lu}_{0.8}\text{Y}_{0.2}\text{AP}$ crystals delivered in August 2000 and the pure LuAP crystal obtained from A. Petrosyan were studied at CERN as well as at the Soltan Institute for Nuclear Studies in Swierk (Poland). The energy spectra measured with a ^{137}Cs source in Swierk are shown in Figure 5.9. The light yield was measured with the crystal coupled in horizontal and in vertical position to the PMT. The single photoelectron spectrum is shown for comparison.

The light output for the 17 tested crystals from the first batch varied from 1510 to 2370 photoelectrons per MeV (phe/MeV) for the mixed samples and we obtained a value of 1710 phe/MeV for the pure LuAP crystal.

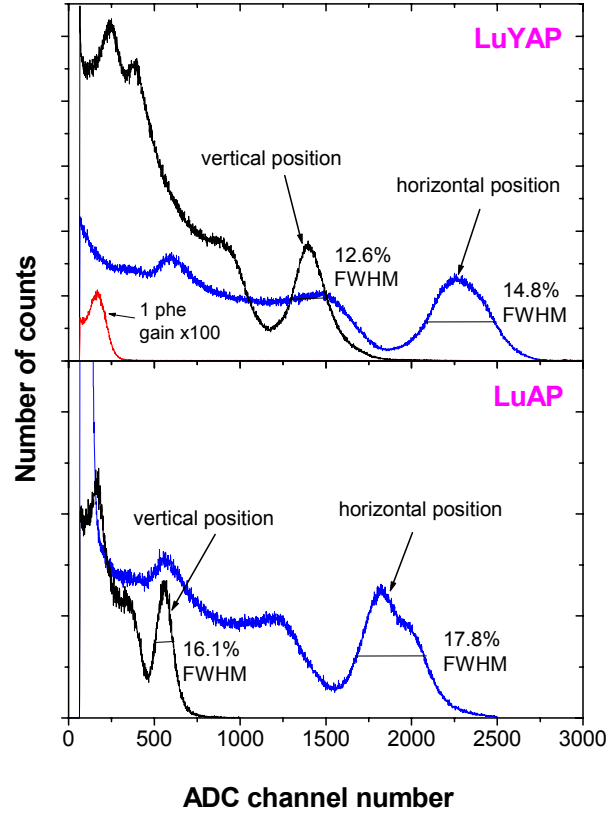


Figure 5.9 Energy spectra obtained in Swierk with a Cs-137 source for a selected LuYAP and LuAP crystal. Both crystals were measured in horizontal and in vertical position. The position of the single electron peak is shown for comparison.

Note that the light output from the LuAP sample is comparable to that of the mixed crystal in horizontal position whereas in vertical position the photoelectron yield is much lower. The ratio between vertical and horizontal position is about 30% for the LuAP crystal and around 55% for the $\text{Lu}_{0.8}\text{Y}_{0.2}\text{AP}$ crystals, which means that the self-absorption from the mixed crystals is much weaker. Dujardin *et al.* report in Ref. [3] light yield values for LuAP:Ce (0.9 at.%) in percentage of BGO of about 70% and 40% for 2 mm and 11 mm, respectively. This corresponds to a ratio of around 57%.

The energy resolution varied from 10 to 21% for different crystals. No relation was found between the measured light output and energy resolution for the tested samples as expected from equation 3.16. This is related to double or triple photoelectric peaks in the energy spectrum leading to a poor energy resolution and reflecting inhomogeneities in the crystal. The presence of a gradient of the cerium concentration in the sample was confirmed by the absorption measurements, see Figure 5.3.

The depolished crystals (number 18 to 20) with higher cerium concentration (0.55%) show lower light yield in horizontal position but the measured number is still within the uncertainties.

Note the intense full-energy peak in the spectra. The peak to total ratio of the mixed crystals was found to be 20.5% compared to the pure crystal 24%. This high photoelectric fraction confirms the high detection efficiency even from a small sample with a volume of 0.04 cm^3 .

The **second batch** of $\text{Lu}_{0.8}\text{Y}_{0.2}\text{AP}$ crystals were grown by the Bridgman method in the Institute of Physical Research (Armenia). They were placed to our disposal for light yield measurements by C. Dujardin (INPL Lyon) in November 2001.

For these ten crystals the double photoelectric peaks in the energy spectra in horizontal geometry were even more pronounced than for the first batch of crystals. An example for this double photoelectric peak is shown in Figure 5.10.

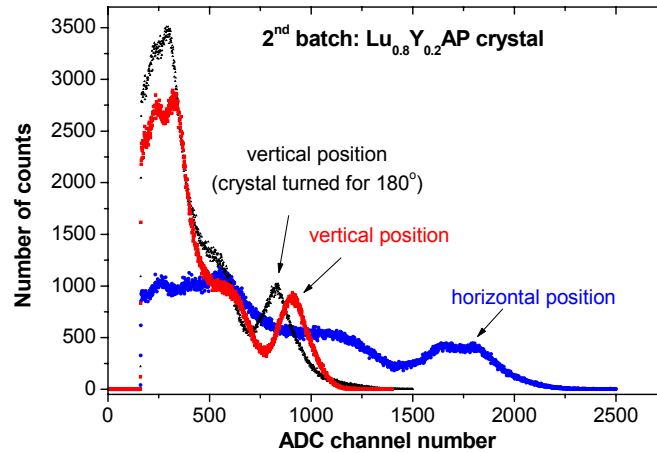


Figure 5.10 Energy spectra measured with a Cs-137 source at CERN for a selected 2nd batch LuYAP crystal. The spectra were taken in both vertical (up and down) and horizontal positions.

This behavior of the crystal together with the difference of the photopeak position for the two vertical measurements directly lead to the assumption, that there are inhomogeneities in the crystal. The presence of imperfections in the crystal was confirmed by analyzing the crystal with a red laser beam (helium-neon). The beam was clearly visible at certain parts in the crystal.

The histogram in Figure 5.11 presents the light output (photons per MeV) of the tested $\text{Lu}_{0.8}\text{Y}_{0.2}\text{AP}$ crystals from batch 1 and batch 2.

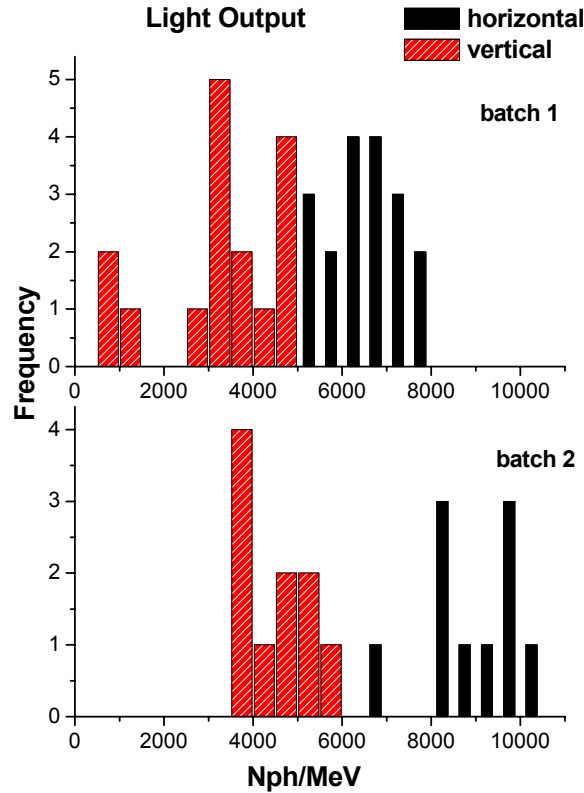


Figure 5.11 Light yield histogram given in the number of photons/MeV of the two batches of $\text{Lu}_{0.8}\text{Y}_{0.2}\text{AP}$ crystals. The light output was measured in vertical (red bars) and in horizontal position (black bars) using a Cs-137 source.

The second batch of crystals exhibited a higher light yield than the first batch. The measured light yields are lower than expected [6]. However, for some crystals they are comparable to 2670 phe/MeV found for the LuAP crystal with 0.105 mol% Ce as reported in Ref. [7].

Figure 5.12 shows the histogram for the respective energy resolutions. Note that there is no definite difference between the energy resolution measured in vertical and in horizontal position. As mentioned before, this is related to the double photoelectric peaks found in the energy spectrum broadening the energy resolution. When fitting the curve with a sum of two gauss functions, an energy resolution of approximately 10% was found.

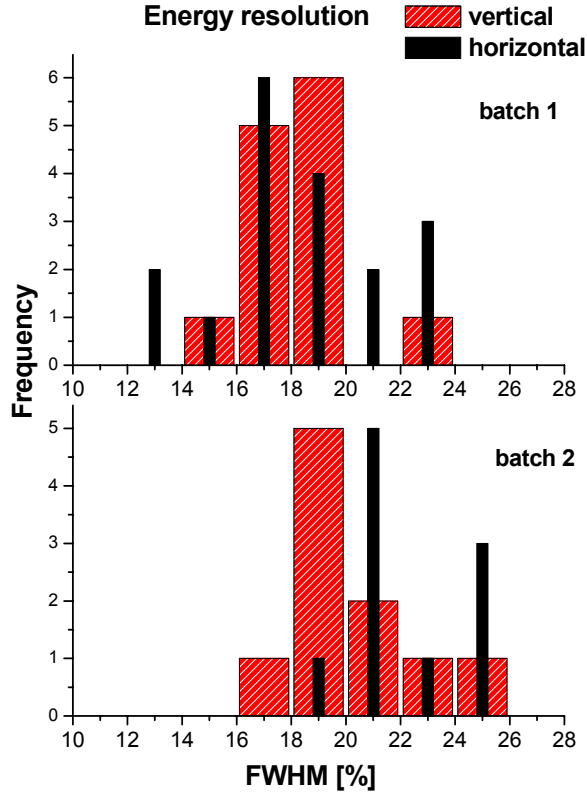


Figure 5.12 Distribution of the energy resolution for the two batches of $\text{Lu}_{0.8}\text{Y}_{0.2}\text{AP}$ crystals. The energy resolution was measured in vertical (red bars) and horizontal (black bars) position using a Cs-137 source.

5.2.3 Results for the $\text{Lu}_{0.7}\text{Y}_{0.3}\text{AP}$ Samples from BTCP

A pulse height spectrum measured with a ^{137}Cs source for a $\text{Lu}_{0.7}\text{Y}_{0.3}\text{AP}$ crystal can be seen in Figure 5.13. Note that the Lu K_{α} escape peak (63 keV) can be seen in the spectrum, which confirms the excellent energy resolution.

Figure 5.14 summarizes the results of the light yield (ph/MeV) measurements in horizontal and vertical position for the three batches of crystals. The light output in horizontal position obtained for mixed crystals varied from 1710 to 2190 phe/MeV. These values are comparable to the results recently measured for the $\text{Lu}_{0.8}\text{Y}_{0.2}\text{AP}$ crystal [8].

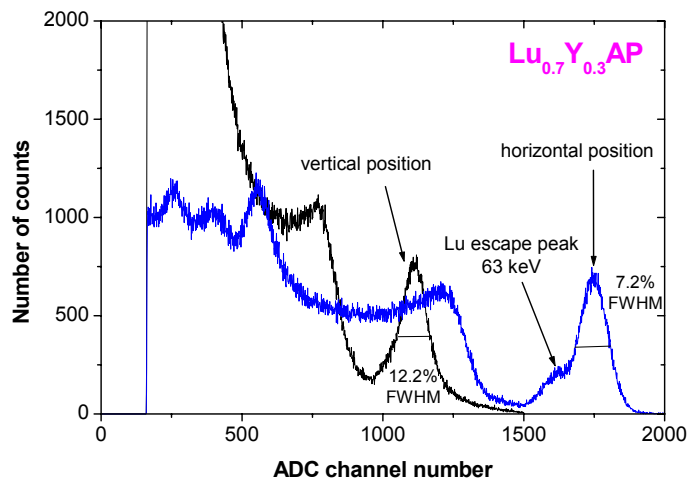


Figure 5.13 Pulse height spectra of a Cs-137 source measured with the LuYAP crystal in vertical and horizontal position.

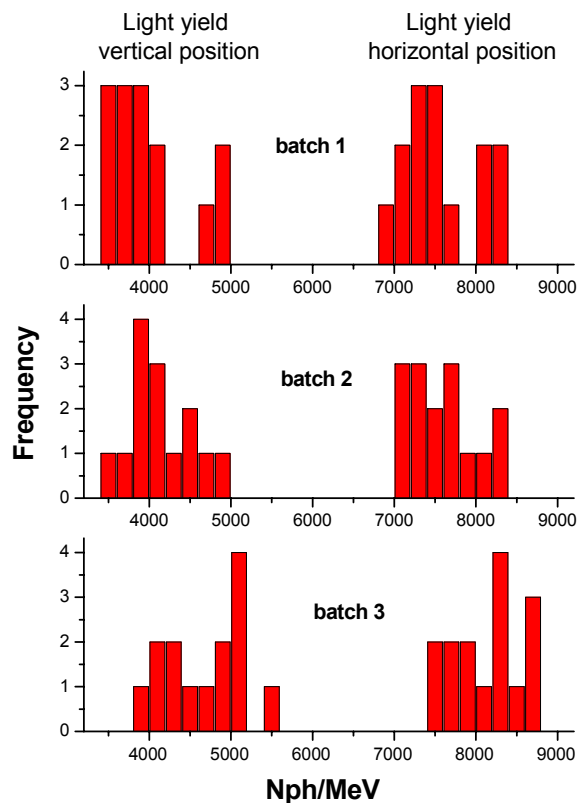


Figure 5.14 Light yield histogram given in the number of photons/MeV of the three batches of LuYAP crystals. The light output was measured in vertical (left part of the histogram) and in horizontal position (right group) using a Cs-137 source.

A trend towards the improvement of the light yield from the first to the third batch can be seen for horizontal as well as for vertical measurements. The light yield ratio between vertical and horizontal position increased from about 52% for the first to around 57% for the third batch of crystals.

The energy resolution of the 662 keV peak of ^{137}Cs was found to be around 7.75% in horizontal geometry for all studied crystals. In vertical geometry a weak improvement in the energy resolution, from $14.6 \pm 0.7\%$ (1st batch) to $13.7 \pm 0.7\%$ (3rd batch), was observed. This is related to lower self-absorption and thus the higher vertical light output for the latter crystals. Figure 5.15 shows the energy resolution distribution from three studied batches.

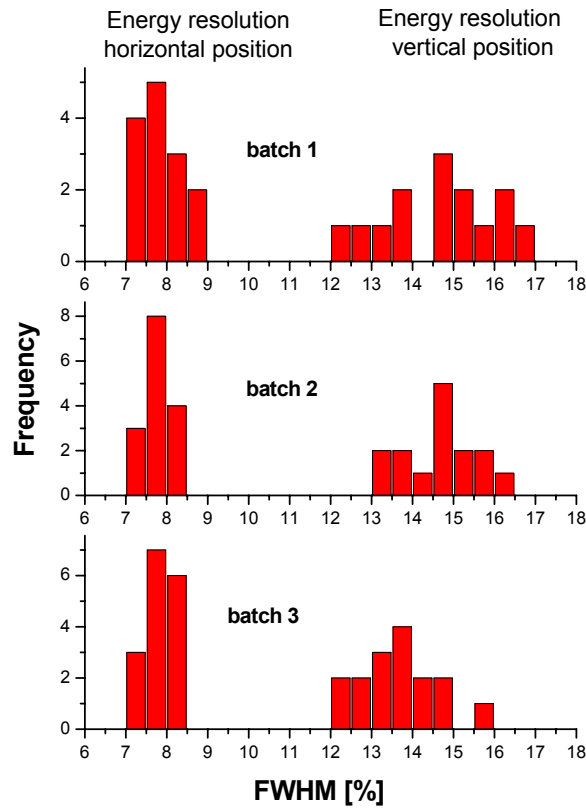


Figure 5.15 Distribution of the energy resolution for three batches of $\text{Lu}_{0.7}\text{Y}_{0.3}\text{AP}$ crystals. The energy resolution was measured in vertical and horizontal position using a Cs-137 source.

5.2.4 Reproducibility of the Measurements

One selected $\text{Lu}_{0.7}\text{Y}_{0.3}\text{AP}$ crystal was measured several times over the year to check the reproducibility of the measurements. The variations in the determination of the number of photoelectrons and in energy resolutions were within the measurement uncertainties. The given value is the mean value of two measurements.

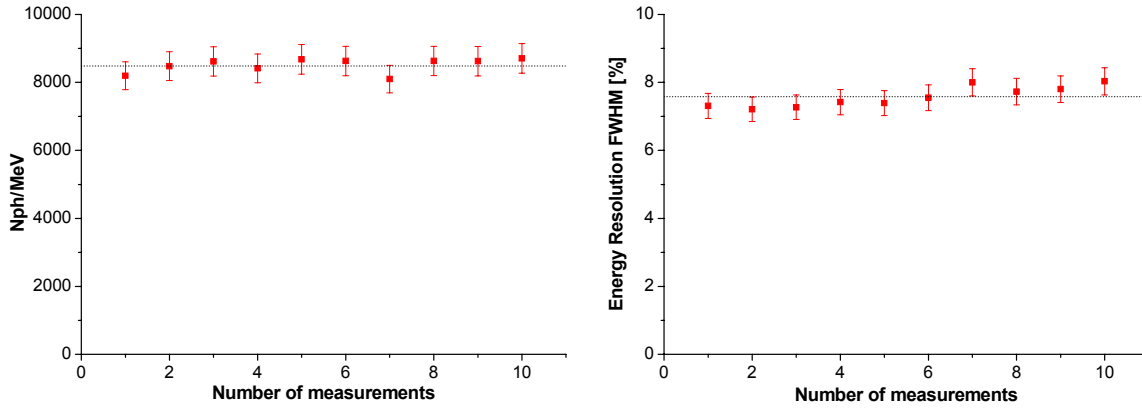


Figure 5.16 Stability of the light yield and energy resolution measurements performed with a selected LuYAP sample. The dotted line represents the average over all measurements.

5.3 Intrinsic Energy Resolution

The intrinsic resolution was calculated for the $\text{Lu}_{0.7}\text{Y}_{0.3}\text{AP}$ samples using formula 3.17. For the 662 keV peak from the ^{137}Cs source, the statistical spread in FWHM of $7.0 \pm 0.01\%$, $6.98 \pm 0.01\%$, and $6.75 \pm 0.01\%$, was calculated from the measured light yields of the first, second and third batch, respectively. Note that this term is already very close to the mean overall measured energy resolution of $7.81 \pm 0.39\%$. This leads to an overall intrinsic energy resolution of the $\text{Lu}_{0.7}\text{Y}_{0.3}\text{AP}$ samples of $3.6 \pm 0.88\%$. The distribution of the intrinsic energy resolution for the three studied batches is shown in Figure 5.17.

A further improvement of the energy resolution may be expected in the near future due to better technology. It must be pointed out that this crystal comes from a batch grown in the pre-production phase where not all the crystal growing parameters were yet optimized.

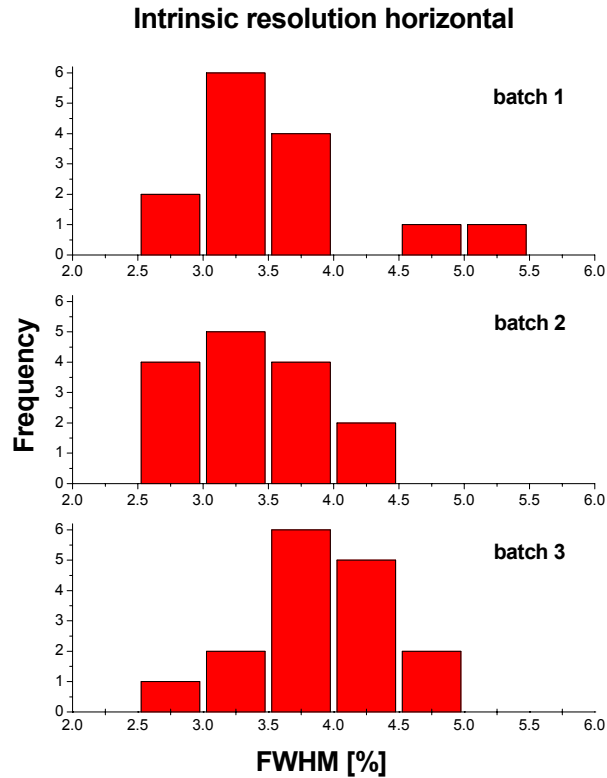


Figure 5.17 Distribution of the calculated intrinsic energy resolution for the three batches of $\text{Lu}_{0.7}\text{Y}_{0.3}\text{AP}$ crystals.

5.4 Non-Proportional Response

Due to the good results in energy resolution of the 1st batch $\text{Lu}_{0.7}\text{Y}_{0.3}\text{AP}$ crystals received in February 2002 from the BTCP, the response of the light output on various photon energies was studied. The different radioactive sources used in this test are listed in Table 4.2.

One crystal was selected and mounted in horizontal geometry on the PMT by means of silicon grease and covered with several layers of Teflon tape.

One LSO crystal from CTI was also studied in the same way to compare the results of other authors and to the results obtained with the LuYAP crystal.

As usual, the number of photoelectrons per MeV was calculated by comparing the position of the photopeak with that of the single photoelectron peak. The relative light output was obtained by comparing the number of photoelectrons measured at energy E with the number measured with the reference source (^{137}Cs , 662 keV). Depending on the

type of excitation source used, the photopeak of interest was accompanied by satellite peaks. These peaks are either due to escape of characteristic lutetium K_{α} photons from the crystal or because the source emits more than one type of γ -rays. The energy spectra obtained with ^{22}Na , ^{133}Ba , ^{60}Co , and ^{54}Mn are shown in Figure 5.18. Note that the upper spectra are illustrated in logarithmic scale.

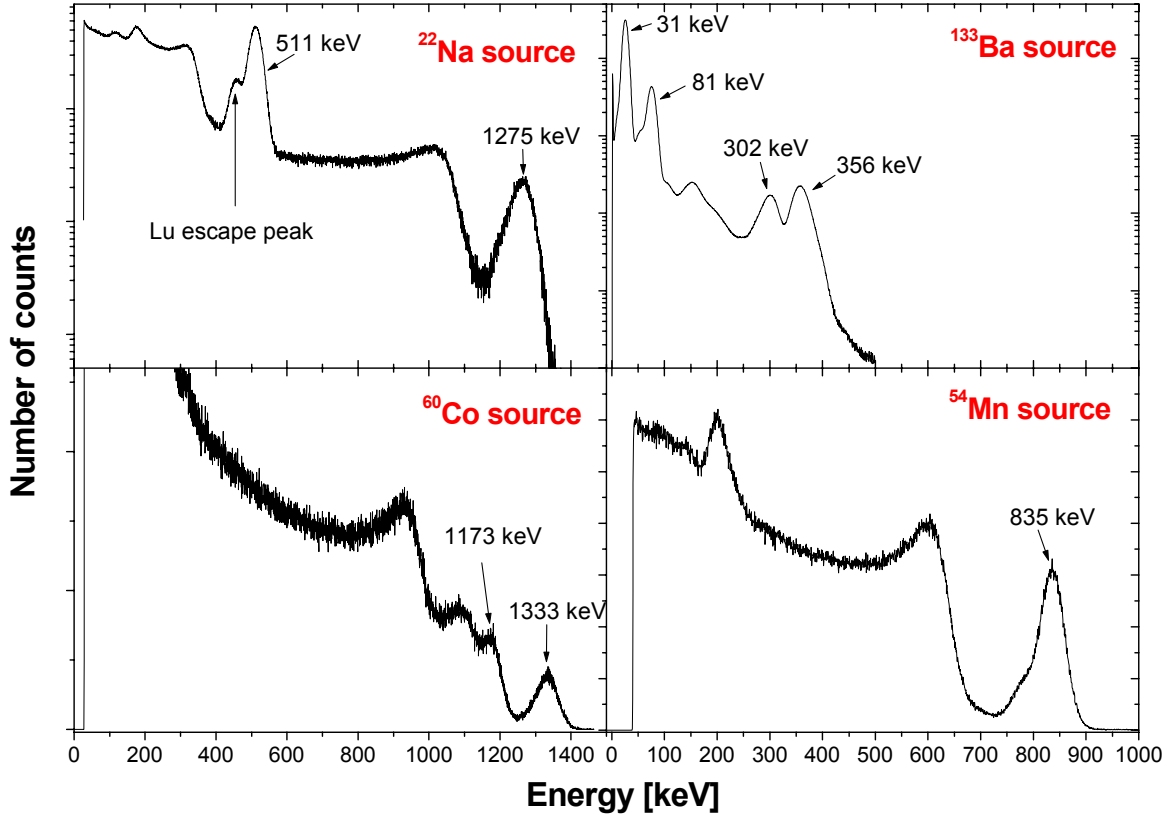


Figure 5.18 Energy spectra of γ -rays from a ^{22}Na , ^{133}Ba , ^{60}Co , and ^{54}Mn source measured with a LuYAP crystal. The upper spectra are given in logarithmic.

Figure 5.19 shows the response curve of the $\text{Lu}_{0.7}\text{Y}_{0.3}\text{AP}$ and the LSO crystal in the energy range of 31 keV to 1.333 MeV. The curve of LSO decreases down to 65% at 31 keV and shows a small drop near the K-edge of lutetium ions (63.3 keV). Whereas for LuYAP, the decrease is more shallow and no drop is visible. A decrease in light output of the LSO crystal can also be noticed for higher energies. The response curve of LSO is comparable to the results of Ref. [9] but the losses are more distinct in our measurements.

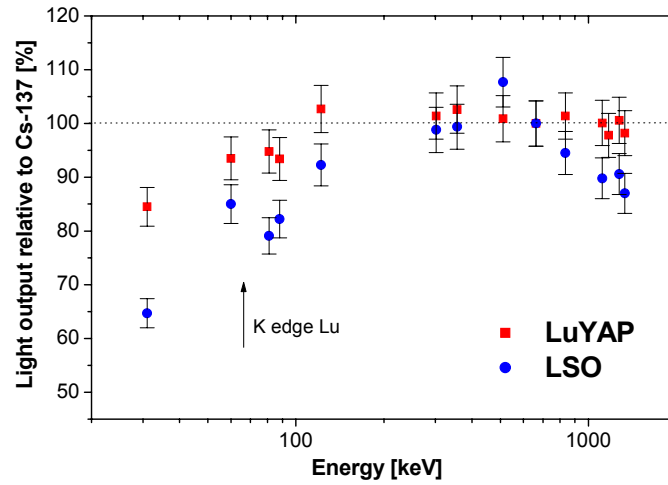


Figure 5.19 Scintillation light output as a function of excitation energy relative to the light output at 662 keV excitation.

As mentioned before (section 3.4.3), the energy resolution of scintillation detectors is due to three factors, the intrinsic resolution, the transfer resolution and the photomultiplier resolution. In Figure 5.20, the measured energy resolution, the photomultiplier resolution and the intrinsic resolution are shown for LuYAP and LSO. These results indicate that the measured energy resolution of LuYAP is mainly influenced by the statistical term coming from the PMT. For the LSO energy resolution the statistical term has not such a big influence, which means that the LSO energy resolution is principally affected by the intrinsic energy resolution.

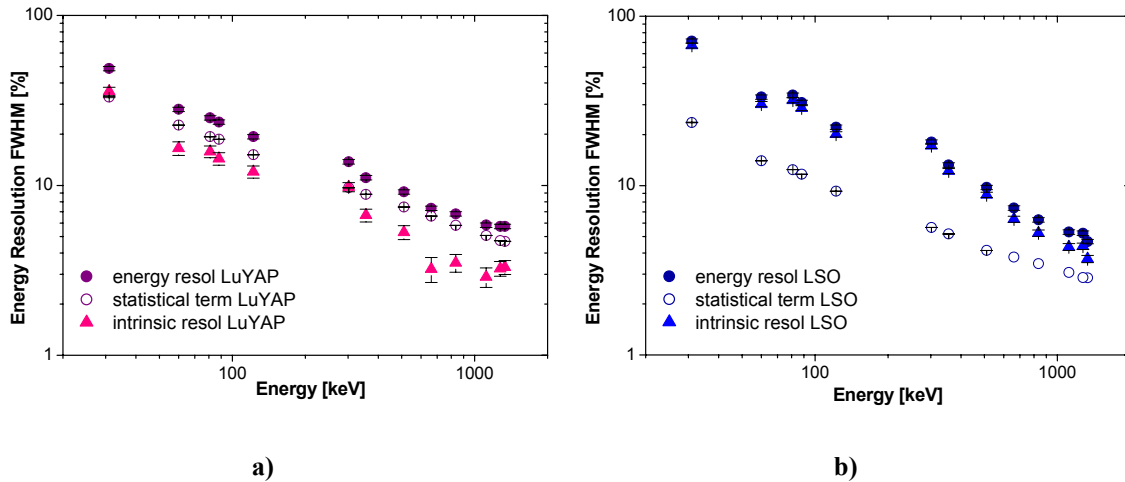


Figure 5.20 Overall energy resolution, statistical resolution of the PMT and intrinsic resolution for a selected a) $\text{Lu}_{0.7}\text{Y}_{0.3}\text{AP}$ and b) LSO sample.

5.4.1 Degree of Non-Proportionality σ_{np}

As proposed by Dorenbos [10] the degree of non-proportionality of the light output on energy can be calculated as

$$\sigma_{np} = \sqrt{\frac{1}{N} \sum_{i=1}^N \left(\frac{Y(E_i)}{Y(662)} - 1 \right)^2} . \quad (5.1)$$

where $Y(E_i)$ is the light yield (photons/MeV) at energy E_i and $Y(662)$ is the light yield obtained with the ^{137}Cs source.

A summation of the given energies (31 keV to 1.333 MeV, see Table 4.2) was used. With these energies, we obtained a value of 0.176 for LSO and 0.054 for $\text{Lu}_{0.7}\text{Y}_{0.3}\text{AP}$. For LSO, Dorenbos [10] reported a value of around 0.216 as shown in Figure 5.21, but this cannot be directly compared to our results because the used energy region (10 keV to 1 MeV) was different. Due to the higher divergence of the light output in the lower energy region, there is no real discrepancy. Nevertheless, the low value of σ_{np} obtained for LuYAP seems to be promising.

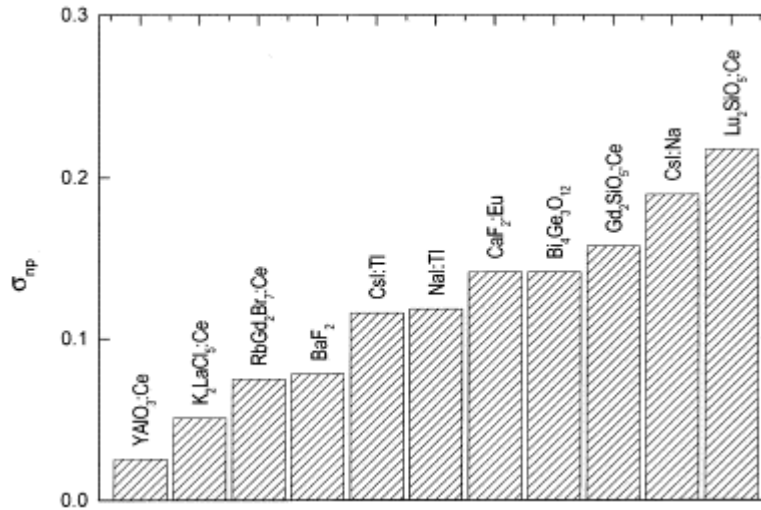


Figure 5.21 Calculated degree of non-proportionality of the light output on photon energy. (Reproduced from P. Dorenbos, Ref [10]). The used photon energies ranged from 10 keV to 1 MeV.

5.5 Scintillation Decay Time

5.5.1 Results for the LuAP and $\text{Lu}_{0.8}\text{Y}_{0.2}\text{AP}$ Samples

The light pulse shape of the LuAP and $\text{Lu}_{0.8}\text{Y}_{0.2}\text{AP}$ samples was measured at Swierk as well as at CERN. The time distributions of the light pulse from LuAP and LuYAP doped with 0.5 and 0.4% Ce, respectively, are presented in Figure 5.22. Note that for LuYAP the fast component with decay time constant of 20.5 ± 1 ns and intensity of 65% is followed by a slower component, with a 160 ns decay time constant and an intensity of 35%. The pulse shape from the LuAP sample exhibits a fast component of 18.2 ± 0.4 ns contributing with 82.8% to the total light output and a slow component of 149.8 ± 11.0 ns with intensity of 17.2%. The solid line in Figure 5.22 represents the fitted curve. Both time constants were obtained from the best fit to the light pulse shape.

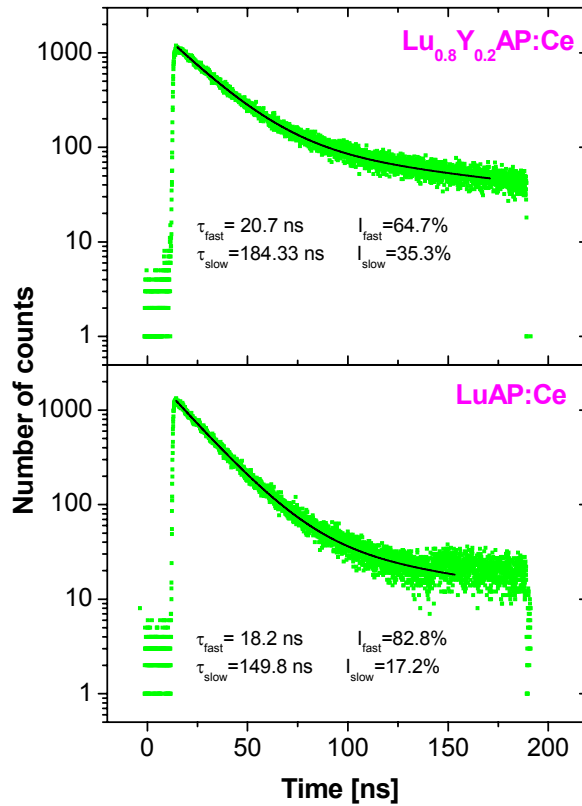


Figure 5.22 Light pulse shapes of the LuAP and LuYAP crystal excited by γ rays for 200 ns TAC range.

Table 5.2 summarizes the results in scintillation pulse shape from the LuAP and the $\text{Lu}_{0.8}\text{Y}_{0.2}\text{AP}$ samples measured at Swierk. The TAC range was set to 200 ns.

Table 5.2 Decay time constants of the light pulse shape from LuAP and $\text{Lu}_{0.8}\text{Y}_{0.2}\text{AP}$ samples doped with cerium measured at Swierk. The TAC range was set to 200 ns.

Crystal	Ce Conc.	Fast Component		Slow Component	
		τ_{fast} [ns]	Intensity	τ_{slow} [ns]	Intensity
LuAP 1013	0.5% Ce	18.2 ± 0.4	82.80%	149.8 ± 11.0	17.20%
LuYAP 1029	0.4% Ce	20.7 ± 0.4	64.70%	184.3 ± 7.0	35.30%
LuYAP 1032	0.4% Ce	20.2 ± 0.4	65.90%	157.9 ± 3.5	34.10%
LuYAP 1037	0.4% Ce	20.5 ± 0.4	64.90%	162 ± 3.1	35.10%
LuYAP 1038	0.4% Ce	19.4 ± 0.4	60.80%	134.7 ± 3.9	39.20%
LuYAP 1044	0.4% Ce	20.5 ± 0.4	62.50%	170.1 ± 8.8	37.50%
LuYAP 1068	0.55% Ce	21.6 ± 0.4	67.30%	216.8 ± 23.3	32.70%

5.5.2 Results for the $\text{Lu}_{0.7}\text{Y}_{0.3}\text{AP}$ Samples

The time distribution of the light pulse from a selected LuYAP sample is presented in Figure 5.23. The solid line represents the fitted curve. Both time constants were obtained from the best fit of the total light pulse shape. With a 2-exponential fit the decay time constants were found to be around 25 ± 1 ns and intensity of 46% followed by a slower component, with around 250 ± 25 ns decay time constant and intensity of 54%.

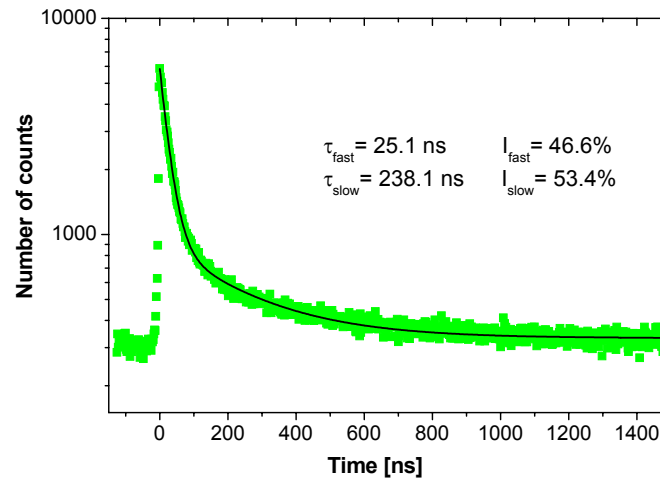


Figure 5.23 Scintillation light pulse shape of the $\text{Lu}_{0.7}\text{Y}_{0.3}\text{AP}:\text{Ce}$ crystal excited by gamma-rays for 2000 ns TAC range.

The results of the scintillation light pulse shape measurements performed at CERN are presented in Table 5.3 to 5.5. The spectra were taken for 2000 ns TAC range. The decay time constants were obtained from the best fit with a 2-exponential function to the measured data.

From the third batch of samples the slow component seems to be a little faster (~ 250 ns) compared to the first and the second batch (average around 330 ns). The same trend was observed for the fast component, 28 ns for the 1st and 2nd batch compared to 26 ns for the 3rd batch. Anyhow, these little differences in decay time are within the uncertainty of the measurements.

The decay time constants from the $\text{Lu}_{0.7}\text{Y}_{0.3}\text{AP}$ crystals are a little slower and the slow component is more intense compared to the results measured for the $\text{Lu}_{0.8}\text{Y}_{0.2}\text{AP}$ scintillator.

Table 5.3 Decay time constants of the light pulse shape from the first batch of $\text{Lu}_{0.7}\text{Y}_{0.3}\text{AP}$ samples doped with cerium measured at CERN. The TAC range was set to 2000 ns.

Crystal	Fast Component		Slow Component	
	τ_{fast} [ns]	Intensity	τ_{slow} [ns]	Intensity
LuYAP 1085	27.9 ± 0.3	46.7%	320.7 ± 21.4	53.3%
LuYAP 1086	27.8 ± 0.4	45.6%	335.0 ± 24.8	54.4%
LuYAP 1087	28.1 ± 0.3	45.5%	340.0 ± 23.0	54.5%
LuYAP 1088	29.0 ± 0.3	46.0%	365.0 ± 24.3	54.0%
LuYAP 1089	26.0 ± 0.5	46.3%	287.0 ± 22.4	53.7%
LuYAP 1090	28.7 ± 0.3	47.1%	340.0 ± 23.0	52.9%
LuYAP 1091	27.7 ± 0.5	46.4%	330.0 ± 25.5	53.6%
LuYAP 1092	27.6 ± 0.3	47.0%	340.0 ± 22.0	53.0%
LuYAP 1093	27.3 ± 0.5	46.7%	290.0 ± 23.5	53.3%
LuYAP 1094	27.6 ± 0.3	46.5%	335.4 ± 21.4	53.5%
LuYAP 1095	28.2 ± 0.3	47.0%	319.3 ± 21.1	53.0%
LuYAP 1096	29.0 ± 0.3	44.8%	389.9 ± 25.7	55.2%
LuYAP 1097	27.5 ± 0.3	48.1%	312.0 ± 20.6	51.9%
LuYAP 1098	26.7 ± 0.5	46.4%	292.0 ± 21.6	53.6%

Table 5.4 Decay time constants of the light pulse shape from the second batch of $\text{Lu}_{0.7}\text{Y}_{0.3}\text{AP}$ samples doped with cerium measured at CERN. The TAC range was set to 2000 ns.

Crystal	Fast Component		Slow Component	
	τ_{fast} [ns]	Intensity	τ_{slow} [ns]	Intensity
LuYAP 1100	28.4 ± 1.8	47.7%	334.1 ± 23.0	52.3%
LuYAP 1101	28.1 ± 2.2	45.4%	444.4 ± 42.4	54.6%
LuYAP 1102	29.5 ± 1.9	45.1%	368.7 ± 25.7	54.9%
LuYAP 1103	28.2 ± 2.0	48.0%	313.3 ± 25.1	52.0%
LuYAP 1104	25.3 ± 2.2	45.1%	288.0 ± 28.4	54.9%
LuYAP 1105	27.4 ± 1.8	46.1%	316.1 ± 23.4	53.9%
LuYAP 1106	27.0 ± 2.0	50.0%	305.4 ± 26.1	50.0%
LuYAP 1107	28.4 ± 2.2	50.0%	309.2 ± 28.7	50.0%
LuYAP 1108	26.7 ± 2.0	48.8%	281.2 ± 24.2	51.2%
LuYAP 1109	28.1 ± 2.0	49.5%	295.4 ± 25.4	50.5%
LuYAP 1110	29.7 ± 2.1	47.8%	403.3 ± 34.5	52.2%
LuYAP 1111	27.4 ± 2.0	48.4%	318.8 ± 28.4	51.6%
LuYAP 1112	28.1 ± 1.9	47.2%	359.8 ± 28.3	52.8%
LuYAP 1113	28.3 ± 1.8	46.5%	356.2 ± 30.2	53.5%
LuYAP 1114	29.2 ± 2.1	47.5%	359.0 ± 30.2	52.5%

Table 5.5 Decay time constants of the light pulse shape from the third batch of $\text{Lu}_{0.7}\text{Y}_{0.3}\text{AP}$ samples doped with cerium measured at CERN. The TAC range was set to 2000 ns.

Crystal	Fast Component		Slow Component	
	τ_{fast} [ns]	Intensity	τ_{slow} [ns]	Intensity
LuYAP 1134	26.3 ± 1.9	44.9%	269.5 ± 27.2	55.1%
LuYAP 1136	24.0 ± 1.8	45.3%	236.2 ± 23.6	54.7%
LuYAP 1137	26.6 ± 1.9	45.6%	262.8 ± 26.0	54.4%
LuYAP 1138	26.0 ± 1.8	44.0%	269.2 ± 24.7	56.0%
LuYAP 1139	25.0 ± 1.8	45.9%	243.3 ± 23.5	54.1%
LuYAP 1140	26.4 ± 1.8	45.8%	260.9 ± 23.7	54.2%
LuYAP 1141	25.6 ± 1.8	44.8%	247.5 ± 22.9	55.2%
LuYAP 1142	26.0 ± 1.8	46.7%	272.5 ± 25.5	55.3%
LuYAP 1143	25.6 ± 1.8	45.9%	231.7 ± 20.1	54.1%
LuYAP 1144	26.5 ± 2.0	47.6%	249.8 ± 24.4	52.4%

5.6 Low Temperature TL

5.6.1 Thermoluminescence Study on LuAP

The tested LuAP:Ce crystal was grown by A. Petrosyan (Institute for Physical Research, Armenia) by the Bridgman method and had a size of $2 \times 2 \times 10 \text{ mm}^3$. The TL spectrum from the sample was compared to the spectrum of a crystal produced by Airtron and measured previously on a different set-up by the group of A. Wojtowicz in Boston. As shown in Figure 5.24, the spectra have approximately the same shape. The glow peaks are at about the same position, which means that the traps have about the same depth i.e. activation energy.

The spectrum was simulated using the first-order kinetic equation (4.13) proposed by Randall and Wilkins. The measured glow curve illustrated in Figure 5.25 is represented by small circles, whereas the simulated curve is shown by a solid line. The frequency factor was estimated to $5 \cdot 10^{12} \text{ s}^{-1}$. The values found for the activation energy and the lifetime of the carriers in the traps at room temperature are given in Table 5.6.

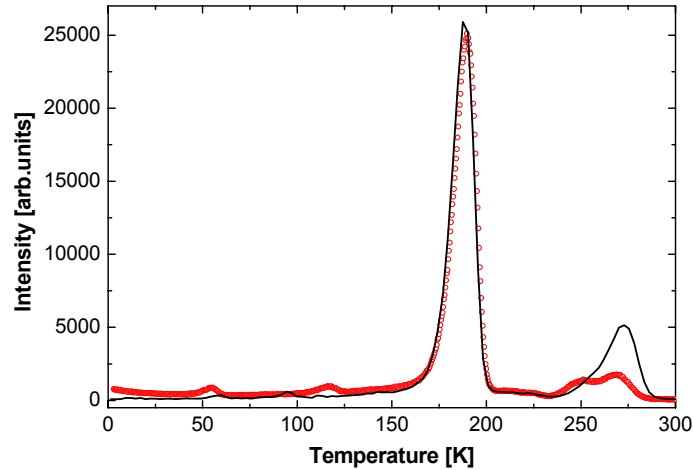


Figure 5.24 Low temperature thermoluminescence spectra of two different LuAP crystals. Thin line – the Airtron crystal measured in Boston, scattered line – crystal grown by Petrosyan. The Boston spectrum was shifted towards higher temperatures by 5 K.

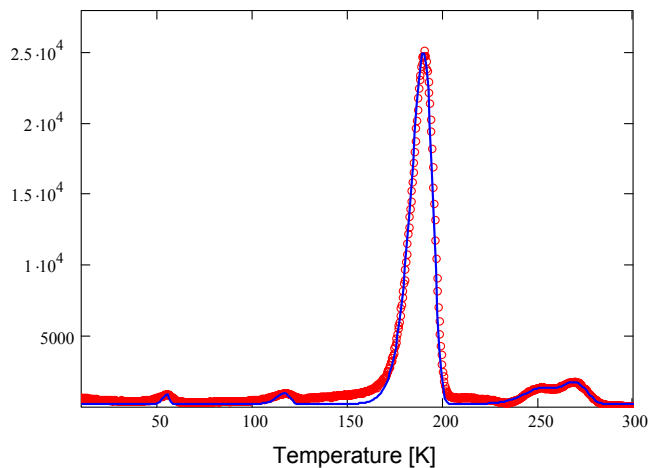


Figure 5.25 Measured and simulated glow curve of LuAP:Ce at temperatures below room temperature. The heating rate was 0.151 K/s. Experimental points are shown by circles while solid lines represent simulated glow curves calculated from a simple first-order Randall and Wilkins formula.

Note that the major glow peak at 189 K has a rather asymmetric shape. The simulated and measured curves are in a good agreement. The position of the TL peaks is comparable to the values found by [11].

5.6.2 Thermoluminescence Study on $\text{Lu}_{0.8}\text{Y}_{0.2}\text{AP}$

The six selected $\text{Lu}_{0.8}\text{Y}_{0.2}\text{AP}:\text{Ce}$ crystals were grown, like the pure LuAP, from A. Petrosyan by the Bridgman method. The data for the pure YAP:Ce and the $\text{Lu}_{0.2}\text{Y}_{0.8}\text{AP}:\text{Ce}$ crystal were provided for comparison of the results by A. Wojtowicz.

The glow curves of LuAP:Ce, YAP:Ce and $\text{Lu}_x\text{Y}_{x-1}\text{AlO}_3:\text{Ce}$ are presented in Figure 5.26. The LuAP spectrum contains 5 peaks where the dominant one is peaking at 189 K. The YAP spectrum has 2 major glow peaks at 108 K and 154 K.

The spectra of mixed crystals with 80% lutetium and 20% yttrium, respectively, show 5 glow peaks at approximately the same temperature range as the LuAP and YAP spectra. The $\text{Lu}_{0.2}\text{Y}_{0.8}\text{AP}$ spectrum measured on a different set-up by the group of A. Wojtowicz in Boston is shown to compare the position of the glow peaks.

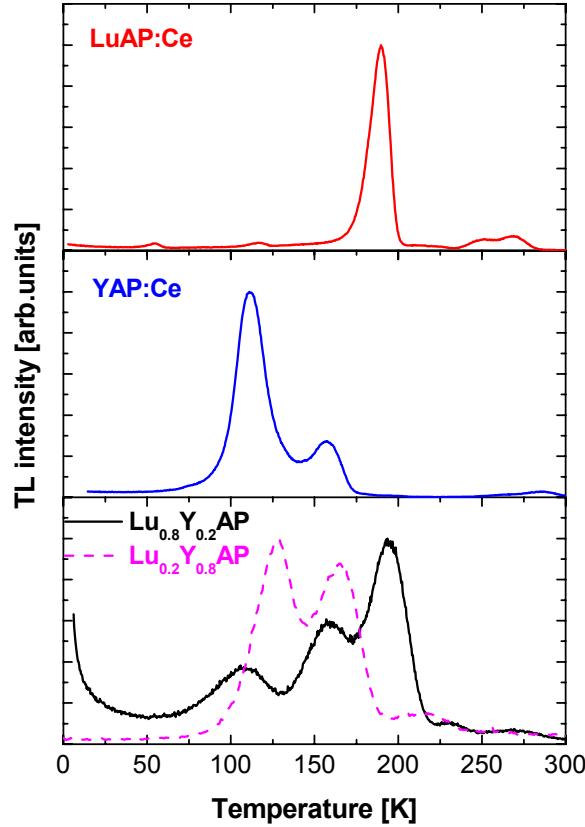


Figure 5.26 TL glow curves of LuAP:Ce, YAP:Ce and mixed LuYAP:Ce crystals with 80% lutetium and 20% yttrium, respectively. The heating rate β is 0.151 K/s. The curves are not adjusted to thermal lag. The spectrum of the $\text{Lu}_{0.2}\text{Y}_{0.8}\text{AP}$ crystal was measured by the group of A. Wojtowicz on a different set-up in Boston.

Bartram *et al.* [12] showed a linear relation between the integrated scintillation light output and the radiation time. They reported a value of 0.14 (LuAP) for the ratio of integrated light output under the glow curve to the integrated scintillation light output for high temperature TL.

According to that, we decided to repeat his measurement, which means to record the emitted light during irradiation with the given samples.

Before starting the measurements, the x-ray tube operated 5 min (with the shielding block) to assure voltage stability. After the block was removed, the sample was irradiated for 10 min. Due to the occurring phosphorescence of the LuYAP samples, the TL was started approximately 5 min later. The recorded curves can be seen in Figure 5.27 for two different LuYAP samples. The ratio of integrated light output under the glow curve to the integrated scintillation light output varied from 0.09 to 0.14 for the

LuYAP samples with 0.4% Ce and was found to be 0.19 for the sample with 0.55% Ce concentration.

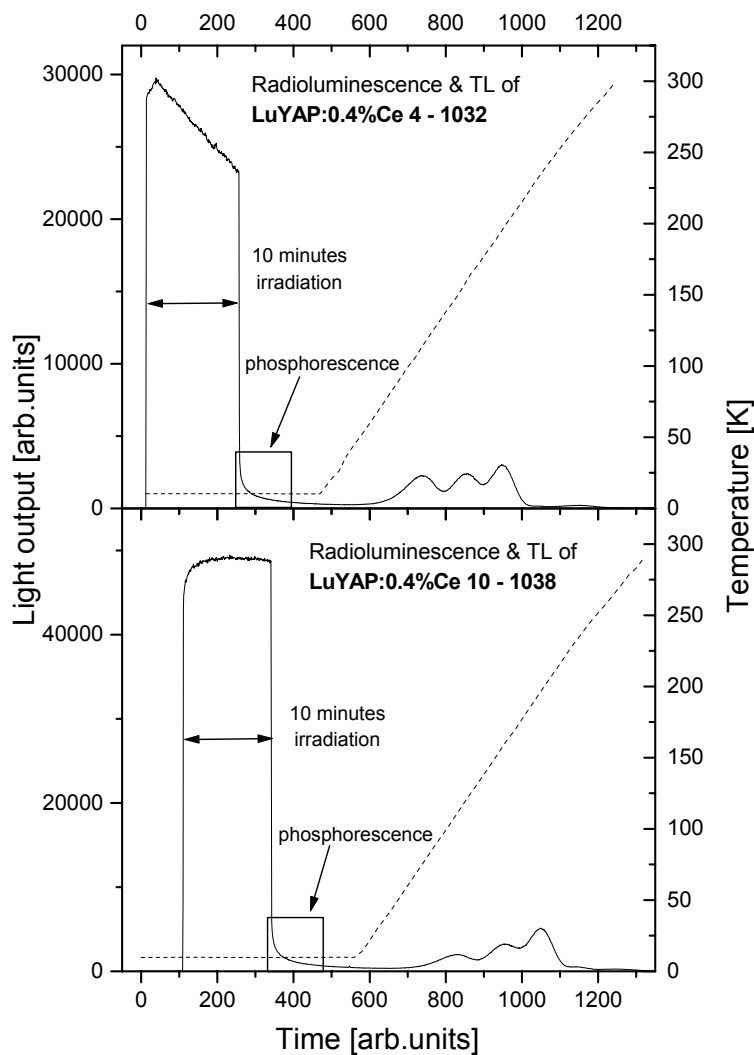


Figure 5.27 Light output (continuous curve) and sample temperature (dashed curve) as a function of time for a 10 min irradiation of two LuYAP:Ce samples with low (upper graph) and high (lower graph) light yield.

The shape of the scintillation light output during irradiation varied from sample to sample and was not reproducible when performing a second measurement.

The ltTL measurements were performed for 6 selected crystals with high and low light yield. One important point was the question of normalization for different samples. We choose two types of normalization to compare the samples.

In the first figure (Figure 5.28) the curves are normalized to the integrated scintillation light output (see Figure 5.27). As already mentioned before, the LuYAP sample number 17 has a different cerium concentration (0.55%) than the rest. This is reflected in the ratio of the integrated light output under the glow curve versus the integrated scintillation light output (0.19) as well as in the higher intensity of the glow peaks in the figure above.

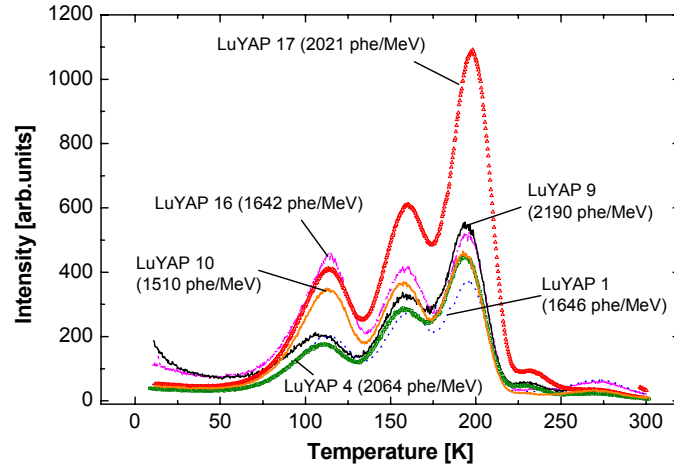


Figure 5.28 Low temperature thermoluminescence curves for $\text{Lu}_{0.8}\text{Y}_{0.2}\text{AlO}_3:\text{Ce}$ crystals normalized to the integrated scintillation light output during the irradiation.

The second type of normalization was related to the maximum glow peak at 195 K. With this type of normalization it is easier to compare the relative intensities of the glow peaks with each other as shown in Figure 5.29.

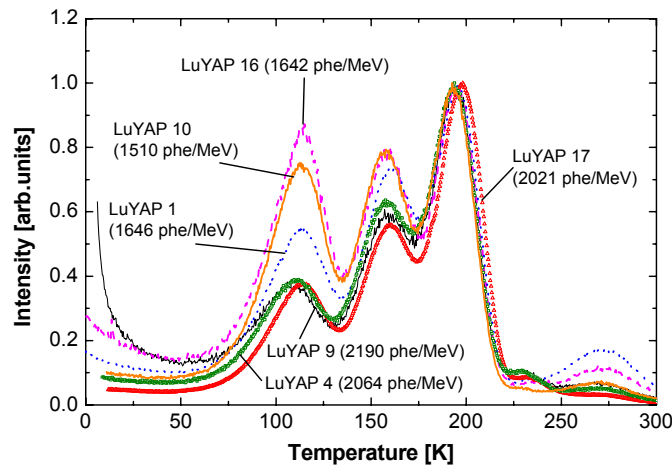


Figure 5.29 Low temperature thermoluminescence curves for $\text{Lu}_{0.8}\text{Y}_{0.2}\text{AlO}_3:\text{Ce}$ crystals normalized to the maximum glow peak at 195 K.

The little shift to higher temperatures from LuYAP 17 can be explained by the use of another glue for thermal coupling. The light yield is given in photoelectrons per MeV (phe/MeV) for the XP2020Q photomultiplier.

The spectra of samples with lower light yield show a more intense glow peak at 109 K than the spectra measured for higher light yield samples. A visible glow peak at 273 K can be seen for lower light yield samples.

The samples with high light output show almost the same shape with a ratio of 37% to 39% between the peak at 109 K and 195 K and a ratio of 56% to 63% between the peak at 160 K and 195 K.

For the samples with low light output these relations are not that clear. The ratio between the 109 K and 195 K peak varies from 54% to 87% whereas the ratio between the 160 K and 195 K peak shows smaller divergence (74% to 79%). The relationship between the glow peak ratios and the light output is illustrated in Figure 5.30.

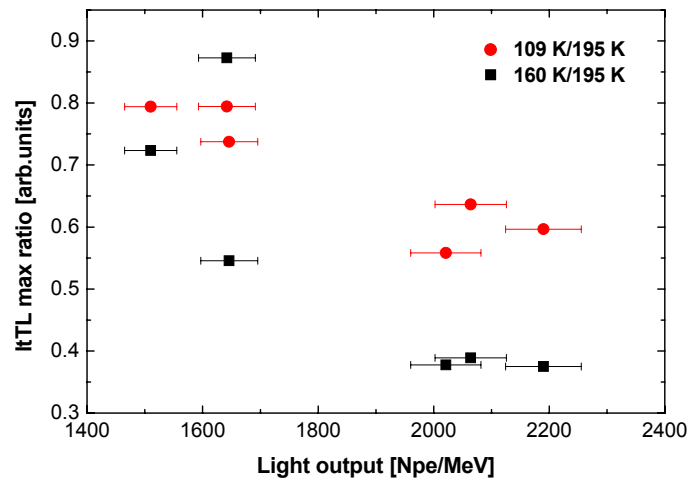


Figure 5.30 Relationship between the I_{TL} ratio from the glow peaks at 109 K and 160 K to the maximum glow peak and the light output.

As for the LuAP sample, the measured glow curves were simulated by the first-order Randall and Wilkins equation. In Figure 5.31 the measured glow curves represented by small circles are compared with the simulated glow curves shown by solid lines for one selected LuYAP crystal.

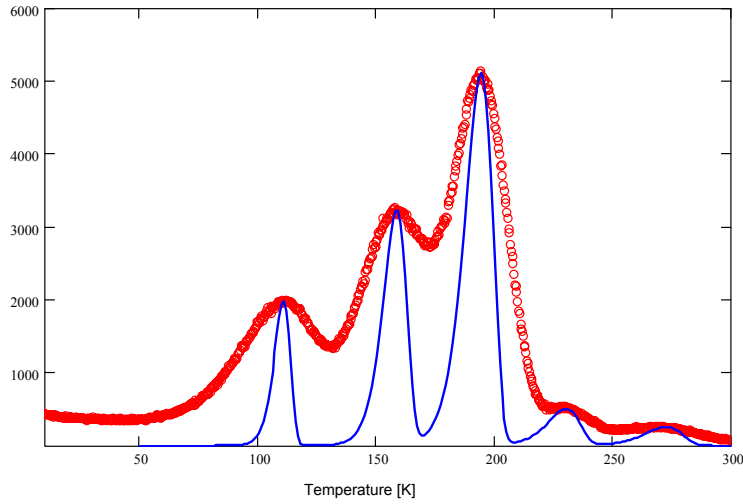


Figure 5.31 Measured and simulated glow curves of LuYAP:Ce at temperatures below room temperature. The heating rate was 0.151 K/s. Experimental points are shown by circles while solid lines represent simulated glow curves calculated from a simple first-order Randall and Wilkins formula.

This time, the glow peaks of the LuYAP crystal show a rather symmetric shape. This can be explained by trap distribution or by second order kinetics. Second order kinetics can be studied by irradiating the crystals for different times. The shape of the glow curves will be different if there is second order kinetics. By irradiating the samples for different time periods, we confirmed that there is no second order kinetics, so a trap distribution seems to be a reasonable explanation for the symmetric peaks as also reported by Ref. [13] for YAP:Ce.

The results for the major peaks and also the average lifetime of the traps obtained from the simulation are given in Table 5.6.

5.6.3 Thermoluminescence Study on $\text{Lu}_{0.7}\text{Y}_{0.3}\text{AP}$

Low temperature thermoluminescence spectra were also measured for the 3rd batch of $\text{Lu}_{0.7}\text{Y}_{0.3}\text{AP}$ crystals grown by the Czochralski method in the BTCP (Russia). One sample was sent to A. Wojtowicz (Institute of Physics, N. Copernicus University, Torun, Poland) and the result of the ItTL measurement can be seen in Figure 5.32.

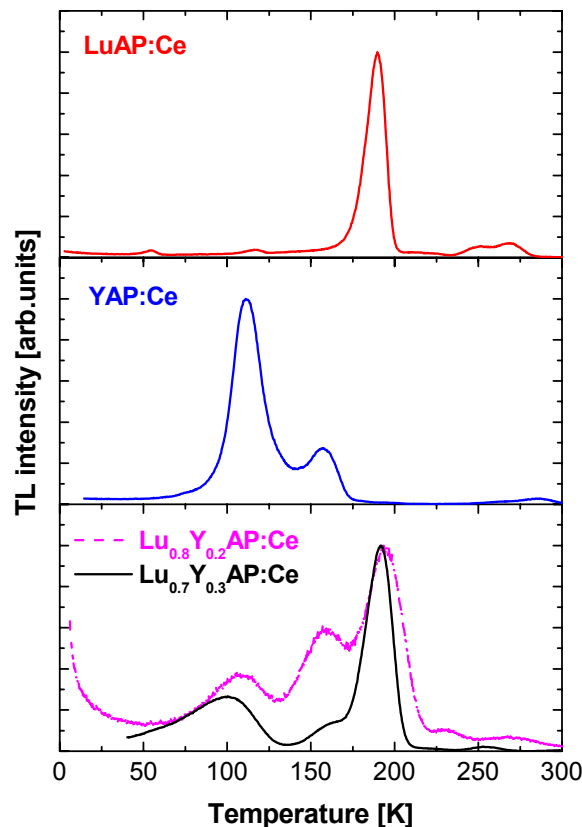


Figure 5.32 Low temperature thermoluminescence spectra for pure LuAP, YAP and the mixed crystals. The crystals with 70% Lu were grown by the Czochralski method whereas the samples with 80% Lu were produced with the Bridgman technique.

As before, thermoluminescence spectra of LuAP, YAP and the old $\text{Lu}_{0.8}\text{Y}_{0.2}\text{AP}$ samples are shown for comparison.

Note that this time the shape of the glow curves is different than the measured curves for the $\text{Lu}_{0.8}\text{Y}_{0.2}\text{AP}$ crystals. The major glow peak at 192 K shows a more asymmetric peak like the pure LuAP crystal. The glow peak at 158 K is not so pronounced as for the samples with 80% Lu. The peak at around 102 K is comparable in intensity with the peak of the Bridgman grown crystal.

The intensities of the glow peaks are much higher for the 70% Lu crystals compared to the 80% LuYAP crystals and the pure LuAP. The ratios between the integrated scintillation light output and the area under the glow curve were found to be 0.27 for the two selected crystal.

Table 5.6 Summary of the trap parameters (temperature of glow peak, activation energy, frequency factor and lifetime of the carriers) of LuAP, YAP, and LuYAP doped with Ce^{3+} . The bold values are the results from the simulation and the others were taken from references. For the simulation the frequency factor s was estimated to be $5 \cdot 10^{12} \text{ s}^{-1}$.

Crystal	T_{max} [K]	E [eV]	$\ln s$ [s^{-1}]	τ at RT (298 K)	Reference
LuAP	53	0.0606	10.37	330 μs	[11]
	183	0.490	27.90	140 μs	[11]
	219	0.390	16.89	180 ms	[11]
	264	0.814	32.23	560 ms	[11]
	55	0.149	29.24	66.21 ps	
	117	0.325	29.24	62.72 ns	
	189	0.537	29.24	241.4 μs	
	251	0.712	29.24	0.22 s	
	268	0.768	29.24	1.947 s	
YAP	108	0.30	29.24	23.7 ns	[13]
	154	0.50	34.18	409 ns	[13]
Lu_{0.8}Y_{0.2}AP	109	0.314	29.24	41.11 ns	
	160	0.448	29.24	7.53 μs	
	195	0.550	29.24	507.9 μs	
	229	0.665	29.24	32 ms	
	270	0.780	29.24	3.11 s	
Lu_{0.7}Y_{0.3}AP	100	0.282	29.24	11.75 ns	
	160	0.453	29.24	9.165 μs	
	192	0.544	29.24	317 μs	
	224	0.627	29.24	8.031 ms	
	255	0.728	29.24	0.41 s	

5.7 Discussion and Conclusion

One of the primary motivation for the present work was to quantify and explain the differences in light yield, energy resolution and decay time exhibited by the tested cerium doped $\text{Lu}_{1-x}\text{Y}_x\text{AP}$ crystals.

5.7.1 Bridgman Samples – LuAP and $\text{Lu}_{0.8}\text{Y}_{0.2}\text{AP}$

The UV spectroscopy study exhibited the presence of an additional absorption tail in the absorption spectrum. The origin of this tail might be the presence of small quantities of Ce^{4+} instead of Ce^{3+} as an activator, but is still unclear.

The absorption tail was found to be more intense for the LuAP samples and the samples with 80% lutetium leading to a strong overlap with the emission spectrum and thus a rather high self-absorption. As a consequence the emission at the rear end of the crystal is cut by the absorption edge and is therefore much lower compared to the 70% samples. Another consequence of the high self-absorption is the rather low ratio of the light yield measured in vertical and horizontal position (30% for LuAP), see also Figure 5.33.

The absorption measurements also allowed studying the homogeneity of the samples by taking spectra at different points along the crystal axis. The LuAP and LuYAP samples grown with the Bridgman technique showed different absorption spectra measured at the three points. Following our assumption, this means that there is a cerium concentration gradient along the sample – and thus also along the ingot – leading to the poor energy resolution (~20%). Samples with variations in the absorption spectra taken at different points along the crystal exhibited double or more photoelectric peaks in the energy spectrum.

However, it is not yet clear if the double photoelectric peaks originate from the gradient in the cerium concentration along the sample or from the growing method. In the unseeded Bridgman method, the crystallization takes place spontaneously, and therefore it might happen that there are polycrystals in one sample.

The measured light outputs from the 1st batch of studied LuYAP crystals in horizontal geometry varied from 5380 to 7970 photons/MeV and the energy resolutions were in the range of 12.5% to 23%. The results of the light yield measurements from the crystals with higher doping level (0.55% Ce) showed no variations in light output. The 2nd batch of studied samples exhibited a higher light yield ranging from 8070 to 10370 ph/MeV in

horizontal position. The energy resolution varied from 20.2% to 24.7%. No relationship between energy resolution and light yield could be drawn from the performed measurements. The reason for the poor energy resolution is the presence of two or more photoelectric peaks in the energy spectrum. Compared to the LuAP crystal, the LuYAP crystals exhibit a weaker self-absorption when measuring the light yield in vertical position.

The light pulse shapes of mixed crystals are comparable with that of LuAP:Ce, with fast components of 20 ns and slow ones of about 160 ns. However the percentage of the slower component is larger (30 - 40%) compared to LuAP:Ce (10 - 20%). This suggests that the expected increase in light yield mainly occurs due to the second component.

Although LuAP:Ce and LuYAP:Ce are two isostructural materials, their scintillation properties differ. In this chapter it was shown that the difference in light output for the tested $\text{Lu}_{0.8}\text{Y}_{0.2}\text{AP}:\text{Ce}$ crystals can be explained by the existence of shallow electron traps. The major glow peaks are at temperatures of 109, 160 and 195 K with a carriers live time in the trap of about 43 ns, 4 μs , and 106 μs , respectively.

The ratio of integrated light output under the glow curve to the integrated scintillation light output seems to depend on the cerium concentration. It was found to be in the range of 0.09 to 0.14 for the LuYAP samples with 0.4% Ce and 0.19 for the sample with 0.55% Ce concentration.

There is a clear correlation between the ratios of the peaks at 109 or 160 K to the major peak, and the light output. Samples with high light yield showed smaller ratios and less intense thermoluminescence peaks at 109 and 160 K. No correlation with light pulse shape was found.

5.7.2 Czochralski Samples – $\text{Lu}_{0.7}\text{Y}_{0.3}\text{AP}$

As for the Bridgman samples, an additional absorption tail was detected in the absorption spectra.

The absorption tail overlaps with the emission spectrum leading to self-absorption in the sample. A clear relation between the absorption spectrum taken at a selected wavelength (335 nm) and the light yield in vertical position was found. The lower the absorption at this wavelength, the higher the light output. An improvement in the absorption tail and thus in the vertical light output from the 1st to the 3rd batch of $\text{Lu}_{0.7}\text{Y}_{0.3}\text{AP}:\text{Ce}$ crystals was achieved by optimizing the crystal growth parameters. The relation between the ratio of the light yield measured in vertical and horizontal position for selected crystals and the absorption coefficient at 335 nm is shown in Figure 5.33.

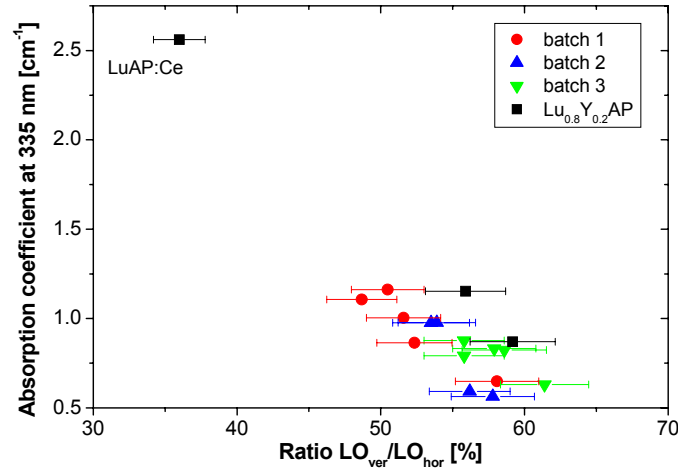


Figure 5.33 Relation between the ratio of the vertical to the horizontal light output and the absorption coefficient at 335 nm.

Absorption spectra taken at three points along the crystal axis exhibited no difference in shape. The variation of the shape in absorption spectra within a batch was negligible. This confirms that the crystal is homogeneous and directly leads to the good measured energy resolution of around 7.7% (horizontal).

Note that, contrary to the Bridgman method, the Czochralski method uses a seed to grow the boule. Therefore there is only one main crystal axis in the boule and no polycrystal zones appear in the ingot.

Another method to study the absorption of a crystal is to measure the emission at the front and rear end of the sample. As for the absorption study, a direct correlation between the emission measured at the rear end of the crystal (taken at a selected wavelength) and the light yield taken in vertical position was found.

The results on light output and energy resolution show an improvement in the crystal quality from the first to the third batch. The intrinsic energy resolution was studied as well as light yield non-proportionality on photon energy.

A mean overall energy resolution of 7.75% FWHM with ^{137}Cs source and crystal measured in horizontal position was found. The light yield was increasing from around 7560 ph/MeV to 8140 ph/MeV and from 4000 ph/MeV to 4650 ph/MeV, for the horizontal and vertical position, respectively.

The relation between the light yield and the energy resolution is given in Figure 5.34. The statistical limit defining the limit of the reachable energy resolution is also illustrated in the figure. The reason for the rather large distance between the light yield

measured in vertical position and the statistical limit is the self-absorption in the crystal and the intrinsic energy resolution. In horizontal position, the self-absorption is nearly irrelevant because of the thin crystal (2 mm). The low calculated intrinsic energy resolution shows that the energy resolution has nearly reached its statistical limit.

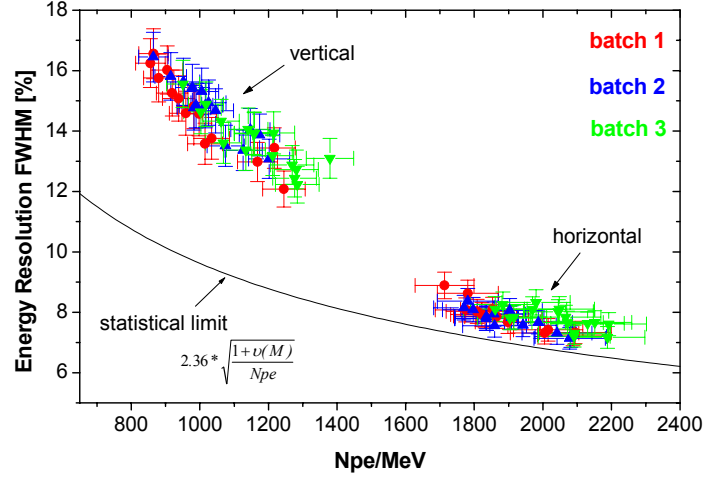


Figure 5.34 Relation between the measured energy resolution and the light output for the three studied LuYAP batches. The thin line indicates the statistical limit for the energy resolution.

The results show that the LuYAP energy resolution is mainly influenced by the statistical contribution of the PMT. The degree of non-proportionality of the light yield on energy was calculated to be 0.054 for LuYAP in the given energy range. This low value found for LuYAP together with the low intrinsic resolution of $3.6 \pm 0.8\%$ seems to confirm that there is a close relation between the energy resolution of scintillators and non-proportionality of their light output versus energy.

The yttrium concentration in the crystal has a strong influence on the light pulse shape. It increases the amount of slow component present in the spectrum. This clear correlation is shown in Figure 5.35. Due to this relationship it is possible to tune the scintillation properties of the crystal, i.e. the amount of slow component in the decay time spectrum, depending on the application.

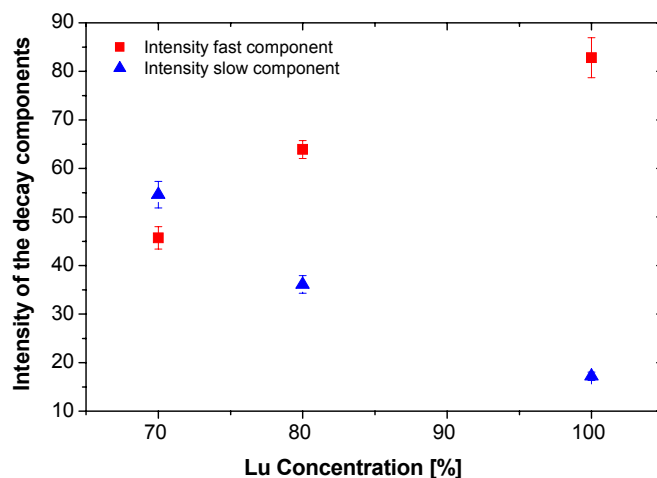


Figure 5.35 Correlation between the Lu concentration in the $\text{Lu}_{1-x}\text{Y}_x\text{AP:Ce}$ crystals (for x being 0, 0.2, and 0.3) and the intensities of the light pulse shape components.

In this chapter, it was demonstrated that the LuYAP crystal can be produced by the BTCP in large quantities with reproducible characteristics. By improving the crystal growth conditions, a reduction of the parasitic absorption tail, probably originating from Ce^{4+} , was obtained leading to higher light output measured in vertical position and better energy resolution.

5.8 References

- [1] P. A. Rodnyi, *Physical Processes in Inorganic Scintillators*, New York, CRC Press (1997).
- [2] A. Lempicki, C. Brecher, D. Wisniewski, E. Zych, A. J. Wojtowicz, *Lutetium Aluminate: Spectroscopic and Scintillation Properties*, IEEE Trans. Nucl. Sci. 43 (1996) 1316-1320.
- [3] C. Dujardin, C. Pedrini, W. Blanc, J. C. Gâcon, *et al.*, *Optical and scintillation properties of large $\text{LuAlO}_3\text{:Ce}^{3+}$ crystals*, J. Phys.: Condens. Matter (1998) 10, 3061-3073.
- [4] E. G. Gumanskaya *et al.*, Opt. Spectrosc. 72 (1992) 215.
- [5] A. Lempicki, C. Brecher, D. Wisniewski, E. Zych, *Cerium-Doped Aluminate Scintillators*, in Proc. Int. Conf. on Inorganic Scintillators and Their Applications, SCINT95, (1996) Delft University Press, The Netherlands, 340-343.

- [6] M. Moszynski, D. Wolski, T. Ludziejewski, M. Kapusta, A. Lempicki, C. Brecher, D. Wisniewski, A. J. Wojtowicz, *Properties of the new LuAP:Ce scintillator*, Nucl. Instr. and Meth. A 385 (1997) 123-131.
- [7] M. Moszynski, M. Kapusta, M. Mayhugh, D. Wolski, S.O. Flyckt, *Absolute Light Output of Scintillators*, IEEE Trans. Nucl. Sci. 44 (1997) 1052-1061.
- [8] C. Kuntner, H. Aiginger, E. Auffray, J. Glodo, M. Kapusta, P. Lecoq, M. Moszynski, M. Schneegans, P. Szupryczynski, A. J. Wojtowicz, *Scintillation properties and mechanism in $\text{Lu}_{0.8}\text{Y}_{0.2}\text{AlO}_3\text{:Ce}$* , Nucl. Instr. and Meth. A 486 (2002) 176-180.
- [9] P. Dorenbos, J. T. M. Haas, C. W. E. van Eijk, C. L. Melcher, J. S. Schweitzer, *Non-linear response in the scintillation yield of $\text{Lu}_2\text{SiO}_5\text{:Ce}^{3+}$* , IEEE Trans. Nucl. Sci. 41 (1994) 735-737.
- [10] P. Dorenbos, *Light output and energy resolution of Ce^{3+} -doped scintillators*, Nucl. Instr. and Meth. A 486 (2002) 208-213.
- [11] A. J. Wojtowicz, W. Drozdowski, D. Wisniewski, K. Wisniewska, K. R. Przegietka, H. L. Oczkowski, T. M. Pitors, *Thermoluminescence and scintillation of $\text{LuAlO}_3\text{:Ce}$* , Rad. Meas. 29 (1998) 323-326.
- [12] R. H. Bartram, D. S. Hamilton, L. A. Kappers, A. Lempicki, *Electron traps and transfer efficiency of cerium-doped aluminate scintillators*, J. Lumin. 75 (1997) 183-192.
- [13] A. J. Wojtowicz, J. Glodo, W. Drozdowski, K. R. Przegietka, *Electron traps and scintillation mechanism in $\text{YAlO}_3\text{:Ce}$ and $\text{LuAlO}_3\text{:Ce}$ scintillators*, J. Lumin. 79 (1998) 275-291.

Chapter 6

Properties of the $\text{Lu}_{0.7}\text{Y}_{0.3}\text{AP}$ Crystals from the Production Phase

In this chapter, the optical and scintillation properties of the first crystals grown in large quantities for the final scanners are presented. Note that the size of the boule is much larger compared to the boules produced in the pre-production phase, enabling to cut around 400 pixels from one large single. Therefore, the crystal growth conditions had to be optimized to produce these large ingots. A change in the scintillation properties might be expected due to the variation in the growth procedure compared to the pre-production phase. The pixels characterized in this chapter have a size of $2 \times 2 \times 8 \text{ mm}^3$. From 1000 samples, 10 were randomly chosen and their preliminary properties are discussed below.

6.1 Optical Properties

For the selected crystals emission, excitation and absorption spectra were measured. The samples exhibited the well-know scintillation properties resulting from 4f-5d transitions, but with some variations compared to the pixels from the pre-production phase.

6.1.1 Excitation Spectra

The samples were irradiated with the light emitted by a xenon lamp at room temperature. The emitted light from the crystals was recorded at 370 nm.

In Figure 6.1, the excitation spectra for five selected crystals are presented. Four bands can be seen peaking at around 230 nm, 269 nm, 288 nm, and 309 nm. Comparing the excitation spectra from the selected samples with the respective absorption spectra (see Figure 6.3), one notes that the intensity of the band at 230 nm behaves vice versa. This

means that samples with a high peak in the excitation spectrum exhibit a low peak in the absorption spectrum.

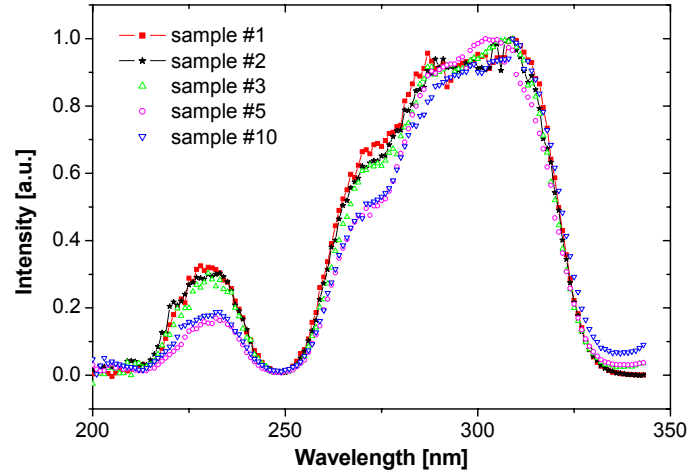


Figure 6.1 UV induced excitation spectra of different $\text{Lu}_{0.7}\text{Y}_{0.3}\text{AP}$ samples taken at room temperature. The emitted light was recorded at a wavelength of 370 nm.

6.1.2 Absorption Spectra

The absorption spectra were measured at three points along the crystal axis to study the homogeneity of the pixel (see section 4.2). The spectra taken for one crystal at these three points exhibited around the same shape as presented in Figure 6.2.

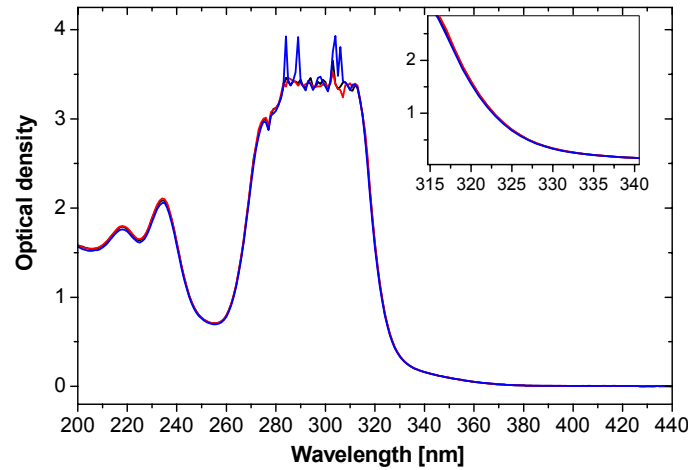


Figure 6.2 Absorption spectra measured at three different points along the crystal axis for a selected LuYAP crystal.

In the former measurements, performed with the crystals from the pre-production phase, the absorption spectra were very similar for pixels cut from one boule.

This time, no information about the origin of the pixels was available, which means that we don't know which pixel was cut from which boule. Thus the homogeneity of the ingot could not be studied.

The measured absorption spectra showed differences in shape. Some spectra had nearly the same shape, indicating that they were either cut from the same boule or from boules with similar properties. An example of the absorption spectra from 5 different crystals is given in Figure 6.3.

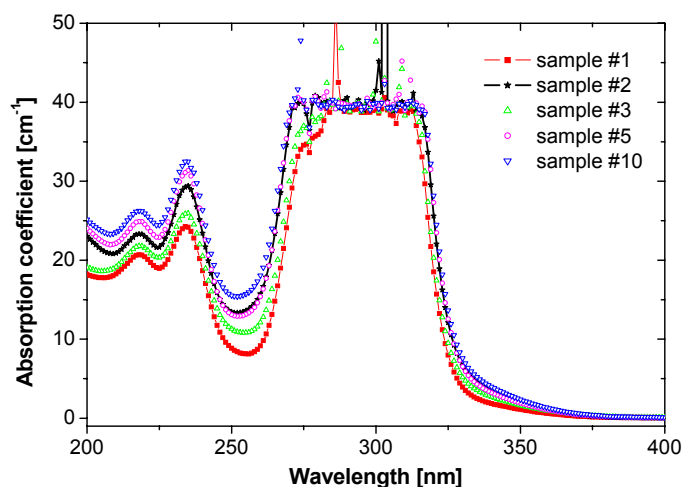


Figure 6.3 Absorption spectra measured for 5 different crystals from the production phase.

Note that from the five 4f-5d bands, only two can be clearly seen in the spectra around 217 nm and 234 nm.

When comparing the absorption spectra from the production phase to the respective spectra from the previous LuYAP samples (Bridgman grown and pre-production Czochralski samples), the absorption spectra exhibited a different shape. The additional absorption tail is much more pronounced for the crystal produced in the production phase as shown in Figure 6.4. In the same way the valley at around 250 nm has a higher absorption coefficient for the crystals of the production phase compared to the samples from the pre-production phase (compare the open circles with the squares in the graph). A similar effect was found when measuring the emission spectra at the rear side of the crystals (compare Figure 5.6 and Figure 6.7).

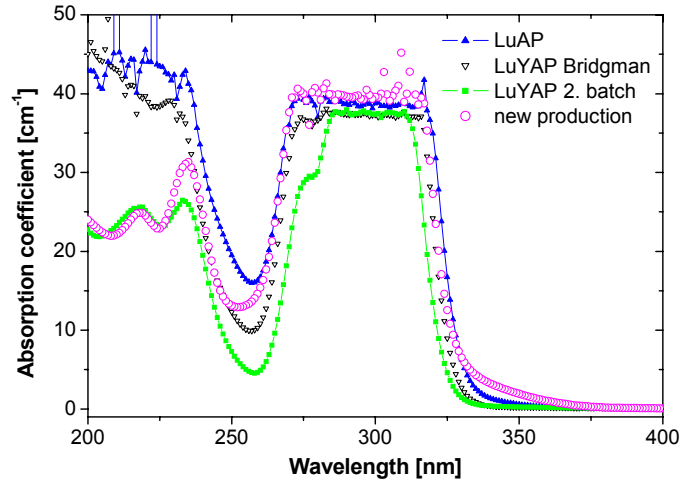


Figure 6.4 Comparison between the absorption spectra measured with different Lu(Y)AP samples.

As for the other $\text{Lu}_{0.7}\text{Y}_{0.3}\text{AP}:\text{Ce}$, an explicit correlation between the absorption coefficient at 335 nm and the light yield taken in vertical position was found. The wavelength used for this correlation was chosen such as to be influenced only by the absorption tail and not by the Ce^{3+} transitions. The correlation is presented in Figure 6.5. This graph definitely shows how strongly the absorption tail influences the light yield.

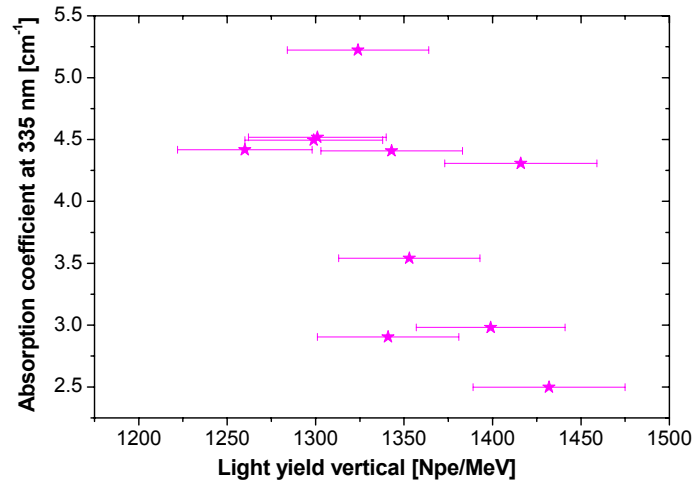


Figure 6.5 Correlation between the absorption coefficient at 335 nm and the light output measured in vertical position.

The cerium concentration was deduced by comparing the absorption coefficient at 320 nm with the coefficient of a sample with known cerium concentration (see equation 4.3). From this derivation, the Ce content was found to be higher, as compared to the samples of the pre-production phase. The producer confirmed this fact.

When looking only at the 10 studied samples, no definite correlation between the cerium concentration and the light yield can be found, as shown in Figure 6.6 a). However, when drawing the results from the pre-production and the production phase in one graph (Figure 6.6 b), one can see that crystals with higher cerium concentration exhibited a higher light yield. In the two graphs, the Ce values derived from the absorption coefficient at the three points of measurements along the crystal axis (up, middle and down) are given.

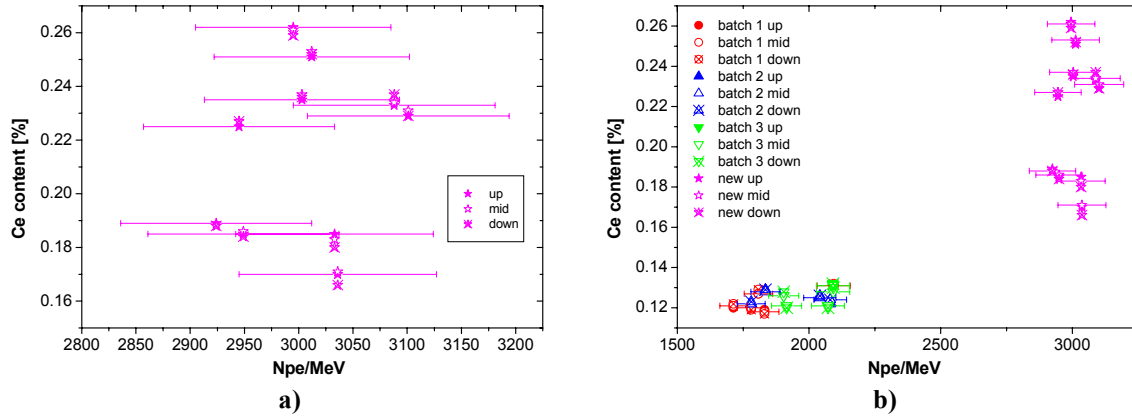


Figure 6.6 Correlation between the cerium content derived from the absorption coefficient at 320 nm and the horizontal light yield (number of photoelectron per MeV) for the $\text{Lu}_{0.7}\text{Y}_{0.3}\text{AP}$ samples from a) the production phase and b) for all the studied samples.

Yet, it is still unclear how exact the method for deducing the cerium concentration really is. The samples from the production phase all had more intense absorption tails between 330 nm and 370 nm compared to the samples from batch 1 to 3 (pre-production) (see Figure 6.4). For this reason, it might be necessary to subtract this additional tail before comparing the absorption coefficient at 320 nm with that of a sample with well-known Ce content.

Even if the absorption tail is not originating from Ce^{4+} , it is definitely not coming from Ce^{3+} transitions.

6.1.3 Emission Spectra

The UV induced emission spectra were taken at the front and at the back side of the crystal. This is an indirect way to study the absorption tail in the crystal and therefore to verify the results from the direct absorption measurements.

In the emission spectra measured at the front side of the sample, the $^2\text{F}_{5/2}$ and $^2\text{F}_{7/2}$ transitions from the lowest excited 5d level to the 4f level can even be seen at room

temperature. An example of the emission spectra measured at the two sides of the crystal together with the respective absorption spectra is given in Figure 6.7 for two selected crystals.

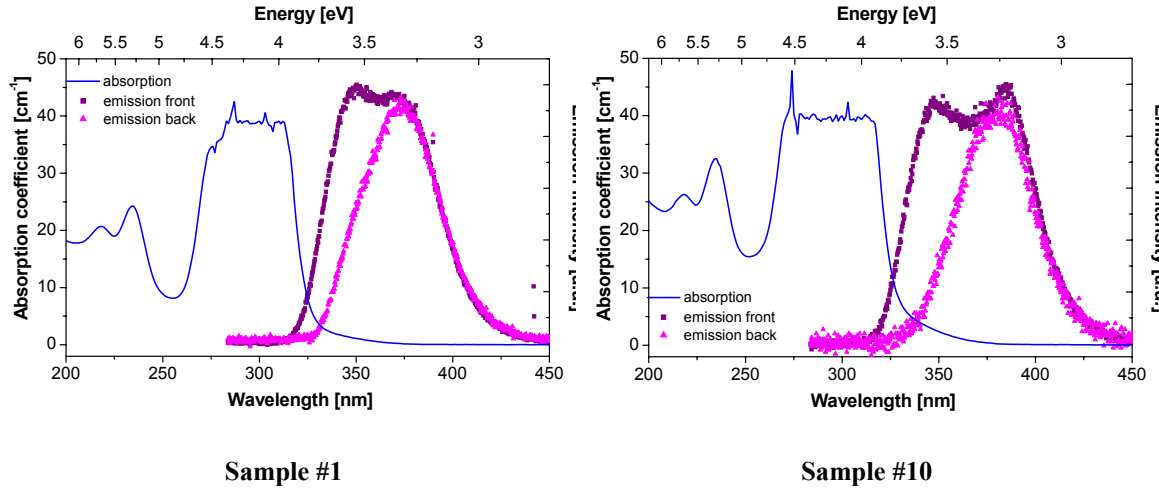


Figure 6.7 Absorption and UV excited emission spectra for two selected samples. The emission was measured at the side of excitation (violet points) and on the opposite side of the crystal (pink curve).

Note that for sample number 10, the overlap between the absorption and the emission spectrum measured at the front side (dark points) is much larger compared to sample #1. This leads to the result that the absorption tail cuts the emission recorded at the opposite side of the crystal, where the emitted light had to pass through 8 mm crystal length.

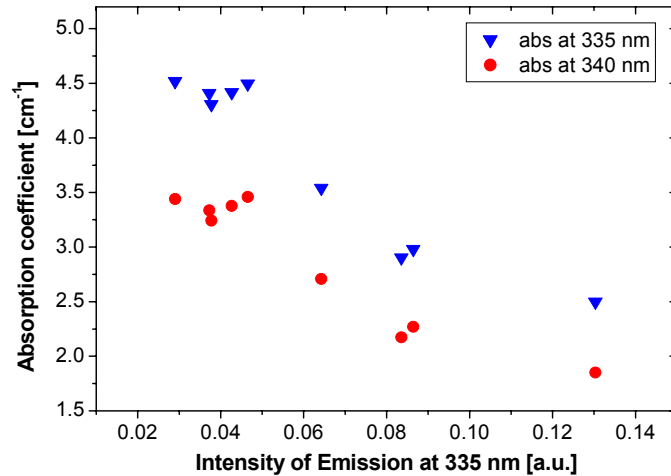


Figure 6.8 Correlation between the absorption coefficient determined at 335 nm and 340 nm and the intensity of the emission measured at the back side of the crystal (8 mm crystal length).

As expected, a clear correlation between the absorption coefficient at a certain wavelength (335 nm) and the emission intensity recorded at the back side of the crystal (8 mm crystal length) was found. The correlation is illustrated in Figure 6.8.

The lower the absorption coefficient at 335 nm or 340 nm, the more intense is the emission intensity at the chosen wavelength. This clearly reflects the importance of a low or even better a nonexistent absorption tail for having a more intense emission and thus a high light output in fingerlike crystals.

6.2 Light Yield, Energy Resolution and Decay Time

As usual, the light yield was determined by coupling the sample in vertical and horizontal position to the XP2020Q PMT by means of silicon grease. The samples were covered with several layers of Teflon tape to collect the maximum of the emitted light.

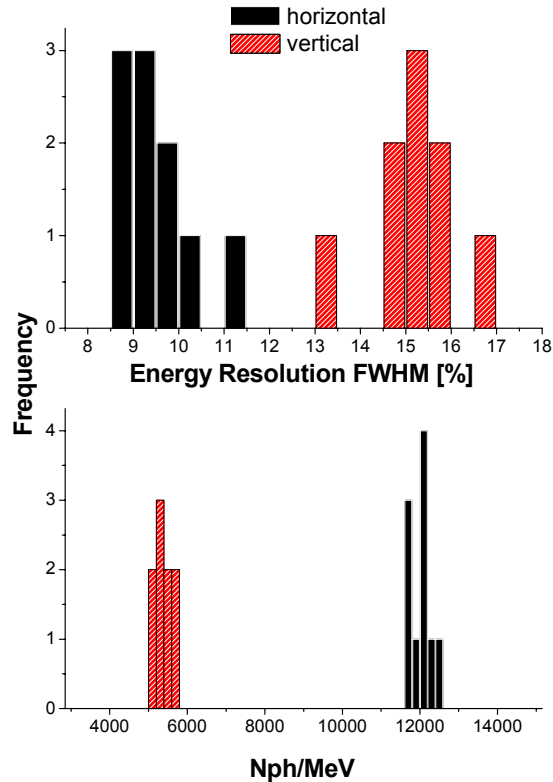


Figure 6.9 Light yield and energy resolution histogram of the ten studied $\text{Lu}_{0.7}\text{Y}_{0.3}\text{AP}$ crystals. The light output was measured in vertical and in horizontal position using a Cs-137 source.

The photon yields, and energy resolutions are summarized in Figure 6.9. The light output in horizontal position obtained for mixed crystals varied from 11700 to 12400 (± 600) ph/MeV. Note that the light yield is around 50% higher (~ 12000 ph/MeV) compared to the batches from the pre-production phase (8000 ph/MeV) measured in horizontal position. The light output is comparable to the value of 11400 ± 1500 ph/MeV measured by Moszynski *et al.* [1] for a LuAP sample (0.105 mol% Ce). The spread in light yield is very narrow, which is of great importance regarding the fact that the crystals were cut from different ingots. An energy spectrum measured with the Cs source for horizontal and vertical position is presented in Figure 6.10.

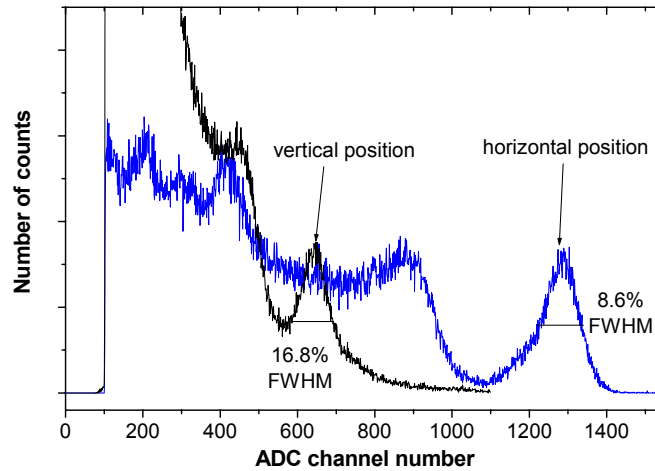


Figure 6.10 Energy spectra obtained with a Cs-137 source for a selected LuYAP crystal. The crystal was measured in horizontal and in vertical position.

The mean energy resolution of the 662 keV photopeak of ^{137}Cs was found to be around $9.5 \pm 0.5\%$ in horizontal geometry for the studied crystals.

In vertical position an energy resolution of around $15 \pm 1\%$ FWHM and a light yield of 5400 ± 270 photons per MeV were found. The vertical light yield is around 20% higher than for the 3rd batch from the pre-production phase.

The ratio between the light yield measured in vertical and horizontal position is around 47%.

For one selected crystal, energy spectra of γ -rays from a ^{22}Na and a ^{60}Co source were also taken and light yields and energy resolutions were determined. The spectra are shown in Figure 6.11.

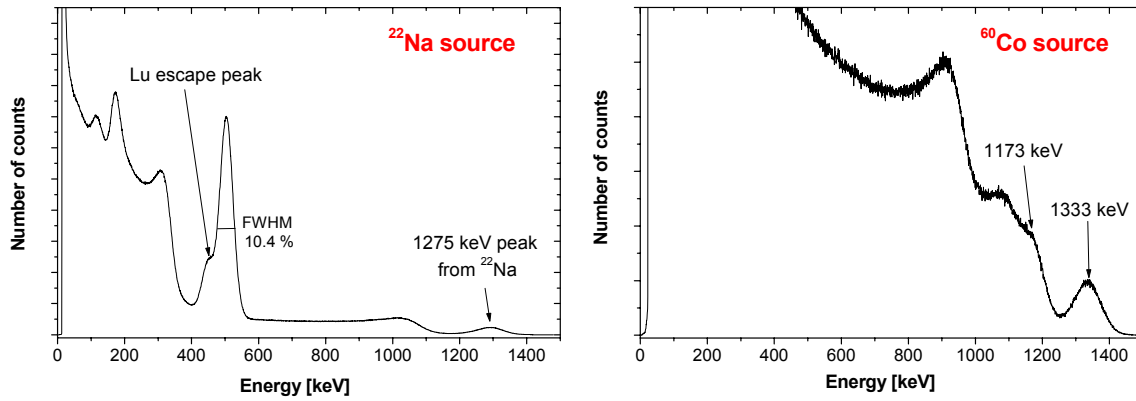


Figure 6.11 Energy spectrum of γ -rays from a ^{22}Na source (left spectrum) and a ^{60}Co source (right spectrum).

The obtained photoelectron yield, energy resolution and light yield using these sources are given in Table 6.1.

Table 6.1 Photoelectron yield, energy resolution and light output of LuYAP crystals for different radioactive sources.

Source	Energy [keV]	PhotoelectronYield [phe/MeV]	Energy Resolution FWHM	Light Output [ph/MeV]	% of Cs
Cs-137	662	3040 ± 90	$8.8 \pm 0.4\%$	12150 ± 600	$100 \pm 4.2\%$
Na-22	511	2970 ± 90	$10.4 \pm 0.5\%$	11870 ± 600	$97.8 \pm 4.1\%$
Na-22	1275	3060 ± 90	$7.4 \pm 0.4\%$	12260 ± 600	$100.9 \pm 4.3\%$
Co-60	1333	3050 ± 90	$7.1 \pm 0.4\%$	12200 ± 600	$100.4 \pm 4.3\%$

Note that the difference in the light yield measured with these three sources is negligible.

The scintillation light pulse shape was determined using the single photon counting method.

The scintillation light pulse shape consists of two components. The fast one has a decay time of 27 ± 0.6 ns with intensity of 43.6% followed by a slow component of $\sim 280 \pm 25$ ns and intensity of 56.4%. The decay time spectrum for a selected crystal is shown in Figure 6.12. The decay time constants plus the respective intensities obtained from the 2-exponential fit are given in Table 6.2.

No further additional slow component was observed in the time window of 2 μs .

The decay time components are comparable to the ones from the preproduction phase, where a fast component with 25 ± 1 ns and intensity of 46%, was followed by a slow component with $\sim 250 \pm 25$ ns and intensity of 54%.

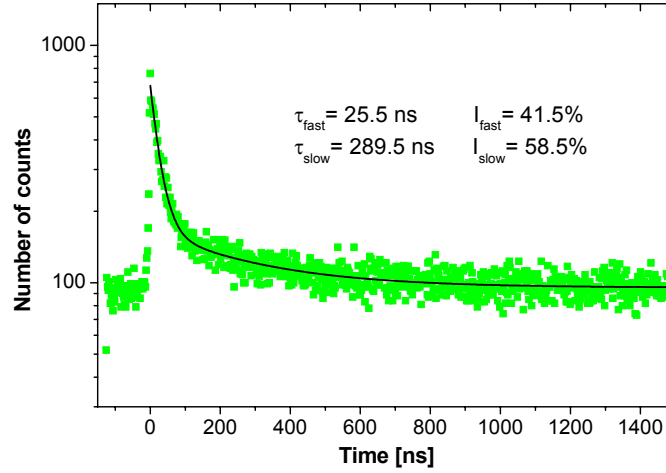


Figure 6.12 Scintillation light pulse shape of the $\text{Lu}_{0.7}\text{Y}_{0.3}\text{AP}:\text{Ce}$ crystal excited by gamma-rays for 2000 ns TAC range.

Table 6.2 Decay time constants of the light pulse for the $\text{Lu}_{0.7}\text{Y}_{0.3}\text{AP}:\text{Ce}$ crystals from the mass production phase.

Crystal	Fast Component		Slow Component	
	τ [ns]	Intensity	τ [ns]	Intensity
LuYAP 1	27.4 ± 0.8	41.5%	284.3 ± 25	58.5%
LuYAP 2	26.7 ± 0.6	44.5%	278.0 ± 22	55.5%
LuYAP 3	27.9 ± 0.7	42.4%	294.2 ± 28	57.6%
LuYAP 4	26.9 ± 0.6	42.7%	293.4 ± 26	57.3%
LuYAP 5	24.6 ± 0.5	44.1%	267.7 ± 22	55.9%
LuYAP 6	26.7 ± 0.5	45.6%	266.1 ± 18	54.4%
LuYAP 7	26.3 ± 0.6	44.4%	262.9 ± 22	55.6%

6.3 Discussion and Conclusion

In this chapter, first results on the properties of the $\text{Lu}_{0.7}\text{Y}_{0.3}\text{AlO}_3:\text{Ce}$ crystals used in the final small animal PET scanners were presented.

The scintillation light pulse shape consists of two components. The fast one has a decay time of 27 ± 0.6 ns with intensity of 43.6% followed by a slow component of $\sim 280 \pm 25$ ns and intensity of 56.4%. The light yield showed an improvement of around

50% in horizontal position compared to the crystals from the pre-production phase. The energy resolution was found to be around 9.5% FWHM. The increase in light yield did not lead to an improvement in energy resolution. From the measured number of photoelectrons a statistical resolution from the photomultiplier of 5.5% is expected. The deviation between the statistical limit and the measured resolution is not clear. An increase in local fluctuations of the activation centres leading to a stronger distinct intrinsic energy resolution might be the reason.

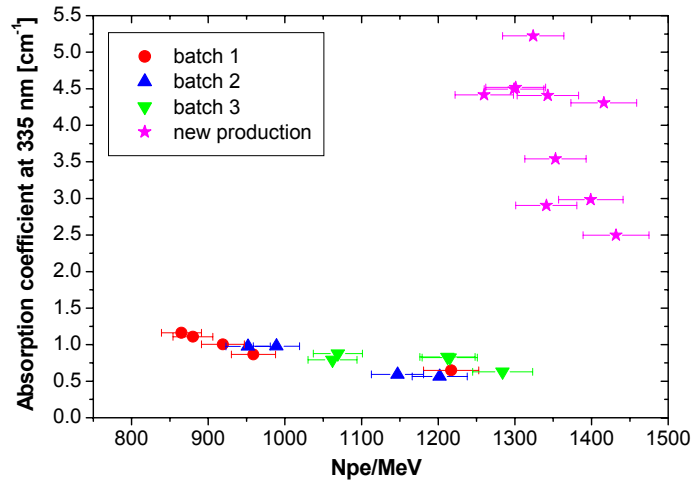


Figure 6.13 Correlation between the absorption coefficient at 335 nm and the light output measured in vertical position for all studied $\text{Lu}_{0.7}\text{Y}_{0.3}\text{AlO}_3\text{:Ce}$ samples.

The ratio between the vertical and the horizontal light yield is around 47%. One reason for this rather low ratio is the present additional absorption tail in the absorption spectra. A clear correlation between this tail and the light yield measured in vertical position was found. Still, when comparing this correlation with the respective correlation from crystals of the pre-production phase, they do not have the same correlation as shown in Figure 6.13.

One reason for this non-correlation might be the higher cerium content that we deduced from the absorption spectrum and the non-correlation of this cerium concentration with horizontal light yield.

Another explanation for this mismatch might be that light absorbed by the additional absorption tail is reemitted and thus not lost. This would lead to a change in the scintillation pulse shape. Unfortunately, no variation of the decay time components and intensities was observed.

Thus it is clear that more detailed investigations to understand the origin of the absorption tail and its effects on the scintillation properties are necessary.

The spread in light yield and energy resolution of the tested samples was very narrow (within the uncertainties). This is of importance when construction the final scanner with more than 1000 pixels for one ring. Similar properties of each pixel used in the 8 x 8 assembly assure a uniform response of each detector module and therefore of the whole scanner. Looking at the discrimination between the two crystal layers (LSO and LuYAP), the similar decay time components for the LuYAP layer enable to set one separation threshold (compare chapter 8) per multiplier or even per detector array (cassette). This simplifies the read-out electronics.

6.4 References

- [1] M. Moszynski, D. Wolski, T. Ludziejewski, M. Kapusta, A. Lempicki, C. Brecher, D. Wisniewski, A. J. Wojtowicz, *Properties of the new LuAP:Ce scintillator*, Nucl. Instr. and Meth. A 385 (1997) 123-131.

Chapter 7

Luminescence and Scintillation Properties of LSO Crystals and Derivates

7.1 Optical Properties

When studying the optical properties of a crystal, the scintillation mechanism can be investigated. For LSO crystal, it has been shown that there are two different cerium sites present in the material. Thus, the study of the optical properties gives you important information about the populations of these centres and their influence on the scintillation properties like decay time or energy resolution.

The measurements were taken at room temperature and therefore the clear distinction between the Ce1 and Ce2 sites could not be studied. However, an estimation about the intensity of these two centres could be made.

7.1.1 The Role of Cerium Sites in LSO

The host material $\text{Lu}_2(\text{SiO}_4)\text{O}$ is one of the oxyorthosilicates $\text{RE}_2(\text{SiO}_4)\text{O}$ (RE = rare earth) which displays two different structure types. Each structure consists of (SiO_4) tetrahedral with extra silicon-bonded oxygens. One structure type is stable for the rare earths with large radius, La to Tb, and forms the monoclinic structure of space group $\text{P2}_1/\text{c}$. The rare earths in this structure occupy two crystallographically different sites. One site has an oxygen coordination number of 7 and the other site has 9 [1]. The other structure type includes the rare earths with smaller radius, Dy to Lu, and has the monoclinic structure of space group $\text{C2}/\text{c}$. The rare earths in this group have 6 or 7 oxygen ligands. As mentioned before (Table 3.2), LSO belongs to the latter group, namely the monoclinic structure $\text{C2}/\text{c}$ [2].

When $\text{RE}_2(\text{SiO}_4)\text{O}$ is doped with Ce, the cerium substitutes for the host rare earth and exists as Ce^{3+} ion. The Ce^{3+} ion has the electron in the 4f shell, which can be excited into the 5d level. The 5d level is split by the crystal field of the host lattice into 3 sublevels, and the 4f ground state is split by the spin-orbit interaction into two levels, with an energy separation of 2253 cm^{-1} [3]. The luminescence of LSO is due to parity-allowed electric dipole transitions from the lowest 5d sublevel to the split 4f ground state. The typical decay time of Ce^{3+} is of the order of tens of nanoseconds.

Under UV-excitation, LSO exhibits two distinct types of excitation and emission spectra. Since there are two crystallographically independent sites in $\text{Lu}_2(\text{SiO}_4)\text{O}$, it is reasonable to assume that there are also two Ce^{3+} sites in $\text{Lu}_2(\text{SiO}_4)\text{O}:\text{Ce}$. A two-activation-centre model has been proposed, in which the two sets of excitation and emission spectra are identified with Ce^{3+} substituted at the two different Lu sites, designated Ce1 and Ce2. It has been demonstrated, that the γ -ray excited emission can be reconstructed from weighted combinations of the Ce1 and Ce2 emission spectra. It has been shown that at low temperatures (77 K) two different decay time constants of the order of tens of nanoseconds (32 ns and 54 ns) exist [4].

A different interpretation of this issue – two types of excitation and emission spectra - was proposed by Naud *et al.* [3]. In this report, they propose an alternative model in which the Ce1 luminescence is due to Ce substituted at either Lu lattice site, and the Ce2 luminescence may be due to interstitial Ce centres. The evidence for the interstitial sites is a disappearance of the doublet structure in the emission spectra at low temperatures and a large variation in the population of the sites as a function of total cerium concentration.

7.1.2 UV-Excitation Spectra

The LSO samples were obtained from CTI (sample 1026, 1050, 1051, 1052, and 1053). Other LSO samples (sample 1121, 1122, and 1123) and $\text{Lu}_{1.95}\text{Y}_{0.05}\text{SiO}_5$ were studied and produced by Photonic Materials (PM). The MLS (mixed lutetium silicate) samples were obtained from UTAR. All samples had a size of $2 \times 2 \times 10 \text{ mm}^3$.

Typical LSO excitation spectra are shown in Figure 7.1. The spectra are normalized to the maximum peak for a better comparison. In the upper two graphs excitation spectra for various LSO samples are shown. The lower graphs present spectra measured for LYSO and MLS crystals. The emission was recorded at a) 420 nm and at b) 500 nm to study the Ce2 site. The Ce2 site leads to emission at 460 nm [4], but at that wavelength

the Ce1 site is still dominant. For that reason we choose 500 nm to record the light mainly emitted by the Ce2 site.

The excitation peaks at 263 nm, 296 nm and 356 nm correspond to the Ce1 site and following [4] lead to emission at 393 nm and 427 nm. The excitation bands at 323 nm and 371 nm are related to the Ce2 site. At room temperature, they can be clearly seen for some LSO, LYSO, and MLS samples. Although Pepin *et al.* [5] also performed their study at room temperature, they observe significantly stronger bands at 325 nm and 375 nm recorded at 500 nm for LSO and LYSO samples compared to our study.

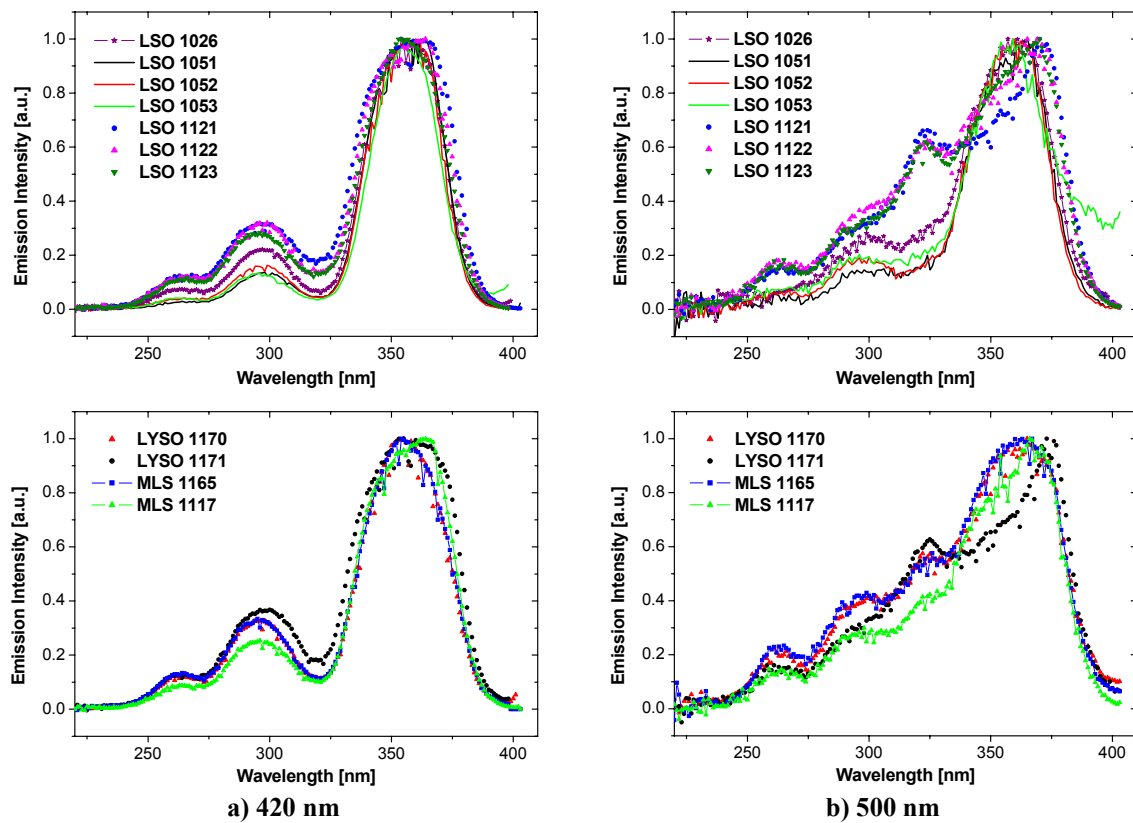


Figure 7.1 UV-excitation spectra measured for selected LSO samples (upper graphs), LYSO and MLS crystals (lower graphs). The emission was recorded at a) 420 nm and b) 500 nm. The spectra are normalized to the maximum for better comparison.

The excitation spectra measured for the same type and batch of crystals exhibit around the same shape (compare crystal 1051-1053 and 1121-1123). When looking at the excitation spectra measured at 420 nm, the LSO CTI samples exhibit less pronounced peaks at 263 nm and 296 nm, and the major bands at around 360 nm are narrower.

Comparing the various studied LSO samples, it appears that the latest LSO samples from CTI show the least intense band at 323 nm, which is related to Ce2 emission. As already reported by Melcher *et al.* [6] the difference from the older (#1026) and newer LSO samples obtained from CTI is due to optimization of the crystal growth conditions leading to a reduction of the Ce2 site in the crystal lattice over the years of development.

Even at 500 nm, the three Ce1 excitation bands are very dominant. More detailed information about the population of these two sites could be obtained by taking excitation spectra at low temperatures as shown by other authors [3, 4]

In Figure 7.2, excitation spectra measured for selected LYSO, MLS and LSO samples are compared. The difference in excitation spectra of the studied crystals does not necessarily seem to be related to the difference in the starting material. Although the LYSO has a small amount of yttrium inside the crystal lattice (2.5%), this does not seem to enhance the population of the Ce2 site.

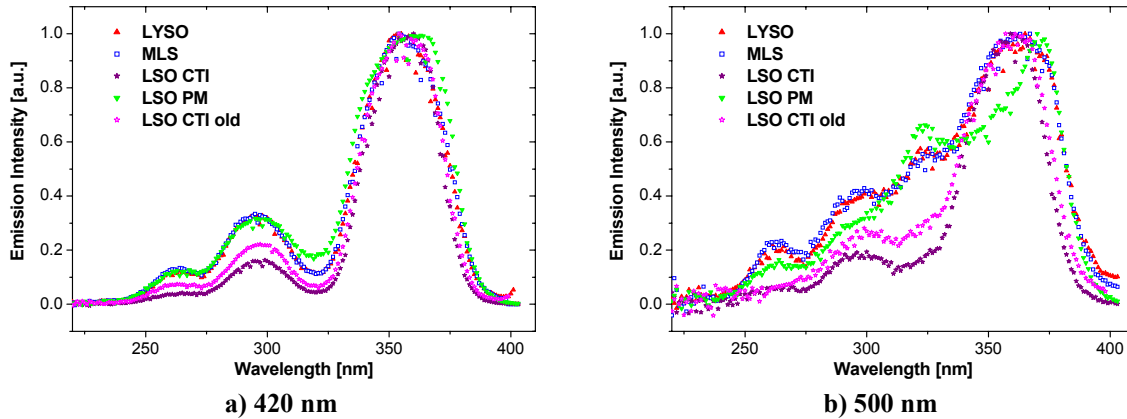


Figure 7.2 UV-excitation spectra measured for selected LYSO, MLS and LSO samples. The emission was recorded at a) 420 nm and b) 500 nm. The spectra are normalized to the maximum for better comparison.

7.1.3 UV induced Emission Spectra

The assumption of the more intense Ce2 site for some samples was also confirmed by the emission spectra measurements.

The measurements of emission spectra were made using excitation wavelengths corresponding to the excitation bands found for the studied crystals. The samples were

excited at wavelengths of 303 nm, 326 nm and 363 nm and the emission was recorded (see Figure 7.3).

One observes that the emission spectra excited with 326 nm, associated with Ce2 emission, are significantly enhanced for the PM LSO, MLS and LYSO samples.

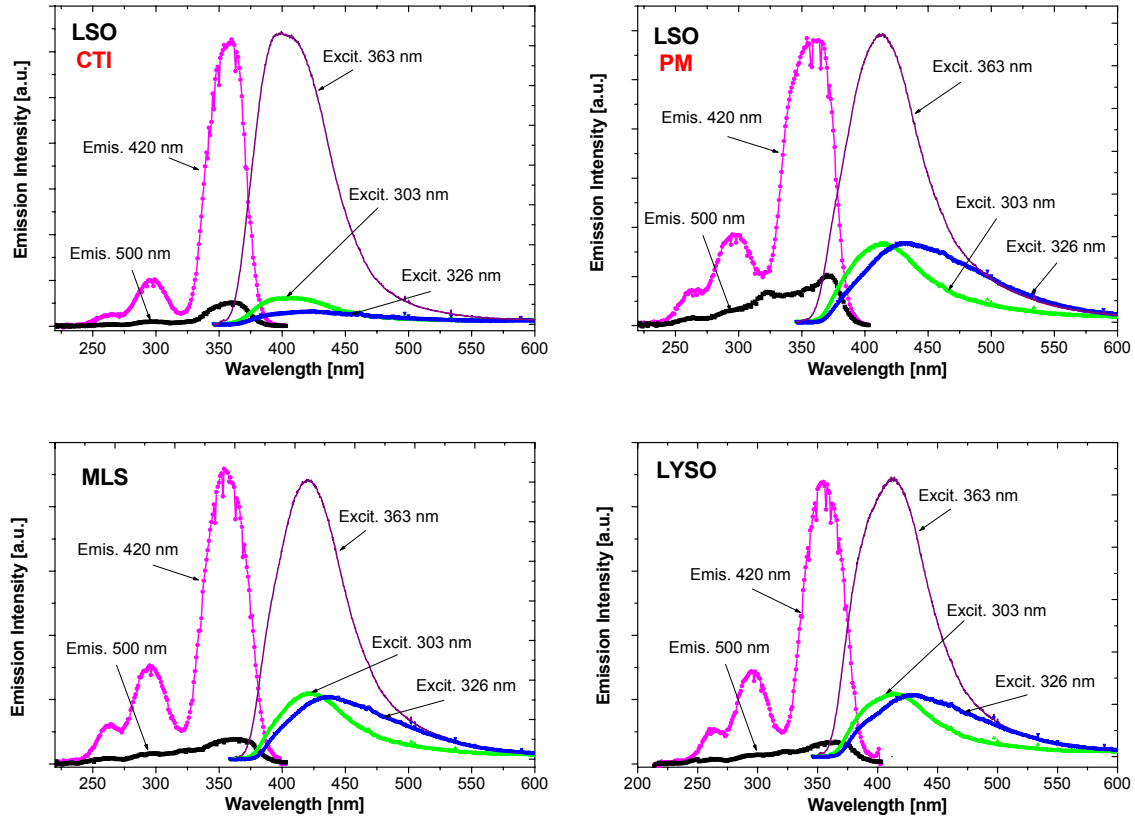


Figure 7.3 UV excited excitation (left curves) and emission spectra (right curves) of LSO (CTI and PM), MLS and $\text{Lu}_{1.95}\text{Y}_{0.05}\text{SiO}_5$ at room temperature. In the excitation spectra the emitted light was measured at 420 nm and 500 nm. The emission spectra were taken by exciting the samples with 303 nm, 326 nm, and 363 nm.

The Ce2 luminescence mode is revealed by comparing the emission spectra for five studied samples (CTI LSO old and new, PM LSO, MLS and LYSO) excited with 326 nm and 363 nm (see Figure 7.4). For the PM LSO, LYSO and MLS crystals the emission spectra are clearly shifted towards higher wavelength. It is a well-known effect that for the perturbed sites the emission spectra are shifted to smaller energies and thus higher wavelengths.

The results of this study are comparable to the curves measured by Pepin *et al.* [5], who measured UV excited emission and excitation spectra for $\text{Lu}_{0.6}\text{Y}_{1.4}\text{SiO}_5\text{:Ce}$ and recent LSO scintillators compared to older LSO samples .

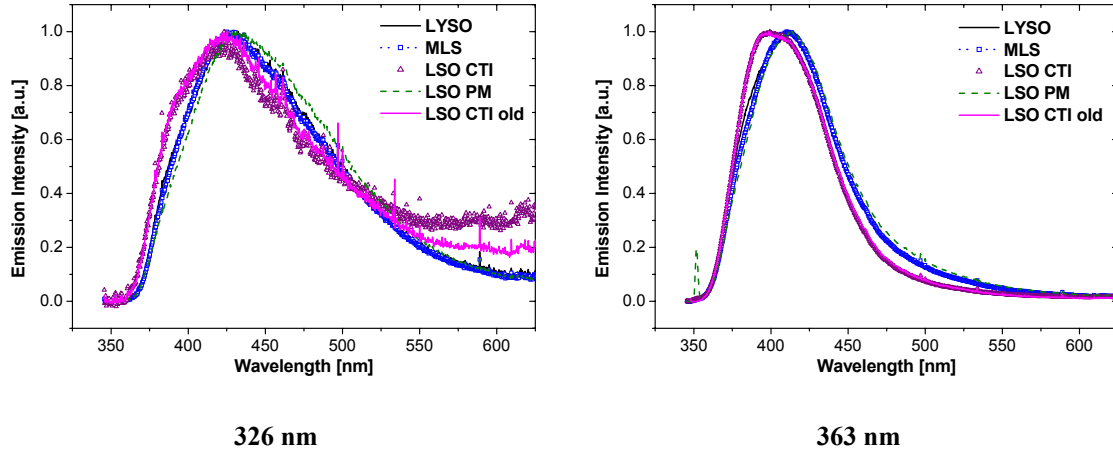


Figure 7.4 UV excited emission spectra for LSO, MLS and LYSO samples. Excitation with 326 nm (left side) and 363 nm (right side).

Although the two studied LSO samples from CTI exhibit a difference in the excitation spectrum, which we related to a more pronounced Ce2 emission, a shift in the emission spectra to higher wavelength was not observed. The normalized emission spectra excited with 326 nm and 363 nm show nearly an identical shape for these two samples.

7.1.4 Absorption Spectra

The absorption bands correspond to transitions from the 4f ground state to the 5d sublevels of Ce^{3+} . The energies of the 5d sublevels, and consequently the wavelengths of the absorption bands, are influenced by the crystal field of the host lattice. As noted earlier, LSO has two rare earth sites, and thus, two cerium luminescence centres, Ce1 and Ce2. The band structure of these two centres cannot be distinguished on the room temperature spectra, although they can be seen at low temperatures [7]. At room temperature, the excitation, absorption and emission spectra are dominated by the Ce1 centre.

As for the LuYAP crystals, emission spectra were taken at the front and the rear end (10 mm crystal length) of the sample. This time, one cannot directly relate the measured emission spectra at the back side of the crystal to the light output measured in vertical

position. This is related to the two cerium sites in the crystal. Light that is absorbed by the crystal can be reemitted at a higher wavelength and is thus not lost.

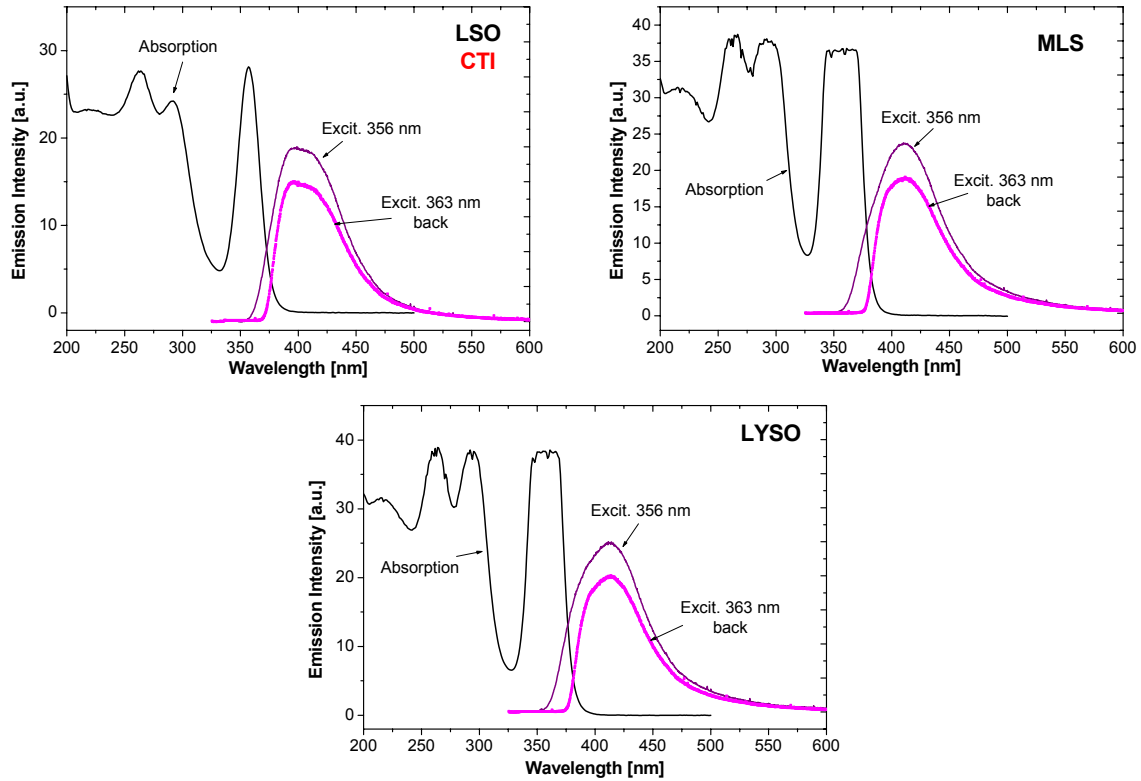


Figure 7.5 Absorption and emission spectra (measured on both sides of the crystal) are presented.

In the absorption spectra, there is one main band located at around 360 nm, which corresponds to the main broad band in the excitation spectra. The bands at 295 nm and 260 nm are also revealed in the excitation spectra.

7.2 Light Output and Energy Resolution

7.2.1 Experimental Procedure

The study included LSO, LYSO and MLS (mixed lutetium silicate) samples. Table 7.1 summarizes the quantity, producer, surface finish and delivery time of all the studied crystals.

Table 7.1 Summary of the cerium doped oxyorthosilicate crystals studied in this work.

Crystal	Quantity	CCC Number	Producer	Surface	Delivery time
Lu ₂ SiO ₅	1	1026	CTI	polished	Sep 2000
Lu ₂ SiO ₅	20	1046 – 1065	CTI	8 polished 8 unpolished 4 damaged	Dec 2000
MLS	3	1115 – 1117	UTAR	Polished	March 2002
Lu ₂ SiO ₅	12	1121 – 1132	Photonic Material Glasgow	6 polished 6 polished on end faces only	May 2002
Lu _{1.7} Y _{0.3} SiO ₅	2	1150 – 1151	Photonic Material	Polished	June 2002
Lu _{1.95} Y _{0.05} SiO ₅	2	1152 – 1153	Photonic Material	Polished	June 2002
Lu _{1.98} Y _{0.02} SiO ₅	1	1154	Photonic Material	Polished	July 2002
Lu _{1.95} Y _{0.05} SiO ₅	2	1156-1157	Photonic Material	Polished	July 2002
Lu _{1.95} Y _{0.05} SiO ₅	2	1159-1160	Photonic Material	Polished	July 2002
MLS	1	1165	UTAR	Polished	Aug 2002
Lu _{1.95} Y _{0.05} SiO ₅	5	1167-1171	Photonic Material	Polished	Sept 2002

The size and the weight of the crystals were determined using a Vernier caliper (Digitcal, TESA, Type 05.30032) and a balance (Mettler Toledo (min 0.1 mg)). The obtained values plus the calculated density can be seen in Appendix B.

Figure 7.6 shows a picture of a MLS, LSO and LuYAP sample at daylight and excited with a xenon lamp attached to a blue filter. The higher brightness of LSO and MLS under UV excitation results from their higher light yield, but also from a smaller sensitivity of the picture to the emission wavelength of the LuYAP crystal.

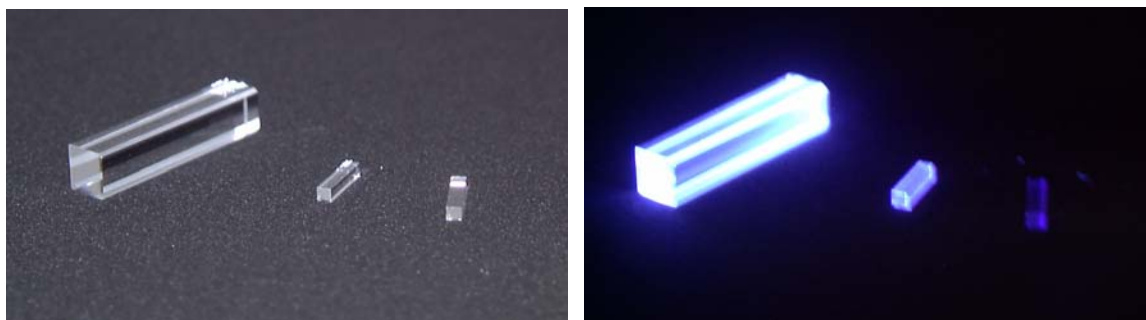


Figure 7.6 Photo of a MLS, LSO and LuYAP sample taken at daylight (left side) and during excitation with light produced by a xenon lamp after passing a blue filter.

The light yield measurement procedure is already described in detail in section 4.2. As before, the crystals were optically coupled with silicon grease (Rhodorsil Silicones pâte

4) to the XP2020Q PMT. Energy spectra were taken with the standard source (Cs-137, 662 keV) as well as with other radioactive sources noted in Table 4.3.

7.2.2 Results for the LSO Crystals from CTI

The histograms of the results in energy resolution and light yield are presented in Figure 7.7. In horizontal position, a mean value of around 30500 ± 1500 photons/MeV and $7.9 \pm 0.4\%$ (FWHM) were found. The values are in the range of 27800 ± 1600 ph/MeV reported by Moszynski *et al.* [8] for a $4 \times 5 \times 14.5$ mm³ sample. The measured energy resolution for the ¹³⁷Cs source (662 keV) is comparable to the 7.9% measured by Melcher *et al.* [1]. In vertical position a light yield of 21000 ± 1060 ph/MeV and an energy resolution of $12.6 \pm 0.6\%$ were measured.

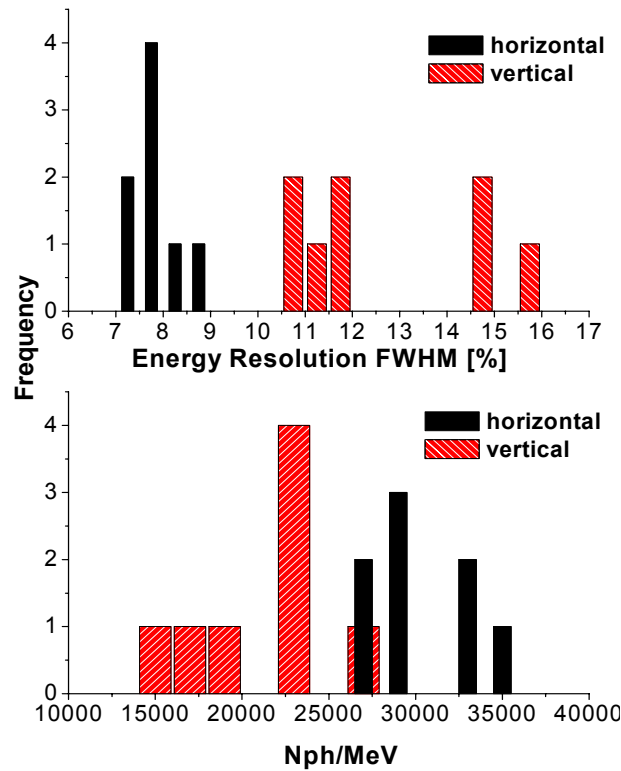


Figure 7.7 Energy resolution and light yield histogram of the LSO samples. The crystals were studied in vertical (red bars) and in horizontal position (black bars) using a Cs-137 source.

From the measured number of photoelectrons and energy resolution, the intrinsic energy resolution was calculated. As already mentioned in section 5.4, the energy resolution for the LSO samples is mainly affected by the intrinsic energy resolution (see Figure

5.20 b). The values for the energy resolution, Npe and the calculated intrinsic resolution are given in Table 7.2.

Table 7.2 Number of photoelectrons, energy resolution and intrinsic resolution for 662 keV photons from a Cs-137 source measured with several LSO crystals.

Crystal	Energy resolution	Npe	Intrinsic resolution
LSO 1046	$7.7 \pm 0.4\%$	4370 ± 130	$6.8 \pm 0.4\%$
LSO 1047	$8.6 \pm 0.4\%$	4050 ± 120	$7.6 \pm 0.5\%$
LSO 1048	$7.3 \pm 0.4\%$	3920 ± 120	$6.2 \pm 0.4\%$
LSO 1049	$7.3 \pm 0.4\%$	4200 ± 130	$6.3 \pm 0.4\%$
LSO 1050	$7.9 \pm 0.4\%$	5210 ± 160	$7.2 \pm 0.4\%$
LSO 1051	$7.9 \pm 0.4\%$	4280 ± 130	$6.9 \pm 0.5\%$
LSO 1052	$7.9 \pm 0.4\%$	4690 ± 140	$7.1 \pm 0.5\%$
LSO 1053	$8.5 \pm 0.4\%$	4830 ± 150	$7.9 \pm 0.5\%$

This is in agreement with the scintillator resolution presented by Dorenbos *et al.* [9] of $6.6 \pm 0.4\%$ measured with a R878 photomultiplier.

One of the reasons for this rather poor energy resolution is the non-proportionality of the light output on the energy of the incident γ -ray, as already discussed in section 5.4 (see Figure 5.19). Another factor is the presence of the two Ce sites in the crystal lattice.

Energy spectra for γ -rays from a ^{22}Na and a ^{60}Co source taken with a LSO sample in horizontal position are shown in Figure 7.8. The ADC energy calibration was done with the position of the photopeak measured with the Cs-137 source.

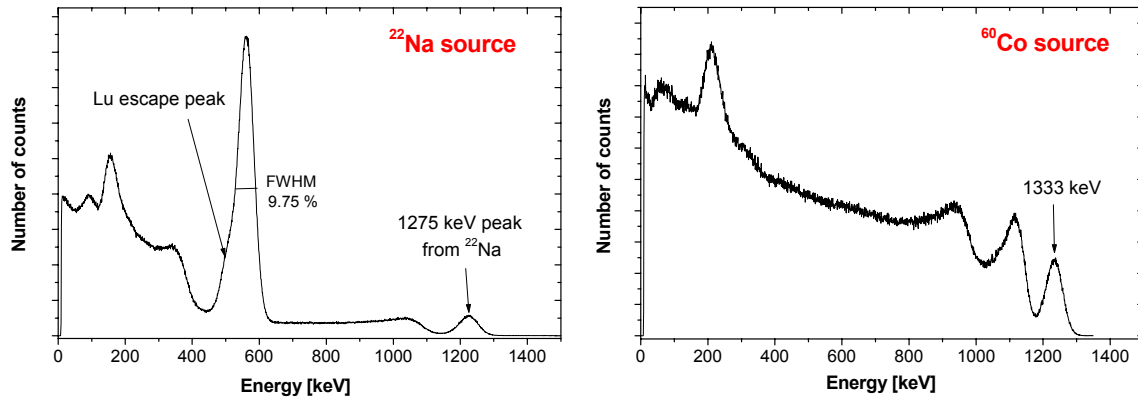


Figure 7.8 Energy spectrum of γ -rays from a ^{22}Na source (left spectrum) and a ^{60}Co source (right spectrum) measured with a selected LSO CTI crystal.

The non-linearity of the light yield on γ -energy can even be observed in the energy spectra shown above. The photopeaks are not exactly at 511 keV and 1275 keV, but at higher or lower energies, respectively. When the position of the photopeak is at a lower energy than expected, as for Co-60, this means that the light yield is lower than the one measured with Cs-137.

7.2.3 Results for the LSO PM Samples

The energy resolution, number of photoelectrons and light yield of the studied LSO samples is given in Table 7.3. For calculating the light yield, the convoluted quantum efficiency of $QE = 22\%$ was used (see Table 4.1). The crystals were measured in vertical and horizontal position. Energy spectra taken in these two positions are presented in Figure 7.9.

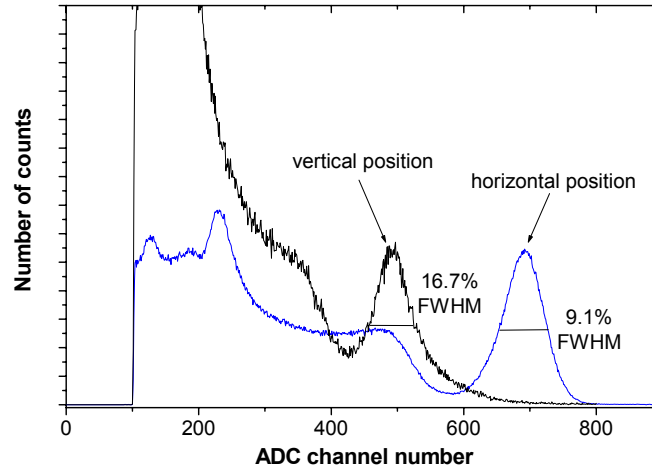


Figure 7.9 Pulse height spectra obtained with a Cs-137 source for a selected LSO (PM) crystal. The crystal was measured in horizontal and in vertical position.

The mean light yield of the studied crystals is 27680 ± 1380 ph/MeV and is comparable to the results for the CTI LSO samples. In horizontal position, a mean energy resolution of around $9.4 \pm 0.5\%$ (FWHM) for the Cs-137 source was found.

In vertical geometry an energy resolution of $16.1 \pm 0.8\%$ and a light yield of 22160 ± 1110 ph/MeV was found. The ratio between the light yield measured in vertical and in horizontal position is 79.6%.

Table 7.3 Number of photoelectrons, energy resolution and light yield (Nph/MeV) for 662 keV photons from a Cs-137 source measured with several LSO crystals in vertical and horizontal position.

Crystal	Energy resol	Vertical		Energy resol	Horizontal		ratio
		Npe/MeV	Nph/MeV		Npe/MeV	Nph/MeV	
LSO 1121	16.7 ± 0.8%	4780 ± 140	20000 ± 1000	9.1 ± 0.5%	6230 ± 190	28300 ± 1420	76.8%
LSO 1122	16.3 ± 0.8%	5010 ± 150	22780 ± 1140	10.4 ± 0.5%	6410 ± 190	29150 ± 1460	78.2%
LSO 1123	15.2 ± 0.8%	5250 ± 160	22900 ± 1150	9.5 ± 0.5%	6340 ± 190	28820 ± 1440	82.7%
LSO 1124	16.3 ± 0.8%	5050 ± 150	22960 ± 1150	8.8 ± 0.4%	6250 ± 190	28420 ± 1420	80.8%
LSO 1125				9.9 ± 0.5%	5810 ± 170	26430 ± 1320	
LSO 1126				9.1 ± 0.5%	5490 ± 170	24980 ± 1250	
Average	16.1 ± 0.8%	5020 ± 150	22160 ± 1110	9.4 ± 0.5%	6090 ± 180	27680 ± 1380	79.6%

From the measured energy resolution and the number of photoelectrons the intrinsic energy resolution was calculated. The results are shown in Table 7.4.

Table 7.4 Number of photoelectrons, energy resolution and intrinsic resolution for 662 keV photons from a Cs-137 source measured with several LSO (PM) crystals.

Crystal	Energy resolution	Npe	Intrinsic resolution
LSO 1121	9.1 ± 0.5%	4120 ± 120	8.2 ± 0.5%
LSO 1122	10.4 ± 0.5%	4250 ± 130	9.6 ± 0.6%
LSO 1123	9.5 ± 0.5%	4200 ± 130	8.7 ± 0.5%
LSO 1124	8.8 ± 0.4%	4140 ± 120	7.9 ± 0.5%
LSO 1125	9.9 ± 0.5%	3850 ± 120	9.0 ± 0.5%
LSO 1126	9.1 ± 0.5%	3640 ± 110	8.1 ± 0.5%

For these crystals, the mean intrinsic energy resolution is around 8.6%.

7.2.4 Results for the LYSO and MLS Samples

Several LYSO crystals with varying yttrium content were studied. A summary of the results in energy resolution and light yield is given in Table 7.5 and Table 7.6.

Table 7.5 Energy resolution and light yield measured with several LYSO samples with different yttrium concentration in horizontal position.

Crystal	Y content	Energy resolution	Npe/MeV	Nph/MeV
LYSO 1150	15%	19.4 ± 1%	980 ± 50	4440 ± 220
LYSO 1152	2.5%	16.0 ± 0.8%	1780 ± 90	8090 ± 400
LYSO 1153	2.5%	15.9 ± 0.8%	1540 ± 80	7010 ± 350
LYSO 1154	1%	17.7 ± 0.9%	1950 ± 100	8880 ± 440
LYSO 1156	2.5%	24.5 ± 1.2%	740 ± 40	3350 ± 170
LYSO 1157	2.5%	24.5 ± 1.2%	670 ± 30	3060 ± 150
LYSO 1159	2.5%	17.2 ± 0.9%	4070 ± 200	18490 ± 920
LYSO 1160	2.5%	14.9 ± 0.8%	3890 ± 200	17680 ± 880

Table 7.6 Energy resolution and light yield measured with several LYSO (2.5% Y) samples in horizontal position and vertical position.

Crystal	Energy resol	Vertical		Energy resol	Horizontal		ratio
		Npe/MeV	Nph/MeV		Npe/MeV	Nph/MeV	
LYSO 1167	$14.2 \pm 0.7\%$	4520 ± 140	20550 ± 1030	$13.0 \pm 0.7\%$	6180 ± 190	28090 ± 1400	73.2%
LYSO 1168	$15.4 \pm 0.8\%$	3830 ± 120	17410 ± 870	$10.7 \pm 0.5\%$	6060 ± 180	27520 ± 1380	63.3%
LYSO 1169	$15.7 \pm 0.8\%$	4290 ± 130	19510 ± 980	$9.9 \pm 0.5\%$	6090 ± 180	27690 ± 1390	70.4%
LYSO 1170	$16.5 \pm 0.8\%$	3850 ± 120	17500 ± 880	$10.7 \pm 0.5\%$	5870 ± 180	26690 ± 1330	65.5%
LYSO 1171				$10.6 \pm 0.5\%$	6180 ± 190	28070 ± 1400	
Average	$15.4 \pm 0.8\%$	4120 ± 120	18740 ± 940	$11.0 \pm 0.6\%$	6080 ± 180	27610 ± 1380	68.1%

The rather low light yield and energy resolution of the first sets of crystals can be explained by problems that occurred during the growing procedure such as for example oxygen leaks. We also observed a very strong afterglow for most of these crystals that was even visible by eye.

The later batch of LYSO:Ce crystals (2.5% Y) showed an improvement in light yield and energy resolution. The light yield and energy resolution derived from the pulse height spectra are given in Table 7.6.

The derived values are similar to the light output and energy resolution determined for the LSO crystals. The low percentage of yttrium in the mixed samples does not seem to change the scintillation properties compared to LSO.

The MLS samples (1115 – 1117) were obtained from UTAR and had a size of $6 \times 6 \times 30 \text{ mm}^3$ at the time of delivery. To compare them with the other studied oxyorthosilicates, one crystal (#1117) was cut in little pixels with dimension of $2 \times 2 \times 10 \text{ mm}^3$.

The results in energy resolution and light yield obtained with these crystals are given in Table 7.7.

Table 7.7 Energy resolution and light yield measured with several MLS samples in horizontal position. The crystals number 1115 – 1117 have a size of $6 \times 6 \times 30 \text{ mm}^3$ whereas the crystals number 1117a, 1117c and 1165 have a size of $2 \times 2 \times 10 \text{ mm}^3$.

Crystal	Energy resolution	Npe/MeV	Nph/MeV
MLS 1115	$10.9 \pm 0.6\%$	4870 ± 150	22160 ± 1110
MLS 1116	$12.5 \pm 0.6\%$	5220 ± 160	23710 ± 1190
MLS 1117	$11.4 \pm 0.6\%$	4470 ± 130	20300 ± 1020
MLS 1117a	$9.8 \pm 0.5\%$	6650 ± 200	30230 ± 1510
MLS 1117c	$9.6 \pm 0.5\%$	6460 ± 190	29370 ± 1470
MLS 1165	$8.8 \pm 0.4\%$	7850 ± 390	35670 ± 1780

The lower light yield values found for the MLS 1115 to 1117 samples is due to the larger size of the crystals and thus the increased absorption.

The results in light yield and energy resolution are comparable to the previously studied LSO and LYSO samples.

7.3 Scintillation Pulse Shape

The decay time was measured by using the single photon counting technique as described in section 4.4. The decay times were obtained by fitting the measured curve with a double exponential. Two components with around 24 ns (for LSO and LYSO) and ~ 45 ns were found. These values are very close to the decay times measured by direct UV-excitation of the two cerium centres by Suzuki *et al.* [7]. He reported that the decay time of Ce1 was 34 ns and that of Ce2 was 42 ns.

No additional slow component was found from the fit.

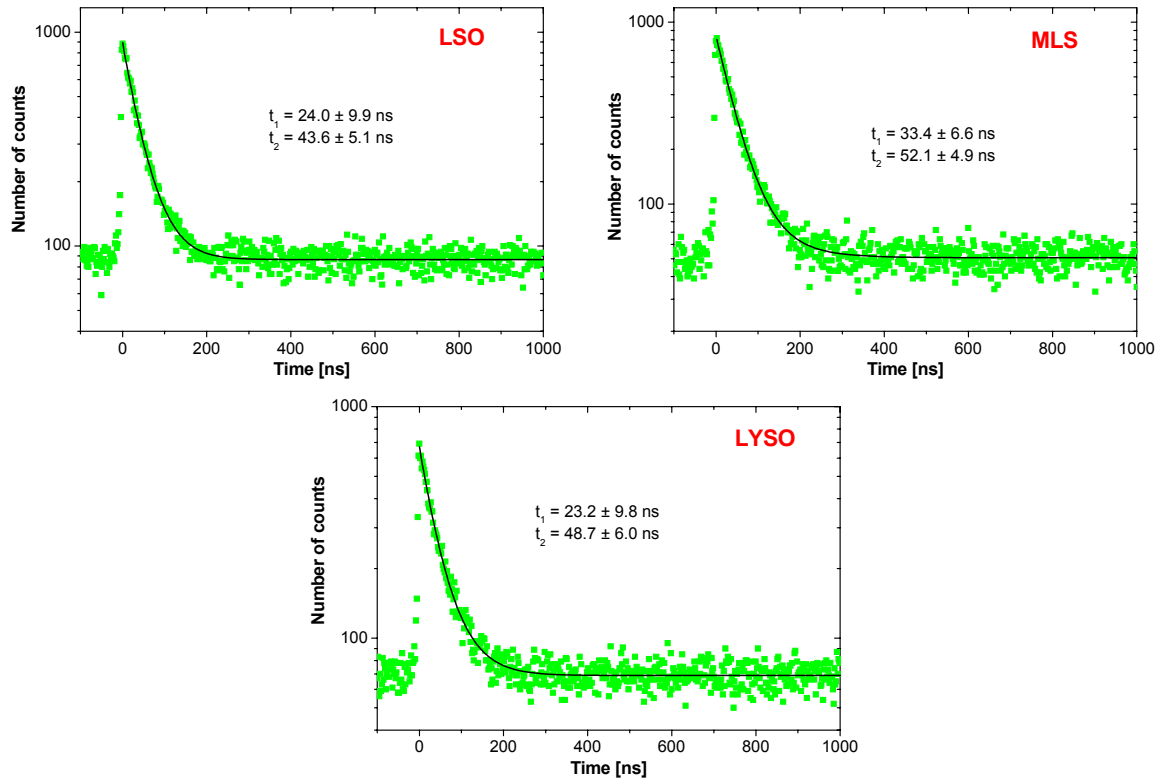


Figure 7.10 The gamma-ray excited decay curve of LSO, MLS and LYSO at room temperature determined with a single photon counting technique. ^{22}Na was used as the source and the TAC range was 2000 ns.

With a single exponential fit, decay times of 38.5 ± 2.2 ns, 45.2 ± 2.7 ns and 42.0 ± 2.7 ns for LSO, MLS and LYSO, respectively were calculated.

The slower decay time for MLS with the single exponential fit was also found with the two exponentials fit.

The low amount of yttrium in the LYSO sample (only 2.5%) does not seem to have a significant influence on the scintillation properties. This might change by increasing the amount of yttrium in the sample. A decay time of 53 ns for a $\text{Lu}_{0.6}\text{Y}_{1.4}\text{SiO}_5\text{:Ce}$ sample was reported [5].

A summary of the measured scintillation light pulse shape of all the studied samples is given in Table 7.8 and Table 7.9.

Table 7.8 Decay time constant of the light pulse shape from LSO samples doped with cerium measured at CERN. The TAC range was set to 2000 ns. The samples were obtained from CTI and from Photonic Materials.

Crystal	τ [ns]	Crystal	τ [ns]
LSO 1046	37.8 ± 2.1	LSO 1121	43.4 ± 2.5
LSO 1047	38.7 ± 2.2	LSO 1122	43.6 ± 2.5
LSO 1048	38.9 ± 2.2	LSO 1123	43.9 ± 2.5
LSO 1049	38.7 ± 2.2	LSO 1124	42.9 ± 2.5
LSO 1050	38.3 ± 2.1	LSO 1125	43.0 ± 2.5
LSO 1051	39.0 ± 2.3	LSO 1226	43.5 ± 2.6
LSO 1052	38.4 ± 2.2		

Table 7.9 Decay time constant of the light pulse shape from LYSO samples with different yttrium concentration and MLS samples doped with cerium measured at CERN. The TAC range was set to 2000 ns. The LYSO samples were produced by Photonic Materials and the MLS samples were obtained from UTAR.

Crystal	Y conc.	τ [ns]	Crystal	τ [ns]
LYSO 1150	15%	35.7 ± 2.5	MLS 1115	43.5 ± 2.7
LYSO 1151	15%	34.4 ± 2.4	MLS 1116	43.4 ± 2.7
LYSO 1152	2.5%	36.5 ± 2.5	MLS 1117	43.5 ± 2.6
LYSO 1153	2.5%	36.1 ± 2.3	MLS 1165	45.2 ± 2.7
LYSO 1154	1%	36.9 ± 2.4		
LYSO 1156	2.5%	35.3 ± 2.9		
LYSO 1159	2.5%	39.5 ± 2.3		
LYSO 1168	2.5%	41.4 ± 2.7		
LYSO 1169	2.5%	42.5 ± 2.8		
LYSO 1170	2.5%	41.5 ± 2.7		
LYSO 1171	2.5%	42.7 ± 2.5		

7.4 Low Temperature TL

7.4.1 Thermoluminescence Spectra LSO

The ltTL spectrum for the LSO sample showed no thermoluminescence in the temperature region from 10 to 300 K, as presented in Figure 7.11. This is in agreement with measurements reported by Lempicki *et al.* [10] for LSO-high, who observed only one peak at 334 K.

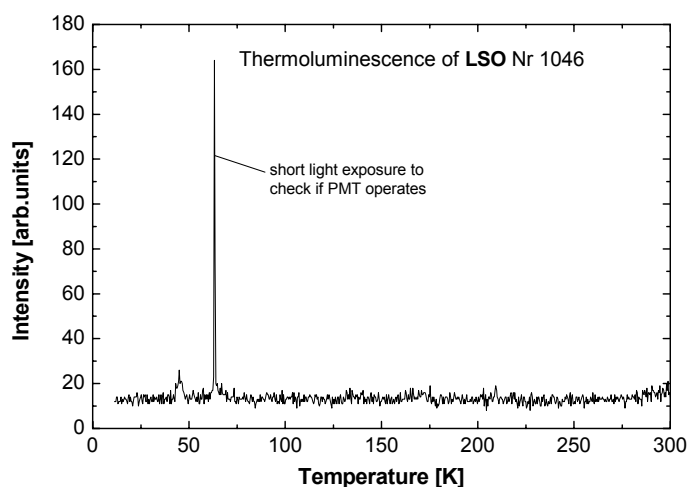


Figure 7.11 Low temperature TL glow curves of LSO. The heating rate β is 0.151 K/s.

7.5 Discussion and Conclusion

For the last batch of studied LYSO samples, a light yield of 27600 ph/MeV and a decay time of 42 ns were observed. No additional slow decay component was found.

In this study it has been demonstrated, that LYSO could be another promising candidate in comparison to the LSO scintillator. Due to the low amount of yttrium in the melt (only 2.5%), the density is not negatively impaired, while the desired scintillation properties are conserved.

The existence of two emission centres in cerium-doped rare-earth oxyorthosilicates has been demonstrated, and it has been postulated that the presence of these two luminescence processes may have consequences for the energy resolution performance of the scintillators [5]. There is evidence that the two centres are present, with variable

efficiency, in all the scintillators investigated in this study. The major emission centred at 420 nm is due to the activation of Ce1 luminescence, whereas the emission band observed at around 440 nm is related to the activation of Ce2 centres. This latter process tends to shift the corresponding emission to higher wavelength.

As already reported by Melcher *et al.* [11], the population of these two Ce sites also influences the decay time. The crystals with faster decay times are apparently dominated by the Ce1 emission (32 ns) and have very little contribution from Ce2 (55 ns). A correlation between the measured decay times of the tested samples and the relative intensity of the excitation band at 323 nm (Ce2 band) is illustrated in Figure 7.12. Moving from lower left to upper right in the plot, the crystals apparently have increasing contributions from Ce2 centres. Note that the emission is never due to Ce2 alone, since such crystals would have 55 ns decay times.

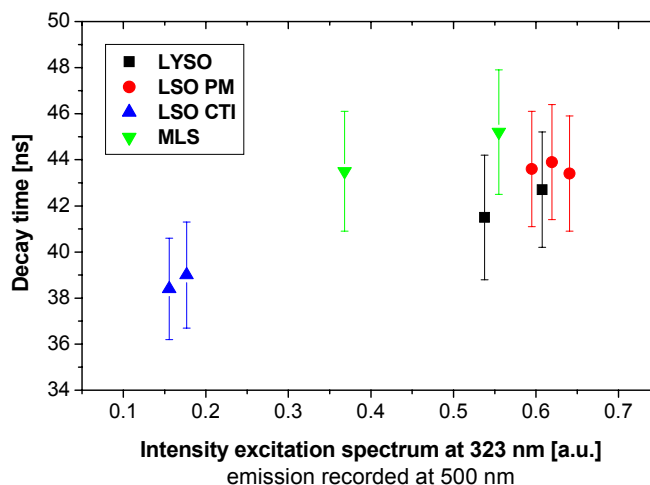


Figure 7.12 Decay time versus the relative intensity of the 323 nm excitation band related to the Ce2 centers. The emission was recorded at 500 nm.

It is still unclear how far the addition of yttrium into the melt influences the presence and intensity of the Ce1 and Ce2 site. It would be premature to conclude that the presence of impurities in the lutetium oxyorthosilicate crystal lattice, as for the mixed lutetium silicates or the LYSO crystals, increases the amount of Ce2 sites. It has been shown in this study that the older LSO sample exhibits about the same optical properties as the MLS and LYSO samples. An improvement in decrease of the perturbed site for the CTI LSO crystals was achieved by the company, due to the optimization of the crystal growth condition over the last ten years of research and development.

It was reported by Melcher *et al.* [6] that the changing growth conditions during the course of a crystal growth run may influence the relative contributions from the Ce1 and Ce2 centres both in light output and in decay time.

It already has been shown in chapter 5, that in spite of the high light output, the LSO scintillator exhibits a rather poor energy resolution. This is related to the non-proportional response from the light yield on photon energy. Starting at 662 keV, the response curve of LSO decreases to almost 55% when lowering the γ -ray energy to 31 keV. Another factor influencing the energy resolution are local variations in the scintillation efficiency, due to a non-uniform distribution of activator ions, crystal defects or flaws. Therefore, the presence of two cerium luminescence processes might have an influence on energy resolution. As shown by the measurements, the CTI LSO samples reveal the best energy resolution measured of all the studied oxyorthosilicate crystals and the lowest intensity of Ce2 luminescence. In Figure 7.13, the calculated intrinsic energy resolution is plotted versus the relative intensity of the excitation band at 323 nm (recorded at 500 nm and related to the Ce2 site). As presented in the graph, a correlation between the intensity of the excitation band, and thus the population of the Ce2 site, and the intrinsic energy resolution can be seen.

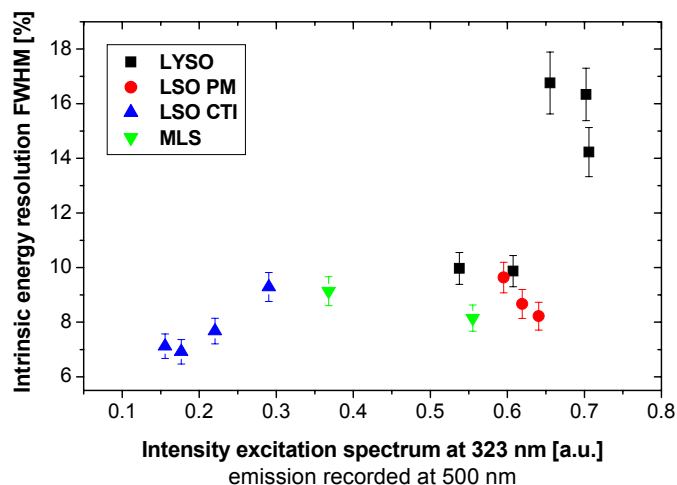


Figure 7.13 Correlation between the calculated intrinsic energy resolution and the excitation band at 323 nm. The emission was recorded at 500 nm.

As shown by [6], significant progress has been made in the crystal growth process for LSO and in the consistency of the scintillation properties of the resulting crystals. Advances in crystal growth technology allowed better control of the relative populations of the two Ce luminescence centres and of the quenching effect of defects and led to more consistent scintillation properties in LSO crystals.

7.6 References

- [1] C. L. Melcher, J. S. Schweitzer, C. A. Peterson, R. A. Manente, H. Suzuki, *Crystal Growth and Scintillation Properties of the Rare Earth Oxyorthosilicates*, Proc. Int. Conf on Inorganic Scintillators, SCINT95, 1996, Delft University Press.
- [2] C. L. Melcher, J. S. Schweitzer, *Cerium-doped Lutetium Oxyorthosilicate: A Fast, Efficient New Scintillator*, IEEE Trans. Nucl. Sci. 39 (1992) 502-505.
- [3] J. D. Naud, T. A. Tombrello, C. L. Melcher, J. S. Schweitzer, *The Role of Cerium Sites in the Scintillation Mechanism of LSO*, IEEE Trans. Nucl. Sci. 43 (1996) 1324-1328.
- [4] H. Suzuki, T. A. Tombrello, C. L. Melcher, J. S. Schweitzer, *Light Emission Mechanism of $\text{Lu}_2(\text{SiO}_4)\text{O}:\text{Ce}$* , IEEE Trans. Nucl. Sci. 40 (1993) 380-383.
- [5] C. M. Pepin, A. L. Perrot, P. Berard, C. Pepin, D. Houde, R. Lecomte, C. L. Melcher, H. Dautet, *Investigation of the Properties of New Scintillator LYSO and Recent LSO Scintillators for Phoswich PET Detectors*, Proc. IEEE Nuclear Science Symposium and Medical Imaging Conference (2002), Norfolk, Virginia.
- [6] C. L. Melcher, M. A. Spurrier, L. Eriksson, M. Eriksson, M. Schmand, G. Givens, R. Nutt, *Advances in the Scintillation Performance of $\text{LSO}:\text{Ce}$ Single Crystals*, Proc. IEEE Nuclear Science Symposium and Medical Imaging Conference (2002), Norfolk, Virginia.
- [7] H. Suzuki, T. A. Tombrello, C. L. Melcher, J. S. Schweitzer, *UV and gamma-ray excited luminescence of cerium-doped rare-earth oxyorthosilicates*, Nucl. Instr. and Meth. A 320 (1992) 263-272.
- [8] M. Moszynski, M. Kapusta, M. Mayhugh, D. Wolski, S. O. Flyckt, *Absolute Light Output of Scintillators*, IEEE Trans. Nucl. Sci. 44 (1997) 1052-1061.
- [9] P. Dorenbos, J. T. M. de Haas, C. W. E. van Eijk, *Non-Proportionality in the Scintillation Response and the Energy Resolution Obtainable with Scintillation Crystals*, IEEE Trans. Nucl. Sci. 42 (1995) 2190-2202.
- [10] A. Lempicki, J. Glodo, *Ce-doped scintillators: LSO and LuAP*, Nucl. Instr. and Meth. A 416 (1998) 333-344.
- [11] C. L. Melcher, M. Schmand, M. Eriksson, L. Eriksson, M. Casey, T. Nutt, *Scintillation Properties of $\text{LSO}:\text{Ce}$ Boules*, IEEE Trans. Nucl. Sci. 47 (2000) 965-968.

Chapter 8

Detector Design and Electronics

Within the Crystal Clear Collaboration, four centres are developing 2nd generation small animal PET scanners with high resolution and high sensitivity, for different medical applications and for various kinds of animals (mice, rats, primates). Due to these individual applications, which range from the study of the transgenesis and oncology to neurology, the different designs vary in the field of view (FOV) caused by different detector configurations. In this chapter the results of the simulation working-group are described as well as the detector design of the ClearPET prototype. In the last section the electronic read-out system developed by the Zentrallabor für Elektronik (Forschungszentrum Jülich) is reproduced.

8.1 Simulation

For the development of the scanners the simulation of the single detector module up to the whole scanner is of special importance. The aim of the simulation group was to optimize sensitivity and spatial resolution of the preliminary PMT-based ClearPET prototypes. For this purpose the simulation tools GEANT3, GEANT4 (CERN, Geneva, Switzerland) and SORTEO were used.

In this work, we will only reproduce the results obtained with GEANT3 and provided by U. Heinrichs (Forschungszentrum Jülich, Germany) [1].

8.1.1 Assumption for the Monte Carlo Simulation

All mentioned simulations represent the ideal case. The different scanner designs are only composed of the crystal matrices including the reflector material. The initial condition for the simulation were given by the following points:

- *Scanner geometry*: multi-ring or multi-head design.
- *Crystal matrices*: 8 x 8 LSO and LuAP crystals arranged in phoswich geometry with a cross-section of 2 x 2 mm² and variable length (8 or 10 mm).
- *Reflector material*: assumed to be SiO₂ which has similar reflective properties as Tyvek® paper.
- *Positron Source*: ideal β^+ source, no momentum.
- *Environment*: air, no magnetic field.
- *Interactions*: all possible interactions down to 10 keV.

The information about the energy deposition and the crystal identification are stored in a list mode file. Timing information and light transmission are not provided by GEANT3.

8.1.2 Multi-Ring versus Multi-Head Design

The important factors for the design of the ClearPET prototype using photomultiplier tubes were the axial sensitivity profile and the sensitivity in the centre of the field of view (CFOV). For the PrimatePET version constructed in the Forschungszentrum Jülich, a field of view (FOV) of 12 cm diameter was required. This led to two possible designs: an octahedron or a ring both with 24 cassettes, as shown in Figure 8.1.

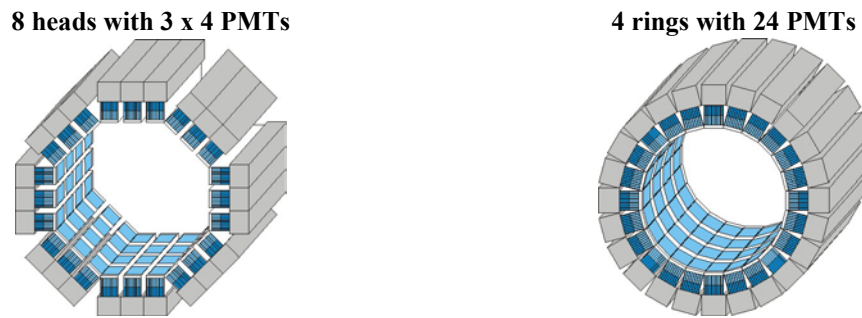


Figure 8.1 Detector design with 24 detector cassettes. Multi-head design of multi-ring design (pictures reproduced from U. Heinrichs with permission).

The results of the simulation showed that a multi-ring design is favourable in terms of sensitivity. The CFOV sensitivity increased from 2.9% for the octahedron to 3.7% for the ring design. Due to this increase of 25%, in spite of the same number of PMTs, it was decided to build the PrimatePET as a multi-ring system.

Another problem that was solved by the simulations was the nonlinear axial sensitivity profile caused by the 10 mm axial gap between the crystal matrices. By shifting the detector cassettes in axial direction the axial sensitivity profile can be improved

essentially. It was found that shifting every other detector cassette by $\frac{1}{4}$ of the PMTs centre-to-centre length in axial direction seems to be the optimum. Figure 8.2 shows the improvement of the axial sensitivity profile for the 4 x 20 PMT ring design with and without shifting and Figure 8.3 illustrates the shifting of the detector cassettes.

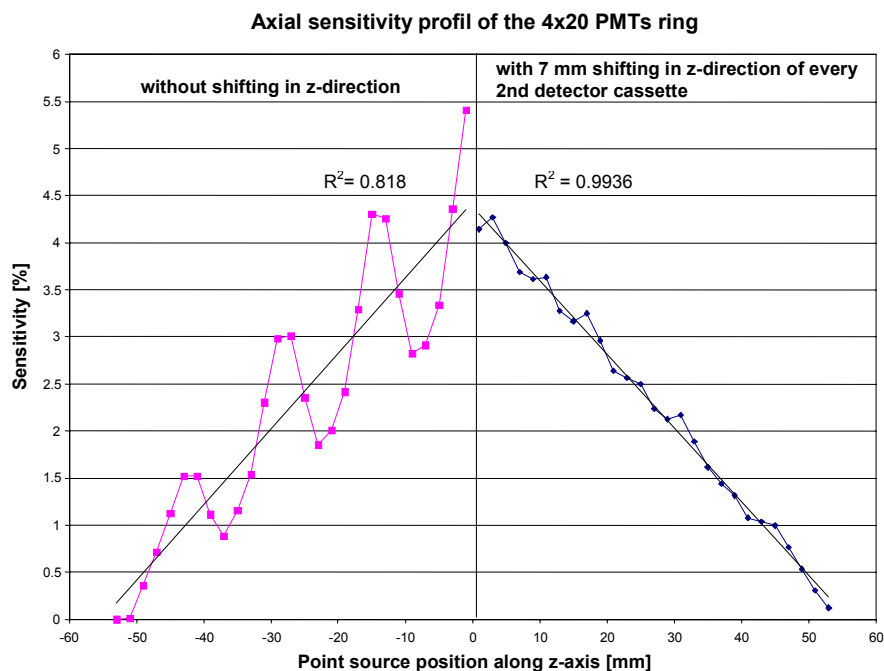


Figure 8.2 Axial sensitivity profile of the non-shifted 4 x 20 PMT ClearPET ring design using an energy threshold of 350 keV. The left side indicates the high fluctuations caused by the axial gaps whereas in the right graph the profile is smoothened due to the 7 mm shift of every 2nd detector cassette (pictures reproduced from U. Heinrichs).

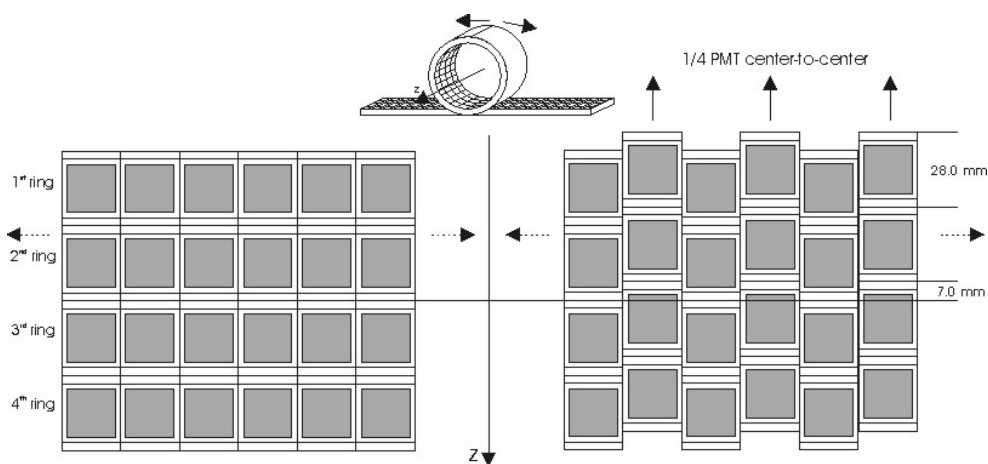


Figure 8.3 Simple drawing of the arrangement of the PMT modules. Each module contains 4 PMTs and the modules are shifted by $\frac{1}{4}$ of the PMT lengths with respect to each other (pictures reproduced from [1]).

Among several single ring designs, the Crystal Clear Collaboration favours two four-ring ClearPET systems. One with 20 PMTs and crystals length of 10 mm LSO plus 10 mm LuYAP and flexible detector diameter for primates (PrimatePET in Jülich) and one with 16 PMTs and crystals length of 8 mm LSO plus 8 mm LuYAP for studies on rats and mice (Brussels).

The 20 PMT design for primates is a compromise between the increase of the peak system sensitivity from 3.0% to 4.2% at the CFOV with a threshold of 350 keV, and the reduction of the FOV diameter from 12 cm to 10 cm compared to the originally planed 24 PMT design. For larger objects the detector diameter can be enlarged from 130 mm to 300 mm. In the case of 12 cm FOV, the peak system sensitivity is still 2.7%.

The sensitivity for a point source placed in the centre of the field of view is given in Table 8.1.

Table 8.1 Sensitivity of a point source placed in the centre of the field of view (values reproduced from [1]).

	Energy threshold		
	0 keV	250 keV	350 keV
16 PMTs (8 + 8 mm crystal length)	9.8%	4.8%	3.8%
20 PMTs (10 + 10 mm crystal length)	10.0%	5.2%	4.2%

More detailed information on the outcome of the simulations can be found in the work by U. Heinrichs [2].

8.2 General Design ClearPET

In this section, the general design of the ClearPET machines is described. As already mentioned before, there are different designs built in the collaboration varying in the number of photomultipliers and length of crystals used.

8.2.1 Construction of a Detector Module

The construction of the detector modules is mainly done in Brussels. There, they have developed a procedure to build the detector matrices and to assemble the crystal matrices with the PMTs [3].

The first step is the construction of a Tyvek matrix (see Figure 8.4), which acts both as reflector and holder for the crystals. Pieces of Tyvek paper are cut and assembled to a

matrix. Then the matrix is inserted into a plastic cap, which should protect the matrix from humidity and damage. Afterwards, the LSO and the LuYAP crystals are inserted with no optical contact in between. A light-shielding mask, developed in Jülich, is glued on the multianode PMT to correct for variation in the sensitivity of the 64 channels. The final step is the gluing of the crystal holder onto the multianode photomultiplier. A computer controlled positioning system assures the accurate assembly. Pictures of the construction of the Tyvek matrix, the PMT and the plastic cap are shown below.

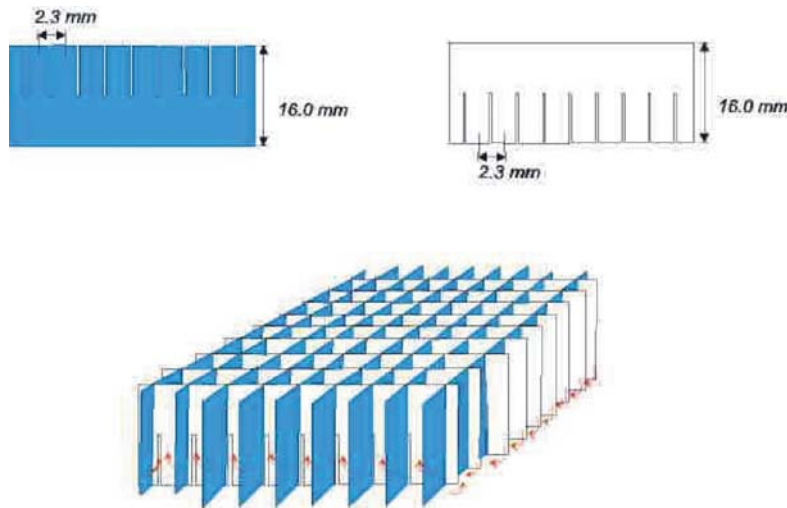


Figure 8.4 Sketch of the construction of a Tyvek matrix. The paper is cut in and assembled by using a brass mold (reproduced from S. Léonard).

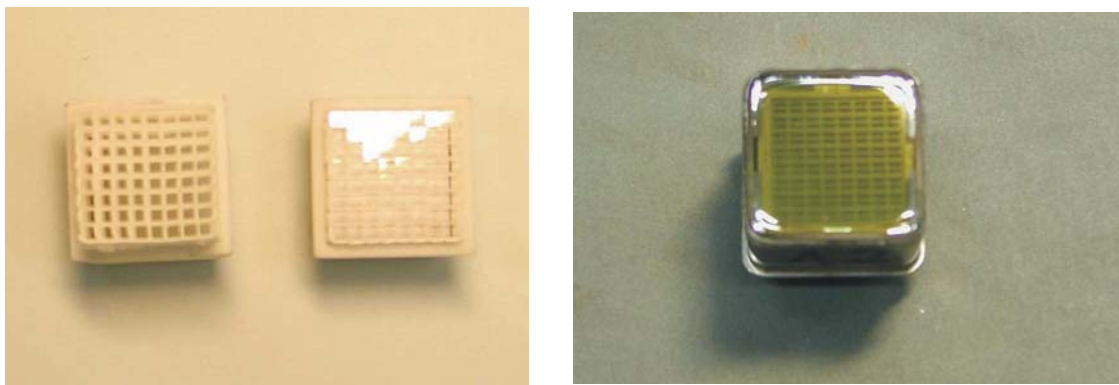


Figure 8.5 Pictures of the Tyvek matrix inserted into the plastic cap, the holder with the crystals and the R7600-00-M64 multianode photomultiplier tube (right side).

To assemble the matrix with the multianode PMT, the PMT is adjusted depending on the position markers on the photocathode. Afterwards, the crystal matrix is aligned and the two pieces are glued together using the Epotek 301 glue (2-component). A picture of a single detector module is shown in Figure 8.6 on the right side.

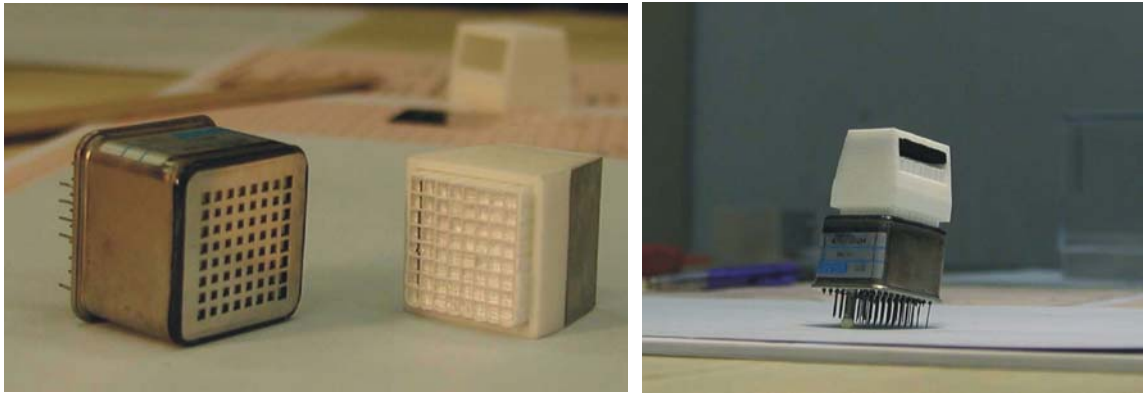


Figure 8.6 Photo of light-shielding mask glued on the PMT and the plastic cap holder. On the right side a final detector module is illustrated.

8.2.2 Design Study for the Scanner

The design study for the ClearPET 4-Ring scanners was done by O. Dietzel from the company Raytest (Germany) [4] and the results were placed to our disposal.

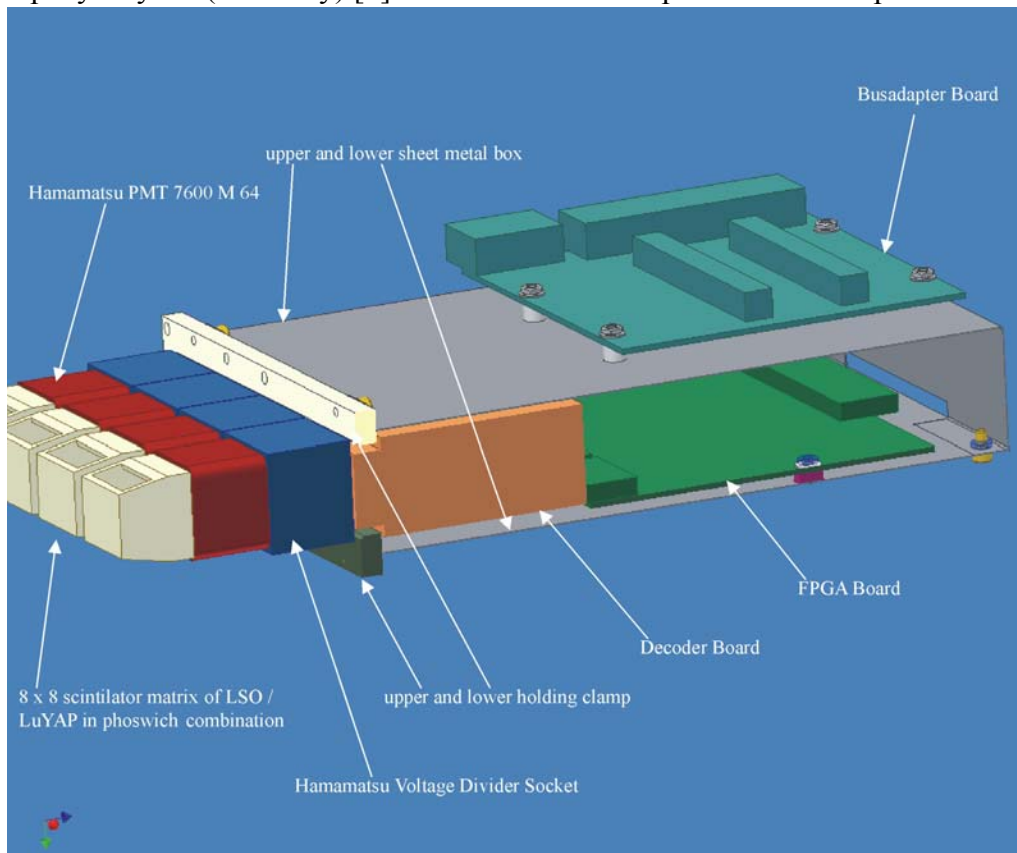


Figure 8.7 Scheme of the detector cassette for the ClearPET 4-ring scanners.

The detector modules are arranged in a cassette consisting of 4 modules, which are connected to the voltage divider socket, the decoder board and finally the FPGA (field programmable gate array) board. A scheme of the detector cassette is illustrated in Figure 8.7. The detector cassettes are arranged in the ring, with either 16 or 20 cassettes, depending on the different designs in the crystal clear laboratories. They are shifted with respect to each other by a distance of 7 mm ($\frac{1}{4}$ MA-PMT length), which was the outcome of the simulation. A picture of the cut inner ring is shown in Figure 8.8. The open piece of the plastic cap is going to be covered with a thin aluminum foil to reduce the dead space between the crystal blocks. The dead space is mainly influenced by the size of the multianode PMT and the voltage dividers.

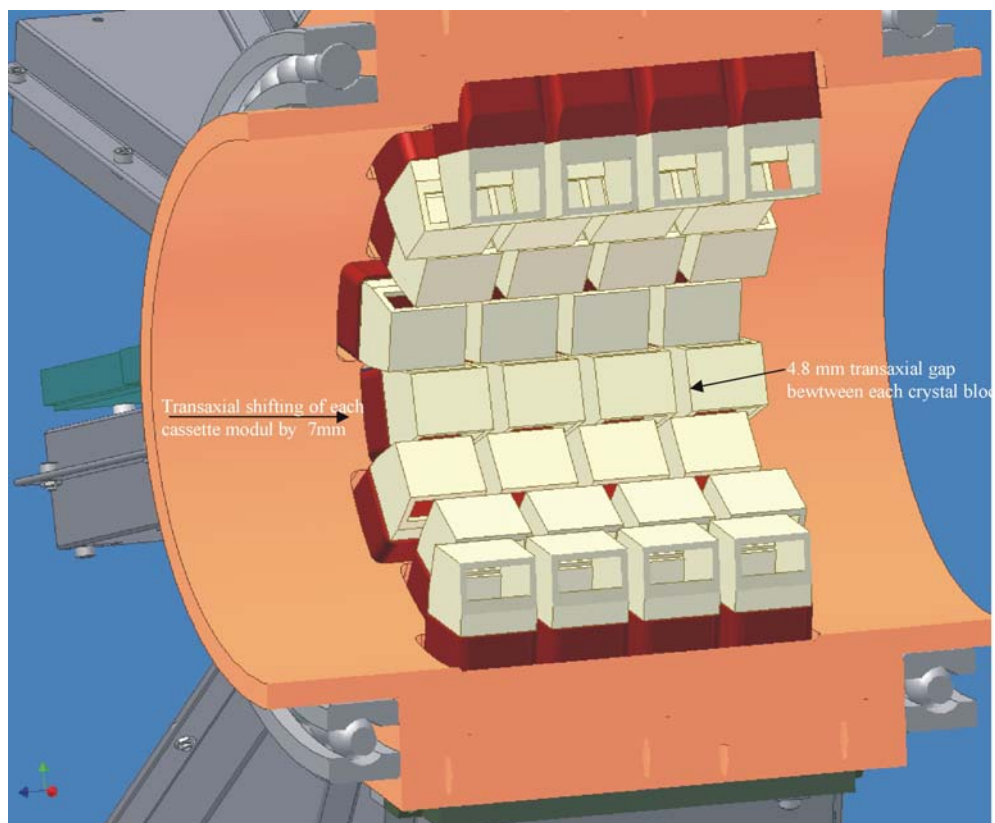


Figure 8.8 2D view of the final scanner and cut through the inner ring. The shift of the detector cassettes is indicated in the picture on the left side.

The inner diameter of the ring is 94.8 mm for the 20 PMT design. The outer diameter of the scanner – only with the cassettes – is about 610 mm.

A 3D-view of the 16 PMT scanner is illustrated in Figure 8.9. On every second cassette, a bus-adaptor board is connected. Ball bearings are mounted on both sides of the scanner to enable the rotation.

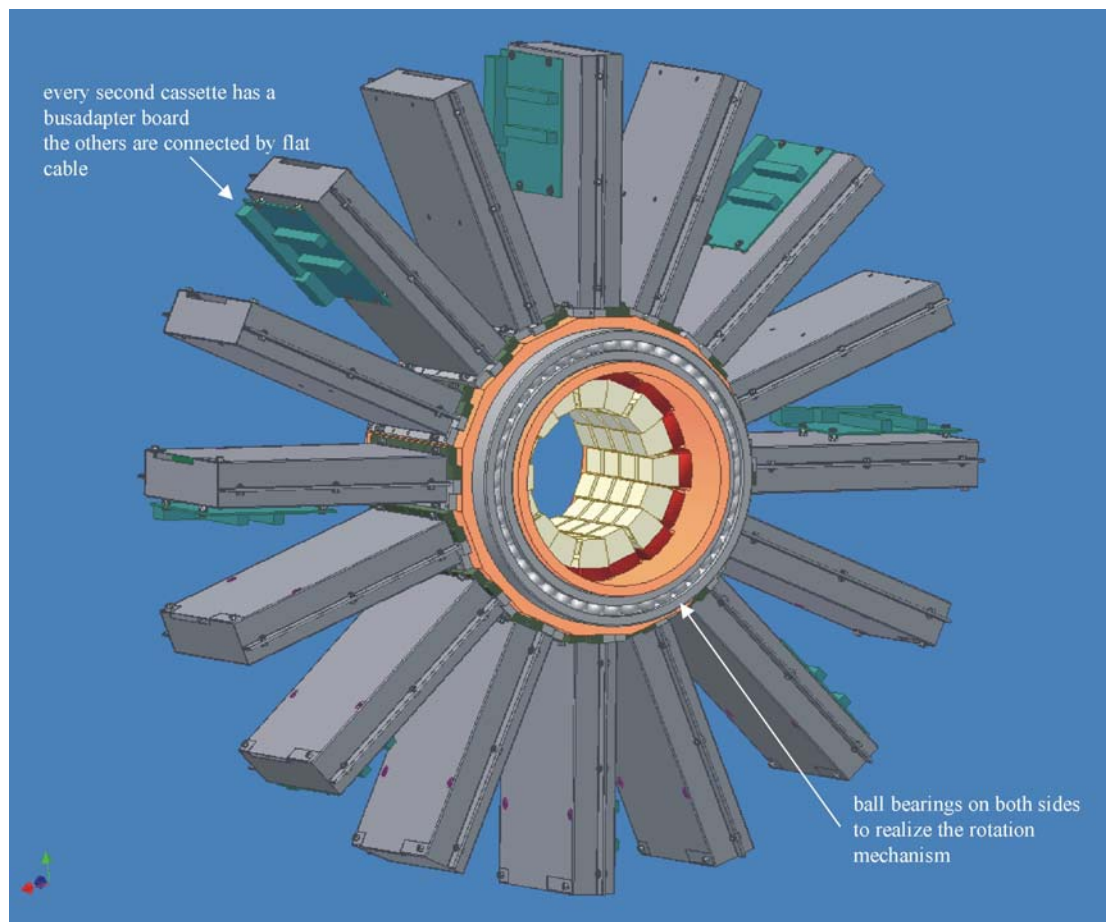


Figure 8.9 3D view of the final 4-ring ClearPET scanner consisting of 16 PMTs per ring.

8.2.3 Design of the PrimatePET in Jülich

The design of the PrimatePET is a little bit different from the common ClearPET design. The arrangement of the cassettes and the ring design is approximately the same but it has additional features.

It offers the possibility to enlarge the field of view by retracting the cassettes to perform studies not only on mice and rats but also on small monkeys. The monkey will be in an upright sitting position. The gantry allows rotation of the detector modules around the field of view as well as tilting by 90° to image the head of the animal. A scheme of the PrimatePET design is illustrated in Figure 8.10.

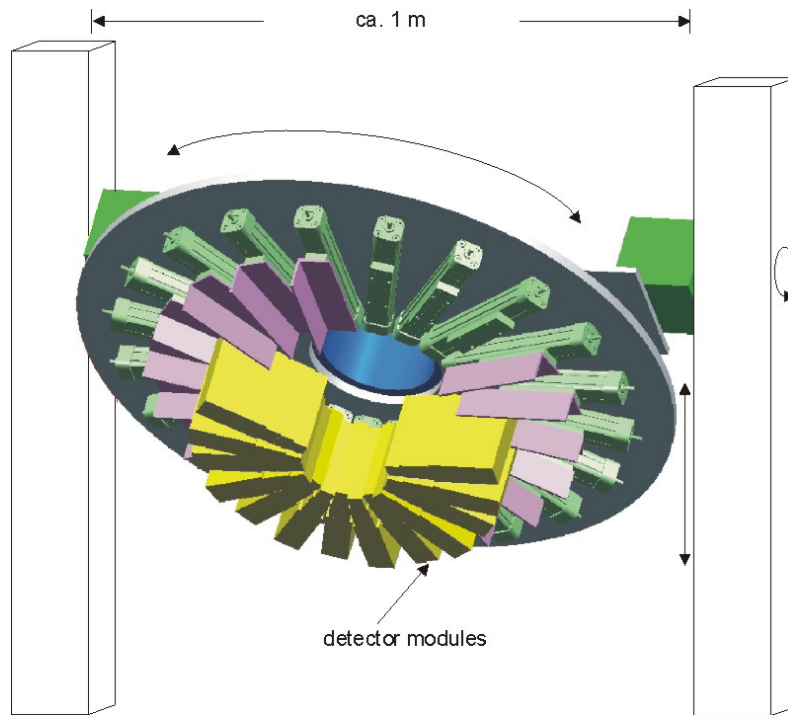


Figure 8.10 Schematic drawing of the PrimatePET design. Note that the detector modules can be retract to enlarge the field of view and that the scanner can be tilted [1].

8.3 Electronic Read-Out

The electronics should be capable to distinguish the decay times of the two scintillators used in the phoswich assembly. Thus, it should provide information about the depth of interaction, which means information about the crystal layer in which the scintillation took place.

In a conventional set-up, the γ -energy is generally obtained by a triggered ADC from the amplified, integrated and shaped photodetector pulse. Coincidence detection is usually performed by constant fraction discriminators and hardware gates. If the scintillator decay time should be furthermore detected, a separated hardware pulse shape analyzing circuit would become necessary.

All this information of energy, time and scintillation pulse shape is contained in the detected pulse, so it seems to be an obvious method, to sample this pulse and extract all the information by software data processing.

The next section describes the electronic set-up developed in Jülich and made available to the institutes of the Crystal Clear Collaboration.

8.3.1 Front End Unit

In the CCC electronic set-up, each multianode photomultiplier requires only one ADC, to read out all 64 channels. This is possible because the pulse length is much shorter than the average pulse interval at the expected counting rate per PMT [5]. The energy and pulse shape discrimination is performed at the last dynode, which is a common signal of all channels. Hence the dynode pulse is amplified, filtered and sampled with 12 bits by a free-running 40 MHz ADC (AD 9224, Analog Devices). The passive second-order low pass filters are necessary to satisfy the Nyquist theorem. 2nd order filters with a cut-off frequency of 3.6 MHz are used. This guarantees that the pulse rise time exceeds the sampling period in order to allow the use of our method for determining the pulse starting time. A schematic block diagram of the electronic set-up is shown in Figure 8.11.

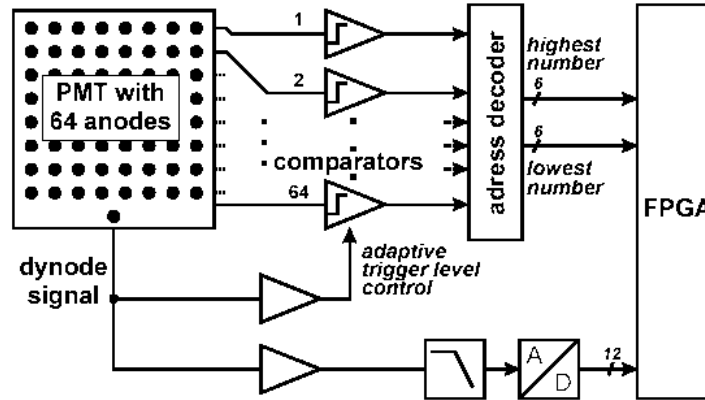


Figure 8.11 Read-out electronics for one multianode photomultiplier.

The sample sum is the measure of the pulse energy in the planned system.

To obtain the position of the event, each anode is connected to a comparator. Whenever an anode signal exceeds the threshold, which is an adjustable common voltage for all 64 comparators, the comparator output is triggered indicating that an event has been detected in the corresponding channel. The 64 trigger bits are decoded into channel addresses and fed into a Virtex FPGA (Xilinx) together with the 12 ADC bits. The decoder provides both the highest and the lowest address in order to detect simultaneous triggering of more than a single anode. Whenever a triggered event is detected, the FPGA sends a data package through a fast PCI I/O-card (PXI-6533, National Instruments) with 20 MB/s to the host PC. These data packages contain a time mark, the addresses of the trigger position and 16 subsequent samples covering the complete pulse. The time mark is a 64 bit number representing the actual state of a counter being clocked by the 40 MHz sampling clock.

8.3.2 Evaluation

After an event is detected, the pulse starting time is calculated. The differences of all pulses from opposite heads are finally checked for whether they lie within the borders of the previously defined coincidence window.

Several criteria have to be fulfilled for the algorithm that generates the pulse starting times. On the one hand, it has to be precise enough to allow narrow coincidence time windows, while on the other hand it should be simple enough to enable fast performance. To achieve good precision, only the first samples of the pulse should be used as input for the algorithm. This is because the starting time is indicated by the steep rising edge of the unfiltered PMT pulse, while the exact shape of the whole pulse is influenced by statistical processes in the scintillator and photomultiplier tube [6].

These considerations have been taken into account for the algorithm used. At first, it detects the two adjacent samples of the record with the maximum difference, which is corresponding to the steepest rise of the recorded pulse. The starting time is then obtained by calculating the intersection of the line through these samples with the baseline of the pulse. Thus, the rising edge is approximated by a straight line. The principle is illustrated in Figure 8.12. The level of the baseline is taken from the first sample of the record.

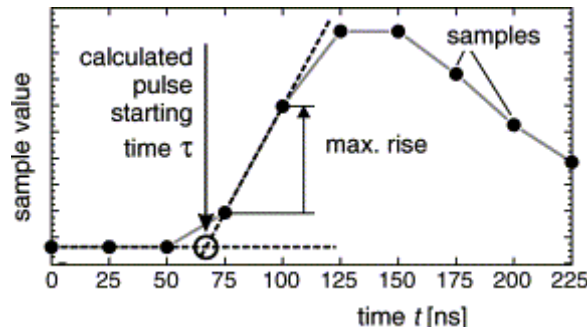


Figure 8.12 The pulse starting time is determined by calculating the baseline crossing of the line through the two adjacent samples where the pulse rise has its maximum (reproduced from [6]).

It is obvious that the accuracy of this algorithm depends on the low pass filter as it determines the pulse rise time. With a lower frequency filter, the samples of maximum rise will be located far behind the pulse start, which will cause an increased influence of statistical effects. On the other hand a higher-frequency filter will reduce the number of samples on the rising edge of the pulse. This causes errors due to the fact that the representation of the maximum rise by the two chosen samples becomes poorer. To overcome this problem the use of a higher sampling rate would be necessary.

8.3.3 Distinction of Pulses (LSO – LuYAP)

The distinction of the LSO and LuYAP pulses is done by taking the different decay times into account. The LSO crystal has a decay time of 40 ns whereas the two different kind of LuYAP crystals consist of two components. The $\text{Lu}_{0.7}\text{Y}_{0.3}\text{AP}$ scintillation pulse shape constitutes of 26 ns (fast component) and 250 ns (slow component) with intensities of 45% and 55%, respectively. Whereas, the $\text{Lu}_{0.8}\text{Y}_{0.2}\text{AP}$ crystal exhibits a slow component of around 160 ns contributing with 34% to the overall light output. The slow component of the LuYAP pulse is used to discriminate between the pulses whereas the fast component makes sure that most of the light is detected in the given time window (400 ns). The influence of the slow component leads to an ADC value significantly above the ground level after the 400 ns. This is presented in Figure 8.13.

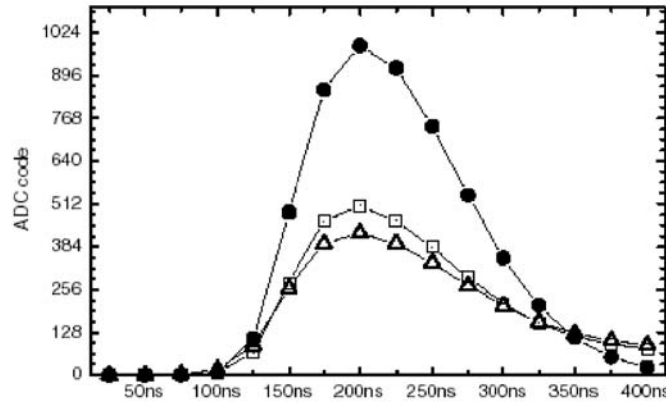


Figure 8.13 Sampled pulses from LSO (bullets), $\text{Lu}_{0.8}\text{Y}_{0.2}\text{AP}$ (open squares) and $\text{Lu}_{0.7}\text{Y}_{0.3}\text{AP}$ (open triangles) averaged over all recorded events. (Picture is reproduced from [7]).

Two different algorithms have been evaluated for their application in the DAQ software in terms of their complexity and accuracy. Detailed information about the two algorithms and the results for distinguishing LSO from LuYAP pulses can be found in [7].

To summarize the most important results from this study, it was found that the direct use of the slow component in the LuYAP pulse shape simplifies the calculation. For the optimum threshold, 99.2% of the events have been correctly identified for the $\text{Lu}_{0.7}\text{Y}_{0.3}\text{AP}$ samples and 97.7% for the $\text{Lu}_{0.8}\text{Y}_{0.2}\text{AP}$ crystals.

In Figure 8.14, the energy spectrum of a phoswich arrangement of LSO and $\text{Lu}_{0.7}\text{Y}_{0.3}\text{AP}$ irradiated with a ^{68}Ge source is shown. The recorded pulses were applied to the

described pulse shape discrimination algorithm. The separated spectra for the two crystals are plotted in the figure.

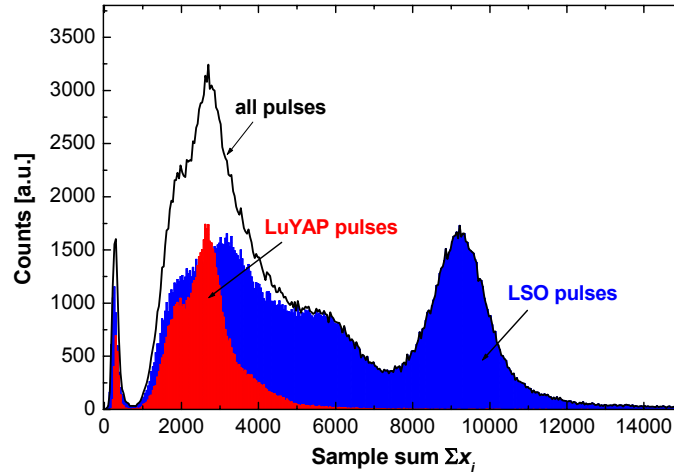


Figure 8.14 Common energy spectrum of optically coupled LSO and $\text{Lu}_{0.7}\text{Y}_{0.3}\text{AP}$ pixel. The black line shows the sum of all pulses as acquired, and the areas illustrate the different spectra for LSO and LuYAP separated by the pulse shape discrimination method.

As shown in the spectra, the separation works well. The two spectra of the scintillators with different light yield can be clearly recognized.

8.4 Phoswich Combination Study with the XP2020Q

For the final PET scanner, a pulse shape discrimination read-out electronics is going to be used to identify the crystal of interaction. To verify the pulse height spectra obtained with this pulse shape discrimination read-out, and to study the effect on energy resolution and light output of the crystal assembly, the constructed phoswich test module was used (see section 4.6). In particular, the influence on the scintillation light from the LSO crystal passing through the LuYAP was of special interest.

This test module was excited along the crystal axis with an electronically collimated beam of annihilation photons from a ^{22}Na source as shown in Figure 4.6. To vary the position and dimension of the beam the entire phoswich assembly was moved, allowing a small part (< 2 mm) of the test module to be excited. The depth coordinate system of the scan is chosen such, that 0 mm corresponds to the end of the LSO crystal and 14 mm is the reachable end of the LuYAP crystal closest to the photomultiplier tube. Whenever a coincidence between the phoswich assembly and the tagging BGO crystal occurred,

the signal in the test module was read into the computer. Figure 8.15 displays the pulse height spectrum observed with the PMT at two different scan positions – one in the LuYAP crystal and one in the LSO crystal. A clear 511 keV photopeak can be observed for both crystals.

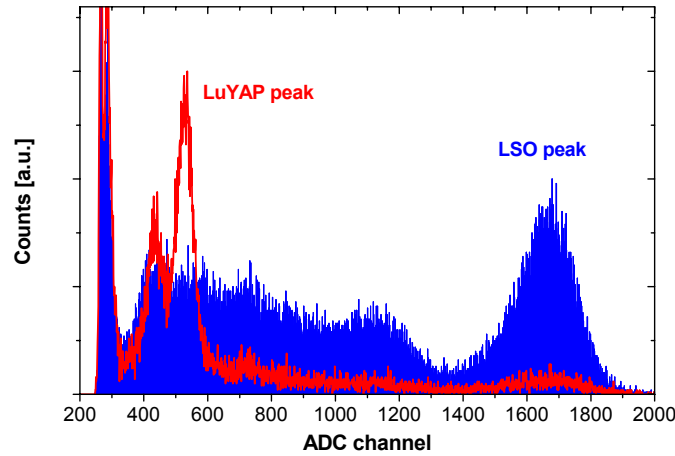


Figure 8.15 Pulse height spectra of the phoswich crystal assembly at 2 scan positions. Excitation of the LuYAP crystal (line curve) and excitation of the LSO crystal (full curve) with Na-22.

The pulse height spectra obtained by scanning the crystal assembly and thus defining the crystal of interaction, are in agreement with results from M. Streun [7] (see also Figure 8.14), who identified the crystal of interaction using a light pulse shape discrimination read-out.

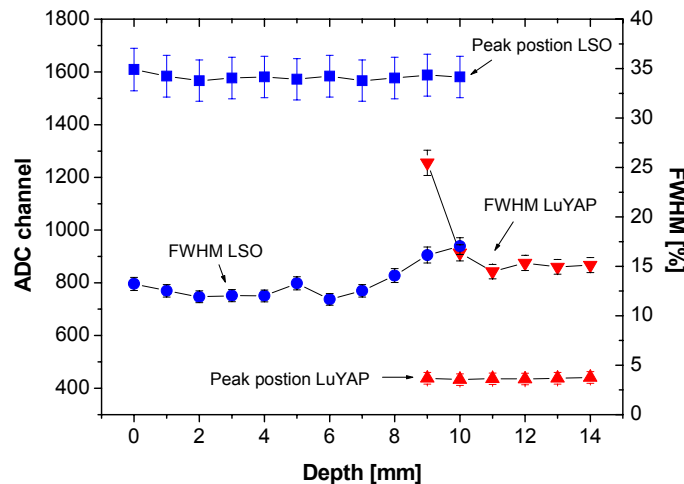


Figure 8.16 Position of the center and FWHM of the 511 keV photon peak as a function of excitation position. Note that for both crystals the response is uniform.

The collimated excitation beam was scanned along the crystal axis of the test module, and at each scan position the centre and FWHM of the 511 keV photopeak was computed and plotted in Figure 8.16. While the centre of the photopeak and thus the light output is constant, the FWHM shows a nonlinear response at the crystal boundaries. Anyhow, the overall energy resolution of the LSO crystal and the LuYAP crystal was measured to be around 12% to 16%. This allows to set a relatively small energy window and thus to have a good Compton rejection.

8.5 Discussion and Conclusion

In this chapter, the design proposals for the ClearPET scanners resulting from important information obtained by simulations have been presented. The simulations revealed that shifting every 2nd detector cassette by $\frac{1}{4}$ of the PMT lengths leads to a significant improvement of the axial sensitivity profile.

Another important outcome of the simulation is the scanner design. A multi-ring design is favorable in terms of sensitivity compared to the multi-head design. Therefore, two design proposals with 20 PMTs and 10 mm crystals length and 16 PMT and 8 mm crystal length are going to be constructed.

The successful layer identification in a phoswich detector of LSO and LuYAP has been shown. Due to the slow component present in the LuYAP scintillator, the differentiation is rather simple. The slow component can be easily detected and may also reduce the necessary hardware requirements, compared to a system distinguishing two fast decay times. In the case of the tested system a bandwidth of 3.6 MHz was sufficient. In the future, an effort will be made to discriminate the scintillators by their fast component, which will imply to increase the sampling rate from 40 MHz to approximately > 80 MHz.

Nevertheless, it has been proven that the fast decay component is of importance as it assures the collection of the majority of photons at the beginning of the pulse. Therefore, the necessary recording time for each pulse can be kept moderately short without losing too much light, e.g. in our case approximately 300 ns of a pulse are recorded. With the slow component of around 250 ns for Lu_{0.7}Y_{0.3}AP scintillator, contributing with 54% to the overall light output, still 86% of the light is caught.

Two different algorithms to distinguish between LSO and LuYAP were tested. Although the result of the simpler method is strongly depending on a single sample, its safety for distinguishing between crystals turned out to be similar to the more complex spectral analysis method.

The phoswich combination study performed with a normal photomultiplier showed, that the energy spectra obtained with the phoswich assembly and a collimated source are in good agreement with the spectra using the pulse shape discrimination read-out. This confirms the correctness of our pulse distinction algorithm.

The energy resolution of the crystal assembly was found to be around 12% to 16%, allowing a high Compton rejection to be implemented in the read-out electronics.

8.6 References

- [1] U. Heinrichs, U. Pietrzyk, K. Ziemons, *Design optimization of the PMT-ClearPET prototypes based on simulation studies with GEANT3*, Proc. IEEE Nuclear Science Symposium and Medical Imaging Conference (2002), Norfolk, Virginia.
- [2] U. Heinrichs, *Auslegung des Detektorsystems für einen hochauflösenden Positronen Emissions Tomographen mit hoher Sensitivität*, doctoral thesis, Medizinische Universität Lübeck, Germany (2003).
- [3] S. Léonard, personal communication (2002).
- [4] O. Dietzel, Raytest Germany, personal communication (2002).
- [5] M. Streun, G. Brandenburg, H. Larue, E. Zimmermann, K. Ziemons, H. Halling, *A PET system with free running ADCs*, Nucl. Instr. and Meth. A 486 (2002) 18-21.
- [6] M. Streun, G. Brandenburg, H. Larue, E. Zimmermann, K. Ziemons, H. Halling, *Coincidence detection by digital processing of free-running sampled pulses*, Nucl. Instr. and Meth. A 487 (2002) 530-534.
- [7] M. Streun, G. Brandenburg, H. Larue, H. Saleh, E. Zimmermann, K. Ziemons, H. Halling, *Pulse Shape Discrimination of LSO and LuYAP Scintillators for Depth of Interaction Detection in PET*, Proc. IEEE Nuclear Science Symposium and Medical Imaging Conference (2002), Norfolk, Virginia.

Chapter 9

Test Measurements with the 2-Head Prototype

In this chapter, the first results of test measurements performed with the 2-head prototype are presented. The 2-head prototype is a simplified version of the ClearPET scanner with approximately the same transaxial inner dimensions. It allows sampling of the same angular region as the rotating gantry of the ClearPET system. Therefore, it is possible to evaluate the detectors and the further processing of the measured data using this 2-head prototype in view of the ClearPET system. The system is read out by the Crystal Clear electronics. The tests were done at the Forschungszentrum Jülich.

Unfortunately, at the time of the measurements, the 2-head system consists only of one layer LSO crystals. The double layer modules, composed of LuYAP:Ce and LSO:Ce pixels in phoswich geometry for the final ClearPET scanner, will be delivered in the next months.

9.1 Set-Up of the 2-Head System

One head is build up by 2 x 2 multianode PMTs with 64 readout channels (8 x 8) per PMT. The LSO crystals ($2 \times 2 \times 10 \text{ mm}^3$) are inserted into a silvered steel matrix, which acts both as holder and reflector for the crystals. At the time of the construction of the two-head prototype, the Tyvek paper matrices were not yet available. The whole matrix is attached to the multianode photomultiplier (R7600-00-64, Hamamatsu) without optical glue. A metal housing that is fixed on a table covers the matrices. The two heads are aligned with a face-to-face distance of 12 cm on a table. The sensitive area is around $50 \times 50 \text{ mm}^2$ and therefore a field of view with a diameter and an axial length of 50 mm, was achieved. A rotating plate is placed between the two heads, which allows scanning of an object in steps of 1.8° . Thus the whole object can be mapped. In Figure 9.1 the set-up of the test system is illustrated.

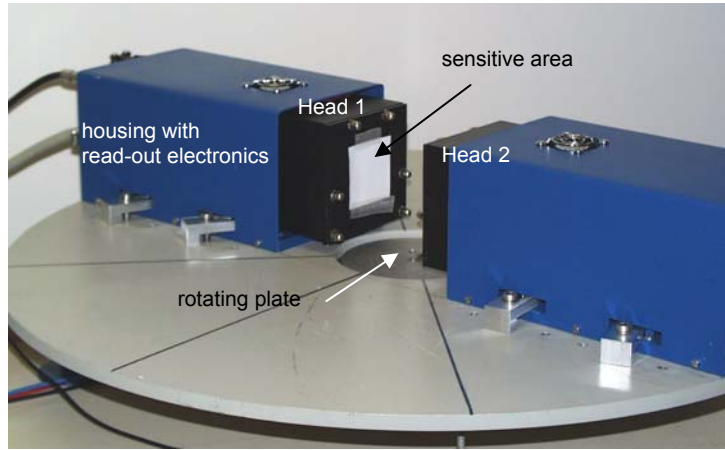


Figure 9.1 Picture of the 2-head prototype. It consists of 2 x 2 multianode PMTs per head and a rotating plate, which is located centrally between the heads.

The inner dimensions of the prototype test system with a face-to-face distance of 120 mm between the two heads, and a PMT centre-to-centre distance in axial direction of 28 mm, can be compared to the PrimatePET scanner, where the inner diameter is around 130 mm and the PMT centre-to-centre distance is also 28 mm. The difference is the missing shift in axial direction to achieve a more homogenous axial sensitivity profile (see Figure 8.3) and the missing LuYAP:Ce layer. Therefore, the achievable sensitivity with this prototype system is smaller, compared to the ClearPET scanner. A schematic view of the assembly of one detector head is given in Figure 9.2.

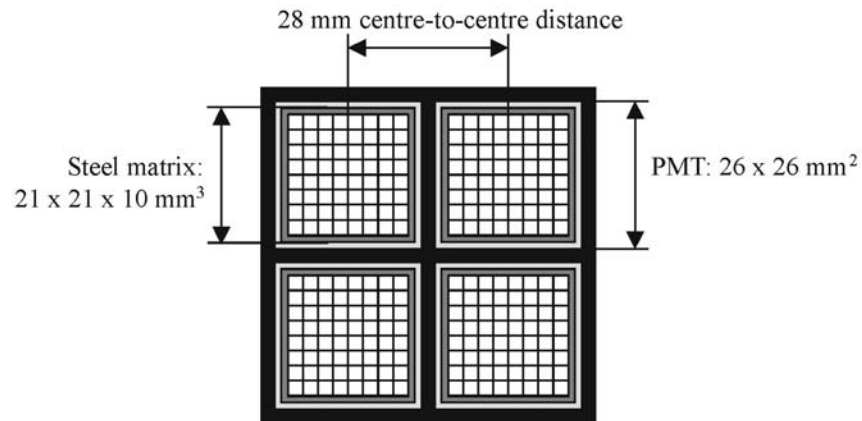


Figure 9.2 Schematic view of the detector head. The LSO crystals have a size of $2 \times 2 \times 10 \text{ mm}^3$.

All the measurements were performed with a general voltage of 810 V for all PMTs. The energy thresholds were selected depending on the gain of the respective multiplier.

The scans were performed in angular steps of 1.8° . At each angle, the signals were recorded for 5 sec.

9.2 Line Source

One of the objectives of this study was to test not only the 2-head system but also the whole chain by obtaining a measurement up to the final reconstructed picture. The Crystal Clear Collaboration has developed a special program for converting the measured data into list mode format (LMF). Afterwards, the coincidences are sorted out and the sinograms can be created. For the reconstruction, we used an iterative method, the so-called ordered-subsets expectation maximization (OSEM). This method was proposed by Hudson and Larkin [1] to accelerate the reconstruction process using the maximum likelihood expectation maximization (MLEM) algorithm. As reconstruction database, the STIR library (Software for Tomographic Image Reconstruction) available in the World Wide Web (<http://stir.irsl.org/homepage.shtml>) was used.

As a line source, we used a capillary with an inner diameter of 1 mm, and filled it with a small amount (approximately 1 ml) of F-18 (0.7775 mCi in 2 ml). The height of the liquid inside the capillary was around 4 cm. The line source was positioned in vertical position in the centre of the field of view. A picture of the measurement set-up can be seen in Figure 9.3.

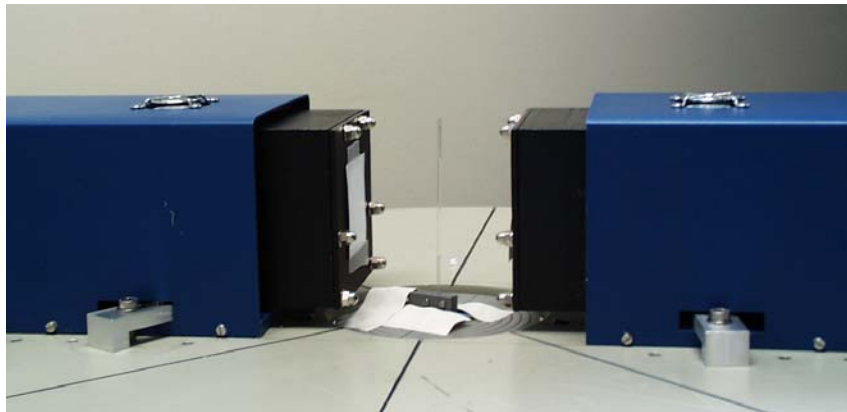


Figure 9.3 Measurement set-up to image a line source. The capillary was positioned in the centre of the field of view.

In the measured data, all the Singles were recorded and the file was converted into list mode format. Afterwards, the coincidences were sorted out. We take all coincidences into account that happen in a time window of 25 ns.

A very high-statistics data acquisition has to be performed one time after initial installation of a scanner to obtain the geometric normalization factors, whereas routine normalization needs only the acquisition of data from which to calculate the intrinsic detector efficiencies. Due to a data transfer problem, we had no time to perform the geometric normalization of the data. Therefore, the images suffer from huge distortions due to the missing geometric normalization factors. The reconstructed picture can be seen in Figure 9.4.

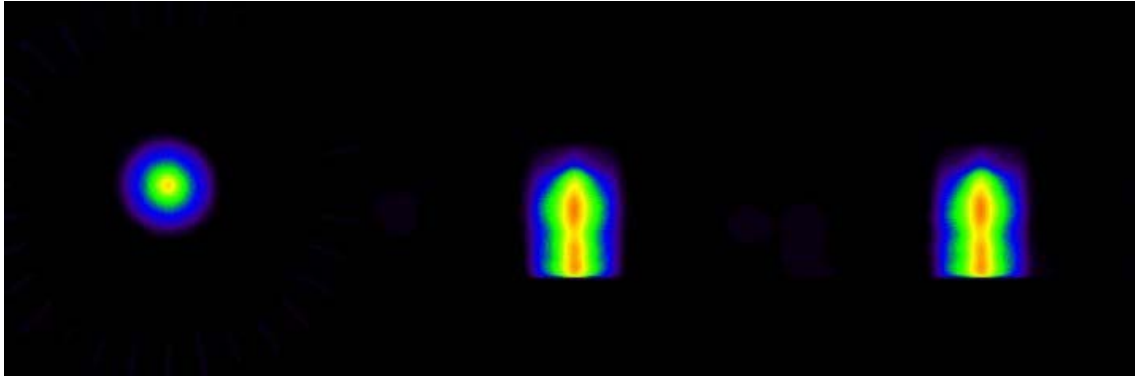


Figure 9.4 Reconstructed image of the line source. The picture shows the axial, frontal, and sagittal view.

9.3 Point-Like Source

To test the prototype for smaller sources we used a point-like source of Ge-68 with a diameter of 3 mm and a height of 2 mm. The source was housed in a lucite cylinder with dimensions of 6 mm heights and 25 mm diameter. Due to the rather high energy of the positrons emitted in the decay process of ^{68}Ge (max. energy 1.899 MeV) the mean free path length is longer compared to ^{18}F , and thus the physical origin of the γ -rays created in the annihilation process of the positrons with electrons from the lucite will be larger as the dimensions of the source given above. Therefore, it can be expected that the two detector heads will see a bigger object.

The image obtained with the reconstruction using the OSEM algorithm is shown in Figure 9.5.

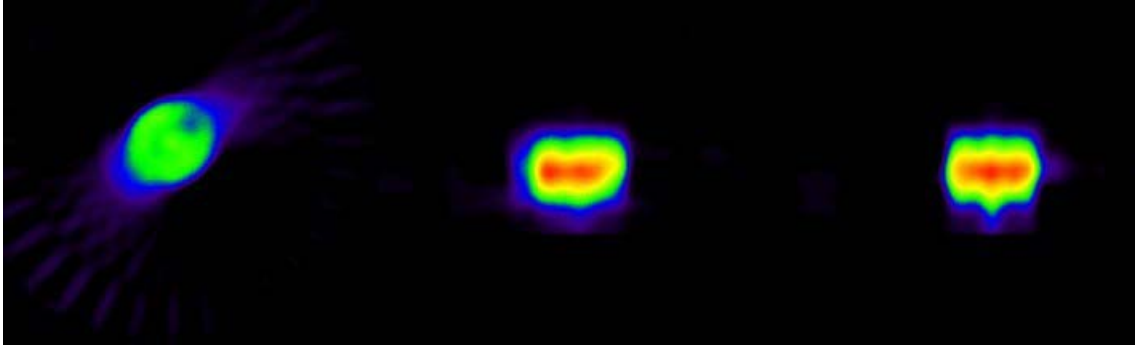


Figure 9.5 Reconstructed image of the point-like source. The picture shows the axial, frontal, and sagittal view.

Even though the picture is not normalized, one can clearly see that the diameter of the source is larger than the height.

9.4 Conclusion

The measurements described in this chapter were performed to test the chain by obtaining a measured dataset up to the reconstructed image. It was shown that the program to convert the measured data into list mode format works well and that the reconstruction delivers reasonable images.

At the time of the measurements, neither geometric normalization nor detector efficiency normalization was available and thus the image quality suffers from the respective distortions. No quantitative conclusion of the image could be drawn since the other correction methods, which are necessary for quantitative PET (e.g. attenuation correction, dead time correction, randoms correction and scatter correction), are not yet implemented.

9.5 References

- [1] H. M. Hudson, R. S. Larkin, *Accelerated image reconstruction using ordered subsets of projection data*, IEEE Trans. Med. Imaging 13 (1994) 601-609.

Chapter 10

Summary and Outlook

The development of high-resolution positron emission tomography has facilitated measurements of tissue function and regional tracer pharmacokinetics in small animals. This extension in the use of existing clinical PET systems has helped in the evaluation of new radiolabelled ligands and has improved the interpretation of the “in vivo” kinetics of established PET tracers. Clinical PET systems are not, however, optimal for small animal studies with respect to speed, spatial resolution and sensitivity. Therefore, the need for small-diameter PET systems, dedicated to experimental studies for new pharmaceuticals and in genetic research has been recognized in the last years.

In PET, inorganic scintillators are used to detect γ -rays produced by the annihilation of positrons emitted by injected tracers. The ultimate performance of the PET scanner is strongly tied to both the physical and scintillation properties of the crystals. For this reason, researchers have investigated virtually all known scintillator crystals for possible use in PET. Despite this massive research effort, only a few different scintillators have been found that have a suitable combination of characteristics, and only two (NaI:Tl and BGO) have found widespread use.

For the next generation of PET scanners, necessary improvements on speed, position resolution and sensitivity have triggered new research on even better crystals.

The investigations described in this thesis are focused on evaluation of new inorganic scintillators, namely Lu(Y)AP:Ce and lutetium based oxyorthosilicates (LSO, LYSO and MLS), for application in medical imaging. Also the need for high-resolution small animal PET scanners for validation of sophisticated models of human disease has increased during the last years.

In this thesis, it has been shown, that $\text{Lu}_{1-x}\text{Y}_x\text{AlO}_3$ doped with cerium is a promising candidate for the next generation PET cameras. Especially the combination of this crystal with LSO:Ce in phoswich geometry seems to be a powerful technique for the construction of high resolution and high sensitivity scanners.

LuYAP crystals produced with two different growth techniques, Czochralski and Bridgman, from two different manufacturers, were investigated. It has been shown that the light yield measured in all these crystals is roughly the same. But, large differences in the measured energy resolutions were found, related to double photoelectric peaks in the energy spectra for the Bridgman samples. One explanation for this might be, that the crystallization in the unseeded Bridgman method takes place spontaneously, which results in polycrystals in a pixel.

The UV spectroscopy study exhibits an additional tail in the absorption spectra. The overlap between the absorption spectrum and the emission spectrum leads to self-absorption in the scintillator. A definite correlation between this absorption tail and the light yield measured in vertical position was found.

The results in light yield and energy resolution of the $\text{Lu}_{0.7}\text{Y}_{0.3}\text{AlO}_3$ (BTCF) show an improvement in the crystal quality from the first to the third batch of the pre-production phase. A mean energy resolution of 7.75% FWHM and a light yield of around 8000 ph/MeV using a ^{137}Cs source and measured in horizontal position was found. From the measured number of photoelectrons, the intrinsic energy resolution was calculated. It was shown that the energy resolution is mainly influenced by the statistical contribution of the photomultiplier. The light yield (photons/MeV) measured with varying photon energies was constant from 1.333 MeV down to 100 keV. This confirms the effect of the non-proportionality of the light output versus energy on the energy resolution.

$\text{Lu}_{0.7}\text{Y}_{0.3}\text{AP}$ crystals produced in the mass-production phase show an increase in light yield of around 50% (horizontal) compared to the crystals produced in the pre-production phase. The spread in light yield and energy resolution of the randomly selected crystals (10 out of 1000) was very narrow (within the uncertainty). The scintillation light pulse shape consists of two components. The fast one has a decay time of 27 ± 0.6 ns with intensity of 43.6% followed by a slow component of $\sim 280 \pm 25$ ns and intensity of 56.4%. As for the other samples, an additional absorption tail was present in the absorption spectra. The ratio between the light yield taken in vertical and horizontal position is around 47%.

The most important step in the development of the LuYAP crystal was the demonstration of successful growth of large ingots with reproducible characteristics, which was not shown until now. The Bogoroditsk Techno Chemical Plant is able to produce crystals in large quantities with equal scintillation parameters, which will be implemented in several PET scanners.

In this study, it has been demonstrated that LYSO could be another promising candidate in comparison to the LSO scintillator. Due to the low amount of yttrium in the melt (only 2.5%), the density is not negatively impaired, while the desired scintillation

properties are conserved. For the last batch of studied LYSO samples, a light yield of 27600 ph/MeV and a decay time of 42 ns were observed. No additional slow decay component was found.

The existence of two emission centres with variable efficiency has been demonstrated for all the investigated scintillators. There is evidence, that the presence of these two centres has an influence on energy resolution and decay time. Samples with good energy resolution ($\sim 7\%$ FWHM) exhibited a low intensity of the Ce2 emission. The population of the two cerium sites also affects the scintillation pulse shape. Crystals with faster decay time are dominated by the Ce1 emission (32 ns), whereas crystals with longer decay time constants of around 42 ns have approximately equal contributions from Ce1 and Ce2 (55 ns).

In spite of the high light yield, the lutetium oxyorthosilicates show a rather poor energy resolution. Another factor, apart from the two cerium sites, influencing the resolution is the non-proportional response from the light yield on photon energy. Starting at 662 keV, the response curve of LSO decreases to almost 65% when lowering the γ -ray energy to 31 keV. It was shown that the energy resolution measured with LSO is mainly dominated by the intrinsic resolution.

The successful layer identification in a phoswich detector consisting of LSO and LuYAP crystals has been shown. Due to the slow component present in the LuYAP scintillator the discrimination is rather simple. Nevertheless, it has been proven that the fast component from LuYAP is of importance as it assures the collection of the majority of photons in the given time window of approximately 300 ns.

The PET technology development phase has not yet run its course. The potential of the latest generation of small animal PET scanners has to be further explored, and it would be foolhardy to suggest that dramatic improvements are not going to be obtained in the future. It can, however, reasonably be predicted that future improvements in spatial resolution will not be of the same magnitude as those seen over the last years.

At the resolution level of 1 mm FWHM, two limiting properties of positron annihilation become significant, namely the distance which positrons travel prior to annihilation and the departure from co-linearity of the annihilation photons. While it is possible to take these factors into account with iterative reconstruction methodology, the errors imposed by the corrections will become more and more important as spatial resolution dips below 1 mm.

During the next months the construction of the ClearPET scanner will take place. At the moment, the phoswich detector modules with the LSO and LuYAP crystals are being assembled. The first tests on the final scanner will be in October 2003.

The results from the simulation are very promising. For the scanner consisting of 20 PMTs and double layer LSO-LuYAP crystals (each 10 mm) a sensitivity of 4.2% in the central FOV with an energy threshold of 350 keV was calculated. The position resolution resulting from the simulation was smaller than 2 mm FWHM for a point source located between 0 and 2.5 cm axially to the central field of view. This good spatial resolution for object arranged within 2.5 cm axially from the central FOV matches well to the diameter of a rat (~ 5 cm).

We believe that this small animal PET scanner will outperform existing small animal PET scanners in speed, sensitivity and spatial resolution and therefore be a powerful tool in the study of new pharmaceuticals.

Appendix A

Detection of Scintillation

A.1 Light Collection

This section will reflect the processes involved in the collection of the photons emitted by the scintillator and their conversion into photoelectrons at the photocathode of the photomultiplier. It is desirable that a large fraction of the emitted photons are collected at the photocathode. The measured quantity, that is the total number of photoelectrons $N_{phe}(E)$, collected at the anode due to the full-energy gamma-ray events is proportional to the absolute number of photons as follows:

$$N_{phe}(E) \propto N_{ph}(E) \times \eta_L \times QE(\lambda) \times \varepsilon \quad (\text{A.1})$$

where $N_{ph}(E)$ is the number of photons per energy unit produced in the scintillator at a given energy, η_L is the light collection efficiency, $QE(\lambda)$ is the quantum efficiency, and ε is the efficiency of the photoelectron collection.

In general, at low energies the number of photons per energy unit created by γ -rays in the scintillator depends on the γ -energy, and is lower below 100 keV. This non-linearity was recently studied for a number of scintillators. Thus, one has to define the energy of the source used in the measurement.

The light collection efficiency is a function of the crystal size and shape, surface finish and refractive index. It is highly dependent on the self-absorption of the light in the crystal and on the reflector material used. For small crystals, the error induced by the uncertainty of the light collection is smaller than for large crystals. The estimation of these parameters seems to be crucial for the reproducibility of the light output measurements.

Total Reflection

One important point is the loss of light at the scintillator boundaries. Light emitted at any given point in the scintillator travels in all directions and only a fraction of it directly reaches the PMT. The remainder travels towards the scintillator boundaries where, depending on the angle of incidence, two things can happen. For light impinging at an angle greater than the Brewster angle, θ_B where

$$\theta_B = \sin^{-1} \left(\frac{n_{out}}{n_{scint}} \right) \quad (\text{A.2})$$

with n_{scint} being the index of refraction of the scintillator and n_{out} that of the surrounding medium, total internal reflection occurs so that this light is turned back into the scintillator. At angles less than θ_B , partial reflection occurs and part of the light is transmitted. This loss reduces the light output and the energy resolution of the scintillating crystal and thus also of the detector.

Reflectors

Since the photon emission occurs in all directions, it is advantageous to cover all faces of the scintillator with reflecting material to redirect escaping light. There are different reflectors available – *diffusing reflectors* like Tyvek paper or Teflon tape, *specular reflectors* like aluminium foil and *diffusing paints* like TiO_2 or BaSO_4 . Figure A.1 shows the reflectivity curves of various diffusing and metallic reflectors.

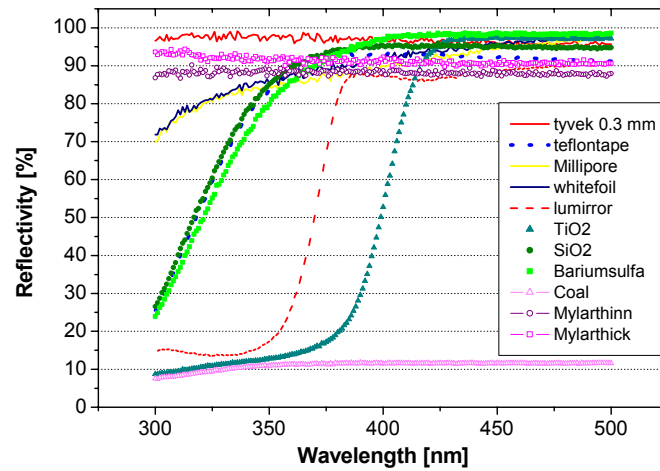


Figure A.1 Reflectivity versus wavelength for various reflecting materials. The measurements were performed by U. Heinrichs (Forschungszentrum Jülich) and set to our disposal.

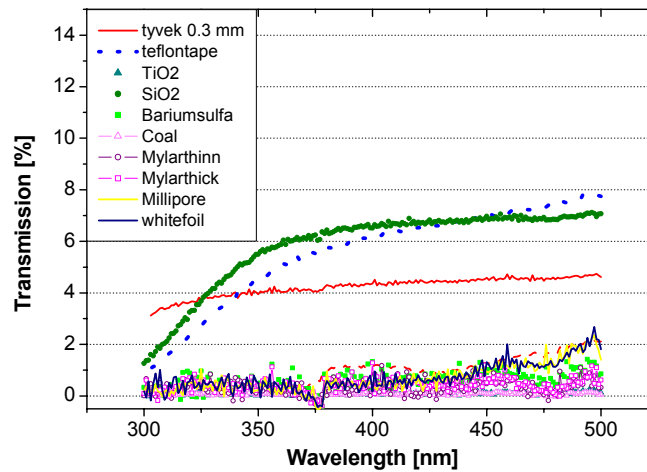


Figure A.2 Transmission versus wavelength for various tested reflecting materials. The measurements were performed by U. Heinrichs (Forschungszentrum Jülich).

The reflector arrangement used for a particular application is usually determined by a compromise between light collection efficiency, convenience and mechanical demands.

In our case, the search for the ideal reflector turned out to be delicate. The specular reflectors like for example the multi-layer polymer mirror film, which has already been used to construct a crystal matrix with LSO pixels, has a rather poor reflectivity at 365 nm. Tyvek paper was found to be a good reflector for LSO crystals as well as for LuYAP crystals. A disadvantage is that the paper is partly transparent. The transmission measurements for the various tested reflectors are shown in Figure A.2.

Anyhow, due to the fact that the largest amount of emitted light needs to be collected, the Tyvek paper is used both as reflector and holder of the crystals.

Self-Absorption in the Scintillator

The effect of the overlap of the absorption and emission spectra leads to self-absorption of the emitted light in the crystal. This can easily be studied by measuring the emission and absorption spectra. The requirement to obtain a clear absorption spectrum, where all absorption bands are clearly visible is a very thin crystal (~ 1 mm).

If it is not possible to provide such a thin crystal, the order of magnitude of this self-absorption can be studied by measuring the crystal with the same size of the coupling face but decreasing thickness.

In our case the crystals should remain in the delivered size (not cut) and so the crystals with a normal size of $2 \times 2 \times 10 \text{ mm}^3$ are measured in horizontal position (long side of the crystal coupled to the PMT) as well as in vertical position (small end face of the crystal coupled to the PMT) to have an estimate of the importance of self-absorption.

Photoelectron Collection

The next factor, which can limit the measured number of photoelectrons is the efficiency of the photoelectron collection. For a PMT this quantity is usually not given by the manufacturers. For a well-designed PMT, one can assume that at least in the central part of the photocathode the collection efficiency approaches 100%.

Temperature

As mentioned in 3.4.5, the temperature of a crystal also affects its light output. This temperature dependence is variable for different crystals. Thus, precautions have to be taken when measuring light output. Due to the opposite temperature dependence of LSO and LuYAP, an operation of the detector at slightly higher temperature than room temperature (for instance 40°C) would significantly reduce the light yield difference between these two crystals.

A.2 Spectral Response

For a given crystal, the intensity $I(\lambda)$ of the scintillation depends on the wavelength λ . In addition to that, the quantum efficiency of a photomultiplier $qe(\lambda)$ also varies with the wavelength. The effective quantum efficiency has to be calculated from:

$$QE = \frac{\int qe(\lambda)I(\lambda)d\lambda}{\int I(\lambda)d\lambda} \quad (\text{A.3})$$

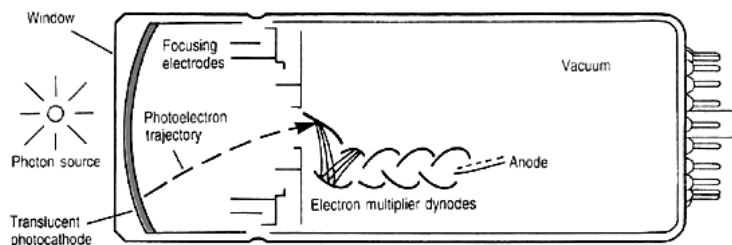
In practice, this formula cannot be applied as only a finite number of points can be measured. Then it turns into

$$QE = \frac{\sum_i qe(\lambda_i)I(\lambda_i)}{\sum_i I(\lambda_i)} \quad (\text{A.4})$$

When choosing a PM, therefore, the primary consideration should be its sensitivity to the wavelength of the incident light.

A.3 Photomultipliers

Photomultipliers (PMT's) are electron tube devices, which convert light into a measurable electric current. The basic construction of a typical photomultiplier is shown in Figure A.3. It consists of a cathode made of a photosensitive material followed by an electron collection system, an electron multiplier section and finally an anode from which the signal can be taken. All parts are usually housed in an evacuated glass tube. When an incident photon impinges upon the photocathode, an electron is emitted via the photoelectric effect. Because of the applied high voltage, the electron is then directed and accelerated toward the first dynode. This causes secondary electrons to be emitted, which are accelerated toward the next dynode. At the anode this electron cascade is collected. If the anode and dynode system is linear, the current of the output of the PM is directly proportional to the number of incident photons. Thus coupling a scintillator - which produces photons in proportion to the energy deposited in the scintillator - to the PMT, one is capable of determining the energy of the incident particle.



Operating principle of a photomultiplier tube. Electrodes focus and accelerate photoelectrons.

Figure A.3 Operating principle of a photomultiplier tube and picture of a standard PMT.



Multianode PMT

In a conventional PMT when light is incident on the photocathode the spatial information about the light signal is lost. However by using a special cathode

configuration and special dynodes that retain spatial information, it is possible to create position sensitive PMT arrays in a single vacuum envelope.

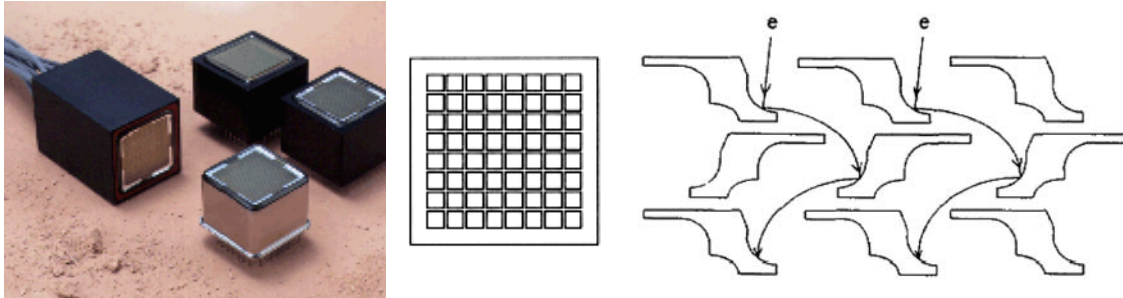


Figure A.4 Picture of some Hamamatsu multianode PMT's, sketch of the 64 anode PMT and cross section of a metal channel dynode structure (from Yoshizawa and Takeuchi).

To meet the increasing need for small photodetectors with high sensitivity, Hamamatsu has developed subminiature PMTs using a metal package in place of the traditional glass envelope. These tubes have a size as small as semiconductor sensors, without sacrificing high sensitivity, and have the high speed response offered by conventional PMTs. The R5900-00-M64 PMT produced by Hamamatsu Photonics has 64 discrete channels arranged in an 8 x 8 array with individual read-out through the segmented anodes. It incorporates 10 to 12 stages of metal channel dynodes into a metal package of 28 mm x 28 mm square and 20 mm height.

As the metal channel dynode is a sort of an array of small linear focused dynodes, secondary electrons hardly go to the adjacent dynode channel in a process or multiplication. A picture of this structure can be seen on the right side of Figure A.4.

The main problem of these multianode PMTs is the cross-talk, which consists of:

- 1) *Optical cross-talk*: the light signal (coming from the scintillation) diffuses and so the aperture cone is enlarged in the glass window of the MA-PMT.
- 2) *Electron trajectory cross-talk*: the electron trajectory is gradually enlarged while photoelectrons coming from the photocathode reach the anode pixels in the MA-PMT.
- 3) *Electromagnetic cross-talk*: the anode signal may affect adjacent anode signals electromagnetically in an electric circuit.

Photocathode

The photocathode converts incident light into a current of electrons by the photoelectric effect. From Einstein's equation we know that

$$E = h\nu - \Phi \quad (\text{A.5})$$

Where E is the kinetic energy of emitted electrons, ν the frequency of incident light and Φ the work function. It is clear that a certain minimum frequency is required before the photoelectric effect takes place. Above this threshold, however, the probability for this effect is far from being unity. Indeed, the efficiency for photoelectric conversion varies strongly with the frequency of the incident photons and the structure of the material. This overall spectral response is expressed by the quantum efficiency $qe(\lambda)$,

$$qe(\lambda) = \frac{\text{number of photoelectrons released}}{\text{number of incident photons on cathode } (\lambda)} \quad (\text{A.6})$$

Where λ is the wavelength of the incident photons.

The photoemissive surface usually consists of alkali metals. The photocathode materials most commonly used in photomultiplier tubes are as follows:

1) *Sb-Cs*

This is a widely used photocathode and has a spectral response in the ultraviolet to visible range. It is not suited for transmission mode photocathodes and mainly used for reflection mode photocathodes.

2) *Bialkali (Sb-Rb-Cs, Sb-K-Cs)*

These photocathodes have a spectral response range similar to the Sb-Cs photocathodes, but have higher sensitivity and lower noise than Sb-Cs. This transmission mode bialkali photocathodes have a favourable blue sensitivity for scintillator flashes and thus are often used for radiation measurement using scintillation counting.

Window Materials

The commonly used window materials are:

1) *Borosilicate glass*

This is the frequently used glass material. It transmits radiation from the near infrared to about 300 nm. It is not suitable for detection in the ultraviolet region. For some applications, the combination of a bi-alkali photocathode and a low-noise borosilicate glass (so called K-free glass) is used.

2) *UV-transmitting glass (UV glass)*

This glass transmits ultraviolet radiation well and is widely used for spectroscopy application. The UV cut-off is at about 185 nm.

3) *Synthetic silica – fused silica (Quartz)*

The synthetic silica transmits ultraviolet radiation down to 160 nm and offers lower absorption in the UV range compared to fused silica.

A diagram of the transmittance versus wavelength for the different window materials is shown below.

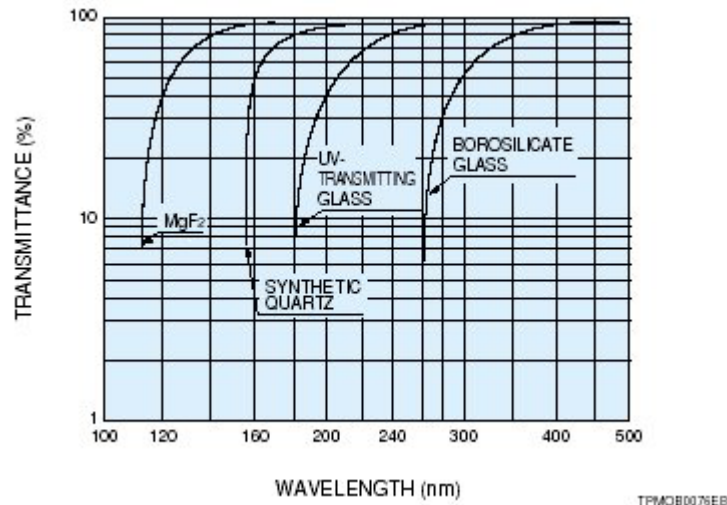


Figure A.5 Typical transmittance of various window materials.

Despite the rather low transmittance of the borosilicate window at 350 nm, a PMT with this window is going to be used for the PET scanner for cost reason. Multianode PMTs only exist with borosilicate window.

Appendix B

Material and Methods

B.1 Dimensions and Density of the Crystals

The size and the weight of the crystals were determined using a Vernier caliper (Digitical, TESA, Type 05.30032) and a balance (Mettler Toledo (min 0.1 mg)). The obtained values plus the calculated density can be seen in the following tables. The error for the dimension measurement is given as 0.02 mm and for the weight 0.2 mg.

Table B.1 Dimensions, weight and calculated density of the $\text{Lu}_{0.8}\text{Y}_{0.2}\text{AlO}_3$ crystals grown by A. Petrosyan in Armenia.

Crystal	CCC Number	X [mm]	Y [mm]	Z [mm]	Volume [mm ³]	Weight [g]	Density [g/cm ³]
Lu_{0.8}Y_{0.2}AP 1	1029	2.23	2.31	10.19	52.49	0.4002	7.62 ± 0.10
Lu_{0.8}Y_{0.2}AP 2	1030	1.92	1.93	10.23	37.91	0.2806	7.40 ± 0.11
Lu_{0.8}Y_{0.2}AP 3	1031	1.87	1.91	10.23	36.54	0.2792	7.64 ± 0.12
Lu_{0.8}Y_{0.2}AP 4	1032	1.86	1.94	10.22	36.88		
Lu_{0.8}Y_{0.2}AP 5	1033	1.89	1.96	10.23	37.90	0.2871	7.58 ± 0.11
Lu_{0.8}Y_{0.2}AP 6	1034	2.3	2.31	10.2	54.19	0.4003	7.39 ± 0.09
Lu_{0.8}Y_{0.2}AP 7	1035	2.26	2.3	10.19	52.97	0.4052	7.65 ± 0.10
Lu_{0.8}Y_{0.2}AP 8	1036	2.25	2.3	10.17	52.63	0.403	7.66 ± 0.10
Lu_{0.8}Y_{0.2}AP 9	1037	1.86	1.93	10.23	36.72	0.284	7.73 ± 0.11
Lu_{0.8}Y_{0.2}AP 10	1038	1.86	1.94	10.23	36.91	0.281	7.61 ± 0.11
Lu_{0.8}Y_{0.2}AP 11	1039	1.87	1.94	10.24	37.15	0.2809	7.56 ± 0.11
Lu_{0.8}Y_{0.2}AP 12	1040	1.87	1.95	10.23	37.30	0.2826	7.58 ± 0.11
Lu_{0.8}Y_{0.2}AP 13	1041	1.87	1.94	10.24	37.15	0.284	7.65 ± 0.11
Lu_{0.8}Y_{0.2}AP 14	1042	1.88	1.91	10.23	36.73	0.2783	7.58 ± 0.11
Lu_{0.8}Y_{0.2}AP 15	1043	1.83	1.95	10.22	36.47	0.2825	7.75 ± 0.12
Lu_{0.8}Y_{0.2}AP 16	1044	1.87	1.93	10.24	36.96		
Average		1.97	2.03	10.22	41.06	0.316	7.6 ± 0.10
Lu_{0.8}Y_{0.2}AP 17	1068	2	2.13	9.97	42.47	0.3236	7.62 ± 0.11
Lu_{0.8}Y_{0.2}AP 18	1069	1.94	2.15	10.18	42.46	0.3096	7.29 ± 0.10
Lu_{0.8}Y_{0.2}AP 19	1070	1.98	2.21	10.14	44.37	0.3161	7.12 ± 0.10
Lu_{0.8}Y_{0.2}AP 20	1071	2.02	2.15	9.99	43.39	0.3178	7.33 ± 0.10
Average		1.99	2.16	10.07	43.17	0.317	7.34 ± 0.10

Note that crystal number 1069 – 1071 were depolished. Crystal number 1029 – 1044 have 0.4% Ce in the melt whereas the concentration is 0.55% Ce for crystal number 1068 – 1071.

Table B.2 Dimensions, weight and calculated density of the $\text{Lu}_{0.7}\text{Y}_{0.3}\text{AlO}_3$ crystals grown by the BTCP (Bogoroditsk Techno Chemical Plant), Russia, batch 1.

Crystal	CCC Number	X [mm]	Y [mm]	Z [mm]	Volume [mm^3]	Weight [g]	Density [g/cm^3]
$\text{Lu}_{0.7}\text{Y}_{0.3}\text{AP}$	1085	2.01	1.93	10.00	38.60	0.2515	6.51 ± 0.09
$\text{Lu}_{0.7}\text{Y}_{0.3}\text{AP}$	1086	2.01	2.01	9.94	40.16	0.2613	6.51 ± 0.09
$\text{Lu}_{0.7}\text{Y}_{0.3}\text{AP}$	1087	2.01	1.93	10.01	38.72	0.2534	6.54 ± 0.10
$\text{Lu}_{0.7}\text{Y}_{0.3}\text{AP}$	1088	2.02	2.02	9.94	40.34	0.2641	6.55 ± 0.09
$\text{Lu}_{0.7}\text{Y}_{0.3}\text{AP}$	1089	2.02	1.94	10.01	39.01	0.2542	6.52 ± 0.09
$\text{Lu}_{0.7}\text{Y}_{0.3}\text{AP}$	1090	2.01	2.01	9.94	40.16	0.2619	6.52 ± 0.09
$\text{Lu}_{0.7}\text{Y}_{0.3}\text{AP}$	1091	2.01	1.94	10.01	38.82	0.2521	6.49 ± 0.09
$\text{Lu}_{0.7}\text{Y}_{0.3}\text{AP}$	1092	2.01	2.01	9.98	40.20	0.2589	6.44 ± 0.09
$\text{Lu}_{0.7}\text{Y}_{0.3}\text{AP}$	1093	2.02	1.98	9.94	39.56	0.2590	6.55 ± 0.09
$\text{Lu}_{0.7}\text{Y}_{0.3}\text{AP}$	1094	2.01	1.99	9.98	39.70	0.2579	6.50 ± 0.09
$\text{Lu}_{0.7}\text{Y}_{0.3}\text{AP}$	1095	2.00	1.98	9.98	39.30	0.2546	6.48 ± 0.09
$\text{Lu}_{0.7}\text{Y}_{0.3}\text{AP}$	1096	2.01	1.99	9.98	39.70	0.2580	6.50 ± 0.09
$\text{Lu}_{0.7}\text{Y}_{0.3}\text{AP}$	1097	2.01	1.98	9.98	39.50	0.2553	6.46 ± 0.09
$\text{Lu}_{0.7}\text{Y}_{0.3}\text{AP}$	1098	2.02	1.99	9.99	40.06	0.2571	6.42 ± 0.09
Average		2.01	1.98	9.97	39.56	0.257	6.50 ± 0.09

Table B.3 Dimensions, weight and calculated density of the $\text{Lu}_{0.7}\text{Y}_{0.3}\text{AlO}_3$ crystals grown by the BTCP (Bogoroditsk Techno Chemical Plant), Russia, batch 2.

Crystal	CCC Number	X [mm]	Y [mm]	Z [mm]	Volume [mm^3]	Weight [g]	Density [g/cm^3]
$\text{Lu}_{0.7}\text{Y}_{0.3}\text{AP}$	1100	1.99	1.98	9.98	39.11	0.2560	6.55 ± 0.09
$\text{Lu}_{0.7}\text{Y}_{0.3}\text{AP}$	1101	2.01	2.02	10.01	40.52	0.2654	6.55 ± 0.09
$\text{Lu}_{0.7}\text{Y}_{0.3}\text{AP}$	1102	2.00	1.99	9.97	39.46	0.2593	6.57 ± 0.09
$\text{Lu}_{0.7}\text{Y}_{0.3}\text{AP}$	1103						
$\text{Lu}_{0.7}\text{Y}_{0.3}\text{AP}$	1104	1.99	1.98	9.97	39.07	0.2556	6.54 ± 0.09
$\text{Lu}_{0.7}\text{Y}_{0.3}\text{AP}$	1105	1.99	1.99	10.05	39.58	0.2576	6.51 ± 0.09
$\text{Lu}_{0.7}\text{Y}_{0.3}\text{AP}$	1106	2.01	1.96	10.05	39.37	0.2555	6.49 ± 0.09
$\text{Lu}_{0.7}\text{Y}_{0.3}\text{AP}$	1107	2.00	1.98	9.97	39.26	0.2576	6.56 ± 0.09
$\text{Lu}_{0.7}\text{Y}_{0.3}\text{AP}$	1108	2.02	1.98	10.05	39.98	0.2610	6.53 ± 0.09
$\text{Lu}_{0.7}\text{Y}_{0.3}\text{AP}$	1109	2.00	1.98	10.04	39.54	0.2579	6.52 ± 0.09
$\text{Lu}_{0.7}\text{Y}_{0.3}\text{AP}$	1110	2.01	2.02	10.01	40.42	0.2653	6.56 ± 0.09
$\text{Lu}_{0.7}\text{Y}_{0.3}\text{AP}$	1111	2.00	2.03	10.00	40.38	0.2637	6.53 ± 0.09
$\text{Lu}_{0.7}\text{Y}_{0.3}\text{AP}$	1112	1.98	1.99	10.05	39.38	0.2569	6.52 ± 0.09
$\text{Lu}_{0.7}\text{Y}_{0.3}\text{AP}$	1113	2.01	2.02	10.00	40.38	0.2667	6.60 ± 0.09
$\text{Lu}_{0.7}\text{Y}_{0.3}\text{AP}$	1114	1.99	2.02	10.04	40.24	0.2628	6.53 ± 0.09
Average		2.00	1.99	10.01	39.76	0.260	6.54 ± 0.09

Table B.4 Dimensions, weight and calculated density of the $\text{Lu}_{0.7}\text{Y}_{0.3}\text{AlO}_3$ crystals grown by the BTCP (Bogoroditsk Techno Chemical Plant), Russia, batch 3.

Crystal	CCC Number	X [mm]	Y [mm]	Z [mm]	Volume [mm ³]	Weight [g]	Density [g/cm ³]
Lu_{0.7}Y_{0.3}AP	1134	1.99	1.99	10.06	39.77	0.2560	6.44 ± 0.09
Lu_{0.7}Y_{0.3}AP	1135	2.01	2.01	9.86	39.73	0.2592	6.52 ± 0.09
Lu_{0.7}Y_{0.3}AP	1136	2.01	2.02	9.85	39.79	0.2564	6.44 ± 0.09
Lu_{0.7}Y_{0.3}AP	1137	2.00	2.00	9.86	39.42	0.2543	6.45 ± 0.09
Lu_{0.7}Y_{0.3}AP	1138	2.02	2.03	9.86	40.31	0.2600	6.45 ± 0.09
Lu_{0.7}Y_{0.3}AP	1139	2.02	2.02	9.85	40.19	0.2590	6.44 ± 0.09
Lu_{0.7}Y_{0.3}AP	1140	1.98	2.01	10.06	39.92	0.2582	6.47 ± 0.09
Lu_{0.7}Y_{0.3}AP	1141	2.00	2.01	9.85	39.41	0.2549	6.47 ± 0.09
Lu_{0.7}Y_{0.3}AP	1142	2.01	2.02	9.85	39.97	0.2594	6.49 ± 0.09
Lu_{0.7}Y_{0.3}AP	1143	1.99	2.00	10.05	40.05	0.2587	6.46 ± 0.09
Lu_{0.7}Y_{0.3}AP	1144	2.01	2.01	9.85	39.68	0.2572	6.48 ± 0.09
Lu_{0.7}Y_{0.3}AP	1145	2.02	2.02	9.86	40.11	0.2587	6.45 ± 0.09
Lu_{0.7}Y_{0.3}AP	1146	2.01	2.02	9.85	39.99	0.2587	6.47 ± 0.09
Lu_{0.7}Y_{0.3}AP	1147	2.01	2.02	9.87	39.95	0.2576	6.45 ± 0.09
Lu_{0.7}Y_{0.3}AP	1148	2.02	2.02	9.86	40.11	0.2597	6.47 ± 0.09
Lu_{0.7}Y_{0.3}AP	1149	1.98	2.01	10.05	39.90	0.2574	6.45 ± 0.09
Average		2.00	2.01	9.90	39.89	0.258	6.46 ± 0.09

Table B.5 Dimensions, weight and calculated density of the $\text{Lu}_{0.7}\text{Y}_{0.3}\text{AlO}_3$ crystals grown in the mass-production phase by the BTCP (Bogoroditsk Techno Chemical Plant), Russia.

Crystal	X [mm]	Y [mm]	Z [mm]	Volume [mm ³]	Weight [g]	Density [g/cm ³]
LuYAP 1	2.00	1.99	7.94	31.60	0.2055	6.50 ± 0.09
LuYAP 2	2.00	1.98	7.94	31.44	0.2060	6.55 ± 0.09
LuYAP 3	1.99	1.99	7.95	31.48	0.2064	6.55 ± 0.09
LuYAP 4	2.00	2.00	7.97	31.88	0.2087	6.54 ± 0.09
LuYAP 5	2.01	2.01	7.94	32.08	0.2089	6.51 ± 0.09
LuYAP 6	2.00	2.00	7.90	31.60	0.2069	6.55 ± 0.09
LuYAP 7					0.2069	
LuYAP 8	1.99	1.99	7.98	31.60	0.2057	6.51 ± 0.09
LuYAP 9	1.99	1.98	7.97	31.40	0.2049	6.52 ± 0.09
LuYAP 10	2.01	1.99	7.95	31.80	0.2083	6.55 ± 0.09
Average	2.00	1.99	7.95	31.65	0.207	6.53 ± 0.09

Table B.6 Dimensions, weight and calculated density of the MLS crystals grown by UTAR.

Crystal	CCC Number	X [mm]	Y [mm]	Z [mm]	Volume [mm ³]	Weight [g]	Density [g/cm ³]
MLS 12105		1.98	1.97	10.06	39.24	0.2872	7.32 ± 0.11
MLS 12107		1.98	1.98	10.03	39.32	0.2849	7.25 ± 0.10
MLS 13021	1165	2.05	1.95	9.95	39.78	0.2884	7.25 ± 0.10
MLS	1117a	2.02	1.94	10.33	40.48	0.2899	7.16 ± 0.21

Table B.7 Dimensions, weight and calculated density of the Lu₂SiO₅ crystals grown by CTI, Knoxville

Crystal	CCC Number	X [mm]	Y [mm]	Z [mm]	Volume [mm ³]	Weight [g]	Density [g/cm ³]
LSO 1	1046	1.92	1.9	9.6	35.02	0.2568	7.33 ± 0.11
LSO 2	1047	1.94	1.91	9.59	35.53	0.2563	7.21 ± 0.11
LSO 3	1048	1.93	1.92	9.6	35.57	0.2584	7.26 ± 0.11
LSO 4	1049	1.92	1.9	9.62	35.09	0.2579	7.35 ± 0.11
LSO 5	1050	1.92	1.93	9.6	35.57	0.2603	7.32 ± 0.11
LSO 6	1051	1.92	1.9	9.59	34.98	0.2571	7.35 ± 0.11
LSO 7	1052	1.92	1.87	9.61	34.50	0.2515	7.29 ± 0.11
LSO 8	1053					0.2575	
Average		1.92	1.90	9.60	35.18	0.257	7.30 ± 0.11

Table B.8 Dimensions, weight and calculated density of the Lu₂SiO₅ crystals grown by Photonic Materials, Glasgow

Crystal	CCC Number	X [mm]	Y [mm]	Z [mm]	Volume [mm ³]	Weight [g]	Density [g/cm ³]
LSO 7	1121	2.04	1.91	10.07	39.24	0.2889	7.36 ± 0.11
LSO 8	1122	1.87	1.98	10.05	37.10	0.2754	7.42 ± 0.11
LSO 9	1123	1.88	1.98	10.03	37.22	0.2774	7.45 ± 0.11
LSO 10	1124	2.01	1.87	10.06	37.62	0.2777	7.38 ± 0.11
LSO 11	1125	1.90	1.96	10.05	37.33	0.2779	7.44 ± 0.11
LSO 12	1126	1.90	1.99	10.08	37.99	0.2812	7.40 ± 0.11
Average		1.93	1.95	10.05	37.75	0.280	7.41 ± 0.11

Table B.9 Dimensions, weight and calculated density of the LYSO crystals grown by Photonic Materials, Glasgow. The crystals have different compositions. The yttrium concentration is given in the table.

Crystal	CCC Number	X [mm]	Y [mm]	Z [mm]	Volume [mm ³]	Weight [g]	Density [g/cm ³]
LYSO 15%	1150	2.23	2.21	10.25	50.38	0.3437	6.82 ± 0.18
LYSO 15%	1151	2.24	2.20	10.33	50.65	0.3587	7.08 ± 0.18
LYSO 2.5%	1152	2.04	1.87	10.05	38.24	0.2716	7.10 ± 0.21
LYSO 2.5%	1153	2.04	2.10	10.07	42.91	0.3067	7.15 ± 0.20
LYSO 1%	1154	2.05	1.87	9.68	37.11	0.2712	7.31 ± 0.21
LYSO 2.5%	1156	2.10	1.88	9.83	38.81	0.2864	7.38 ± 0.21
LYSO 2.5%	1157	2.08	1.88	9.24	36.13	0.2692	7.45 ± 0.22
LYSO 2.5%	1159	2.07	2.02	10.12	42.32	0.3013	7.12 ± 0.20
LYSO 2.5%	1160	2.10	2.05	10.15	43.70	0.3117	7.13 ± 0.20
LYSO 2.5%	1170	2.01	2.00	10.07	40.48	0.2984	7.37 ± 0.11
LYSO 2.5%	1171	2.01	2.00	10.07	40.48	0.2976	7.35 ± 0.10

Acknowledgments

Without the help and support of promoters, colleagues and friends I would not have been able to write this thesis.

First of all I want to thank Prof. Dr. Hannes Aiginger, Atominstitut der Österreichischen Universitäten, for his encouragement, guidance and his support. He accompanied and guided me in the last 4 years with continuous support and competence. It was also him who proposed me to apply to the doctoral program at CERN and who initiated this thesis in the technology transfer division. I am grateful to Dr. Karin Poljanc for her support and for the proof reading.

My special thank goes to Dr. Paul Lecoq my supervisor at CERN for the many stimulating discussions, his advise related to all aspects of this work, and his patience in answering all my questions and concerns in spite of lack of time.

I am grateful to the other members of the Crystal Clear Collaboration at CERN Dr. Etienne Auffray, Dr. Mark Schneegans and Dr. Pablo Sempere-Roldan, who spent a lot of time correcting my thesis, helping me with the set-up of the measurements or searching equipment with me. Many thanks to Cecilia Pizzolotto for the help with the decay time measurements.

Special thank goes to the technicians Alain, Antonio, Bruno, Erik, Hervé, Norbert, and Rene who always helped me organizing equipment in the CERN jungle and with whom I developed a special friendship.

Not to forget a nice ¿Hola, que tal? to my room colleague Laura. We shared not only the office for one year but also our problems and pleasures of live and friendship.

It was a pleasure for me to work in the laboratories of the other CCC members and I want to thank all of them for sharing their knowledge with me and providing me a lot of pictures and results for my thesis.

A very special experience was the work with Prof. Dr. Marek Moszynski who invited me to his lab in Swierk, where I learned a lot from his knowledge on scintillation crystal. A big part of my work was strongly influenced by his ideas and discussions with him. He and Maciek Kapusta showed great patience in explaining and teaching me spectroscopic techniques. The many discussions with the “master of scintillators” helped me to improve my knowledge on inorganic scintillators and to boost my thesis.

During my stay in Poland I also had the opportunity to work in the laboratory of Prof. Dr. Andrzej Wojtowicz. He and his group (Jarek, Piotr and Winicjusz) introduced me in

the phenomenon of low temperature thermoluminescence. I will never forget the night sessions. Without their hospitality, my stay in Torun would not have been so unforgettable.

Special thanks goes to Dr. Karl Ziemons who organized a trip for me to his lab in the Forschungszentrum Jülich. The group at the ZEL (Dr. Simone Weber, Dr. Matthias Streun, Horst Larue, Alexander) showed great patient when introducing me in their electronic read-out system and they always kept me on the “pulse” of their PrimatePET development. A big thanks and hug goes to Uwe, Maryam and Daniela for providing me a place to sleep (Danke Schön!!!).

I enjoyed working in the laboratory of Prof. Dr. Christian Pedrini and Dr. Christophe Dujardin in Lyon. A big part of my thesis was done in their lab and I am grateful to them for giving me the opportunity to share their knowledge on UV spectroscopy with me.

I also want to thank Prof. Jean-Michel Moreau (ESIA, Annecy, France) for performing the x-ray diffraction measurements.

There are many friends who contributed a lot to my well being in Geneva. Special thanks go to Sabine, Andreas, and Harald for spending time together after work and who were always there when I needed them. I also had a great time with the Badminton group – Peter, Manfred S., Lotte, Manfred H., Angelika, and Daniel – with whom I swung the racket, cooked in the evenings or played “Siedler von Catan” till dawn. I very much enjoyed lunchtime with the “Mittagsrunde” (Martin A., Edda, Werner, Christian, Christoph, Clausi, Martin M., Axl, Thomas uva) where we discussed Austrian politics and many other important things of life.

Also in Austria there are some friends (Alexandra, Andrea, Eva, Karin, Magdalena, Gerold) whom I want to thank for staying in touch with me over the last years and keeping our friendship alive. Its good to have email!

I am grateful to the Austrian Ministry for Science for the financial support, which made my stay at CERN possible.

My biggest gratitude belongs to my family. They gave me steady encouragements and always supported me with unconditional confidence. I especially want to thank my parents for giving me a real home where I can always go to.

Curriculum Vitae

Personal Information

Name	Claudia Kuntner
Citizenship	Austria
Date of birth	8 March 1976, Krems

Educational History

2000 – 2003	Ph.D Studies in Physics at the Vienna University of Technology and at CERN Topic: <i>Evaluation of new inorganic scintillators for application in a prototype small animal PET scanner</i>
30. June 2000	Dipl.-Ing. (M.S.) in Technical Physics
1994 – 2000	Studies of Technical Physics at the Vienna University of Technology, Diploma thesis at the Atomic Institute of the Austrian Universities (Atominstitut der Österreichischen Universitäten) and at the department of Radiotherapy and Radiobiology at the General Hospital Vienna Topic: <i>In-vivo dosimetry using semiconductor detectors: Pre-clinical evaluation of the measurement accuracy</i>
1990 – 1994	BORG Krems (Grammar School), Natural Science branch
1986 – 1990	Secondary School Mautern
1982 – 1986	Elementary School Mautern

Publications

C. Kuntner, E. Auffray, C. Dujardin, P. Lecoq, C. Pedrini, M. Schneegans, *Development of new mixed LuYAP:Ce crystals for application in a small animal PET scanner with DOI capability*, Proc. IEEE Nuclear Science Symposium and Medical Imaging Conference, Norfolk, USA, November 2002, to be published.

C. Kuntner, E. Auffray, P. Lecoq, C. Pizzolotto, M. Schneegans, *Intrinsic energy resolution and light output of the $\text{Lu}_{0.7}\text{Y}_{0.3}\text{AP:Ce}$ scintillator*, Nucl. Instr. and Meth. A 493/3 (2002) pp. 131-136.

C. Kuntner, H. Aiginger, E. Auffray, J. Glodo, M. Kapusta, P. Lecoq, M. Moszynski, M. Schneegans, P. Szupryczynski, A.J. Wojtowicz, *Scintillation properties and mechanism in $\text{Lu}_{0.8}\text{Y}_{0.2}\text{AlO}_3\text{:Ce}$* , Nucl. Instr. and Meth. A 486 (2002) pp. 176-180.